Sensing Animal Group Behavior and Bio-clutter in the Ocean Over Continental Shelf Scales

by

Srinivasan Jagannathan

Submitted to the Department of Mechanical Engineering in partial fulfillment of the requirements for the degree of

Doctor of Philosophy

at the

MASSACHUSETTS INSTITUTE OF TECHNOLOGY

June 2011

Author ....
Department of Mechanical Engineering
March 11, 2011

Certified by ....
Nicholas C. Makris
Professor of Mechanical and Ocean Engineering
Thesis Supervisor

Accepted by ....
David E. Hardt
Chairman, Department Committee on Graduate Students

Sensing Animal Group Behavior and Bio-clutter in the Ocean Over Continental Shelf Scales

by

Srinivasan Jagannathan

Submitted to the Department of Mechanical Engineering
on March 11, 2011, in partial fulfillment of the
requirements for the degree of
Doctor of Philosophy

Abstract

Fish populations often comprise the largest biomass in a productive marine ecosystem. They typically play an essential role in inter-trophic energy transport, and serve as a mainstay for human consumption comprising roughly 16% of the animal protein consumed by the world's population. Despite their ecological importance, there is substantial evidence that fish populations are declining worldwide, motivating the need for an ecosystem approach to fisheries management through ecosystem scale sensing of fish populations and behavior.

In this Thesis, it is shown how the recently developed Ocean Acoustic Waveguide Remote Sensing (OAWRS) technique can be used to (1) quantify the acoustic scattering response of fish and remotely infer their physiological characteristics to enable species classification, and (2) remotely assess shoaling populations and quantify their group behavior in a variety of oceanic ecosystems.

Shoal dynamics is studied by developing a novel Minimum Energy Flow (MEF) method to extract velocity and force fields driving motion from time-varying density images describing compressible or incompressible motion. The MEF method is applied to experimentally obtained density images, spanning spatial scales from micrometers to several kilometers. Using density image sequences describing cell splitting, for example, we show that cell division is driven by gradients in apparent pressure within a cell. By applying MEF to fish population density image sequences collected during the OAWRS 2003 experiment in the New Jersey strataform, we quantify (1) inter-shoal dynamics such as coalescence of fish groups over tens of kilometers, (2) fish mass flow between different parts of a large shoal and (3) the stresses acting on large fish shoals.

Observations of fish shoals made during the OAWRS 2006 experiment in the Georges Bank are used to confirm general theoretical predictions on group behavior believed to apply in nature irrespective of animal species. By quantifying the formation processes of vast oceanic fish shoals during spawning, it is shown that (1) a rapid transition from disordered to highly synchronized behavior occurs as population density reaches a critical value; (2) organized group migration occurs after this transition; and (3) small sets of leaders significantly influence the actions of much larger groups.

Several species of fish, birds, insects, mammals and other self propelled particles (SPPs) are known to group in large numbers and exhibit orderly migrations. The stability of this orderly state of motion in large SPP-groups is studied by developing a fluid-dynamic theory for flocking behavior based on perturbation analysis. It is shown that an SPP group where individuals assume the average velocity of their neighbours behaves as a fluid over large spatial scales. The existence of a critical population density above which perturbations to the orderly state of motion are damped is also shown. Further, it is shown that disturbances can propagate within mobile groups at speeds much higher than that of the individuals, facilitating rapid information transfer. These findings may explain how large shoals of fish and flocks of birds are able to stay together and migrate over large distances without breaking up.

Fish shoals are ubiquitous in continental shelf environments and so are a major cause of acoustic clutter in long-range Navy sonars. It is shown that man-made air-filled cylindrical targets have very different spectral acousic scattering response than fish, so that they can be distinguished using multi-frequency measurements. It is also shown that the use of the Sonar Equation to model scattering from the man-made targets leads to large errors differing by up to an order of magnitude from measurements. A Greens' Theorem-based full-field model that describes scattering from vertically extended cylindrical targets in range-dependent ocean waveguides is shown to accurately describe the statistics of the targets' scattered field measured during OAWRS 2001, 2003 and 2006 experiments.

Measurements of infrasound made during the 2004 Indian Ocean Tsunami event that occured on December 26, 2004 have suggested that large-scale tsunamis may produce deep-infrasonic signals that travel thousands of kilometers in the atmosphere. By developing an analytical model to describe air-borne infrasound generation by tsunamis and applying it to the 2004 Indian Ocean Tsunami, it is shown that the mass flow of air caused by changes in sea-level due to a tsunami can generate infrasound of sufficient amplitude to be picked up thousands of kilometers away. The possibility of detecting tsunamis via seismic means is also examined by developing an analytical model for quantifying very low frequency (0.01-0.1 Hz) Rayleigh waves generated by a tsunami.

Thesis Supervisor: Nicholas C. Makris
Title: Professor of Mechanical and Ocean Engineering

Acknowledgments

First and foremost, I would like to thank my advisor, Prof. Nicholas Makris for his guidance, support and encouragement. He has been an inspiration for me in many ways, and I thank him for his patient guidance through the years.

I would also like to thank my Thesis committee members Prof. Berthold Horn, who guided me through my work on Machine Vision, Prof. Iain Couzin and Dr. Sunwoong Lee who gave me invaluable comments on my Thesis.

Financial support for this work has been provided by Prof. Nicholas Makris via funds from the ONR Geoclutter Program and the ONR Graduate Traineeship Award. I would like to thank Dr. Ellen Livingston at ONR for her financial support.

I am very grateful to my colleagues who have provided helpful comments and engaging conversations. I thank Purnima Ratilal, Joshua Wilson, Sunwoong Lee, Tianrun Chen, Ioannis Bertsatos, Deanelle Symonds, Hyun Joe Kim, Ding Wang, Hadi Tavakoli Nia, Ankita Jain, Anamaria Ingnisca, Ninos Donabed, Mark Andrews, Roger Gong, and Ameya Galinde. Special thanks to Ioannis who helped proof read many parts of my Thesis and papers. I am also grateful to Geoff Fox for his administrative help.

I thank my friends at MIT and Boston, Manikandan Mathur, Ravikanth Annavarapu, Sasan Saidi, Koushik Balasubramaniam, Sivaram Cheekiralla, Srinivas Moorkanikkara, Hariharan Lakshmanan, Vikram Sivakumar, Senthilkumaran Ramaswamy, Mythreyi Solai, Muthazagu Palaniswamy, and Karthik Thyagaraja.

I am forever grateful to my fiancee, Vasudha, who has provided encouragement whenever I needed it.

To my brothers Sampathkumar and Srivatsan and my Parents, none of this would have been possible without your endless love.

Contents

List of Figures

List of Tables

Chapter 1

Introduction

The impermeability of water to electromagnetic waves has made acoustics the primary modality for remote sensing and imaging in the ocean. Long before man discovered their use, sound waves were used by whales and dolphins to communicate and sense their environment under the ocean. This was first noted by Aristotle in his work *Historia Animalium*, where he makes detailed observations of dolphin sounds. Perhaps the earliest use of underwater acoustics in the Navy dates back to the Renaissance period in Europe, when Leonardo da Vinci used sound tubes to listen for distant enemy ships. The world's navies still depend on ocean acoustics, and in particular ocean waveguide acoustics, as the primary remote sensing tool for both surface and subsurface vessels as well as in fixed installations such as the sound surveillance system (SOSUS) network. From the latter part of the 19th century until now, ocean acoustics has been used for a wide variety of oceanographic remote sensing applications, including monitoring fish shoals, quantification of ocean and seabed structure and passive tracking of vocalizing marine mammals.

1.1 Motivation

Besides the many military and commercial uses, the study and monitoring of fish shoals is among the most important scientific application of ocean acoustics. Oceanic fish serve as a mainstay for human consumption and comprise nearly 16% of all animal protien consumed by the world's population. Despite their ecological importance, there is substantial evidence that fish populations are declining worldwide, which has prompted the need to monitor their abundance and study their behavior. Fish also play an important role in inter-trophic energy transport, which makes it often difficult to study fish shoals in isolation from other organisms and ecological processes that constitute a marine ecosystem. Since many ecologically important fish species band together to form vast oceanic fish shoals, it is important to remotely sense fish shoals over ecosystem scales and study their large scale *group behavior*. Techniques for long-range, ecosystem-wide remote sensing and imaging of fish shoals as well as associated methods of studying fish group behavior can then be very helpful in monitoring the health of marine ecosystems.

Since swimbladder-bearing fish are strong acoustic scatterers, acoustic sensing techniques are particularly suitable to detect and study fish schools. The application of a wide-area Ocean Acoustic Waveguide Remote Sensing (OAWRS) system to image large fish shoals over ecosystem scales, remotely characterize fish physiology, and help remotely classify fish species is described in Chapter 2. In particular, results from two experiments, the OAWRS 2003 experiment in the New Jersey strataform and the OAWRS 2006 experiment in the Gulf of Maine, are presented to demonstrate the synoptic wide-area imaging and continuous monitoring capabilities of the OAWRS system. The shoaling behavior of Atlantic herring is studied in detail in both these experiments. The utility of OAWRS to remotely assess populations and study behavior of a variety of fish species and other marine organisms, such as Antarctic krill, in other, different oceanic ecosystems around the world is also demonstrated. Thus the wide-area imaging and continuous monitoring capabilities of OAWRS is shown to help the study of marine ecology and ecosystem-based approach to fisheries management.

In Chapter 3, a novel method is developed to extract fish motion fields and stresses in large fish shoals from time-varying wide-area population density images obtained using OAWRS. The technique, known as the Minimum Energy Flow (MEF) method, can be used to compute velocity and force fields governing motion observed in density image sequence describing compressible or incompressible motion. By applying MEF to wide-area population density images obtained during the OAWRS 2003 experiment, fundamental aspects of the dynamics of large fish shoals are quantified, including (1) inter-shoal dynamics such as coalescence of fish groups over tens of kilometers, (2) fish mass-flow between different parts of a large shoal, and (3) stresses acting on large shoals.

General predictions about animal group behavior believed to apply in nature irrespective of species are confirmed in Chapter 4, using observations of fish shoals made during the OAWRS 2006 experiment conducted in the Gulf of Maine. By quantifying the formation processes of vast Atlantic herring shoals during spawning, it is shown that (1) a rapid transition from disordered to highly synchronized behavior occurs as the population density reaches a critical value; (2) organized group migration happens after this transition; and (3) small sets of leaders significantly influence the actions of larger groups.

The ability to form large organized groups is not just found in fish, but also in several species of birds, insects and mammals. The stability of this orderly state of motion in large groups of self-propelled particles (SPPs) is studied using a perturbation analysis in Chapter 5. It is shown that an SPP group where individuals assume the average velocity of their neighbours behaves as a fluid over large spatial scales. The existence of a critical population density above which perturbations to the orderly state of motion are damped is also shown. Further, it is shown that disturbances can propagate within mobile groups at speeds much higher than that of the individuals, facilitating rapid information transfer. These findings may explain how large shoals of fish and flocks of birds are able to stay together and migrate over large distances without breaking up.

The strong acoustic scattering from fish shoals also makes them dominant sources of clutter or unwanted noise in some applications such as Navy sonars that operate in continental shelf environments. It is shown in Chapter 6, for example, that air-filled vertically extended cylindrical man-made targets appear similar to fish schools in long-range sonar images recorded during the OAWRS 2003 and 2006 experiments. However, the spectral characteristics of the acoustic field scattered by fish schools is shown to be very different from that of man-made targets at frequencies near fish swimbladder resonance, so that man-made targets can be distinguished from fish schools. Using bistatic, long-range measurements of acoustic scattered returns from vertically extended air-filled cylindrical targets, it is shown that the commonly used Sonar Equation model leads to large errors differing by up to an order of magnitude from measurements. A Greens' Theorem-based full-field model that describes scattering from vertically extended cylindrical targets in range-dependent ocean waveguides is shown to accurately describe the statistics of the targets' scattered field measured during the OAWRS 2001, 2003 and 2006 experiments.

Measurements of infrasound made during the 2004 Indian Ocean Tsunami event that occured on December 26, 2004 in the aftermath of the Sumatran-Andaman Earthquake have suggested that large-scale tsunamis may produce deep-infrasonic signals that travel thousands of kilometers in the atmosphere. By developing an analytical model in Chapter 7 to describe air-borne infrasound generation by tsunamis, it is shown that the mass flow of air caused by changes in sea-level due to a passing tsunami can generate infrasound. The analytical model is then used to quantify deep infrasound (0.01-0.1 Hz) generated by the 2004 Indian Ocean Tsunami, which we show is of sufficient amplitude to be picked up thousands of kilometers away. The possibility of detecting tsunamis via seismic means is also examined by developing an analytical model for quantifying very low frequency (0.01-0.1 Hz) Rayleigh waves generated by a tsunami.

1.2 The OAWRS concept: ocean-acoustic waveguides

The use of acoustics to detect oceanic fish dates back to the vertical echo-sounders introduced in the 1930s [17, 18]. As their names imply, echo-sounders detect fish by listening for echoes scattered from schools that may be located directly beneath slow moving research vessels. Since these highly localized line-transect methods rely on in-situ measurements restricted to their immediate vicinity (tens to hundreds of meters), they greatly under-sample the ocean in space and time, leaving an incomplete and ambiguous record of fish abundance and behavior. Recently, a method known as Ocean Waveguide Acoustic Remote Sensing (OAWRS) was developed for instantaneous imaging and continuous monitoring of fish populations over continental shelf-scale areas, covering thousands of square km, at an areal rate tens of thousands to millions of times greater than that of conventional methods such as echo-sounders.

In contrast to the direct-path line-of-sight concepts used in conventional fish finding echo-sounders, OAWRS uses a completely different concept for long-range imaging: acoustic waveguides. OAWRS takes advantage of the fact that it is always possible to form an acoustic waveguide in the ocean by trapping sound between the ocean-atmosphere and the ocean-seabed boundaries [23, 68, 187, 251, 43, 258, 33, 78, 124]. In such acoustic waveguides sound propagates over long ranges via trapped modes that suffer only cylindrical spreading loss rather than the spherical loss suffered in conventional fish-finding technologies. These modes are analogous to those on a vibrating guitar string, where the entire ocean water column acts like the plucked string. Interaction with the ocean surface and bottom, or multipath interference, is typically essential to form the waveguides needed for OAWRS, so the technique is fundamentally different from past 'line-of-sight' methods.

In continental shelf environments, most applications of long range ocean acoustics involve waveguides that are formed by interaction of sound with both of these boundaries [187, 124, 43, 258, 33]. Even though this is often referred to as "shallow-water acoustics" or "littoral acoustics" the acoustic wavelength is much smaller than the ocean depth so that acoustic transmission involves many propagating modes (Fig. 1-1). This type of boundary-interacting, continental-shelf propagation is considered for various fish types in Chapter 2.

Sometimes, it is possible to form acoustic waveguides in the ocean where sound does not interact with the ocean-atmosphere boundary, ocean-seabed boundary or both, by appropriate experimental design involving restriction to sufficiently shallow propagation angles [187, 251, 43, 258, 33, 78, 124]. In the deep ocean in mid-latitudes,

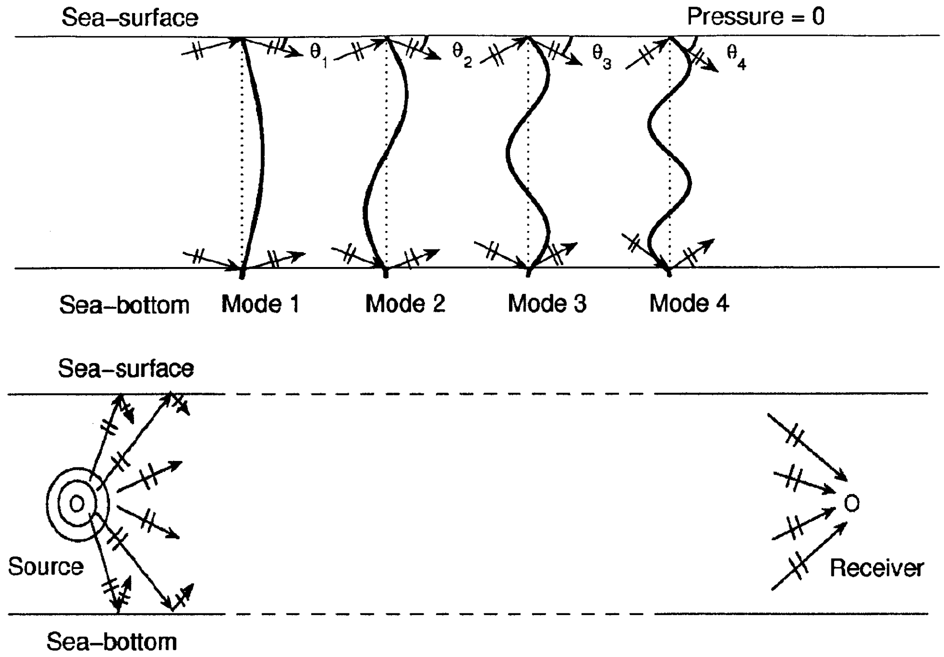

Figure 1-1: Sketch illustrating boundary-interacting, long-range, modal propagation in a typical continental shelf waveguide. Spherically spreading waves from a point source are multiply reflected from the ocean-atmosphere and ocean-seafloor boundaries to form vertical modes that propagate horizontally. In an iso-sound speed layer, each mode can be expressed as a vertical standing wave formed by the interference of an up and down-going plane wave of fixed horizontal grazing angle determined by the layer's boundary conditions. The sketch shows modes and equivalent plane waves for a canonical iso-sound speed continental shelf environment, known as a Pekeris waveguide.

for example, the combination of increasing pressure with depth and relatively warm water near the surface typically leads to a sound speed minimum at approximately 1000 m depth where the acoustic field can be trapped, leading to sound propagation over thousands of km without interacting with either boundary. In polar environments, cold water near the surface leads to sound speed minima at, or near, the surface; so a waveguide can be formed by refraction at depth and surface reflection with sound rays that never interact with the seafloor boundary. Such sound speed structures have been exploited over the years in many remote sensing applications [23, 187, 43, 258, 33, 78, 124].

Regardless of the specific ocean waveguide, there are many standard approaches for determining the acoustic field in an ocean waveguide, including those using normal mode, wave number integration, parabolic equation and ray tracing [124] formulations. Similarly, there are many standard models using each of these approaches, e.g. Kraken, Ocean Accoustics and Seismics Exploration Synthesis (OASES), Range-dependent Acoustic Model (RAM) and Generic Sonar Model (GSM) [206, 124, 45], which have been carefully benchmarked over the years [36, 44, 123, 246, 247, 234, 269]. In Chapter 2, we use the US Navy standard RAM parabolic equation model to determine transmission loss in all of the continental shelf environments investigated.

1.3 Development of OAWRS

During the 1940s, researchers in the University of Californias Division of War Research (UCDWR) noted a mid-water layer scattering agent, which was later called "deep scattering layer" (DSL). After bathypelagic fish with gas-filled swimbladders were proposed to be the cause of this DSL [161], the frequency response of these fish was studied to identify resonance [102, 101, 10, 12, 160, 11]. For a good historical review of the vast literature on the ability of gas-filled fish bladders to scatter sound see [101] and [267]. In all the above experiments, the range at which the fish were imaged was <500 m.

Weston & Revie [268] used a fixed single-beam sonar in a monostatic setting to image underwater sonar returns over long ranges (>10 km) in a narrow horizontal angular sector. They observed temporal variations that were believed to be consistent with fish migrations, but lacked data to confirm this. Rusby et al. [221] generated synthetic aperture images of the continental shelf environment with a towed, single-beam sidescan sonar. Each synthetic aperture image required hours of surveying, which led to high spatiotemporal undersampling and aliasing. They described features as possible fish groups "only when the shape of the groups remain[ed] sufficiently distinctive from run to run," which would bias the analysis towards highly static population distributions. They then guided a fishing vessel to the location of such a feature, where the vessel made a large fish catch. In these and other earlier long range experiments [178, 70], independent confirmation of fish was not available by simultaneous measurements.

Makris et al. [158, 157] used a horizontal array that formed simultaneous beams over a 360° horizontal azimuth, enabling them to conduct OAWRS surveys of marine life instantaneously over wide areas, tens of thousands of km^2. With regular and rapid temporal image updates, they were able to work in a true Eulerian reference frame and map fish distributions without aliasing in space or time. They established long-range ocean acoustics as a method for detecting, imaging, and estimating fish populations (Appendix A) by coregistration with large numbers of simultaneous OAWRS, conventional fish-finding sonar (CFFS) and trawl samples, where the latter provided direct species identification. Large numbers of simultaneous measurements are necessary for confirmation because fish are ubiquitous in continental shelf environments and can easily be found accidentally in a region causing strong acoustic returns. Non-simultaneous correlations can then easily be spurious, as can correlations at only a single or very small number of spatial locations. This lesson was learned with geologic features of the subbottom, which are also ubiquitous in many continental shelf environments, and often have spurious spatial correlation with acoustic returns caused by other mechanisms [212].

In earlier work at very short ranges on the order of the water depth, $\sim$300 m, and so with conventional direct-path rather than waveguide propagation and sensing, Isaacs & Schwartzlose [116] used a U.S. Navy mine hunting sonar operating on the southern California continental shelf to detect strong scatterers which they confirmed to be fish using local trawls.

Chapter 2

Ocean Acoustic Waveguide Remote Sensing (OAWRS) of marine ecosystems

2.1 Introduction

Fish populations often comprise the largest biomass component in a productive marine ecosystem. They typically play an essential role in inter-trophic energy transport [54], and serve as a mainstay for human consumption comprising roughly 16% of the animal protein consumed by the worlds population [73]. Despite their ecological importance, there is substantial evidence that fish populations are declining worldwide [119, 173], which has led to calls for an ecosystem approach to fisheries management [54, 34, 235] through ecosystem-scale sensing and monitoring of marine habitats [86]. This vision, however, is difficult to attain with conventional methods [228] which typically rely on in-situ measurements restricted to the immediate vicinity (tens to hundreds of meters) of slow moving research vessels and greatly undersample the ocean in time and space [239, 17, 169, 165, 228]. Recently, a method known as Ocean Acoustic Waveguide Remote Sensing (OAWRS) was developed for instantaneous imaging and continuous monitoring of fish populations and marine life over continental shelf-scale areas, covering thousands of km^2, at an areal rate tens of thousands to millions of times greater than that of conventional methods [158]. Continuous monitoring with OAWRS produces unaliased wide-area movies of the spatial and temporal distributions of fish populations that can reveal horizontal behavioral patterns on an ecosystem scale. This may enable better modeling and prediction of ecosystem dynamics as well as correlation with physical and biological variables including those describing oceanography, climate, food, predation and human activity, and help to realize ecosystem approaches to fisheries management.

Ocean waveguide acoustics has been used for underwater remote sensing in all oceans for about a century [258]. It takes advantage of the fact that it is always possible to form an acoustic waveguide in the ocean by trapping sound between the ocean-atmosphere and the ocean-seabed boundaries, as is described in numerous textbooks (e.g. [23, 187, 43, 258, 33, 78, 124]. In the early 19th century the principal applications were naval [23, 43, 258]. The worlds navies still depend upon ocean waveguide acoustics as the primary underwater remote sensing tool for both surface and sub-surface vessels as well as in fixed installations such as the sound surveillance system (SOSUS) network [258, 172]. In these applications, horizontal sensing ranges typically span distances many orders of magnitude larger than the water depth [23, 68, 187, 251, 43, 258, 33, 78, 124]. From the latter part of the 19th century until now, ocean waveguide acoustics has been used for a wide variety of oceanographic remote sensing applications, including quantification of ocean and seabed structure and passive tracking of vocalizing marine mammals [187, 251, 43, 258, 33, 78, 124, 164].

In this chapter,we first show some results from two recent OAWRS experiments (OAWRS 2003 and 2006) to demonstrate the utility of OAWRS in studying fish shoaling behavior over ecosystem scales. We then describe a potential method for remote species classification using OAWRS, which we demonstrate with field data. We also show how OAWRS may be used in oceanic ecosystems to remotely assess populations and study the behavior of fish over broad temporal and spatial scales. A technical description of the OAWRS approach appears in Appendices A to D.

2.2 Investigating fish shoaling behavior over ecosystem scales using OAWRS

The OAWRS approach for studying marine life was first demonstrated in 2003 off the US Continental Shelf south of Long Island, NY, i.e. the Mid-Atlantic Bight. With a single transmission of a 1 s duration linear frequency modulated (LFM) waveform, OAWRS surveyed an area as large as the state of Connecticut or New Jersey (Fig. 2-1). The imaging is effectively instantaneous because the entire region is surveyed in less time than it takes a marine organism to traverse a single OAWRS resolution cell [158]. The OAWRS approach was used again with the National Marine Fisheries Service (NMFS) annual herring survey of the Gulf of Maine and Georges Bank to study herring group behavior associated with spawning in September-October 2006 [157]. In both the OAWRS experiments, a vertical source array transmitted sound in the frequency range of 390 to 1400 Hz, i.e. near swimbladder resonance for many fish species in the survey regions. Echoes scattered from fish were received by a towed horizontal receiving array. Instantaneous snapshots of the ocean environment over thousands of km^2 (Fig. 2-2) were then formed by charting acoustic returns in horizontal range and bearing by temporal matched filtering and beamforming.In this Thesis, we will be using data from both these experiments to study both the acoustic scattering characteristics of fish and their group behavior.

With the "first look" of OAWRS in the Mid-Atlantic Bight (Fig. 2-1) it was possible to make a number of fundamental scientific discoveries about the (1) instantaneous horizontal structural characteristics, (2) temporal evolution, and (3) propagation of information within very large fish shoals [158]. These include the findings that: the instantaneous spatial distribution of fish observed follows a fractal or power law process, so that structural similarity exists at all scales from metres to tens of km (previously evidence for structural similarity existed only for small scales <100 m [77]; large shoals (Fig. 2-2) are far more horizontally contiguous in 2D than was previously believed based on 1D line transect methods which sometimes inaccurately portray them as disjoint clusters [203, 77]; the temporal autocorrelation scale of population

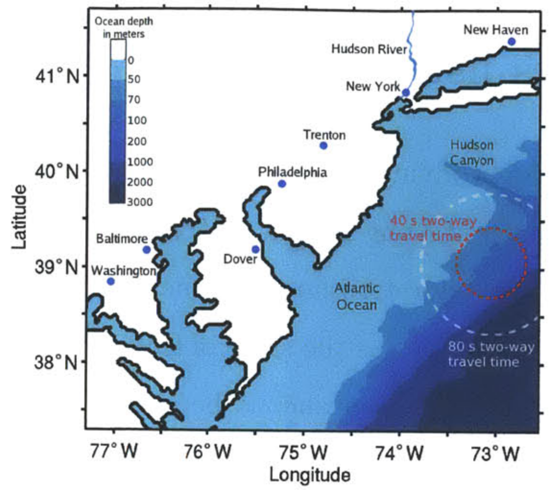

Figure 2-1: Areal coverage of a single Ocean Acoustic Waveguide Remote Sensing (OAWRS) transmission during the 2003 survey on the US east coast continental shelf. An area of 60 km diameter was surveyed every 40 s (red circle), or 120 km every 80 s (white circle), depending on ping repetition rate and recording time.

change within a very large shoal is extremely short, on the order of minutes, which is why fish shoals can suddenly disappear from conventional survey vessels; temporal fluctuations in shoal population also follow a power-law process, making the shoals far more predictable; and fish density waves regularly propagate information over km scales, 3 orders of magnitude larger than previously observed [227, 210], at speeds an order of magnitude faster than fish can swim, which apparently help large shoals remain cohesive. These observations were made from distances >10 km from the shoals with sound at least 3 orders of magnitude less intense than conventional fish-finding sonar (CFFS) due to the efficiency of ocean acoustic waveguide propagation.

General predictions about animal group behavior believed to apply in nature irrespective of species [261, 253, 217, 48, 37] were confirmed by monitoring the Georges Bank marine ecosystem (Fig. 2-3) with OAWRS in the fall of 2006. By quantifying the formation process of vast oceanic herring shoals during spawning, it was shown that (1) a rapid transition from disordered to highly synchronized behavior occurs as fish population density reaches a critical value; (2) organized group migration occurs after this transition; and (3) small sets of leaders significantly influence the actions of

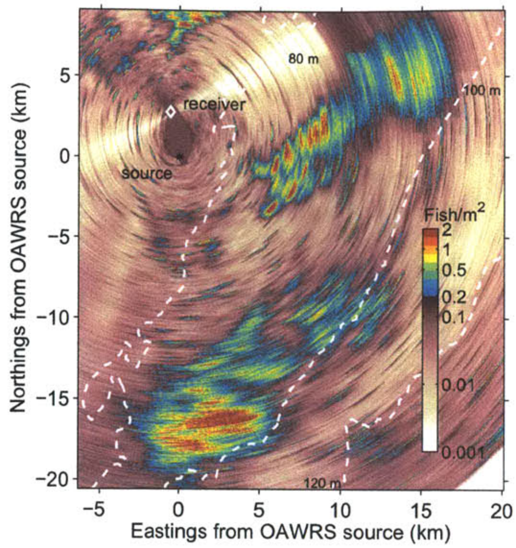

Figure 2-2: Instantaneous OAWRS image showing fish shoals near the continental shelf edge 100 km south of Long Island, New York (May 15, 2003, 10:36 Eastern Daylight Time [EDT]). Dashed white lines mark depth contours. Receiver array resolution decreases as viewing directions go from normal (broadside) to parallel (endfire) to the array axis, leading to blurring of the eastern portion of the northeastern shoal. Population density estimation employs waveguide propagation and scattering models, correction for OAWRS areal resolution, and calibration with local conventional fish-finding sonar (CFFS) measurements as described in Appendices A to D.

much larger groups (Makris et al. 2009a). The spawning process was found to follow a regular diurnal pattern in space and time which proved to be difficult to detect without continuous wide-area sensing abilities (Fig. 2-3). First, pre-existing populations of diffusely scattered herring reached a critical density at one or more discrete locations near the northern flank of Georges Bank just before sunset, apparently in response to diminishing light level. The emergence of leading clusters then triggered a shoal-forming convergence wave (Fig. 2-4) that propagated tens of km in tens of min, i.e. at speeds an order of magnitude greater than herring can swim [111], (Fig. 3 of [157]). Subsequent migrations were observed towards southern spawning grounds on Georges Bank, immediately after shoals formed. The evidence suggests the primary biological function of the shoals is a prelude to synchronized spawning and the shoals form in deeper water with migrations under cover of darkness to avoid predators [157].

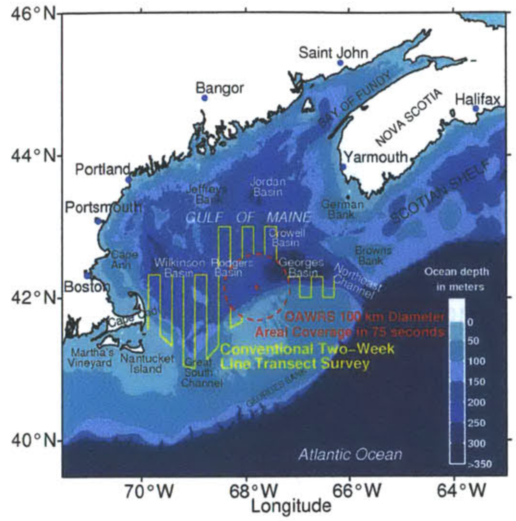

Figure 2-3: Areal coverage of a single OAWRS transmission in the Gulf of Maine, 2006). A region of 100 km diameter (red circle) is surveyed every 75 s. Line transects of National Marine Fisheries Service (NMFS) 2 week survey are shown in yellow.

As Vicsek et al. [261] theoretically predicted, and Buhl et al. [37] showed with laboratory experiments, if an individual assumes the mean speed and direction of those in its sphere of perception, then a rapid transition from disordered to highly synchronized behavior occurs when a critical population density is attained. This may be understood by noting that as the radii of perception begin to overlap with increasing population density, chain reactions become possible. Laboratory experiments [217] and simulations [48] showed that a small number of individuals can significantly influence decision making in large groups.

2.3 Remote sensing of swimbladder properties

For fixed fish length and water depth, acoustic scattering at, or near, swimbladder resonance is a strong function of swimbladder volume (Fig. 2-5, Appendix F).The acoustic scattering can vary significantly across species and so may be helpful in species classification, as has been discussed for salmon [178], blue whiting [142], Pacific hake [177], and Atlantic herring [176]. Swimbladder volume can also be used to estimate neutral buoyancy depth, where a fishs weight is balanced by its buoyancy

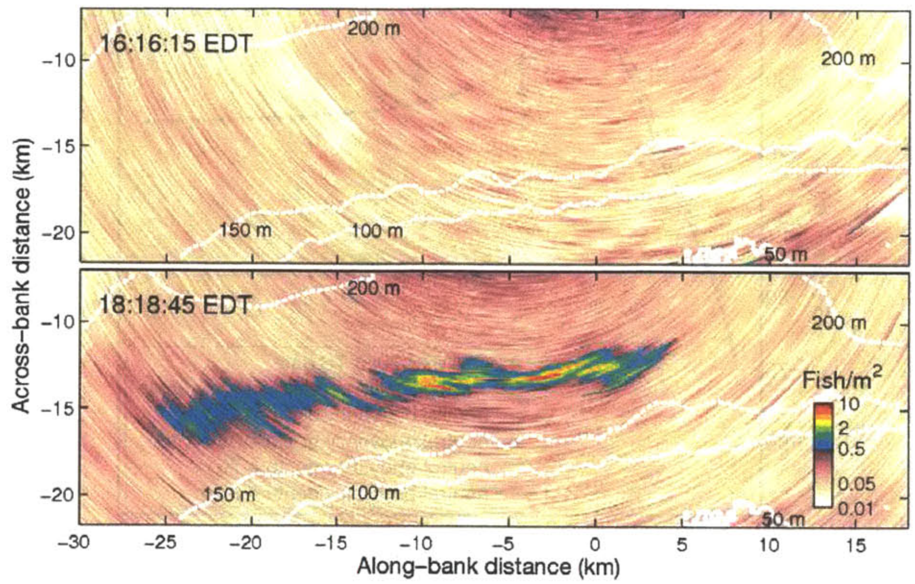

Figure 2-4: Example of regular diurnal pattern of large pre-spawning shoals forming near sunset (18:08 h EDT) on Oct 03, 2006. Top panel: 1 hr 45 min before sunset - no shoal present. Bottom panel: 10 min after sunset - large shoal present. White dashed lines mark depth contours. Population density estimation employs waveguide propagation and scattering models, correction for OAWRS areal resolution, and calibration with local CFFS measurements as described in Appendices A to D. The positive vertical axis points 16° counter-clockwise of true north

[176]. At any given depth, neutral buoyancy requires the swimbladder to occupy ~5% of the total fish volume [125], where more air is required to maintain this ratio as depth increases due to the compressive effects of increasing pressure.

We used OAWRS to determine swimbladder volume and help classify the species of shoaling fish observed during the 2003 OAWRS experiment (Fig. 2-2) [158]. The mean scattering cross-section of a shoaling fish determined with OAWRS 2003 data and local CFFS constraints is shown in Fig. 2-5 in terms of target strength (TS) following the approach given in Appendix D for 3 frequencies 415, 925, and 1325 Hz corresponding to the center frequencies of the 390 to 440, 875 to 975 and 1250 to 1400 Hz LFM waveforms used in OAWRS 2003 [153, 158]. The least squares fit between the empirically determined OAWRS TSs and those determined from a standard fish scattering model (Love model, Appendix F), with CFFS-measured constraints on fish habitation depth and length, leads to a neutral buoyancy depth of 78 m with a

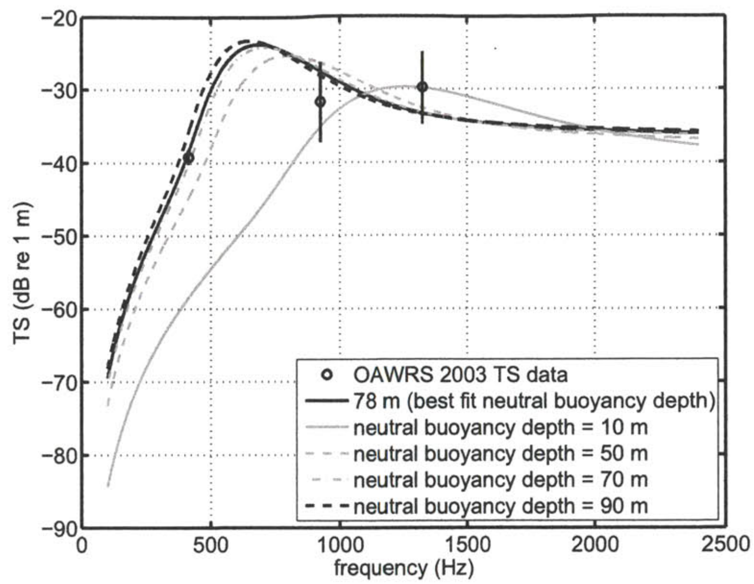

Figure 2-5: Target strength (TS) data for 3 frequencies (circles ± SD; independent samples; 415 Hz: n = 181, SD = 0.7 dB; 925 Hz: n = 46, SD = 5.5 dB; 1325 Hz: n = 46, SD = 5 dB; see Appendix D) corresponding to the mean scattering cross section of a shoaling fish species in the OAWRS 2003 experiment constrained by local CFFS. TS frequency curves for 5 different neutral buoyancy depths are computed with Love's model (US Navy standard for low frequency fish scattering; Appendix F) by depth-averaging the expected scattering cross section of an individual fish over the layer observed by CFFS for the Gaussian length distribution (SD 15% of the 28.6 cm mean) determined by CFFS. The least-squares best-fit buoyancy depth between measured data to Love-model TS is given by the black solid line. If the shoaling fish observed in the 70 to 90 m layer were neutrally buoyant closer to the surface (grey line), they would scatter far too weakly below 1.4 kHz to be consistent with the measured OAWRS and CFFS data.

resonance peak at ~700 Hz (black solid line in Fig. 2-5), consistent with the CFFS-measured shoal layer at 70 to 90 m depth. While buoyancy depth need not correspond to habitation depth, the correspondence is advantageous because it enables fish to expend minimal energy to maintain a depth. While the ability to regulate neutral buoyancy over a wide range of depths is usually associated with physoclist fish (closed swimbladders), physostome fish (swimbladder with open duct to the intestine) also have this ability [32, 240]. Physoclists are known to slowly regulate the swimbladder volume through the blood stream [125] and so can achieve neutral buoyancy at any depth, given enough time to adjust [29, 125]. Physostomes, on the other hand, can fill their swimbladders by gulping air at the surface [28]. If this was the only mechanism for them to increase the volume of gas in their swimbladder, then their maximum neutral buoyancy depth would be limited by the maximum volume they could gulp at the surface [248], [Fig. F-1]. Thorne & Thomas [248] measured neutral buoyancy depths of up to 60 m for herring, a physostome, and suggest additional gas production mechanisms, such as from bacteria in the digestive tract [32]. In 1 of 6 experiments, Brawn [32] found swimbladder volume build-up by non-gulping mechanisms within less than 24 hr in herring that were heavily fed with copepods containing bacteria. Neutral buoyancy depths of 40 to 50 m have been determined from near resonance scattering data [176]. Char, another physostome, have also been found to build up gas in their swimbladder even when denied access to the surface [240]. The fish imaged by OAWRS were consistently observed in a 70 to 90 m layer near the seafloor for >12 h by CFFS. The long periods that the fish spent at these depths could be sufficient for both physoclists and physostomes to build up gas in their swimbladder.

From trawl surveys of the New Jersey continental shelf taken one month prior to the 2003 experiment, we list the most probable species that could have comprised the shoals imaged by OAWRS based on frequency of catch: Atlantic herring, scup, hake, black sea bass and alewife [226, 158]. While dogfish and mackerel are also found in the area [226], their scattering responses are expected to be much lower than those of the mentioned fish as dogfish and mackerel lack gas-filled bladders. Of the species typically found in the region, only Atlantic herring and alewife are physostomes, while scup, hake and black sea bass are physoclists. Since Atlantic herring is the most common species sampled in the region [226], and the only one known to form such large, extended shoals, they are most likely the major constituent of the large shoals imaged by OAWRS in 2003 and the dominant cause of scattering measured by both OAWRS and CFFS. The fit between measured TS data and the Love fish scattering model constrains the suspected herring to neutral buoyancy at 78 m depth, which suggests that they should have a mechanism for building up gas in their swimbladder, or they have damping mechanisms which lower and spread the resonance and have shallower neutral buoyancy depth. It is unlikely that another, less abundant species could have dominated the scattering measured by OAWRS and CFFS, since this would require "contaminants" with unrealistically large target strengths to follow the exact spatial distributions of the shoals observed at both OAWRS and CFFS frequencies. Such contamination is inconsistent with trawl data [226], the observed preference of fish to shoal among similar sized individuals [203], and stationarity of CFFS and OAWRS scattering measurements (Appendix D), which show fish of similar length and target strength. The target strengths of shoaling fish in the OAWRS 2003 experiment are consistent with those measured for herring in the 2006 experiment where trawl samples enabled direct species identification [157].

2.4 Potential ecosystem exploration

OAWRS can be used to remotely sense a variety of fish species and other marine organisms, such as Antarctic krill, over broad temporal and spatial scales in ocean ecosystems from knowledge of (1) the expected scattering cross section of an individual (Appendix F), (2) typical population densities, (3) acoustic propagation (Appendix C) and (4) seafloor scattering in each environment (Appendix E). Since the emphasis of the main text is on marine biology and ecology, we discuss physical acoustics issues in Appendices A to D and Appendix F.

A wide range of transmission frequencies may be used for OAWRS, ranging from very low frequencies of several Hz to high frequencies of tens of kHz. Longrange sound propagation in the ocean is less attenuated at lower frequencies and is less sensitive to oceanographic fluctuations. Reverberation from the seafloor tends to be weaker at lower frequencies.

When designing an OAWRS system we need to consider operating at frequencies where fish scattering responses are high. Optimal OAWRS frequencies should be low enough for scattering from any fish to be effectively omni-directional, to make OAWRS insensitive to variations in fish orientation, which is typically not the case in CFFS. Frequency should also be low enough for the received acoustic field scattered from any given fish to be expressible as the product of the 3 factors "transmission to the given fish", "scattering from the fish", and "transmission from the fish" (Appendix B). At CFFS wavelengths, this factorization is typically not possible because propagation and scattering effects are convolved together in an ocean waveguide [211]. Frequencies should be chosen so that acoustic attenuation from propagation through the fish is negligible even over long ranges. If the frequency is too low, on the other hand, the waveguide may no longer support modal propagation (Chapter 1), and so remote sensing may become inefficient.

Table 2.1: Biological characteristics of species used in this study and sources

Type		Swimbladder	Preferred depth (m)	Shoal density (fish/m^2)	Neutral buoyancy depth estimate (m)	Mean length (cm)	Major axis (% of total length)
Alaskan pollock	Adult	Physoclist [228]	110-130 [271]	1-5[107],a	110-130	45[82]	33[82]
	Juvenile	Physoclist [228]	70-100 [271]	10[236],a	70-100	23[82]	33[82]
Peruvian anchovy		Physostome [228]	0-30 (off-ENSO) [273] 40-70 (ENSO) [31]	500-20000[232, 92]	10-40	14.5[182]	30[46]
Barents Sea capelin		Physostome [228] Physostome [228]	125-175 (day) [127] 24-105 (night) [127]	70-750 (day)[85],b 24-105 (night)[85],b	10-30	16[126, 82]	15[126, 82]
Southern blue whiting		Physoclist [228]	150-200 [39]	1[185],c	140-200	39 (male)[39] 51 (female)[39]	33[163]
Argentine hake	Adult	Physoclist [228]	60-90 [147]	0.5[147],d	50-90	38[147]	33
	Juvenile	Physoclist [228]	60-90 [147]	0.3[147],d	50-90	28[147]	33
Atlantic bluefin tuna		Physoclist [249]	3-40 [144]	0.025[e]	10-40	223[109]	33

[a] Typical dense aggregations, [b] Mean school densities, [c] Average density over 1200 km^2, [d] Average density over 16×10^4 km^2, [e] Average density in an OAWRS resolution footprint.

2.4.1 Alaskan pollock (*Theragra chalcogramma*)

Alaskan pollock are a semi-pelagic schooling fish widely distributed in the North Pacific Ocean. They comprise the largest percentage of biomass of any species in the Bering Sea and are an important predator that feed on smaller fish and also cannibalize their juveniles [62]. So, in the Gulf of Alaska, adults are more often found near the bottom (110 to 130 m) while juveniles prefer to stay separate above (70 to 100 m) [271]. We use the parameters summarized in Table 2.1 to describe the pollock, a physoclist species assumed to be neutrally buoyant at the depths they occupy.

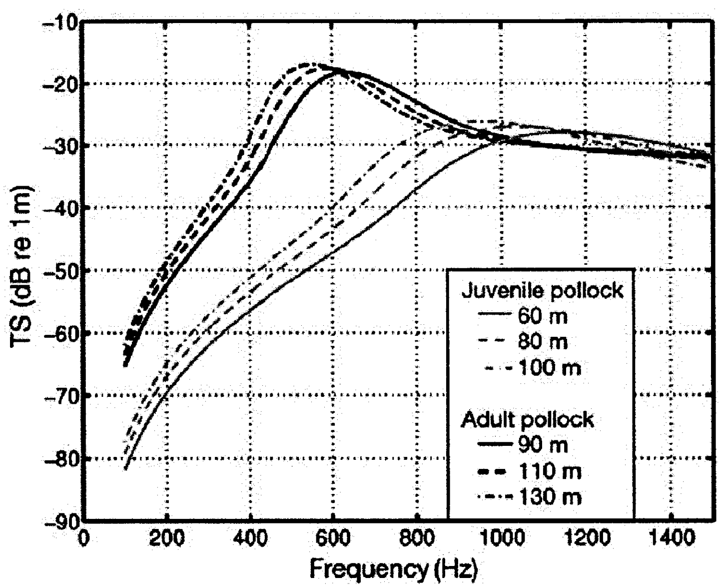

Figure 2-6: *Theragra chalcogramma.* Modeled target strength (TS) 5090 1040 for juvenile and adult pollock in the Gulf of Alaska for varying neutral buoyancy depths (60 to 130 m). The expected TS at a given frequency is found by averaging the scattering cross section over the range of depths and mean body lengths typically associated with these fish (Table 2.1). The body lengths of adults and juveniles are assumed to have a Gaussian distribution, and a SD of 10% of the respective means. Details of the modeling appear in Appendix F.

When operating at the resonance peak near 600 Hz (Fig. 2-6), OAWRS should be able to detect adult pollock schools of a density of 5 fish/m^2 with a signal to noise ratio (SNR) (Appendix E) of 30 to 40 dB (Fig.2-7). OAWRS detections of pollock should then span a dynamic range of 30 to 40 dB in population density, from maximum values of 5 fish/m^2 (Table 2.1) to minimum detectable values of 5×10^{-4} fish/m^2. Single pollock should then be observable to a range of about 3 km with the OAWRS 2003 system. Above resonance, densities of at least 10^2 fish/m^2 are required, but this is still much lower than the typical shoaling densities of pollock (Table 2.1). Even at these higher frequencies, detections above seafloor scattering should span a dynamic range of at least 2 to 3 orders of magnitude, or 20 to 30 dB, in population density. Schools of juvenile pollock should be detectable by OAWRS at resonance, which is relatively broad, over a dynamic range of at least 30 dB (Fig.2-7) in population density, from maximum expected values of 10 fish/m^2 (Table 2.1) to minimum detectable values of 0.01 fish/m^2.

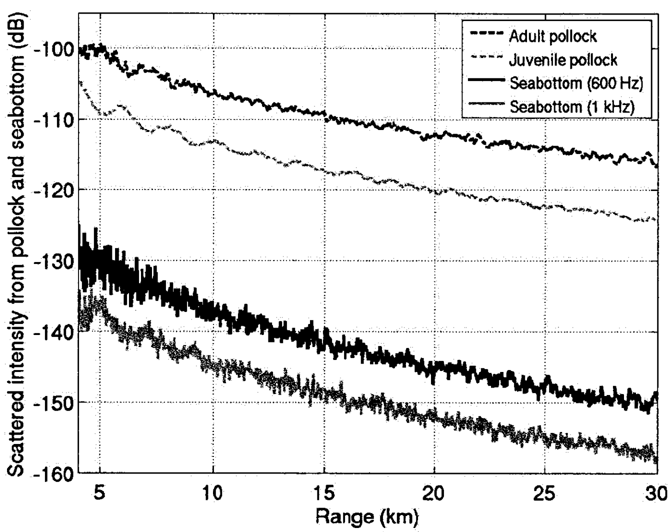

Figure 2-7: *Theragra chalcogramma.* Scattered intensity from adult and juvenile pollock and the seabottom modeled at 600 Hz (black lines) and 1 kHz (grey lines). Pollock are assumed to be uniformly distributed in depth layers (adult: 110 to 130 m; juvenile: 70 to 100 m) and at densities of 5 adult and 10 juvenile ind./m^2 (Table 2.1). A description of the modeling appears in Appendices B, C and E.

2.4.2 Peruvian anchovy (*Engraulis ringens*)

Peruvian anchovy play an essential role in the Humbolt Current upwelling ecosystem as an energy intermediary between phytoplankton and large predatory fish, such as hake and horse mackerel. The diets and livelihood of seabirds, marine mammals, livestock and humans, are also directly tied to anchovy. For details on the Peruvian anchovy fishery see Niquen & Freon [182].

Anchovy have a fairly low tolerance to temperature variations, preferring to stay in the 13 to 23°C range [96]. Therefore, their geographic and depth distributions are highly susceptible to climate change, such as the El Nino Southern Oscillation (ENSO). The deepening of the thermocline and the migration of food sources during ENSO periods cause anchovies to descend to greater depths [181].The average depth range of the Peruvian stock is 0 to 30 m [31, 273] except during ENSO, when they are found at a range of 40 to 70 m [26].

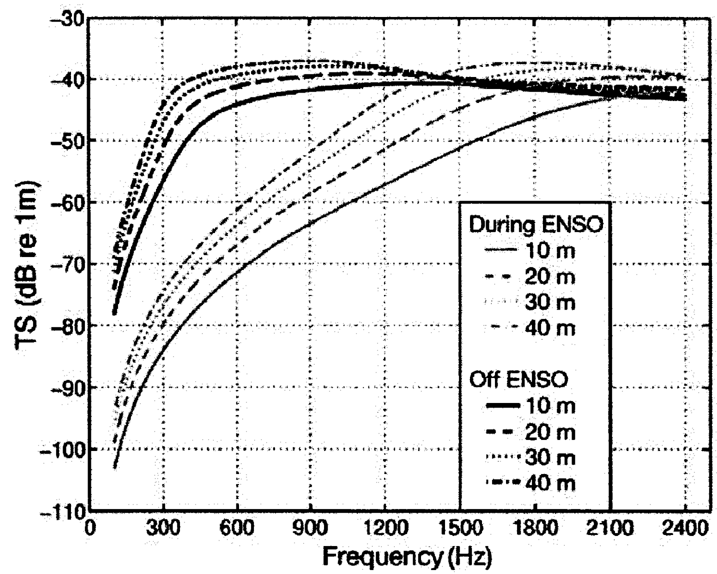

Figure 2-8: *Engraulis ringens.* Modeled target strength for anchovy off the Peruvian coast for different neutral buoyancy depths. Same procedure as that employed in Fig. 2-6. Anchovy in 0 to 30 m during off-ENSO: black lines. Anchovy in 40 to 70 m during ENSO: grey lines. The variation in neutral buoyancy corresponds to minor axis at the surface expanding by a factor of 1.4 to 2.2 (Fig. F-1 in Appendix F).

Anchovy have an average length of 14 to 16 cm [31] (maximum length ~20 cm; [96]. Catches in 2005 showed an average length of 14.5 cm [182]. Anchovy are known to form huge schools [255] and packing densities of 115 [92] to 1312 [232] fish/m^3 have been reported for *Engraulis mordox.* Areal densities then range from 500 to 20000 fish/m^2, given typical vertical school extents of 4 [106] to 15 m [110]. E. ringens, E.

japonicus and E. encrasocolus display similar schooling characteristics as E. mordox [110].

During both ENSO and off-ENSO periods, anchovy should be detectable by OAWRS over a dynamic range of 45 dB in population density, from 20000 to minimum detectable values of 0.6 fish/m^2, which is much lower than typical schooling densities (Table 2.1).

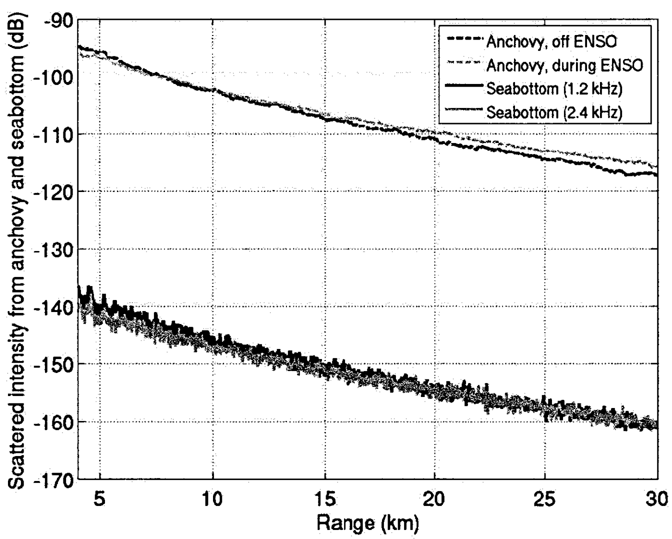

Figure 2-9: Scattered intensity from anchovy during off-ENSO (black lines) and ENSO periods (grey lines) and sea bottom modeled at 1.2 kHz and 2.4 kHz respectively, and for a maximum density of 20000 fish/m^2. The schools are assumed to be distributed with uniform probability within the top 30 m (off- ENSO), and within 40 to 70 m (ENSO) depth.

When operating at 1.2 kHz, where uncertainties in target strengths are lowest (Fig. 2-8), OAWRS should be able to detect anchovy schools with an areal density of 20000 fish/m^2 (15 m thick layer of fish [110]; 1 body-length inter-fish spacing [204]; Table 2.1) with an SNR of 45 dB (Fig. 2-9) during off-ENSO periods. During ENSO, OAWRS should be able to detect anchovy schools of 20000 fish/m^2 with an SNR of 45 dB (Fig. 2-9) when operating at 2.4 kHz, above resonance (Fig. 2-8).

2.4.3 Barents Sea capelin (*Mallotus villosus*)

The Barents Sea holds the largest capelin population in the world and this species is the largest pelagic fish component of the region, with a biomass reaching 6 to 8 $\times$ 10^6 t [85]. Capelin play a key role in energy conversion from zooplankton to higher trophic predators, such as haddock, harp seal, Northeast Arctic cod, whales, and sea birds [85], and is also important to human and livestock consumption [79]. Capelin undergo drastic diel vertical migration patterns, occupying depths of 30 to 60 m at night and 125 to 175 m at day [127]. Packing densities of capelin in the Barents Sea vary from (day) 1.4 to 15 and (night) 0.8 to 3.5 fish/m^3 [225]. Using vertical school extents of (day) 50 and (night) 30 m [127], we obtain mean school densities of (day) 70 to 750 and (night) 24 to 105 fish/m^2. Capelin body lengths average 16 cm [126, 82] (maximum: 20 cm for females, 25 cm for males; [79]. Capelin are characterized by a shorter swimbladder than most fish with a major axis that is approximately 15% of their length [126, 82].

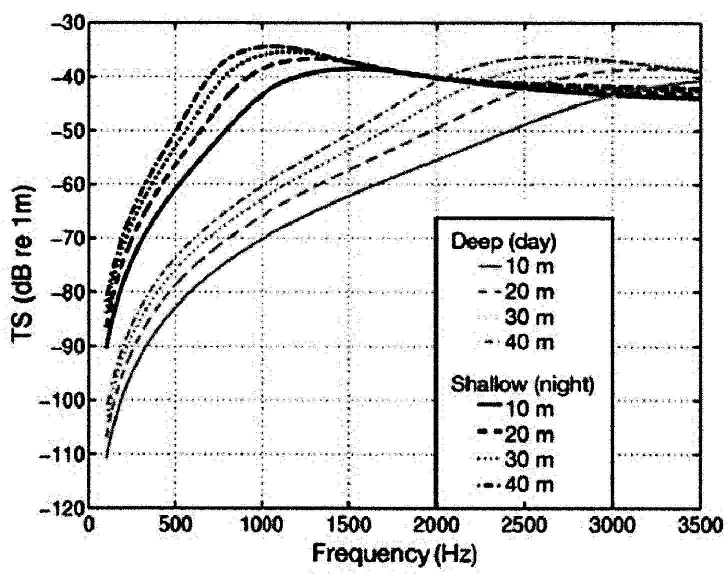

Figure 2-10: *Mallotus villosus.* Modeled target strength (TS) for capelin at 2 different water layers (Table 2.1) in the Barents Sea, for different neutral buoyancy depths. Shallow (night): black lines; deep (day): grey lines. Same procedure as that employed in Fig. 2-6

When operating at the resonance peak near 1.2 kHz (Fig. 2-10), OAWRS should be able to detect capelin schools of a density of 105 fish/m^2 (night; Table 2.1) with an SNR of 30 dB (Fig. 2-11). Capelin should then be detectable by OAWRS over a dynamic range of 30 dB in population density between 105 and 0.1 fish/m^2, which is much lower than typical schooling densities. Daytime schools of capelin (750 fish/m^2, Table 2.1) should be detectable by OAWRS at resonance (2.4 kHz) with an SNR of at least 45 dB (Fig. 2-11). Daytime schools of capelin should then be detectable by OAWRS over a dynamic range of 45 dB in population density from 750 to a minimum value of 0.02 fish/m^2, which are much lower than typical schooling densities (Table 2.1).

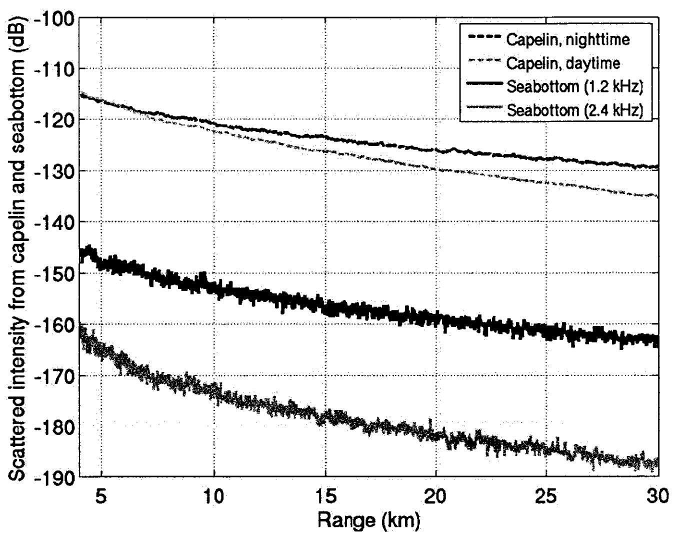

Figure 2-11: *Mallotus villosus.* Scattered intensity from capelin and seabottom modeled at 1.2 kHz (night: black lines) and at 2.4 kHz (day: grey lines). Capelin are assumed to have packing densities of (night) 105 and (day) 750 fish/m^2, and to be uniformly distributed in a depth layer (night: 30 to 60 m; day: 125 to 174 m)

2.4.4 Southern blue whiting (*Micromesistius australis*)

The continental shelf and adjacent waters off Southern Patagonia constitute one of the main fishing grounds of the Argentine Sea. The Southern blue whiting is the most abundant demersal-mesopelagic fish in this region [39], and is the third largest species caught by local fishing fleets [39, 146], after Argentine hake and hoki. Southern blue whiting typically occupy water depths of 100 to 200 m [3] along the Patagonia continental slope and shelf break and provide a major food source for larger higher-trophic predators, such as Argentine hake, whales, sea lions, as well as sea-birds, including the yellow-eyed penguin and black-browed albatross [245, 42, 118].

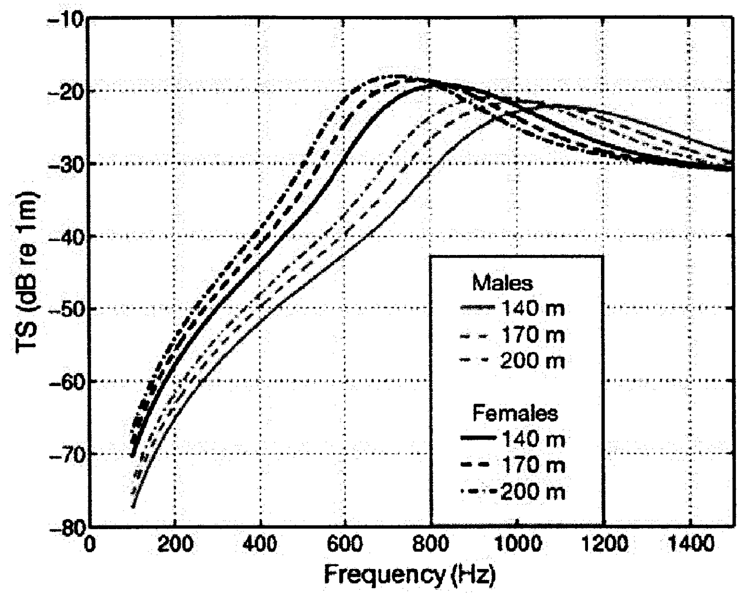

Figure 2-12: *Micromesistius australis.* Modeled target strength (TS) for southern blue whiting in the Argentine-Falklands region for different neutral buoyancy depths. Black lines: female; grey lines: males. Same procedure as that employed in Fig. 2-6.

The TS of southern blue whiting is modeled by assuming a uniform vertical distribution over a 50 m thick layer from 150 to 200 m depth [39]. Since whitings are physoclists, they are expected to be neutrally buoyant over a similar depth range. Trawl samples from typical spawning stocks [39] show a bimodal distribution of lengths associated with age and sex (mean length; male: 39 cm; female: 51 cm [39]. The areal density of 1 fish/m^2 (Table 2.1) is the average density derived from trawl catches over a large area covering hundreds of km^2 [185]. Southern blue whiting are known to mass in dense aggregations wherein the school densities may be much higher than those reported in Table 2.1.

When operating at the resonance peak near 800 Hz (Fig. 2-12, black lines), OAWRS should be able to detect female-dominated schools of an areal density of 1 fish/m^2 with an SNR of 30 dB (Fig. 2-13). Female-dominated schools should then be detectable by OAWRS over a dynamic range of at least 30 dB in population density, from values of 1 to 0.001 fish/m^2, which is much lower than typical schooling densities (Table 2.1). Male-dominated shoals of typical density 1 fish/m^2 should be detectable by OAWRS at resonance (~1 kHz; Fig. 2-12, grey lines) with an SNR of 25 dB (Fig. 2-13). Male-dominated schools should then be detectable by OAWRS over a dynamic range of at least 25 dB in population density from 1 to a minimum detectable value of 0.003 fish/m^2 which is much lower than typical schooling densities (Table 1). It should then be possible to observe both single males and females up to a range of about 2 km.

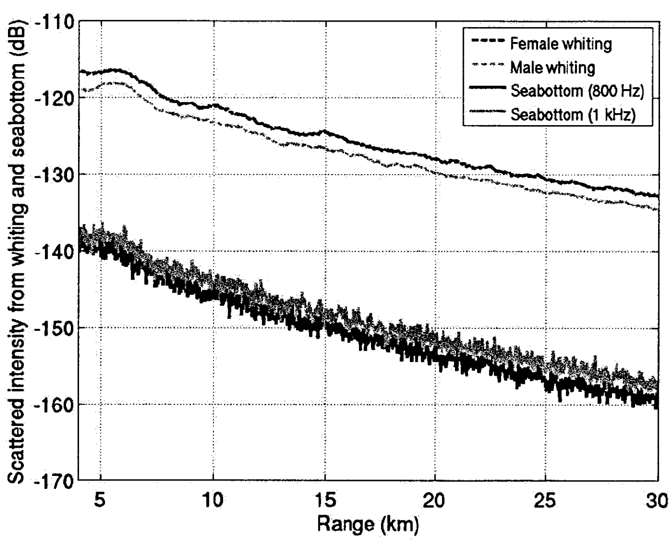

Figure 2-13: *Micromesistius australis.* Scattered intensity from whiting and seabottom modeled at 800 Hz (female: black lines) and at 1 kHz (male: grey lines). The whiting are assumed to have a packing density of 1 fish/m^2, and to be distributed from 150 to 200 m depth with uniform probability.

2.4.5 Argentine hake (*Merluccius hubbsi*)

Argentine hake is a mid-trophic level species providing forage for whales, sea lions, penguins, sea-birds, and other fauna native to the Patagonian ecosystem [6]. Argentine hake are known to feed on smaller fish such as anchovies, juvenile hake, southern blue whiting, squids, and macrozooplankton [74]. Argentine hake are typically found in the coastal and continental shelf environments of Falkland-Malvinas Islands between the 100 to 200 m isobaths. Fishing pressures on Argentine hake in the 1990s caused shifts to deeper water and lower density spawning populations [147].

Argentine hake are known to amass in large shoals in coastal waters at depths between 60 and 90 m. Spawning occurs from October to February, with peak activity in January. Early in the spawning season, hake populations are dominated by juveniles of both sexes with a mean length ~28 cm [147]. Towards the end of the spawning season, larger adult hake (mean lengths ~38 cm) accumulate along with the juveniles [147]. The densities reported in Table 1 are average densities derived from trawl catches over a large area covering 4×10^4 km^2 [147]. Hake are known to mass in dense aggregations wherein the school densities may be much higher than those reported in Table 2.1. Both juvenile and adult hake are physoclist, and are assumed to be neutrally buoyant at 60 to 90 m depth.

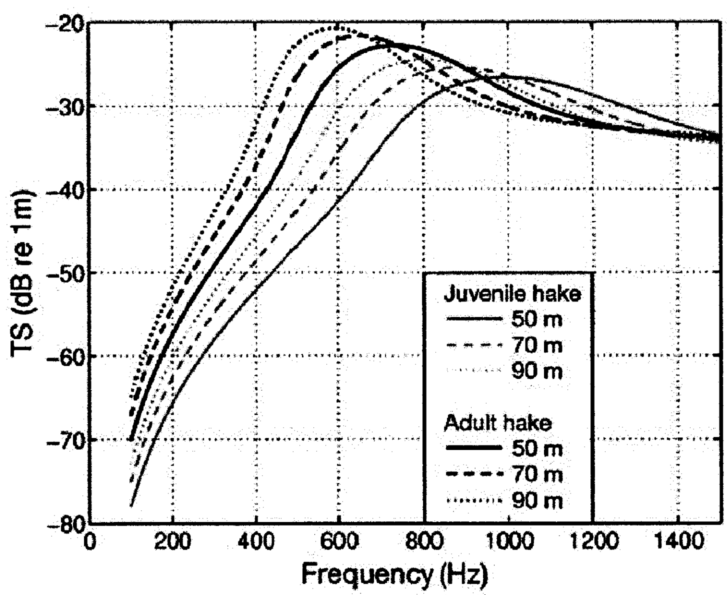

Figure 2-14: *Merluccius hubbsi.* Modeled target strength (TS) for hake in the beginning (corresponding to a majority of juveniles: grey lines) and end (corresponding to a majority of adults: black lines) of the spawning season, off Argentina. Same procedure as that employed in Fig. 2-6.

When operating at the resonance peak near 650 Hz (Fig. 2-14, black lines), OAWRS should be able to image adult hake shoals of population density of 0.5 fish/m^2 (Table 2.1) with an SNR of 25 dB (Fig. 2-15). OAWRS detections of adult hake should then span a dynamic range of at least 25 dB in population density from 0.5 (Table 2.1) to a minimum detectable value of 0.002 fish/m^2. Above resonance, densities of at least 0.02 fish/m^2 are required, but this is still much lower than the average shoaling densities (Table 2.1), so that OAWRS imagery should span a dynamic range of at least 2 orders of magnitude, or 20 dB, in population density.

Schools of juvenile hake with a population density of 0.3 fish/m^2 should be detectable by OAWRS at their resonance of 900 Hz (grey lines in Fig. 2-14) with an SNR of 20 dB (Fig. 2-15). OAWRS detections of juvenile hake should then span a dynamic range of at least 20 dB in population density, from 0.3 fish/m^2 to a minimum detectable value of 0.003 fish/m^2.

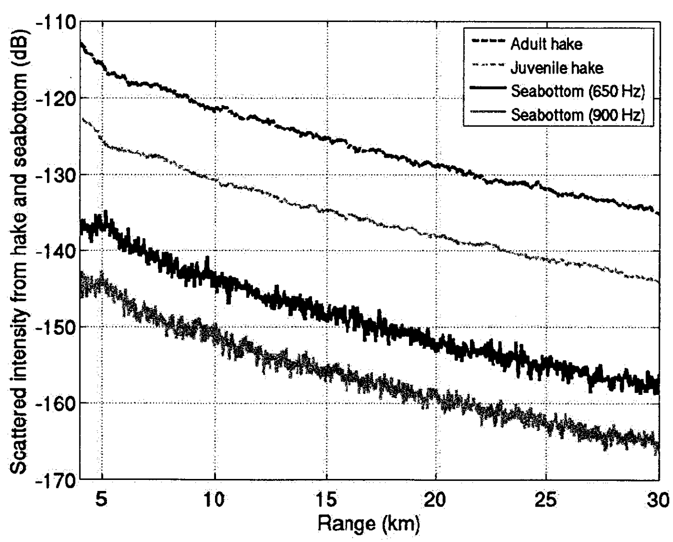

Figure 2-15: *Merluccius hubbsi.* Scattered intensity from hake and seabottom modeled at 650 Hz (adults: black lines) and 900 Hz (juveniles: grey lines). During the day, hake are assumed to be uniformly distributed in depth layers (adults: 60 to 90 m, packing density 0.5 fish/m^2; juveniles: 60 to 90 m, density 0.3 fish/m^2)

2.4.6 Atlantic bluefin tuna (*Thunnus thynnus*)

Atlantic bluefin tuna are large top-predators that feed on mid-sized fish. Their size and speed allows them to evade most predators, with the exception of sharks, larger toothed whales and humans [38]. As physoclists, neutral buoyancy is expected at their common swimming depths of 10 to 40 m [144]. A typical tuna school is ~20 m in diameter [179], with an inter-fish separation of 1 body length (areal density of 0.25 fish/m^2) [195].

For the OAWRS 2003 system, where operating frequencies are above the resonance at ~50 Hz (Fig. 2-16), typical tuna schools occupy areas smaller than an OAWRS resolution cell for ranges > 70 m. The effective areal density of a single school within an OAWRS resolution footprint is then given by the ratio: "area occupied by the tuna school" : "area of the footprint"×"school density of 0.25 fish/m^2". For example, at a range of 10 km the effective areal density is ~0.025 fish/m^2. Since the effective density is a function of the OAWRS resolution footprint area, the SNR varies with range (Fig. 2-17) from 15 to 20 dB.

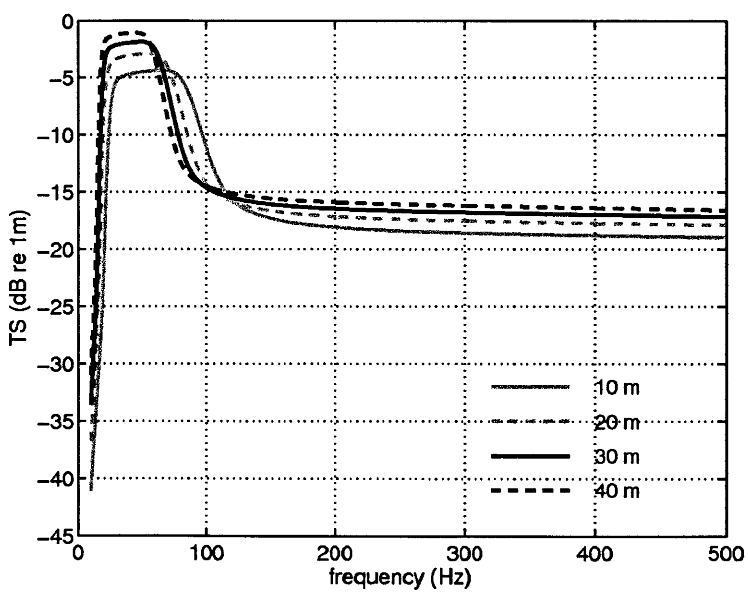

Figure 2-16: *Thunnus thynnus.* Modeled target strength (TS) for bluefin tuna with different neutral buoyancy depths (10 to 40 m). Same procedure as that employed in Fig. 2-6.

An OAWRS system could be designed to operate near resonance (50 Hz) and with sufficiently high resolution so that the "area occupied by a single typical tuna school"$\geq$"OAWRS resolution cell" (AppendixB). In this scenario, OAWRS could image typical tuna schools with an SNR of 50 dB, given the higher TS and effective density. OAWRS detections of tuna should then span a dynamic range of 50 dB in population density, from 0.25 fish/m^2 (Table 2.1) to minimum detectable values of 3×10^{-6} fish/m^2, or $\sim$1 fish in a 600$\times$600 m area.

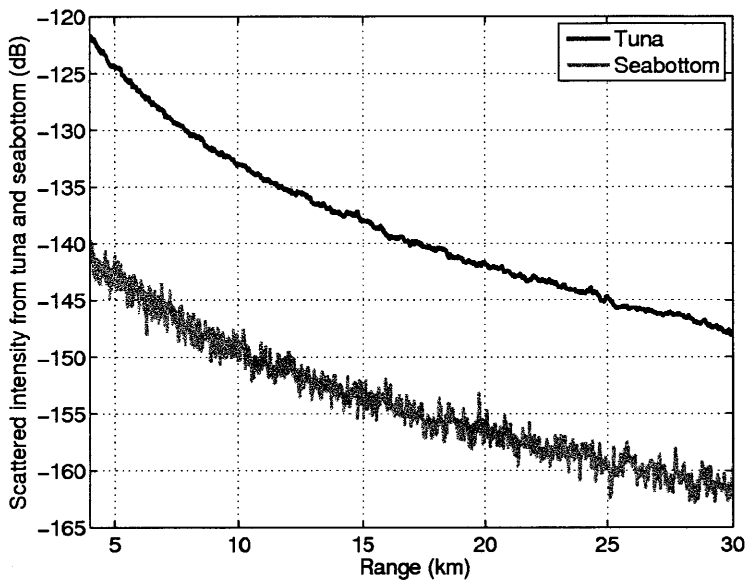

Figure 2-17: *Thunnus thynnus.* Scattered intensity from bluefin tuna and seabottom modeled at 950 Hz. Tuna packing density within an OAWRS resolution footprint is assumed to be range-dependent and is given by the ratio "area occupied by the tuna school" : "area of the resolution footprint" $\times$ "school density of 0.25 fish/m^2". For example, for the OAWRS 2003 system, the effective density of a school within the OAWRS footprint would be 0.025 fish/m^2 at 10 km. At 20 km, the footprint area doubles and the effective density reduces to 0.0125 fish/m^2. This is reflected in the figure as a reduction in the signal to noise ratio as the range increases. The tuna are assumed to be uniformly distributed in a layer from 0 to 30 m water depth.

The wide-area spatial coverage and continuous temporal monitoring of OAWRS can be an asset in studying the behavioral dynamics and spatial distributions of fast-swimming, highly migratory pelagic fish. Since bluefin tuna swim at speeds of 4 km/h [117] and occupy broad geographic scales, they are difficult to survey with conventional methods such as electronic tagging, satellite, or spotter plane aerial imaging which are limited to studying individual fish or surficial populations [144, 179].

The ability of OAWRS to image and continuously track small, but rapidly swimming schools of marine creatures of $\sim$100 m extent was demonstrated in 2003 [158]. For example, a small compact group, located at 9 km south and 3 km east of the OAWRS source, was observed traveling north at $\sim$5 km/h, consistent with a typical tuna school (Fig. 2-18). Similar aggregations were observed within a 1.5 km radius exhibiting the morphological, dynamical spatial distributions, speeds and uniform trajectories typical of fast-swimming tuna schools. The OAWRS-measured densities for these groups of $\sim 5\times10^{-4}$ fish/m^2, after compensating for the expected TS of an individual at 415 Hz (~ -17 dB), follows expectations for tuna.

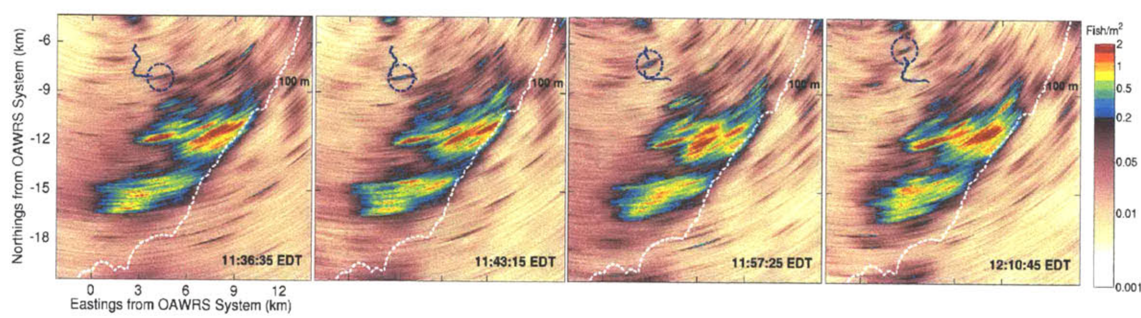

Figure 2-18: *Thunnus thynnus.* A sequence of 4 instantaneous OAWRS images of fish population density (May 14, 2003). A small school of fish (dashed blue circle) covers a distance of $\sim$3 km at an average speed consistent with that of tuna ($\sim$5 km/h; [117]) along the trajectory indicated by the solid blue line. Other small schools appear around the large shoal. Dashed white lines mark 100 m depth contour. A movie of this is found in Supplementary online material of Ref. [158].

2.4.7 Summary

The dynamic range expected in OAWRS imaging is summarized in Fig. 21 for a variety of ecologically significant fish species. For all fish species examined, typical shoaling densities (Fig. 2-19) are at least 2 orders of magnitude greater than the minimum densities detectable by OAWRS, making them viable candidates for future wide-area surveys.

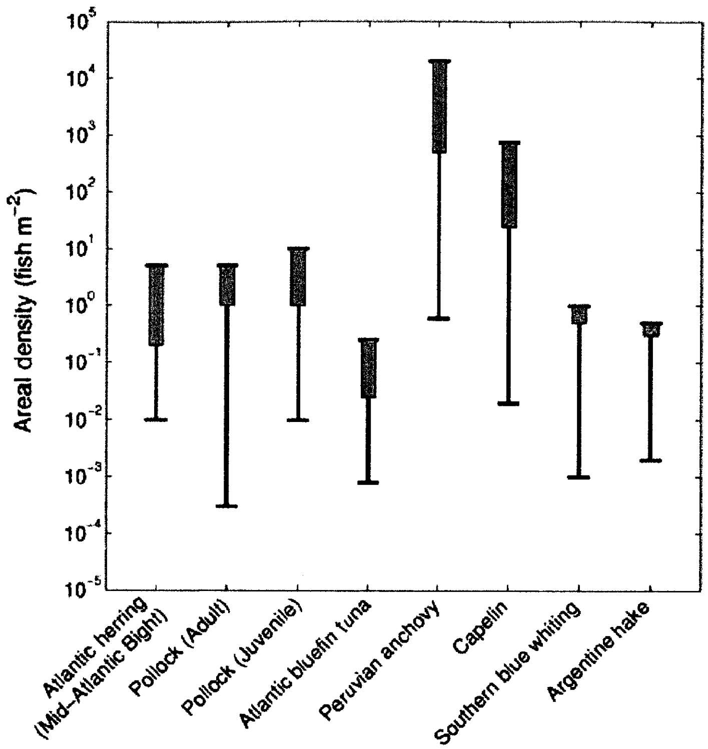

Figure 2-19: Comparison of dynamic ranges in population density expected in wide-area surveys for the 8 fish species discussed. Lower end of vertical bar corresponds to expected minimum individual densities observable with OAWRS. Upper end corresponds to maximum areal fish densities from historical observations. Shaded: typical shoaling density from historical observations.

2.5 Conclusions

We reviewed a number of recent findings in marine ecology related to the behavior of vast oceanic fish shoals that were made possible by Ocean Acoustic Waveguide Remote Sensing (OAWRS), a technique capable of instantaneously imaging and continuously monitoring fish populations over continental shelf-scale areas, spanning thousands of km^2. OAWRS can be used in oceanic ecosystems to remotely assess populations and study the behavior of fish and other marine organisms such as Antarctic krill. The approaches presented here for wide-area and continuous-time monitoring of pelagic species may help to meet the significant demands of the ecosystem-based approach to research and conservation in marine biology [81, 201, 34, 235].

Currently, OAWRS has been deployed from moving research vessels. In the future, it will likely also be deployed at fixed locations to enable continuous long term monitoring of oceanic ecosystems and their variations. A precedent already exists for this in the atmosphere where fixed Doppler-weather radar (DWR) stations have been used to instantaneously image bird populations and study population distributions, migrations and behavior over wide areas. Continuous DWR monitoring has been instrumental in avian conservation and ecosystem-based resource management [128, 129, 222]. With frequent use, OAWRS can likewise play a significant role in scientific exploration, ecosystem management and conservation in the world's oceans.

Chapter 3

Force Estimation and Prediction from Time-Varying Density Images

3.1 Introduction

Estimating velocity and force fields from image sequences is an essential and often first step of analysis in a wide variety of applications such as object detection and tracking, robot navigation, visual odometry, medical imaging, remote sensing and satellite imagery. Image sequences used in these applications describe both compressible and incompressible flows. A variety of methods exist for estimating velocity fields, such as Optical Flow [108], and pressure gradients [175], [263] from time varying images describing *incompressible* motion.

In this chapter, we develop and apply methods for estimating the forces driving motion observed in density image sequences, where pixel values can be modeled as proportional to the density of a *compressible* fluid. Using these forces, we also present methods for predicting future velocity and density values. To do this, we formulate and apply a Minimum Energy Flow (MEF) method to estimate velocity fields from image sequences describing both compressible and incompressible flows.

The MEF and force estimation techniques can be generally applied to any density image sequence, where pixel values can be modeled as proportional to the density of a compressible fluid. Here, for example, we demonstrate these techniques at the micro-scale by quantifying the dynamics of cell division, and at the macro-scale by quantifying fish shoal dynamics over tens of kilometers. Using density images of a cell undergoing mitosis [76], we quantify the velocity, net-force and apparent pressure fields inside the cell. We find that cell division is driven by the formation of two regions of low apparent pressure at opposite sides of the cell, and a region of high apparent pressure at the center. Using fish population density images obtained with an Ocean Acoustic Waveguide Remote Sensing (OAWRS) [158],[120] system, we quantify (1) inter-shoal dynamics such as coalescence of fish groups over tens of kilometers, (2) fish mass flow between different parts of a large shoal and (3) the stresses acting on large fish shoals. To study collective behavior, large animal groups, including fish shoals, are often modeled as compressible fluids [252] [253]. Such theoretical group behavior models predict average velocities and forces inside animal groups, which can be verified using our MEF and force estimation techniques.

3.2 Background

Classical motion estimation from image sequences describing incompressible motion is based on Horn and Schunk's [108] work on determining Optical Flow. Barron et al. [19] review and compare the different optical flow techniques, including [108], [143], [257], [174] [9], [229], [100], [265] and [72], where the 2D velocity field ($\mathbf{u}$) is computed from spatial and temporal variations in the image intensity (E) patterns by minimizing a global cost function of the form

$$\iint_{\Omega} f\left(\frac{\partial E}{\partial t} + \nabla E \cdot \mathbf{u}\right) + \lambda g\left(|\nabla \mathbf{u}|\right) \, \mathrm{d}x \, \mathrm{d}y,$$

where $f(\cdot)$ and $g(\cdot)$ are monotonically increasing functions (usually the magnitude squared of the argument), λ is an empirically determined weight and Ω is the image plane.

The above choice of cost function is especially suited for incompressible motion estimation since (1) the argument of $f(\cdot)$ should be zero in an incompressible fluid [20] when E is proportional to the density ρ of the fluid and (2) minimizing $g(\cdot)$, also known as the "unsmoothness of flow" criterion, suppresses large gradients in velocity, which are usually associated with compressible flows.

In compressible flow estimation, a modification of the Optical Flow technique is to replace the first term in the cost function with the corresponding term from the compressible equation of continuity [20] for fluids. Methods based on this modification [8], [22], [270], however, retain the "unsmoothness of flow" criterion, which may not be suitable for estimating flows with large spatial gradients in the velocity field, as we show in comparisons with the MEF approach (Appendix G). In the case of compressible flows, it is the spatial gradients in velocity which contain information about the compressible nature of the motion , and using the "unsmoothness of flow" criterion may distort the velocity field [61]. Higher order penalty functions such as "second order div-curl" minimization [241] have been suggested for fluid flow estimation. These methods penalize sharp changes in vorticity and divergence of flow, which may not be appropriate in estimating general turbulent flow either.

Penalty functions other than the "unsmoothness of flow" of Optical Flow have also been proposed for non-rigid deformation estimation. Devalminck and Dubus [61], and others [198, 166, 244] propose formulations based on minimizing the strain energy of deformation, which is applicable only for objects that undergo elastic deformations with a known stress-strain relationship but not for fluids undergoing compressible motion.

The MEF technique uses a physically motivated penalty function that does not depend directly on the spatial gradients of velocity. The total kinetic energy is used instead of the "unsmoothness of flow" criterion. The choice of kinetic energy is motivated by the Least Action Principle [59], according to which the evolution of a physical system from one state to another corresponds to the minimum of the action [135]. Since we are interested in estimating compressible fluid flow, this principle reduces to minimizing the kinetic energy of fluid particles corresponding to the density at an image pixel.

Our force estimation technique uses the flow fields computed by MEF as inputs, and is applicable to both steady and unsteady flows. That is, the forces are estimated by taking into account temporal fluctuations in the velocity field. The nonlinear Navier-Stokes equation [20] is used, and both conservative and non-conservative forcing terms are assumed to be present. The force estimation technique itself is a separate "module" that can, in general, have inputs from any motion estimation model. We have developed and applied a MEF technique for motion esimation because our method performs better than existing techniques of compressible flow estimation (Appendix G).

3.3 Formulation

3.3.1 Velocity field

Let $\rho(x, y, t)$ be the density corresponding to a point (x, y) in the image plane Ω at time t. If we assume that ρ is the density of a compressible fluid, then in the absence of any sources and sinks, the velocities are constrained by the equation of continuity [20]:

$$\frac{\partial \rho}{\partial t} + \frac{\partial}{\partial x}(\rho u) + \frac{\partial}{\partial y}(\rho v) = 0, \tag{3.1}$$

where u and v are the components of the flow velocity, in the x and y directions respectively.

Equation 3.1 is a single equation relating the measured spatial and temporal variations of density and the two unknown velocity components u and v. This equation may have many solutions (u, v) matching the observed change in density ρ. To determine a particular velocity field, we set up an optimization problem where we take the square of the error in the constraint (the left side of Equation 3.1) and add a multiple of the kinetic energy of the system

$$T = \rho(u^2 + v^2) \tag{3.2}$$

as a penalty term or objective function, and minimize the following integral over Ω,

$$\iint_\Omega \left[\left(\frac{\partial \rho}{\partial t} + \frac{\partial(\rho u)}{\partial x} + \frac{\partial(\rho v)}{\partial y} \right)^2 + \lambda \rho (u^2 + v^2) \right] \mathrm{d}x \, \mathrm{d}y. \tag{3.3}$$

The velocity field we determine through this minimization is one that results in the least kinetic energy, while making the deviation from satisfying the continuity equation as small as possible.

The term λ is a constant that defines the "penalty for" high kinetic energy in the solution. We expect that large values of λ will tend to suppress high kinetic energy excursions in the solution (at the cost of not matching the constraint equation as well), while small values of λ will tend to make the solution match the constraint equation more closely (at the cost of being more sensitive to measurement noise). The term $\rho(u^2 + v^2)$ may be considered a "regularizer" for the ill-posed problem of recovering (u, v) [250].

For convenience we now define

$$\bar{u} = \rho u \quad \text{and} \quad \bar{v} = \rho v \tag{3.4}$$

representing the mass flow rates in the x and y directions respectively. We can rewrite (3.3) in terms of these flow rates as

$$\begin{aligned} &\iint_\Omega \left(\rho_t + \bar{u}_x + \bar{v}_y \right)^2 + \frac{\lambda}{\rho} (\bar{u}^2 + \bar{v}^2) \, \mathrm{d}x \, \mathrm{d}y \\ &\quad = \iint_\Omega F\left(\bar{u}, \bar{u}_x, \bar{u}_y, \bar{v}, \bar{v}_x, \bar{v}_y \right) \mathrm{d}x \, \mathrm{d}y \end{aligned} \tag{3.5}$$

where the subscripts indicate the variable with respect to which partial derivatives are to be taken. Minimization of (3.5) can be treated as a problem of the calculus of variations, where we solve the following set of Euler-Lagrange equations:

$$F_{\bar{u}} - \frac{\partial}{\partial x} F_{\bar{u}_x} - \frac{\partial}{\partial y} F_{\bar{u}_y} = 0 \tag{3.6}$$

$$F_{\bar{v}} - \frac{\partial}{\partial x} F_{\bar{v}_x} - \frac{\partial}{\partial y} F_{\bar{v}_y} = 0 \tag{3.7}$$

Substituting the expression for F into Equations 3.6 and 3.7 leads to

$$\bar{u} = \frac{\rho}{\lambda}\left(\rho_{tx} + \bar{u}_{xx} + \bar{v}_{xy}\right) \tag{3.8}$$

$$\bar{v} = \frac{\rho}{\lambda}\left(\rho_{ty} + \bar{u}_{xy} + \bar{v}_{yy}\right). \tag{3.9}$$

In Appendix H, we present a numerical technique to solve Equations 3.8 and 3.9. The boundary conditions for this problem are $\frac{\partial \bar{u}}{\partial n} = 0$ and $\frac{\partial \bar{v}}{\partial n} = 0$, where n is the normal to the boundary of the image plane.

Earlier work by Fitzpatrick[71] involves a strict enforcement of the continuity constraint, which may not hold in the presence of measurement noise. A Lagrangian multiplier, denoted by $\lambda(x, y)$, is used as a spatially varying unknown, and closed form analytic solutions are pursued. In the formulation here, departures from satisfying the continuity condition are allowed, but penalized. Additionally, we have used a *fixed* multiplier λ to weigh the energy term. We have assumed that the changes in pixel intensity in the image sequences are purely due to the motion of objects imaged, and not due to the motion of the observer. It is possible to correct for observer motion *prior* to applying MEF. The computational techniques presented in this chapter work well for imaging applications with high frame-rates. For low frame-rate applications, a coarse-to-fine approach as described in Refs. [67, 21] may be employed.

3.3.2 Force field

A velocity field can be the result of an underlying force field driving the motion. We can determine these forces using the Navier-Stokes Equation [20] for compressible flow in two dimensions:

$$\rho\left(\frac{\partial \mathbf{U}}{\partial t} + (\mathbf{U}\cdot\nabla)\mathbf{U}\right) = -\nabla p + \mathbf{F} \tag{3.10}$$

where $\mathbf{U} = (u, v)$ is the vector velocity field, p is the pressure field and $\mathbf{F} = (f_1, f_2)$ is any external "force density" (body force per unit volume) acting on the fluid. The right hand side of Equation 3.10 is the sum of a conservative force per unit volume

(∇p) and a non-conservative force per unit volume ($\mathbf{F}$). The x and y components respectively of this vector equation are:

$$\rho\Big(u_t + uu_x + vu_y\Big) = -p_x + f_1 \tag{3.11}$$

$$\rho\Big(v_t + uv_x + vv_y\Big) = -p_y + f_2 \tag{3.12}$$

where subscripts again indicate the variable with respect to which partial derivatives are to be taken. For special cases of fluid flow when either the conservative force or the non-conservative force is zero, the system of equations 3.11 and 3.12 directly provide us the solution for either (f_1, f_2) or p. In the more general case that we consider here, we assume that neither ∇p nor (f_1, f_2) terms can be neglected and are comparable to each other.

Determining the unknowns p, f_1 and f_2 from Equations 3.11 and 3.12 is an ill-posed problem, which we will reframe as two decoupled variational problems in order to determine approximate least-squares solutions.

Subtraction of the y derivative of Equation 3.11 and the x derivative of Equation 3.12 eliminates p and yields

$$\frac{\partial}{\partial y}\Big[\rho\Big(u_t + uu_x + vu_y\Big)\Big] - \frac{\partial}{\partial x}\Big[\rho\Big(v_t + uv_x + vv_y\Big)\Big] = \frac{\partial f_1}{\partial y} - \frac{\partial f_2}{\partial x}. \tag{3.13}$$

We then find (f_1, f_2) that minimizes

$$\iint_\Omega \left\| \frac{\partial}{\partial y}\Big[\rho\Big(u_t + uu_x + vu_y\Big)\Big] - \frac{\partial}{\partial x}\Big[\rho\Big(v_t + uv_x + vv_y\Big)\Big] - \left(\frac{\partial f_1}{\partial y} - \frac{\partial f_2}{\partial x}\right) \right\|^2 \mathrm{d}x\, \mathrm{d}y.$$

The solutions f_1, f_2 are then given by the following Euler-Lagrange equations:

$$\frac{\partial^2 f_1}{\partial y^2} = \frac{\partial^2}{\partial y^2}\left[\rho\Big(u_t + uu_x + vu_y\Big)\right] - \frac{\partial^2}{\partial x \partial y}\left[\rho\Big(v_t + uv_x + vv_y\Big)\right] + \frac{\partial^2 f_2}{\partial x \partial y} \tag{3.14}$$

$$\frac{\partial^2 f_2}{\partial x^2} = \frac{\partial^2}{\partial x \partial y}\left[\rho\Big(u_t + uu_x + vu_y\Big)\right] - \frac{\partial^2}{\partial x^2}\left[\rho\Big(v_t + uv_x + vv_y\Big)\right] - \frac{\partial^2 f_1}{\partial x \partial y} \tag{3.15}$$

The coupled Equations 3.14 and 3.15 are solved using a fixed point iteration technique, which is described in Appendix I.

After determining (f_1, f_2), we again use Equations 3.11 and 3.12 to solve for p:

$$p_x = -\rho\Big(u_t + uu_x + vu_y\Big) + f_1 \tag{3.16}$$

$$p_y = -\rho\Big(v_t + uv_x + vv_y\Big) + f_2 \tag{3.17}$$

This is a Dirichlet Boundary Value Problem and, in general, is over-constrained. For example, in the computation domain $(x \in [0, L], y \in [0, L])$, explicit integration of Equation 3.16 yields

$$p(x, y) = \int_0^x \left[-\rho\Big(u_t + uu_x + vu_y\Big) + f_1\right] \mathrm{d}x + p(0, y) \tag{3.18}$$

which may not satisfy the boundary condition at $x = L$.

In order to obtain a best fit solution for the system of Equations 3.16 and 3.17, we re-frame it as a variational problem. One way to do this is to find the solution p that minimizes the square of the Euclidean norm of the residues of Equations 3.16

and 3.17, much like the procedure adopted to find (f_1, f_2). We thus minimize

$$\iint_\Omega \left[p_x + \rho\Big(u_t + uu_x + vu_y\Big) - f_1\right]^2 + \left[p_y + \rho\Big(v_t + uv_x + vv_y\Big) - f_2\right]^2 \mathrm{d}x\,\mathrm{d}y.$$

The Euler-Lagrange equation for this variational problem is

$$\nabla^2 p = \frac{\partial}{\partial x}\left[-\rho\Big(u_t + uu_x + vu_y\Big)\right] + \frac{\partial f_1}{\partial x} + \frac{\partial}{\partial y}\left[-\rho\Big(v_t + uv_x + vv_y\Big)\right] + \frac{\partial f_2}{\partial y} \quad (3.19)$$

where ∇^2 is the Laplacian. We solve this inhomogeneous Laplace equation using a fixed point iteration, in Appendix I.

3.3.3 Predicting densities using forces

The ability to quantify forces also provides us with a method to predict future density distributions once we have an initial estimate of the velocity field and the force field.

In order to do this, we assume that the initial force computed stays constant for some time before there is a substantial change in its magnitude and spatial distribution. This means that over some time scale, the accelerations (or the driving forces) remain constant. Under these assumptions we suggest the following prediction scheme:

Step 1

Obtain density data $\rho^{(n)}, \rho^{(n+1)}, \rho^{(n+2)}$.
(superscripts indicate time steps)

Step 2

Compute $\left(u^{(n)}, v^{(n)}\right)$ and $\left(u^{(n+1)}, v^{(n+1)}\right)$ using $\rho^{(n)}, \rho^{(n+1)}, \rho^{(n+2)}$ and Equations 3.8 and 3.9.

Step 3

Calculate $\nabla p^{(n)}$ and $\mathbf{F}^{(n)}$ using Equations 3.14, 3.15 and 3.19.

Step 4

Set

$$\begin{aligned} \nabla p^{(n+1)} &\leftarrow \nabla p^{(n)} \\ \mathbf{F}^{(n+1)} &\leftarrow \mathbf{F}^{(n)} \end{aligned}$$

Step 5

Use $\left(u^{(n+1)}, v^{(n+1)}\right)$, $\rho^{(n+1)}$ in Equations 3.11 and 3.12 and compute $\left(u^{(n+2)}, v^{(n+2)}\right)$.

Step 6

Use $\left(u^{(n+2)}, v^{(n+2)}\right)$ and $\rho^{(n+1)}$ in Equation 3.1 to pedict $\rho^{(n+3)}$.

Step 7

Repeat steps 1-6 by setting

$$\begin{aligned} \rho^{(n)} &\leftarrow \rho^{(n+1)} \\ \rho^{(n+1)} &\leftarrow \rho^{(n+2)} \\ \rho^{(n+2)} &\leftarrow \rho^{(n+3)}. \end{aligned}$$

3.4 Applications

3.4.1 Synthetic image sequences

To evaluate the performance of the MEF method, we use synthetic image sequences describing (i) contraction of a density feature, (ii) coalescence of two density groups and (iii) splitting of one density group into two. In all these examples, the MEF-estimated flows and pressure fields match well with the "ground truth" values, as can be seen from Figures 3-1, 3-2 and 3-3. The places where the MEF-estimated mass flow vectors differ the most from the "ground truth" flows are areas of low density and low density gradient. This is because MEF, similar to the tradional Optical Flow method [108], relies on the spatial gradients and temporal changes of density to provide information about the underlying motion. In a special case, if the observed images describe a constant flow along iso-density lines, the velocity fields are indeterminate.

In this chapter, we use two-dimensional density images and two-dimensional flow fields to illustrate the utility of the force estimation and MEF techniques. The same techniques can be applied to three-dimensional density images in biomedical imaging systems such as MRI [209] and CT.

Illustrative example 1: contraction of a density feature

Here we consider a circular density feature with an initial radius, R, of 20 m at t = 0 seconds (Figure 3-1A), which contracts uniformly so that its radius, at t = 1 seconds is 19 m (Figure 3-1B) and at t = 2 seconds is 18 m (Figure 3-1C). The "ground-truth" flow fields that results in the changes in density distribution observed in Figures 3-1A-C, can be readily computed using pairs of density images, the continuity constraint (Equation 3.1) and the geometrical constraints for this problem:

$$\begin{aligned} u &= -kx \\ v &= -ky. \end{aligned}$$

where $k = 1/R$. The ground-truth flow at each time step is then computed as the product of the known constant velocity field and the known density distribution. Using the ground truth flows at t = 0 s and t = 1 s, we then compute the driving pressure field at t = 0 s (Figure 3-1D) using Equations 3.11 and 3.12.

We now apply the MEF and force estimation techniques developed in Sections 3.3.1 and 3.3.2, to the density image sequence in Figures 3-1A-C. Our MEF-computed flows and pressures are compared to the "ground-truth" values in Figures 3-1E and

F respectively. The maximum error in flow estimates is less than 5%, while the maximum error in the pressure estimate is $\approx 10\%$.

The type of compressible motion we have chosen in Figure 3-1 is commonly encountered in medical imaging, where, for example, CT image sequences describe contraction and expansion of the heart [233] and lungs [95], both of which are elastic deformable objects.

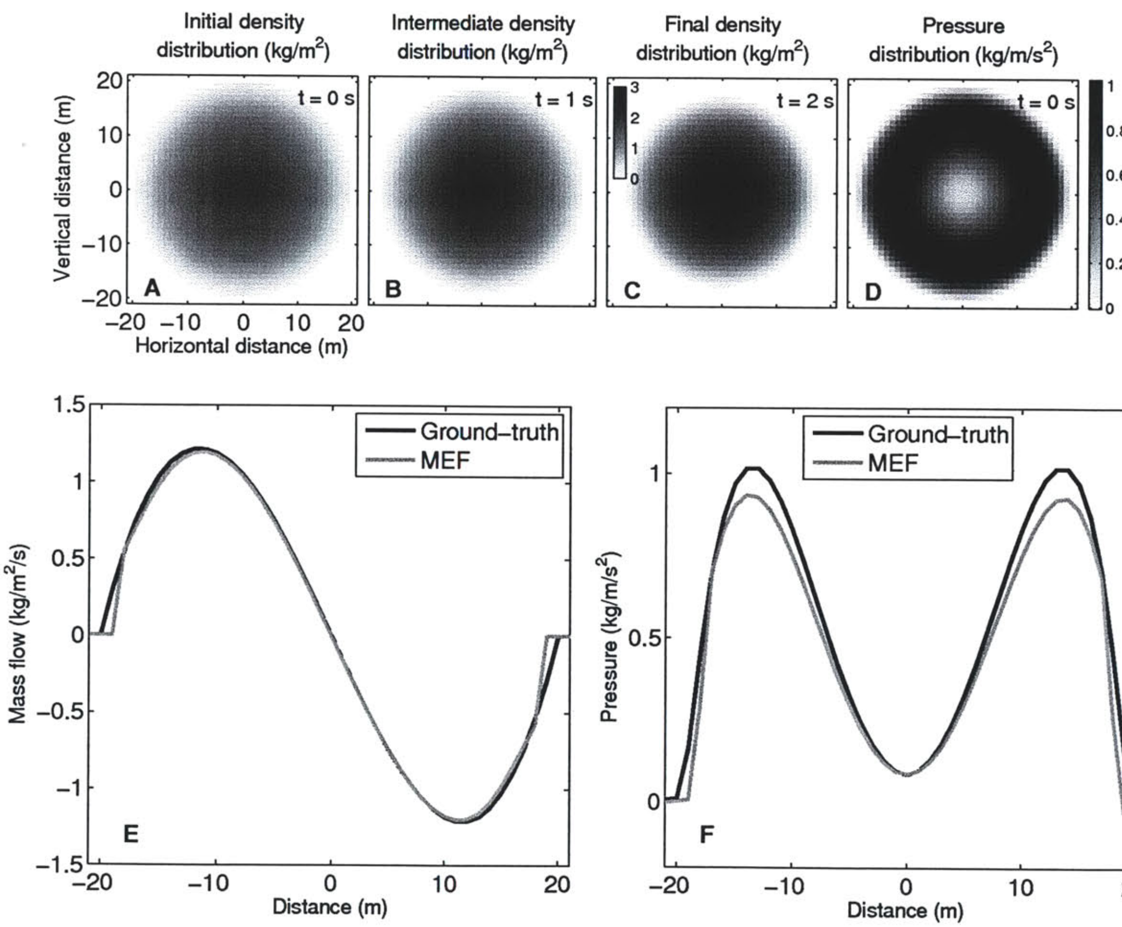

Figure 3-1: (**A,B,C**) Initial, intermediate and final density distributions of a contracting density feature. (**D**) The ground-truth pressure distribution that results in contraction. (**E**) Comparison between ground-truth and MEF-computed horizontal mass flow rates at t = 0 s along the $y = 0$ cut in (A). (**F**) Comparison between Ground-truth and MEF-computed pressures at t = 0 s along the $y = 0$ cut in (A). The maximum error in flow estimates is less than 5%, while the maximum error in the pressure estimate is $\sim 10\%$.

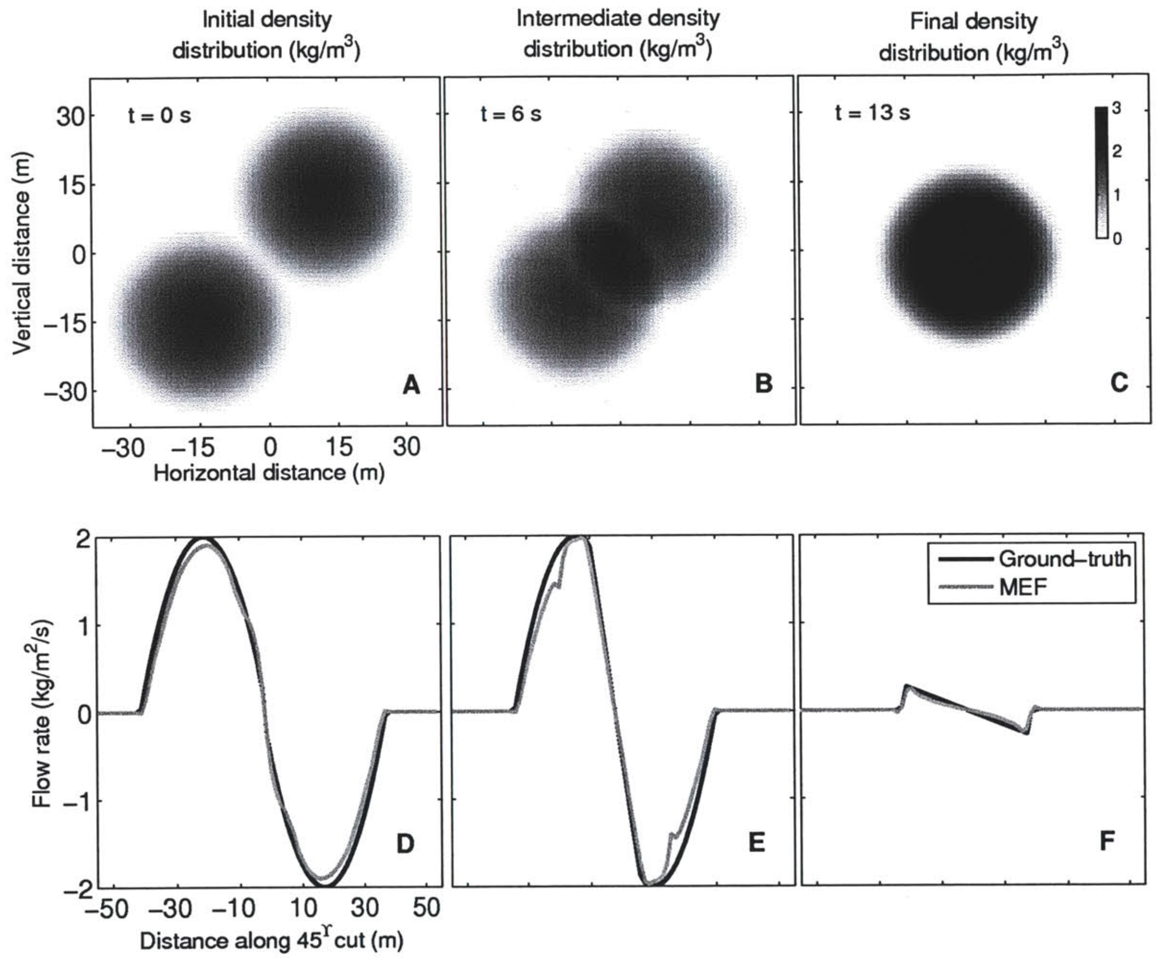

Figure 3-2: Example of two density groups coalescing into one. (**A,B,C**) The density distributions during the initial, intermediate and final stages of coalescence respectively. (**D,E,F**) Comparison between ground-truth and MEF-computed mass flow rates along a 45° cut in A, B and C respectively. The maximum error in the MEF-estimated flow is $\sim 10\%$.

Illustrative example 2: coalescence of two density groups

Here we consider a sequence of density images that describe a coalescence episode, where two density groups (Figure 3-2A) translate towards each other at a constant speed until they merge. The total density at each step and pixel is the algebraic sum of the densities of the two density groups. As seen from Figure 3-2A, the two groups are initially (t = 0 s) separated such that their centers of mass are respectively at (15 m,15 m) and (-15 m, -15 m). At t = 6 s, their centers have moved to (7.5 m, 7.5 m) and (-7.5 m, -7.5 m) (Figure 3-2B), and finally, at t = 13 s, they have merged (Figure 3-2C). The entire sequence consists of 15 frames, each separated by $\Delta t = 1$ s. Since the two density groups translate towards each other at a constant speed, there is no external force or pressure that acts on the groups.

The ground-truth flow at each time step is computed as the product of the known constant velocity field and the known density distribution. The MEF flow field is computed by using Equations 3.8 and 3.9, and corresponding pairs of density distributions $(\rho(t=0),\rho(t=1))$, $(\rho(t=6),\rho(t=7))$, $(\rho(t=13),\rho(t=14))$. In Figure 3-2, we compare MEF and ground truth flows during the initial (Figure 3-2A,D), intermediate (Figure 3-2B,E) and final (Figure 3-2C,F) stages of the coalescence episode. The maximum error in the MEF-estimated flow is $\approx 10\%$.

The example in Figure 3-2 illustrates the application of MEF to estimate both incompressible translation (Figures 3-2A,D) as well as compressible coalescence (Figures 3-2C,F). These motion types are commonly encountered in quantifying cloud field kinematics using satellite images [22] and, as we shall see in section 3.4.3, in imaging large fish shoals [158] using OAWRS.

Illustrative example 3: splitting of density groups

The final example we consider for evaluating the MEF and force estimation techniques, is a density image sequence describing the splitting of one density group into two. In this example, a single dense group (Figure 3-3A) splits into two (Figure 3-3B,C) over a time frame of 6 seconds. The "ground truth" flows and pressures (black solid lines in Figures 3-3D-I) are computed at each time step using the procedure described in Appendix J. We also apply the MEF and force estimation techniques to the density image sequence and estimate the flows and pressures (grey lines in Figures 3-3D-I).

The maximum error in the MEF-estimated flow is less than 5% (Figures 3-3D,E,F), while the maximum error in our estimated pressure is less than 1%.

Image sequences describing splitting of density groups, such as the example we have chosen in Figure 3-3, are encountered in imaging systems that capture cell division, such as Flourescent Speckle Microscopy [57]. We will show an application of the MEF and force estimation techniques in Section 3.4.2, where we quantify the mass flows and pressure distribution inside a cell undergoing mitotic cell division.

3.4.2 Quantifying velocity and force fields driving cell division

Here we quantify the dynamics of cell division using the MEF and force estimation techniques developed in Sections 3.3.1 and 3.3.2. Currently, it is hypothesized [115], [114] that intra-cellular forces driving cell division are generated by long, fiber-like structures called micro-tubules. It is also postulated that the micro-tubules pull apart newly formed chromosome pairs by generating a combination of repulsive forces at the center and attractive forces at the poles of the cell [114], [139]. While several molecular mechanisms have been proposed for force generation [139], it has been difficult to quantify these forces and their distribution within the cell, prompting the need for "a combination of bio-physical force measuring methods and molecular biological muta-genesis methods" [139].

By applying the MEF and force estimation techniques to an image sequence describing mitosis (the process by which a cell replicates itself by splitting in two), we quantify intra-cellular forces driving cell division. We use an image sequence describing mitosis in a *Xenopus laevis* [207] cell (Figure 3-4A). The cell has been injected with a fixed amount of a flourescent marker called GFP alpha-tubulin [57]. The

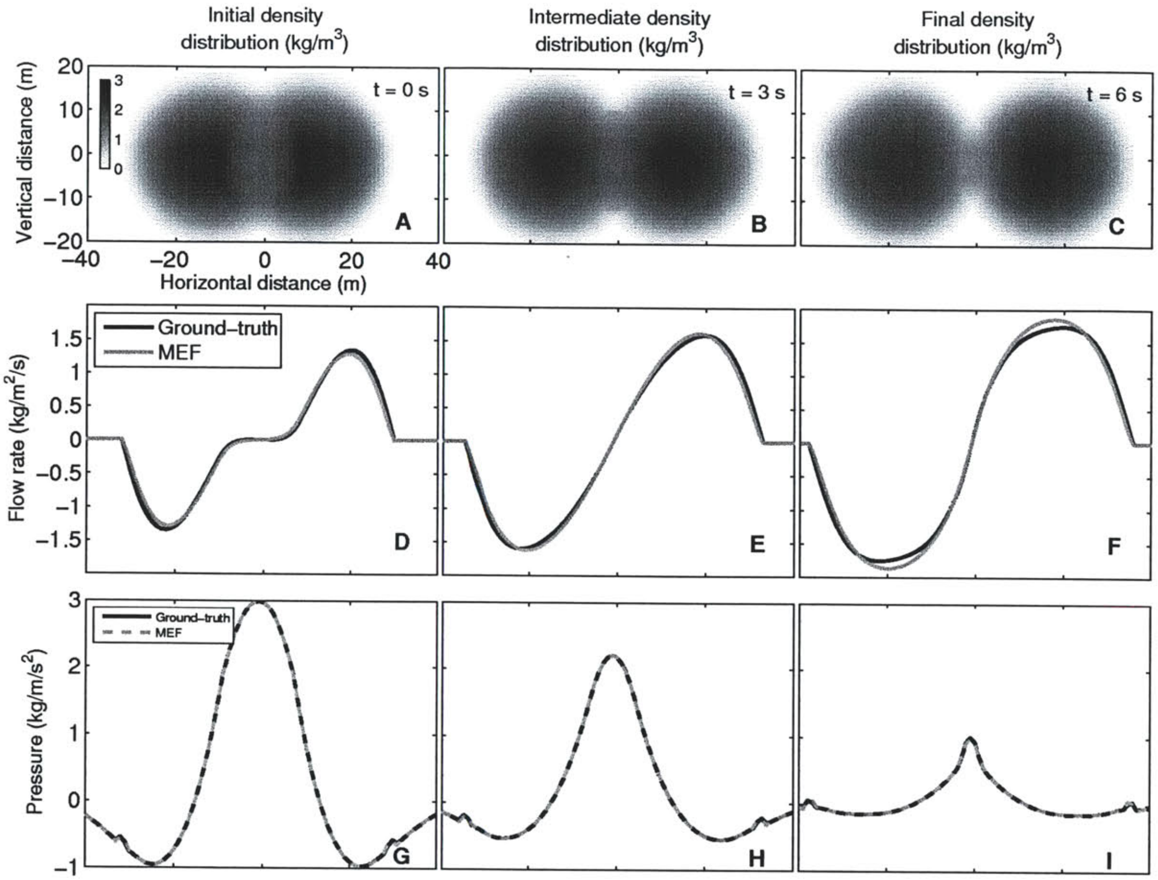

Figure 3-3: (**A,B,C**) The density distributions during the initial, intermediate and final stages of splitting respectively. (**D,E,F**) Comparison between ground-truth and MEF-computed mass flow rates along a horizontal cut, $y = 0$, in A, B and C respectively. (**G,H,I**) Comparison between ground-truth and MEF-computed pressure along a horizontal cut, $y = 0$, in A, B and C respectively. The MEF-estimated pressure lies almost exactly on top of the ground-truth pressures. The maximum error in the MEF-estimated flow is less than 5%, while the maximum error in our estimated pressure is less than 1%.

colorscale in Figure 3-4A is proportional to the areal number density of GFP alpha-tubulin [57]. Before the cell splits, the velocity field inside the cell is random and has a small magnitude (on the order of 0.1 μm/s) compared to the velocity field during mitosis (Figure 3-5).

Figures 3-5A-C describe "Anaphase" [76], one of four stages in mitosis, where newly-formed chromosome pairs [76] within the cell are pulled apart, resulting in cell division. Using the density image sequence (Figures 3-5A-C), we compute the velocity field that describes the effective dynamics of the fluorescent tubulin within the cell

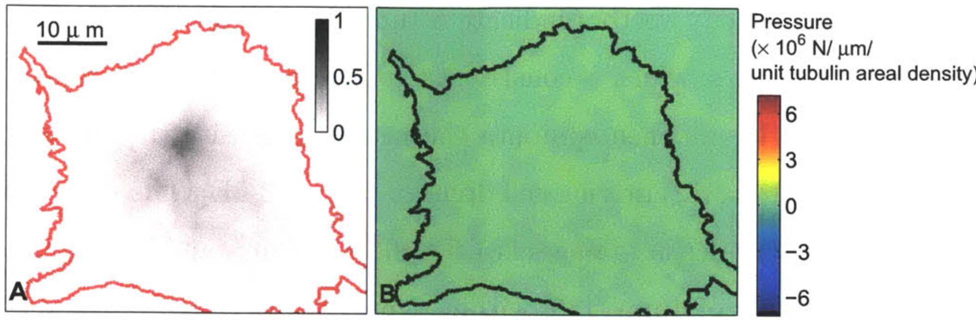

Figure 3-4: (**A**) *Xenopus laevis* cell before undergoing mitosis. The colorscale corresponds to the relative areal density of a flourescent marker, GFP alpha-tubulin, which attaches itself to structures called micro-tubules. The density is normalized so that the maximum number of tubulin per square μm is 1 in Figure 3-5C. Red contour represents the cell boundary (cytoplasm). (**B**) Pressure distribution inside a *Xenopus laevis* cell prior to mitosis. The pressures are one order of magnitude smaller compared to those in Figure 3-5F.

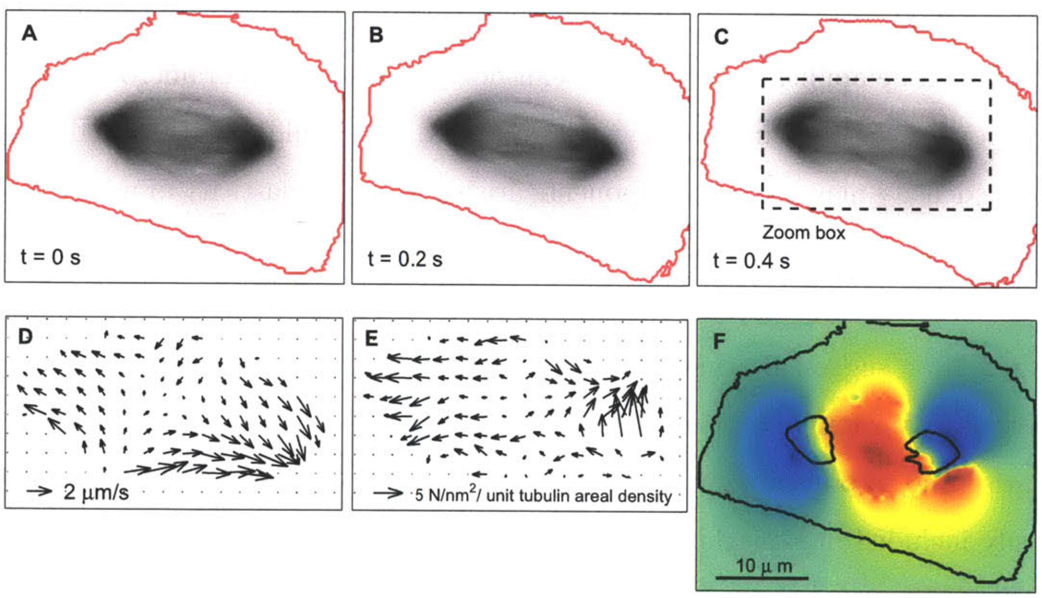

Figure 3-5: (**A,B,C**) Sequence of frames showing mitosis in a *Xenopus laevis* cell. Same colorscale as that in Figure 3-4 A. Cell boundary is marked by red contours. Black box in (C) is the area zoomed in (D,E). Note long fibre-like structures called micro-tubules.(**D**) Velocity field derived from density image pairs (A,B). The vectors are shown every 10 pixels. (**E**) Net force density computed using velocity and density fields in Equations 3.11 and 3.12. (**F**) Pressure field that gives rise to the force field in (E). *Same colorscale as in Figure 3-4B.* Formation of two low apparent pressure regions at the opposite ends of the cell and a high apparent pressure region at the center of the cell is shown. Two regions of high micro-tubule density and the cell boundary are shown as black contours.

(Figure 3-5D). The velocity vectors indicate a tubulin flux towards opposite ends of the cell at rates of 2 μm/s, which is consistent with previous velocity estimates [139]. Using the velocity field, we then compute the net force density (i.e the right hand side of Equations 3.11 & 3.12) driving cell division (Figure 3-5E). The maximum areal density of tubulin in our density images is 1.5×10^{-14} kg/μm^2, and is computed using an inter-tubulin spacing of 4 nm [139] within a microtubule, a molecular mass of 55 kDa ($55 \times 1.66 \times 10^{-24}$ kg) for tubulin and a typical cell thickness of 10 μm [191]. We find that the magnitudes of our net force density vectors are comparable with experimentally measured values of force exerted by micro-tubules on glass microbeads (0.2 *pico* N) [65].

In order to compute our intra-cellular forces, we have made a continuum assumption that is suitable for fluid motion. In the case of cell division, such a fluid assumption may still be applicable, given the semi-flexible nature [132] of micro-tubules that are suspended and moving in a cytoplasmic fluid. It should also be noted that the net force density may include components arising from the elasticity of micro-tubules, which can be estimated only by including additional constraints in our force model. We find that the difference in total tubulin density between Figures 3-5A and C to be less than 10%, suggesting that the approximation we made in neglecting source and sink terms in our fomulation is a good one for this problem. Such source or sink terms may arise due to polymerization or de-polymerization of tubulin molecules, and can be easily included in Equation 3.1.

Under our assumptions of fluid flow in a cell, the net force is the result of the effective pressure field shown in Figure 3-5F. We find that cell division is driven by the formation of two regions of low apparent pressure at opposite sides of the cell, and a region of high apparent pressure at the center. This is in contrast to the random pressure field inside the cell before mitosis (Figure 3-4B), which has a much smaller magnitude. These effective pressures are different from the hydrodynamic pressures related to the flow of the cytoplasmic fluid. The visualization of pressure shown in Figure 3-5F quantifies the repulsive force field at the center as well as the attractive force fields at opposite poles of the cell. Such force fields have been previously postulated to drive cell division [114],[139].

3.4.3 Application to fish population density images

We now apply the MEF and force estimation techniques developed in Sections 3.3.1 and 3.3.2 on fish population density images obtained using an Ocean Acoustic Waveguide Remote Sensing (OAWRS) system, to quantify flow rates and pressure fields driving the dynamics of large fish shoals. Using the MEF-computed flow fields we quantify the behavior of large fish shoals including (i) translation and coalescence of fish groups and (ii) mass exchange between different parts of a large shoal via hourglass patterns.

The OAWRS system has been recently developed [158] to detect, image and continuously monitor large fish shoals over continental shelf-scale areas. It consists of a source that transmits low-frequency sound, in the audible frequency range, which is trapped between the ocean-air and ocean-seabed boundaries as it propagates over long distances and scatters off fish shoals and other submerged targets. These scattered returns are collected by a towed receiver, and charted in range and bearing, resulting in an instantaneous snapshot of the ocean over hundreds of square kilometers. The intensity of the scattered returns from fish shoals is proportional to the fish population density [14] [120], so that by repeating transmissions at regular intervals, a population density image sequence is generated. A detailed technical description of the OAWRS system can be found in Refs. [89], [120], [158], [157].

An example of the type of population density image obtained using OAWRS is shown in Figure 3-6, which shows a large shoal of fish centered roughly 12 km south and 5 km east of the source. This image was obtained on May 14, 2003, off the coast of New Jersey during the OAWRS 2003 experiment [158]. The shoal was observed for an entire day using OAWRS, which provided snapshots of population density every 50 seconds. We will apply MEF to the sequence of fish population density images, in an area defined by the box in Figure 3-6.

To compute force fields using Equations 3.11 & 3.12, we assume that individual fish behave like fluid particles so that the entire fish shoal (Figure 3-6) behaves

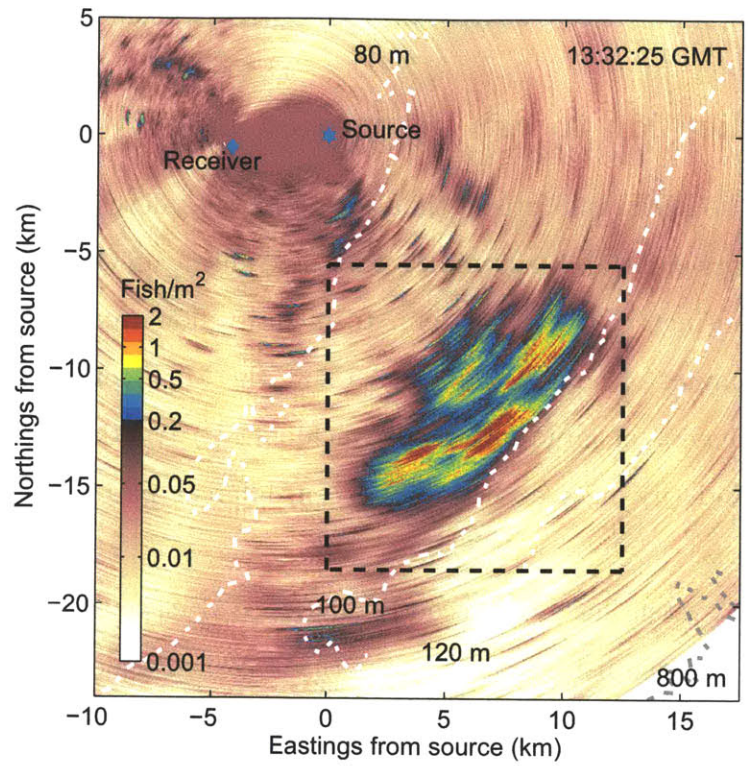

Figure 3-6: Large shoal of fish imaged off the New Jersey coast on May 14, 2003, using OAWRS. The colorscale represents the areal density of the fish. The image resolution is 30 m/pixel. The bathymetric contours are shown using white dashed lines. The black dashed-box is the area over which MEF and force estimation techniques are applied to study the dynamics of the large shoal and is the area shown in Figures 3-7 and 3-10.

like an anisotropic, compressible fluid. This assumption is consistent with OAWRS observations of spatial and temporal variation of population density, which showed that fish could converge or diverge, making their motion highly compressible. Similar observations of fish schools behaving like an "animate fluid" [50] have been reported for small schools of a few meters in extent.

Under our continuum assumptions, the net force can be thought of as the result of a pressure field, with regions of low pressure acting as centers of attraction and regions of high pressure acting as centers of repulsion. These pressures are different from the hydrodynamic pressures related to the flow of water in the ocean. They are effective biological stresses that drive fish shoaling behavior.

3.4.4 Translation and coalescence of fish groups

Here we use the MEF and force-estimation techniques to quantify the rates at which fish groups within a large shoal translate and coalesce. We find that the rate of translation is consistent with the swimming-speeds of individual fish. We also find that coalescence of fish groups can occur due to formation of "attraction zones" or regions of low pressure. These phenomena are quantified by tracking the motion of two high population-density regions, A and B, shown in Figure 3-7. The MEF-estimated velocity vectors, shown in Figure 3-8, describe the translation and coalescence of A and B, occuring at rates of roughly 0.5 to 1 m/s. The merger of A and B can also be thought of as the result of a low pressure, "attraction zone" formed between the schools, as shown in Figure 3-9.

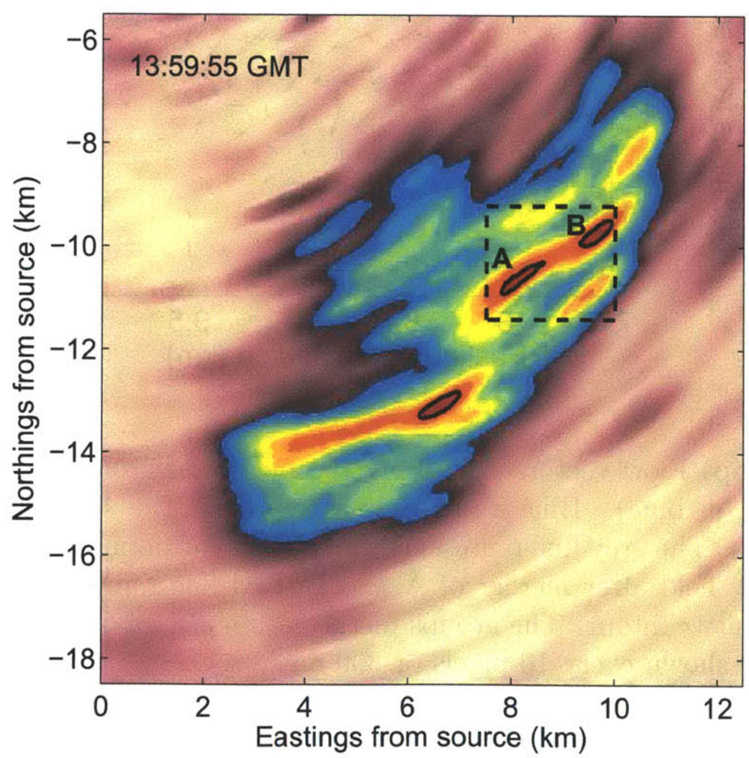

Figure 3-7: Fish population density image showing schools A and B before merger. Same colorscale as in Figure 3-6. The original OAWRS density image has been smoothed such that the areal density at any point in the image shown above, is the unweighted mean of the areal densities over a 120 m $\times$ 120 m square-area centered at that point. The dashed box represents the zoom area over which velocity vectors are shown in Figure 3-8. Black lines are 1.5 fish/m^2 population density contours.

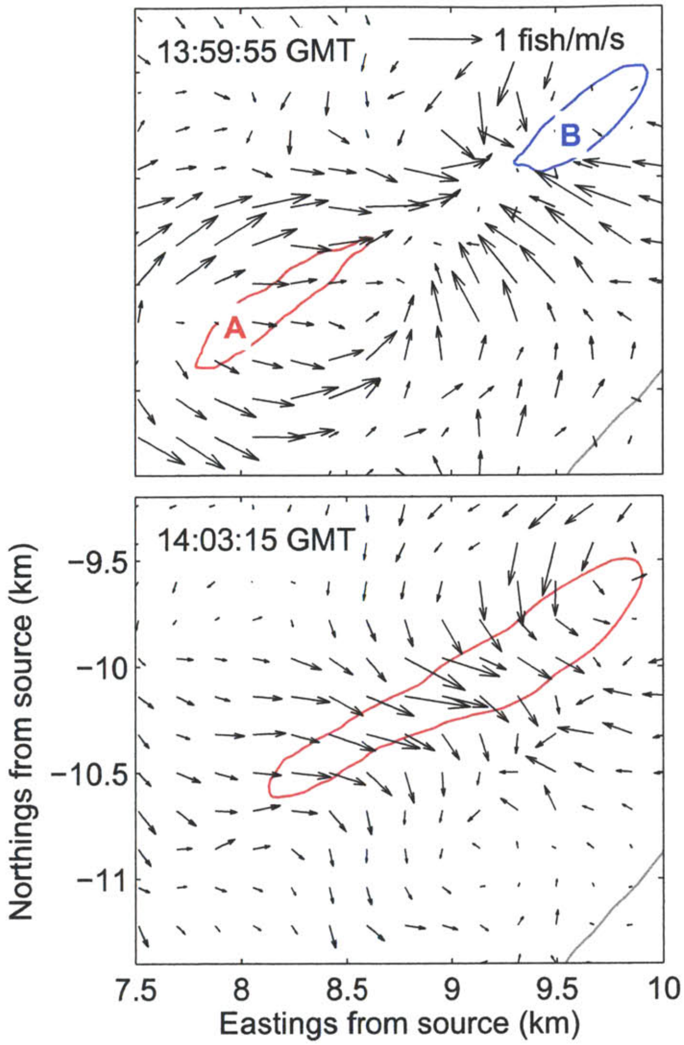

Figure 3-8: (**Top**) Flow vectors describing the merger of groups A (marked in red) and B (marked in blue). Blue and red lines represent the 1.5 fish/m^2 population density contours. The grey line represents the 0.2 fish/m^2 population density contour. (**Bottom**) Flow field after merger of A and B. Red line represents the 1.5 fish/m^2 population density contour. The groups merge within a span of 3 minutes. The mass flow vectors are shown every 10 pixels or 300 m.

The mean velocity of groups A and B can also be estimated by tracking their centers of mass (COM) defined by

$$\bar{X}_A = \frac{\sum_{i\in A} \rho_i x_i}{\sum_{i\in A} \rho_i}, \quad \bar{Y}_A = \frac{\sum_{i\in A} \rho_i y_i}{\sum_{i\in A} \rho_i} \tag{3.20}$$

$$\bar{X}_B = \frac{\sum_{i\in B} \rho_i x_i}{\sum_{i\in B} \rho_i}, \quad \bar{Y}_B = \frac{\sum_{i\in B} \rho_i y_i}{\sum_{i\in B} \rho_i} \tag{3.21}$$

where i represents the pixel number. We find that group A moves towards group B at roughly 1 m/s, which is consistent with the velocities obtained using MEF (Figure 3-8). These values are also consistent with the typical speeds at which individual fish swim [111, 184, 70].

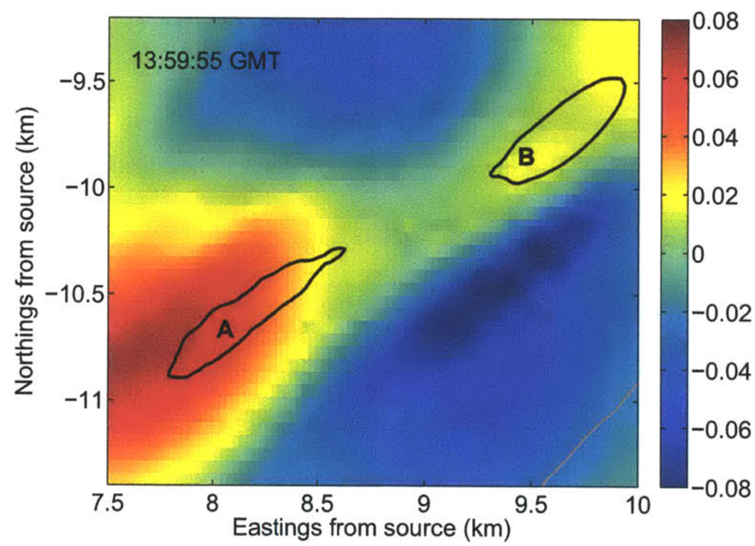

Figure 3-9: Pressure (N/m^2 per unit fish mass) distribution within large fish shoal showing formation of a low pressure region that attracts schools A and B. Black lines represent the 1.5 fish/m^2 population density contours. Gray line represents the 0.2 fish/m^2 population density contour. Same zoom area as Figure 3-8.

3.4.5 Mass exchange between different parts of a shoal

We now quantify fish flow rates between different parts of the large shoal shown in Figure 3-6. In particular, we quantify the rate of mass transfer between two wings of an hourglass pattern formed by the fish shoal, as shown in Figure 3-10. We find that there is a steady de-population of the southern wing and the fish "flow" into the northern wing, as can be seen from the sequence of images in Figure 3-11. There is a steady flow of $\sim 300 - 450$ fish/s across the neck of the hourglass connecting the two wings of the shoal. The depopulation episode can also be explained by the formation of a high-pressure region near the neck of the hourglass (Figure 3-12).

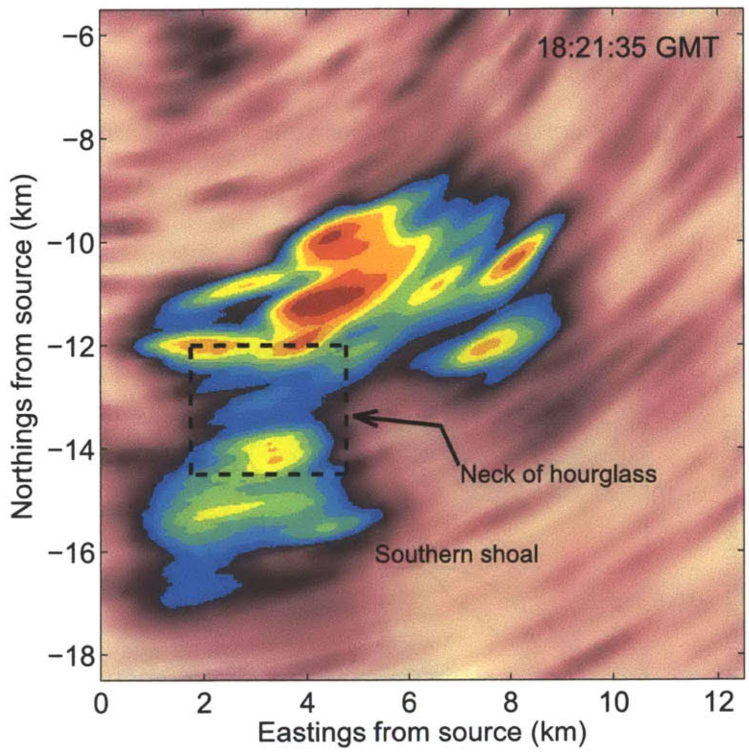

Figure 3-10: Fish density distribution showing hourglass type formation. Same colorscale as in Figure 3-6. The southern shoal gets depopulated and there is mass flow across the neck of the hourglass shown. The black box is the area zoomed in Figures 3-11 and 3-12. The areal density has been smoothed using the same algorithm as that employed in Figure 3-7.

Hourglass patterns have been observed in smaller fish groups spanning spatial scales on the order of a square km [203]. Mass transfers of the kind described above have been known to occur and have been shown in these small groupings. Flow from one part of the shoal to the other via the "neck" usually signifies a predatory pressure on one of the wings [203]. The depopulation described by the MEF calculation could very well be in response to such a pressure acting on the southern wing of the large shoal described by the OAWRS density images.

3.5 Prediction using forces: application to synthetic images

Here we apply the prediction procedure shown in Section 3.3.3, to density images in Figure 3-1, where a circular feature undergoes uniform contraction.

In Figure 3-1, we considered density images for t = 0,1 and 2 s, and computed the flow field and pressure field driving contraction. We now continue this contraction, and predict the density distribution at times t = 3 to 7 s (Figure 3-13). Comparison of our predicted densities with actual values (Figure 3-13) shows a good match (errors $< 10\%$) till t = 7 s, after which the cumulative effect of errors becomes large and causes significant (errors $> 10\%$) difference between predicted and actual densities.

In general, we expect our prediction scheme to work well within some time interval for cases where the pressures and forces driving the flow remain more or less constant for the time interval. This is indeed the case in many natural flows which follow environmental pressure gradients, such as the movement of clouds in the atmosphere driven by the formation of low and high pressure regions.

3.6 Conclusions

We have presented methods for (1) estimating forces that drive motion observed in density image sequences and (2) predicting flow and density evolution. To do this, we developed a Minimum Energy Flow (MEF) method for estimating velocity fields in both compressible and incompressible flow. The MEF and force estimation techniques have been demonstrated with synthetic and experimentally obtained images. Using a density image sequence describing cell mitosis, we showed that cell division is driven by gradients in apparent pressure in the cell. Using density image sequences of fish shoals, we also quantified (1) coalescence of fish groups over tens of kilometers, (2) fish mass flow between different parts of a large shoal and (3) the stresses acting on

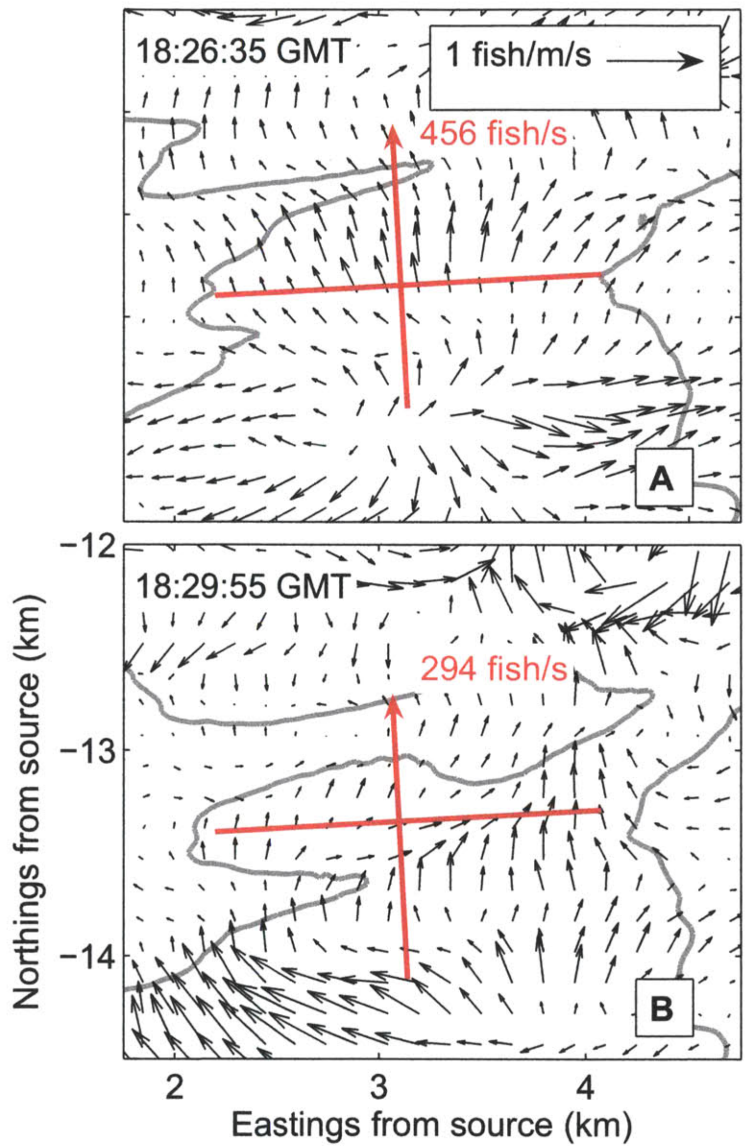

Figure 3-11: Mass flow distribution frames showing depopulation of the southern wing over a span of 3 minutes. The area shown is zoomed around the neck of the hourglass shown in Figure 3-10. The flow rate of fish, normal (red arrow) to the neck (red solid line) is found to be ~ 300-450 fish/s. The flow vectors are shown every 5 pixels. The gray lines are 0.2 fish/m^2 density contours.

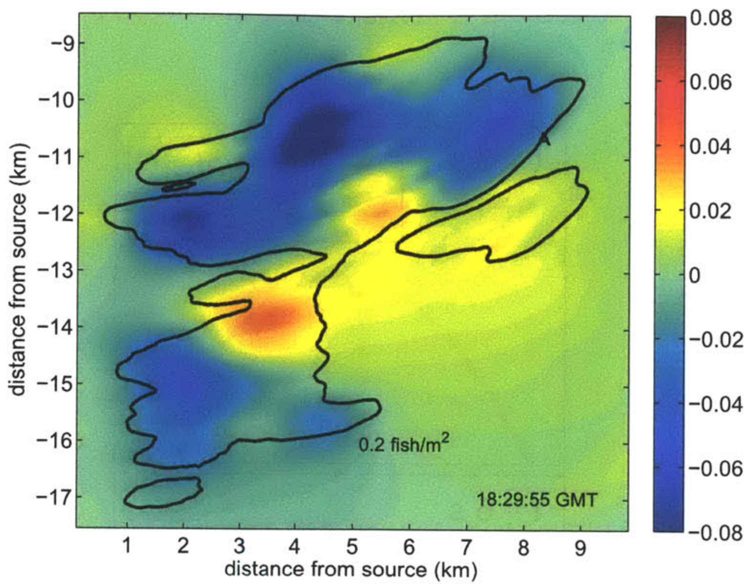

Figure 3-12: Pressure (N/m^2 per unit fish mass) distribution within large fish shoal showing formation of a high pressure region near the "neck" of an hourglass pattern forcing fish mass flow from one wing to the other. The black lines are 0.2 fish/m^2 density contours.

large fish shoals.

The MEF and force estimation techniques can be generally applied to any density image sequence, where pixel values can be modeled as proportional to the density of a compressible fluid. In addition to the examples presented here, such density image sequences are frequently encountered in biomedical imaging and satellite imaging for meteorology and oceanography. Magnetic Resonance Imaging (MRI), for example, provides tomography image sequences of blood flow in arteries, which could be monitored using our MEF and force estimation techniques. Satellite images of density distribution of water-vapor (clouds), for example, can be used to compute flow and force fields in the atmosphere that drive meteorological processes. Other applications are in studies of collective behavior, where the MEF and force estimation tools can be used to verify theoretical models that predict average velocities and forces acting in large animal groups.

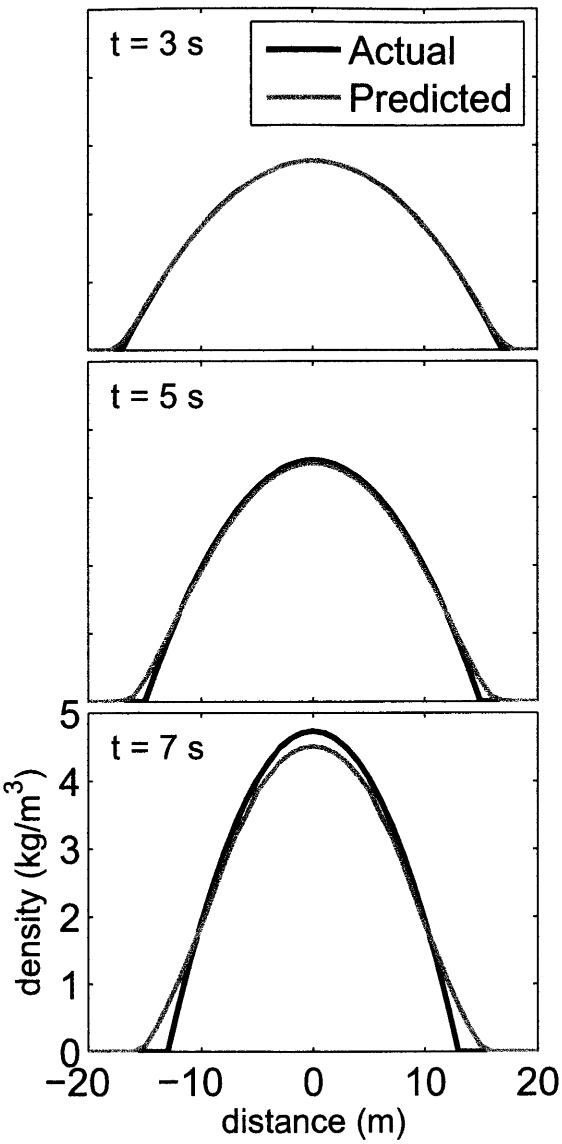

Figure 3-13: Comparison of actual and predicted densities for different times. The same example as that in Figure 3-1 is used. The curves are cuts through $y = 0$ in the actual and predicted density images. The prediction scheme works well within some time interval when the forces remain more or less constant. After some time, the cumulative effect of errors becomes large and causes significant (errors $> 10\%$) difference between predicted and actual densities.

Chapter 4

Critical Population Density Triggers Rapid Formation of Vast Oceanic Fish Shoals

4.1 Introduction

Many species of oceanic fish band together in large shoals [30, 105] that can span tens of kilometers and involve hundreds of millions of individuals. Grouping leads to survival advantages through enhanced spawning, predator avoidance, and feeding mechanisms [203, 168, 52, 202]. Little information has been available about the formation process and behavior of large oceanic fish shoals. Traditional methods rely on local measurements from slow-moving research vessels that enable sampling of only a small fraction of a shoal during an entire survey, typically by vertical profiling, and cannot distinguish between temporal and spatial changes [87, 193, 150]. Here, we describe fundamental temporal and spatial processes by which vast oceanic shoals form by observation of entire shoals in space and time over their full horizontal extent and relate these processes to likely governing mechanisms. We do this using Ocean Acoustic Waveguide Remote Sensing (OAWRS) [158], which enables instantaneous imaging and continuous monitoring of oceanic fish populations over tens of thousands of square kilometers.

4.2 Gulf of Maine (GoM) Experiment 2006

We studied *Clupea harengus* (Atlantic herring), because they are known to regularly mass in large shoals for spawning at specific times and locations like other clupeid fish. Clupeids are keystone species in many of the world's major marine ecosystems, from the coastal upwelling regions of South America and Africa to the temperate areas of the Nordic Sea, Baltic Sea, and Gulf of Maine [214]. They provide trophic links between plankton, such as krill, and larger predators, such as humans, birds, whales, dolphins, seals, sharks, cod, pollock, and haddock [194]. Georges Bank is one of the primary spawning grounds for herring in the Gulf of Maine, which was once one of the world's most productive fisheries before its collapse in the 1970s [193, 192]. Herring migrate to Georges Bank to spawn in early autumn, typically September and October, from offshore regions of the Gulf of Maine and beyond [193, 275].

We used OAWRS to monitor herring behavior continuously on Georges Bank during the autumn 2006 spawning season, in conjunction with traditional conventional fish-finding sonar (CFFS) [150] and trawl [193] line transects. The OAWRS system instantaneously imaged areas spanning 100 km in diameter every 75 s and so enabled continuous time-space monitoring of shoaling behavior over an ecosystem scale. We focused our experiment on regions where herring shoals were most likely to form. We determined these regions by analysis of a decade of National Marine Fisheries Services (NMFS) annual surveys made with conventional line-transect methods. These historic data showed that the herring traditionally first mass in dense layers near the seafloor along the northern flank of Georges Bank in deeper water (150 to 200 m) before spawning just to the south in shallow waters on the bank (<50 m).

4.3 Field Observations

We found shoal formation to depend on initial conditions and to ensue rapidly when these conditions were satisfied. First, we found that the preexisting population density of diffusely scattered individuals had to reach a critical threshold of 0.2 fish per square meter (fish/m^2). Given this, we found shoal formation to consistently commence in a highly organized fashion near sunset, apparently triggered by reduction in light level. The process depended on orderly and coherent horizontal convergences of leading individuals to produce denser and thicker vertical layers at a few discrete horizontal locations. This process occurred within favored bathymetric contours (Fig. 4-1). From preexisting diffuse background levels consistent with scattered individuals displaying no coherent interaction (Fig. 4-1A), small catalyzing clusters of much higher areal population density emerge in OAWRS imagery within the favored bathymetric contours (160 to 190 m) just before sunset (Fig. 4-1B), introducing bursts of coherent horizontal structure. Simultaneous vertical profiles from CFFS line transects show that, before the leading clusters form, the fish are widely distributed in a diffuse low-density layer within 5 m of the seafloor (Fig. 4-2A). The leading clusters (100-m horizontal scale) form as thick (10 to 30 m in the vertical) and dense groups within 20 to 40 m of the seafloor (Fig. 4-2A), when the fish rise slightly and converge in the horizontal as seen in both OAWRS (Fig. 4-1, A and B) and CFFS data (Fig. 4-2A). Formation of these denser clusters requires horizontal convergence by conservation of mass from the original thin, low-density layers.

4.3.1 Critical density triggers shoal formation

The emergence of leading clusters of high population density set off chain reactions that caused rapid growth into vast shoals. We found the growth to propagate horizontally outward as convergence waves emanating from the cluster initiation points, which appeared to act as sources of the wave action. The waves propagated over tens of kilometers in tens of minutes, as can be seen for example in Fig. 4-1, A to F, and Fig. 4-3. The 3.0 to 6.0 m/s propagation speed of these waves (Fig. 4-3A) is

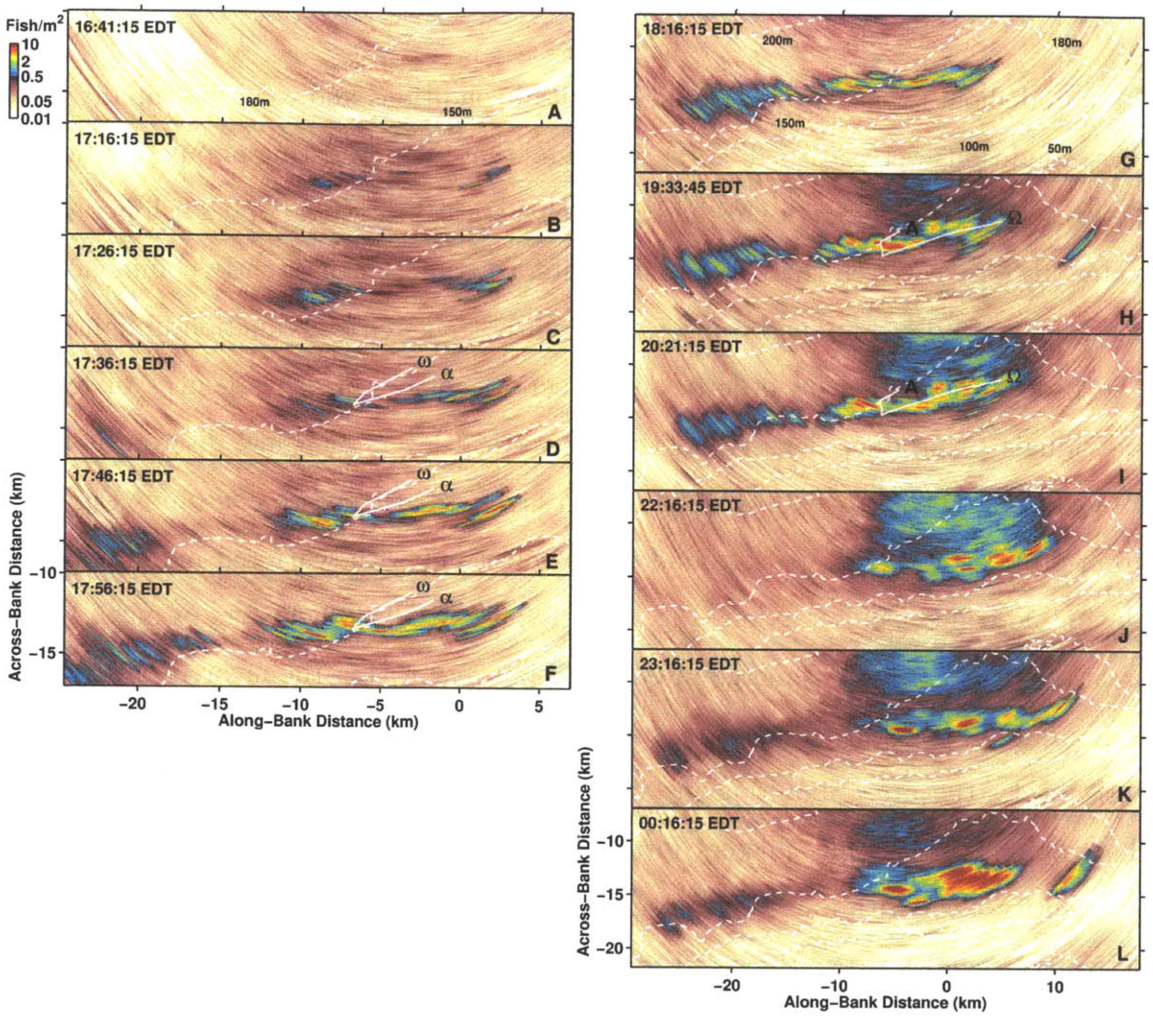

Figure 4-1: Millions of Atlantic herring abruptly form vast shoals on 3 October 2006 just before sunset, which was at 18:08 EDT, on the northern flank of Georges Bank. **(A to F)** Sequence of instantaneous OAWRS areal density (fish/m^2) images illustrating initiation and along-bank shoal growth over tens of kilometers in tens of minutes. **(G to L)** Spatial and temporal evolution of massive herring shoals during the evening of 3 October 2006. Instantaneous OAWRS images taken over 6 hours illustrate shoal thickening in the across-bank direction and gradual migration of its southern edge. Roughly 250 million herring (50,000 tons) are imaged in (L), or 5 to 20% of the entire Georges Bank stock based on NMFS CFFS line-transect surveys (Fig. 4-4E) and combined CFFS, bottom trawls, and catch landings [194]. Our simultaneous capture trawl surveys show that over 99% of the fish imaged by OAWRS within the dense shoals are Atlantic herring, combined with a small fraction of Acadian redfish (Sebastes fasciatus) and haddock (Melanogrammus aeglefinus). The moored OAWRS source is the coordinate origin (0,0) in all OAWRS images, at 42.2089°N, 67.6892°W on 3 October. The positive vertical axis in all OAWRS images points 16° counterclockwise of true north. The dashed lines indicate water depth contours.

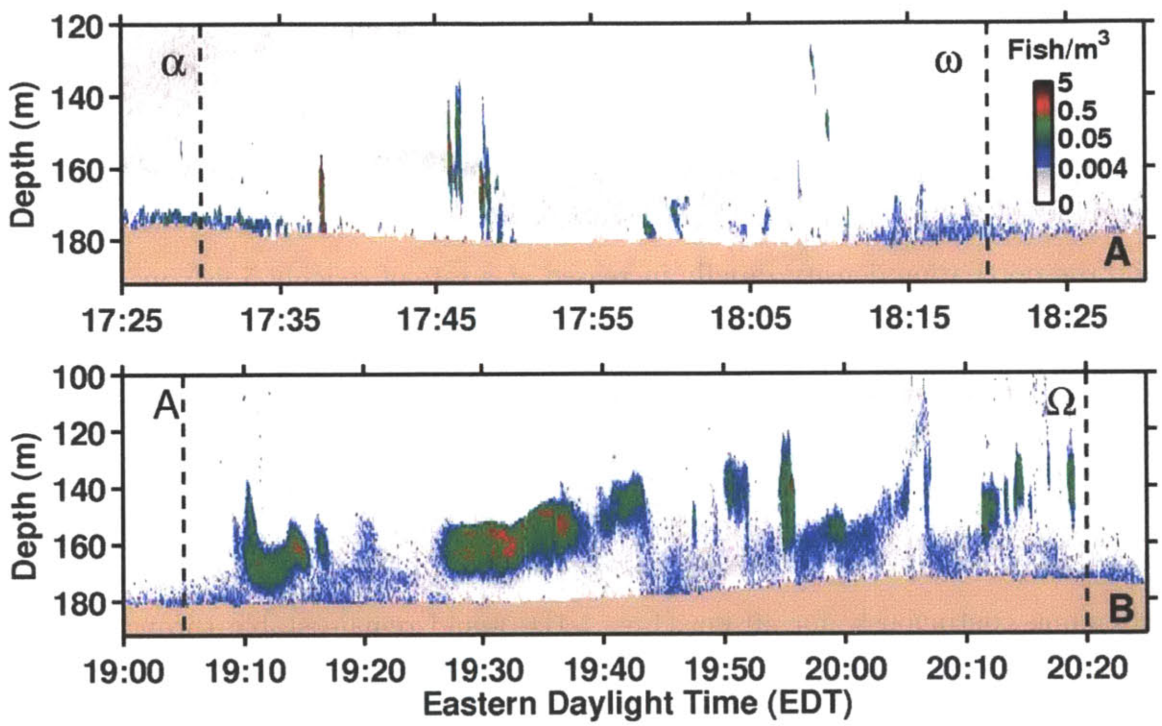

Figure 4-2: Time-depth profile of fish volumetric density (fish/m^3) measured by CFFS along: **(A)** the V-shaped line transect shown in Fig. 4-1, D to F, and **(B)** the J-shaped line transect through the shoal shown in Fig. 4-1, H and I. Black dashed vertical lines correspond to transect start (alpha) and end (omega) points.

an order of magnitude faster than the typical 0.2 m/s speed at which herring swim [111] and so is likely the apparent speed [158] of sequences of local synchronous convergence actions and reactions [183, 230] by members of the shoal. Such local actions define a propagating compressional wave in a medium of variable density [215]. Our observations provide experimental evidence for the existence of compressional waves in vast fish shoals, which have been predicted in physical theories [253]. We found these shoal-forming waves to be highly directional and to propagate most rapidly along the direction of favored bathymetric contours (Fig. 4-1, A to F). Before the waves appeared, areal population density slowly increased at a rate of 0.06 to 0.1 fish/m^2 per hour (Fig. 4-3, B and C). As soon as the critical density of 0.2 fish/m^2 was reached (Fig. 4-3, B and C), coherent shoal-forming waves appeared (Fig. 4-3A), and the population density rapidly increased at a rate of roughly 5 fish/m^2 per hour (Fig. 4-3, B and C).

After formation, we observed growth in shoal width and population as light levels remained low in the evening. Growth normal to the favored bathymetric contours appeared to be from movement of surrounding diffusely scattered fish populations to the shoal, which acted as an attractor (Fig. 4-1, G to L). These vast shoals, sometimes extending continuously for 40 km (Fig. 4-1I), would remain stable throughout the evening and dissipate as light levels increased with sunrise. When viewed vertically with CFFS transects, the shoals evolved from small, isolated, catalyzing clusters (Fig. 4-2A) to extensive, dense layers within 20 to 40 m of the sea floor, but typically disconnected from it by a few meters (Fig. 4-2B). The layer growth required horizontal convergence by conservation of fish mass.

4.3.2 Spawning migrations

Once vast shoals formed, they migrated at speeds consistent with the synchronous swimming of hundreds of millions of individual fish, in accord with the predictions of general behavioral models. The migrations, however, were not in a random direction, as in some theoretical models [253, 94, 261], but toward southern spawning grounds on Georges Bank, apparently for synchronized reproductive activities. Such a migration

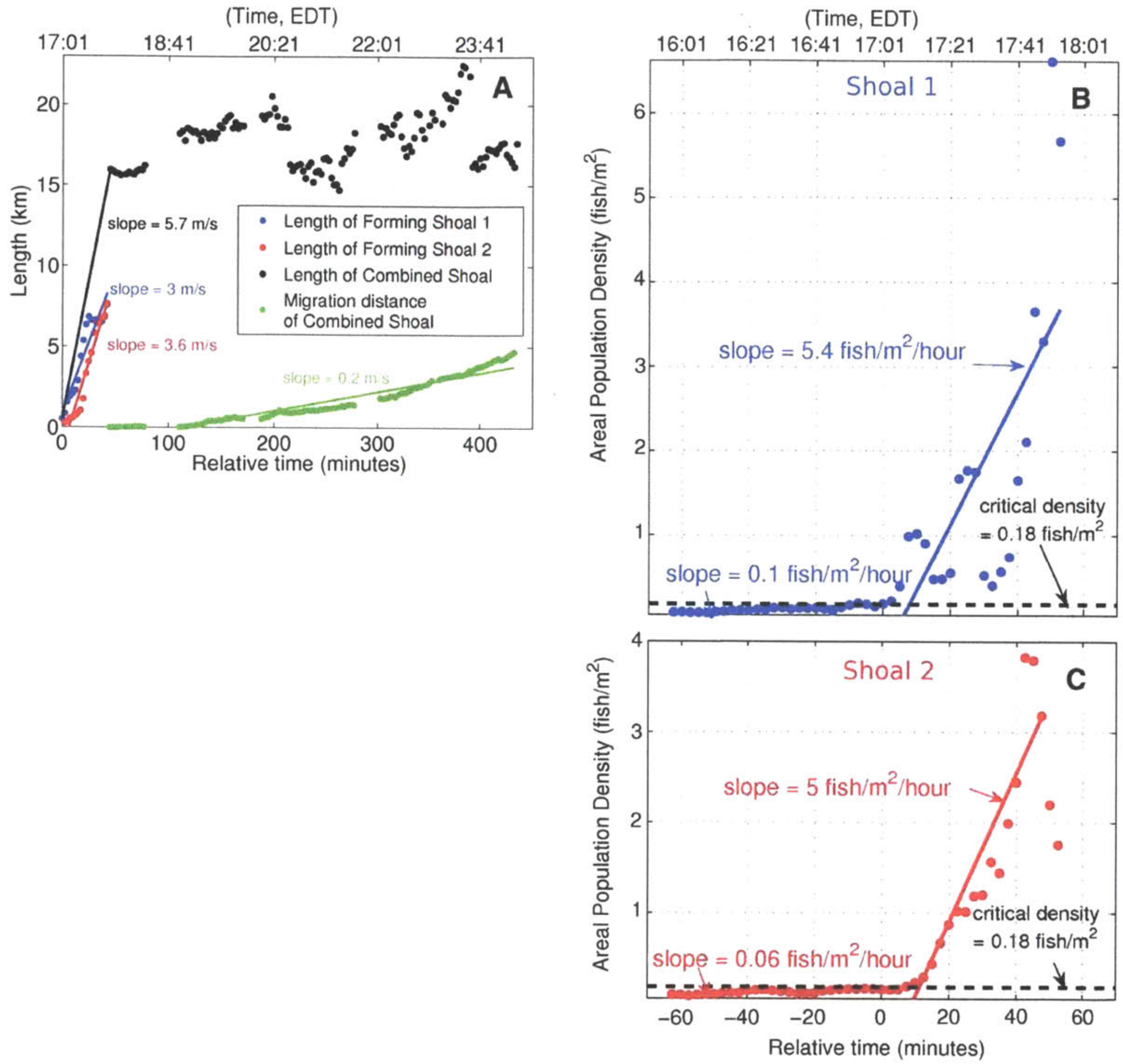

Figure 4-3: **(A)** Shoal length (major axis) and migration distance versus time, including growth and migration speeds on the evening of 3 October 2006 from OAWRS imagery data. Shoal 1 (blue) initiates at (7.5, 13) and shoal 2 at (1, 12.5) in (along-bank, across-bank) coordinates of Fig. 4-1, A to F, at 17:01 EDT. Red and blue solid lines are linear best fits for the data points, with slopes indicating shoal-forming wave speeds. Shoals 1 and 2 combine at 17:43 EDT. Migration distance of combined shoal southern edge (green points) toward spawning area. Green solid line is linear best fit with slope indicating migration speed. **(B and C)** Mean areal population density versus time for shoal 1 (blue data) and 2 (red data) over respective 300 m $\times$ 300 m areas about their initiation coordinates from OAWRS imagery. Slow growth in population density before critical density is attained at 17:01 EDT. Immediately afterward, density increases rapidly (Fig. 4-1, H and I), and the shoal-forming wave initiates (Fig. 4-1G).

of the 3 October shoal's southern edge, from near the alpha-to-omega CFFS transect of Fig. 4-1H to the 150-m contour 2 to 4 km to the south in Fig. 4-1L, is evident in the most populous region and quantified in Fig. 4-3A. The migration is slow, roughly 0.2 m/s (Fig. 4-3A), which is consistent with the average swimming speed of herring in a school [111]. Another example of a southern migration appears in Fig. 4-4 for 29 September. Shoals first form as usual by sunset (Fig. 4-4 A and B). Massive portions of their southern edges then migrate upslope from depths greater than 50 m (Fig. 4-4B) to spawning grounds 2 to 3 km to the south where depths are less than 50 m (Fig. 4-4D). The migration speed is similar to that observed on 3 October, following that expected for the material displacement of millions of swimming herring. Dense evening shoals sometimes developed a diffuse northern component (Fig. 4-1, H to L), which could indicate a north-south migration route for spawning herring from offshore regions of the Gulf of Maine to Georges Bank. The southern edge of the shoals, in contrast, was typically sharp (Fig. 4-1, G to L), following the general bathymetric contour of the spawning grounds of Georges Bank, indicating the leading edge of a synchronous mass migration.

4.4 Discussion

We found the overall process of rapid shoal formation, triggered by attainment of a critical density of 0.2 fish/m^2 near sunset, and subsequent migration toward spawning grounds to define a regular diurnal behavioral pattern that was consistently observed [Appendix K] during our roughly 1-week measurement period as shown in Figs. 1, 2, 3, 4 and Figs. S1 to S4. The evidence suggests the primary biological function of the shoal formation is a prelude to synchronized spawning. Close proximity of individuals can induce synchronous reproductive development through visual and olfactory stimulus [230]. Synchronous development is often critical because each female must typically produce a large number of eggs within very tight time constraints to enable group spawning [230, 259]. Shoal formation at greater depths allows these activities to proceed with reduced risk of attack from predators [148], such as pilot whales,

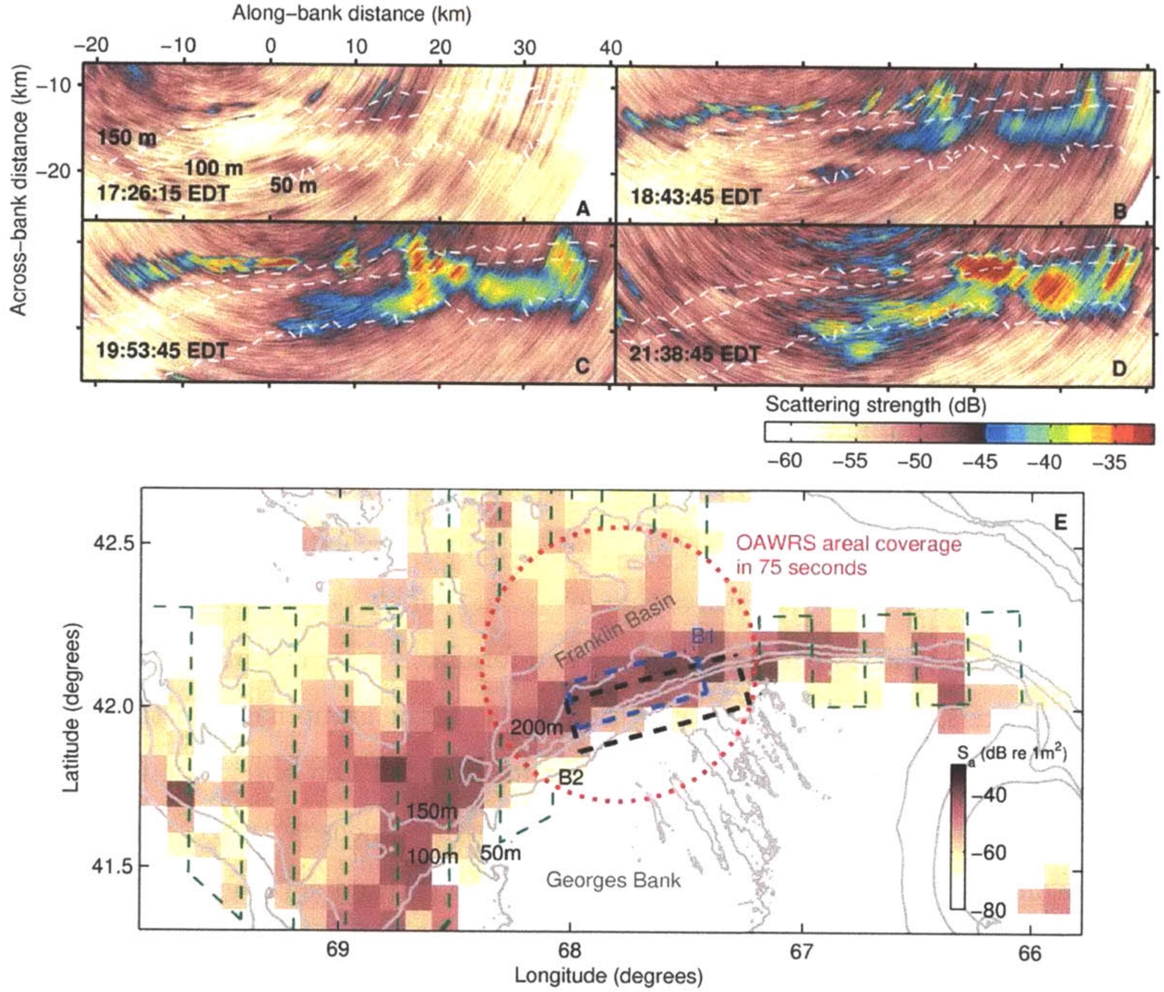

Figure 4-4: **(A to D)** Sequence of OAWRS scattering strength [258] images illustrates formation, growth, and subsequent southern migration of herring shoals toward the Georges Bank spawning grounds on the evening of 29 September 2006. Sunset was at 18:15 EDT. Same region as Fig. 4-1, G to L. **(E)** Backscattering strength s_a [149] at 5 by 5 nautical miles (1 nmi = 1852 m) grid obtained by averaging CFFS line-transect data from 1999 through 2005 NMFS Annual Fall Herring Surveys [122]. Boxes B1 and B2 are regions shown in Fig. 4-1, G to L, and Fig. 4-4, A to D, respectively. Regions of maximum herring concentration are consistent between OAWRS 2006 imagery (Fig. 4-1) and NMFS 6-year average (Fig. 4-4E). Red circle indicates OAWRS areal coverage in 75 s. Green dashed line indicates the line transect of a typical 2-week NMFS survey, not shown within red circle.

porpoise, and tuna, that prefer to hunt in the shallower spawning grounds [168, 254]. Evening formation allows matching and subsequent migration to spawning grounds to occur under cover of darkness, with more safety from predator attack. The shoaling behavior we observed is evidently unrelated to diurnal feeding [168] activities, because trawl samples obtained during our survey show 99% of the herring have empty stomachs and have not yet spawned. This is consistent with historic observations showing that herring do not feed during the spawning period [138].

More generally, our observations during the spawning period show the formation processes of large oceanic fish shoals (i) require initial conditions on population density and external stimuli, such as light level; (ii) follow the actions of a small number of leaders; (iii) rely upon extremely rapid and efficient time-space convergence events that propagate as coherent waves over great distances by chain reaction; and (iv) involve extensive horizontal structures that evolve in a highly organized and predictable manner. The rapidity with which these shoal-forming waves spread once the initial conditions are satisfied is indicative of the advantage the group has over the isolated individual in transferring information over great distances. Our observations also provide ecosystem-scale evidence that a critical population density triggers rapid transition from disordered to highly synchronized behavior, and small groups of leaders often play crucial roles in affecting the actions of much larger groups, as has recently been predicted in general theoretical investigations [253, 261, 37, 217, 48], simulations, and laboratory experiments [138, 37] about animal group behavior [94, 238, 262]. These findings provide information essential to the conservation of marine ecosystems that vast oceanic fish shoals inhabit.

Chapter 5

A Fluid-dynamic Theory for Flocking Behavior

5.1 Introduction

Large scale order in animal groups has been observed in nature for many species, including schools of fish [203, 227, 210], flocks of birds [16], swarms of insects [37], groups of bacteria [93] and herds of mammals such as wildebeest [7]. A number of self-propelled particle (SPP) models have been developed to attempt to describe the collective behavior of animal groups in terms of the individual interactions between group members [188, 219, 55, 112, 49]. Vicsek et al. [261, 55] proposed a simple behavioral rule where each individual assumed the average velocity of its neighbours. Starting from a group of randomly moving SPPs, they found that a rapid change from disordered to organized motion happens when the population density reaches a critical value by performing numerical simulations with SPPs. Couzin et al. [49] used a more complicated model where individual animals follow three behavioral rules: (1) move away from close neighbours located within a zone of repulsion, (2) align with nearby animals located within a zone of orientation, and (3) do not break away from the group (zone of attraction). By varying the radii of the zones, Couzin et al. [49] used numerical simuations to show that it was possible to transition from a loose swarm to a torus, where individuals rotate around the group's center of mass, to highly parallel group migration. Couzin et al. [49] also used their behavioral model to show that few leaders within a group can influence the actions of the entire group. These predictions about animal group behavior, based on numerical simulations of SPP groups, have been confirmed in laboratory experiments using locust swarms, [37] and recently in the wild, using vast fish schools [157].

In this paper, we develop an analytic model to describe the collective behavior of large SPP groups. We start from the simple behavioral rule assumed by Vicsek et al. in Refs. [261, 55] and show that SPP groups behave as a fluid over large spatial scales, with disturbances governed by a linearized form of the Navier-Stokes Equations (NSE). We show the existence of a critical population density which specifies that on an average each particle needs at least one neighbour within its region of perception to sustain synchronous motion within the group. We also show that disturbances propagate as waves within the group, at speeds up to 3-4 times greater than those of any individual SPP. Rapid waves of this kind have been observed in nature, in fish shoals [210, 158] and bird flocks [16]. These findings may explain how rapid information transfer can occur within animal groups, which may ultimately help maintain long-range order. A primary difference between the present work and that of Toner and Tu [253] is that here linear NSE are derived from a simple behavioral rule, i.e. that of Vicsek et al., whereas a general form of NSE was the fundamental assumption of Toner and Tu [253].

5.2 Theoretical formulation

We analyze a system of SPPs (or boids [253, 219]) with a uniform population density of ρ_0 ind. m^{-2} and already in the symmetry-broken state, i.e uniformly moving with a constant velocity (u_0, v_0). We consider the mean number density and mean velocity field that are obtained by averaging the corresponding discrete quantities such that,

$$
\begin{aligned}
\rho(x,y,t) &= \left[\sum_i \delta(x-x_i(t))\delta(y-y_i(t))\right] * W_{sm1}(x,y) && (5.1)\\
u(x,y,t) &= \left[\sum_i \delta(x-x_i(t))\delta(y-y_i(t))u_i(t)\right] * W_{sm2}(x,y) && (5.2)\\
v(x,y,t) &= \left[\sum_i \delta(x-x_i(t))\delta(y-y_i(t))v_i(t)\right] * W_{sm2}(x,y) && (5.3)
\end{aligned}
$$

where $(x_i(t), y_i(t))$ is the instantaneous position of the i^{th} boid, $(u_i(t), v_i(t))$ is its instantaneous velocity, W_{sm1} and W_{sm2} are the smoothing windows for averaging (represented here as a convolution) the discrete density and velocities, respectively, and δ is the Dirac delta. The smoothing functions are defined by

$$
W_{sm1} = \begin{cases} \frac{1}{L_s^2}, \text{ for } (-L_s/2 \le x, y \le L_s/2) \\ 0, \text{ otherwise} \end{cases} \qquad (5.4)
$$

$$
W_{sm2} = \begin{cases} \frac{1}{\rho_0 L_s^2}, \text{ for } (-L_s/2 \le x, y \le L_s/2) \\ 0, \text{ otherwise,} \end{cases} \qquad (5.5)
$$

where L_s is the length-scale used for smoothing the discrete quantities.

The length-scale of smoothing L_s can also be thought of as the resolution scale of any remote sensing system used to observe large animal groups in nature. Large fish schools and plankton aggregations, for example, are observed using acoustic remote sensing techniques such as conventional fish finding sonar (CFFS) [228], multibeam sonars [228] or Ocean Acoustic Waveguide Remote Sensing (OAWRS) systems [158, 157], which have a finite resolution [158] length that is often much greater than the length of separation of the individual fish. The population density [158, 228, 128] and the velocity fields [121, 228] observed using such remote sensing systems are then average quanitites within the resolution footprint. It is probably also worth drawing an analogy between the SPP groups we consider here and a statistical system of interacting molecules in a gas, where the length-scale of molecular interaction is much smaller than the length-scale over which average macroscopic quantities such as pressure are observed [131]. For the continuum description of SPPs to be valid, the total number of particles within the macroscopic length scale ($\rho_0 L_s^2$) has to be much greater than 1.

The system of uniformly distributed particles is subject to a small perturbation (u_1, v_1), so that the total density and velocities are given by:

$$\rho(x,y,t) = \rho_0 + \rho_1(x,y,t) \tag{5.6}$$

$$u(x,y,t) = u_0 + u_1(x,y,t) \tag{5.7}$$

$$v(x,y,t) = v_0 + v_1(x,y,t) \tag{5.8}$$

5.2.1 Incorporating boid behavior

We consider the simple behavioral model of Vicsek et al. [261, 55], according to which the velocity of each boid at some time $t+T$ is the average of the velocities of all its neighbors within its region of perception (ROP) defined by $(x_i - L_x/2 \leq x \leq x_i + L_x/2)$ and $(y_i - L_y/2 \leq y \leq y_i + L_y/2)$ at time t. This behavioral rule was proposed by Vicsek et al. for a discrete time system, where the velocity of a boid changes at discrete time steps of T, which represents the reaction time of the boid. We extend this behavioral rule to a continuous-time system by defining the velocity field for any time $t+\Delta t$, $0 \leq \Delta t \leq T$. To do this, we will assume that the velocity changes *linearly* from $\mathbf{u}(x,y,t)$ to $\mathbf{u}(x,y,t+T)$, so that (Appendix L)

$$\mathbf{u}(x,y,t+\Delta t) = \left[\sum_i \delta(x - x_i(t+\Delta t))\delta(y - y_i(t+\Delta t))\mathbf{u}_i(t)\right] * \left[\delta(x)\delta(y) + \frac{\Delta t}{T}\left(\frac{\Gamma(x,y,L_x,L_y)}{\rho_0 L_x L_y} - \delta(x)\delta(y)\right)\right] * W_{sm2}(x,y), \tag{5.9}$$

where

$$\Gamma(x, y, L_x, L_y) = \begin{cases} \frac{1}{L_x L_y}, & \text{for } (-L_x/2 \leq x \leq L_x/2) \text{ and} \\ & (-L_y/2 \leq y \leq L_y/2) \\ 0, & \text{otherwise.} \end{cases} \quad (5.10)$$

Physically, Equation 5.9 states that each boid takes some time T to change its current velocity to that of the average of its neighbors, and that the velocity change is done in a linear fashion. Such a linear relaxation assumption is also used in statistical physics, when analyzing large systems of interacting particles [218].

5.2.2 Equations of Motion

The spatial Fourier Transforms of Equations 5.2 and 5.9 yield

$$\tilde{u}(k_x, k_y, t) = \left[\sum_i e^{-jk_x x_i(t)} e^{-jk_y y_i(t)} u_i(t) \right] \tilde{W}_{sm2}, \quad (5.11)$$

$$\tilde{u}(k_x, k_y, t + \Delta t) = \left[\sum_i e^{-jk_x x_i(t+\Delta t)} e^{-jk_y y_i(t+\Delta t)} u_i(t) \right] \tilde{W}_{avg} \, \tilde{W}_{sm2} \quad (5.12)$$

where $\tilde{f}(k_x, k_y) \Leftrightarrow f(x, y)$, and

$$x_i(t + \Delta t) = x_i(t) + u_i(t)\Delta t \quad (5.13)$$

$$y_i(t + \Delta t) = y_i(t) + v_i(t)\Delta t \quad (5.14)$$

$$\tilde{W}_{avg} = \left[1 + \frac{\Delta t}{T} B \right], \quad (5.15)$$

where

$$B = \frac{1}{T} \left[\frac{\operatorname{sinc}\left(\frac{k_x L_x}{2}\right) \operatorname{sinc}\left(\frac{k_y L_y}{2}\right)}{\rho_0 L_x L_y} - 1 \right] \quad (5.16)$$

is the behavioral term.

The time derivative of $\tilde{u}(t)$ is, by definition,

$$\frac{\partial \tilde{u}}{\partial t} = \lim_{\Delta t \to 0} \frac{\tilde{u}(k_x, k_y, t+\Delta t) - \tilde{u}(k_x, k_y, t)}{\Delta t}. \tag{5.17}$$

Substituting the expressions for $\tilde{u}(k_x, k_y, t+\Delta t)$ and $\tilde{u}(k_x, k_y, t)$, and retaining terms upto $O(1)$, we have

$$\frac{\partial \tilde{u}_1}{\partial t} = \frac{u_0 \tilde{\rho}_1}{\rho_0} B + \tilde{u}_1 B - 2jk_x u_0 \tilde{u}_1 - jk_y v_0 \tilde{u}_1 - jk_y u_0 \tilde{v}_1. \tag{5.18}$$

Similarly, the governing equation for $\tilde{v}_1$ is

$$\frac{\partial \tilde{v}_1}{\partial t} = \frac{v_0 \tilde{\rho}_1}{\rho_0} B + \tilde{v}_1 B - jk_x u_0 \tilde{v}_1 - 2jk_y v_0 \tilde{v}_1 - jk_x v_0 \tilde{u}_1. \tag{5.19}$$

Additionally, we assume that the total population of SPPs within the group does not change over time, so that the mass conservation equation is valid. Therefore the (linearized) governing equation for $\tilde{\rho}_1$ is

$$\frac{\partial \tilde{\rho}_1}{\partial t} - jk_x \rho_0 \tilde{u}_1 - jk_x u_0 \tilde{\rho}_1 - jk_y \rho_0 \tilde{v}_1 - jk_y v_0 \tilde{\rho}_1 = 0. \tag{5.20}$$

5.3 SPP groups behave like a fluid

At spatial scales that are much larger compared to the length-scale of perception of an individual SPP, $k_x L_x \ll 1$ and $k_y L_y \ll 1$. A small-wavenumber approximation can then be made to simplify the behavioral term in Equation 5.16, which can be written as

$$B \approx \frac{1}{T}\left(\frac{1}{\rho_0 L_x L_y} - 1\right) - \frac{1}{T\rho_0 L_x L_y}\left(\frac{k_x^2 L_x^2}{4!} + \frac{k_y^2 L_y^2}{4!}\right). \tag{5.21}$$

Using Equation 5.21 in Equations 5.18 and 5.19, and computing the inverse spatial Fourier transform, we have the following governing equations for $u_1(x, y, t)$ and $v_1(x, y, t)$, respectively:

$$
\begin{aligned}
\frac{\partial u_1}{\partial t} + u_0 \frac{\partial u_1}{\partial x} + v_0 \frac{\partial u_1}{\partial y} = u_0 \alpha \rho_1 + u_0 \beta \frac{\partial^2 \rho_1}{\partial x^2} + u_0 \gamma \frac{\partial^2 \rho_1}{\partial y^2} + \rho_0 \alpha u_1 \\
+ \rho_0 \beta \frac{\partial^2 u_1}{\partial x^2} + \rho_0 \gamma \frac{\partial^2 u_1}{\partial y^2} - u_0 (\nabla \cdot \mathbf{u}_1) \quad (5.22)
\end{aligned}
$$

$$
\begin{aligned}
\frac{\partial v_1}{\partial t} + u_0 \frac{\partial v_1}{\partial x} + v_0 \frac{\partial v_1}{\partial y} = v_0 \alpha \rho_1 + v_0 \beta \frac{\partial^2 \rho_1}{\partial x^2} + v_0 \gamma \frac{\partial^2 \rho_1}{\partial y^2} + \rho_0 \alpha v_1 \\
+ \rho_0 \beta \frac{\partial^2 v_1}{\partial x^2} + \rho_0 \gamma \frac{\partial^2 v_1}{\partial y^2} - v_0 (\nabla \cdot \mathbf{u}_1), \quad (5.23)
\end{aligned}
$$

where

$$
\begin{aligned}
\alpha &= \frac{1}{T \rho_0} \left(\frac{1}{\rho_0 L_x L_y} - 1 \right) &(5.24)\\
\beta &= \frac{L_x}{\rho_0^2 T L_y 4!} &(5.25)\\
\gamma &= \frac{L_y}{\rho_0^2 T L_x 4!}. &(5.26)
\end{aligned}
$$

Equations 5.22 and 5.23 are a general form of the linearized Navier-Stokes equations for a fluid with additional diffusive terms and terms arising from the compressible nature of the medium (i.e terms with the spatial derivatives of ρ_1). The governing equations 5.22 and 5.23 are similar to the ones *assumed* in Ref.[253]. However, there are a few key differences. Equations 5.22 and 5.23 lack any term proportional to the dynamic pressure (i.e proportional to $\nabla \rho_1$) in contrast to the governing equation assumed in Ref.[253]. Additionally, there are mass diffusion terms proportional to $\nabla^2 \rho_1$ in Equations 5.22 and 5.23, which are not present in the governing equation assumed in Ref.[253].

5.4 Existence of a critical population density in SPP groups

Equations 5.18, 5.19 and 5.20 can be written in matrix form as

$$\frac{\partial}{\partial t}\begin{Bmatrix}\tilde{u}_1\\ \tilde{v}_1\\ \tilde{\rho}_1\end{Bmatrix}+[M]\begin{Bmatrix}\tilde{u}_1\\ \tilde{v}_1\\ \tilde{\rho}_1\end{Bmatrix}=0, \tag{5.27}$$

where

$$[M] = \begin{bmatrix}-B+2jk_xu_0+jk_yv_0 & jk_yu_0 & -\frac{u_0B}{\rho_0}\\ jk_xv_0 & -B+jk_xu_0+2jk_yv_0 & -\frac{v_0B}{\rho_0}\\ jk_x\rho_0 & jk_y\rho_0 & jk_xu_0+jk_yv_0\end{bmatrix}. \tag{5.28}$$

To de-couple the governing equations in the wavenumber domain (Equation 5.27), we define the following transformation :

$$\begin{Bmatrix}\tilde{x}_1\\ \tilde{x}_2\\ \tilde{x}_3\end{Bmatrix}\equiv[S]^{-1}\begin{Bmatrix}\tilde{u}_1\\ \tilde{v}_1\\ \tilde{\rho}_1\end{Bmatrix} \tag{5.29}$$

where $[S]=[\bar{e}_1\;\bar{e}_2\;\bar{e}_3]^{\mathrm{T}}$, and $(\bar{e}_1,\bar{e}_2,\bar{e}_3)$ are the eigenvectors of $[M]$. Applying this transformation to Equation 5.27 (Appendix M), we have

$$\frac{\partial\tilde{x}_1}{\partial t}+\lambda_1\tilde{x}_1 = 0 \tag{5.30}$$
$$\frac{\partial\tilde{x}_2}{\partial t}+\lambda_2\tilde{x}_2 = 0 \tag{5.31}$$
$$\frac{\partial\tilde{x}_3}{\partial t}+\lambda_3\tilde{x}_3 = 0. \tag{5.32}$$

where $\lambda_i, i=1,2,3$ are the eigenvalues of $[M]$ given by

$$\left\{\begin{array}{c}\lambda_1\\ \lambda_2\\ \lambda_3\end{array}\right\} = \left\{\begin{array}{c}-B+j(\mathbf{k}\cdot\mathbf{u_0})\\ \frac{1}{2}\left(-\sqrt{B^2-6jB(\mathbf{k}\cdot\mathbf{u_0})-(\mathbf{k}\cdot\mathbf{u_0})^2}-B+3j(\mathbf{k}\cdot\mathbf{u_0})\right)\\ \frac{1}{2}\left(\sqrt{B^2-6jB(\mathbf{k}\cdot\mathbf{u_0})-(\mathbf{k}\cdot\mathbf{u_0})^2}-B+3j(\mathbf{k}\cdot\mathbf{u_0})\right)\end{array}\right\}. \tag{5.33}$$

The general solutions to Equations 5.30-5.32 are

$$\tilde{x}_1 = \mathrm{e}^{-\lambda_1 t}\tilde{x}_1(t=0) \tag{5.34}$$

$$\tilde{x}_2 = \mathrm{e}^{-\lambda_2 t}\tilde{x}_2(t=0) \tag{5.35}$$

$$\tilde{x}_3 = \mathrm{e}^{-\lambda_3 t}\tilde{x}_3(t=0). \tag{5.36}$$

The quantities $\tilde{x}_1, \tilde{x}_2$ and $\tilde{x}_3$ are related to $\tilde{u}_1, \tilde{v}_1$ and $\tilde{\rho}_1$ via the transformation matrix in Equation 5.29. Expanding the transformation matrix, we have:

$$\tilde{x}_1 = -\frac{k_y v_0 \tilde{u}_1}{\mathbf{k}\cdot\mathbf{u_o}} + \frac{k_x u_0 \tilde{v}_1}{\mathbf{k}\cdot\mathbf{u_o}} \tag{5.37}$$

$$\tilde{x}_2 = \frac{jk_x\rho_0\tilde{u}_1}{\sqrt{Q}} + \frac{jk_y\rho_0\tilde{v}_1}{\sqrt{Q}} + \frac{\left(B+\sqrt{Q}-j(\mathbf{k}\cdot\mathbf{u_0})\right)\tilde{\rho}_1}{2\sqrt{Q}} \tag{5.38}$$

$$\tilde{x}_3 = -\frac{jk_x\rho_0\tilde{u}_1}{\sqrt{Q}} - \frac{jk_y\rho_0\tilde{v}_1}{\sqrt{Q}} + \frac{\left(-B+\sqrt{Q}+j(\mathbf{k}\cdot\mathbf{u_0})\right)\tilde{\rho}_1}{2\sqrt{Q}}, \tag{5.39}$$

where

$$Q = B^2 - j6B(\mathbf{k}\cdot\mathbf{u_0}) - (\mathbf{k}\cdot\mathbf{u_0})^2. \tag{5.40}$$

Taking the inverse Fourier transform of Equations 5.37-5.39, for $u_0 = v_0$ and using a low-wavenumber approximation, we have the following approximate realtions between x_1, x_2, x_3 and u_1, v_1, ρ_1:

$$\left(\frac{\partial}{\partial x}+\frac{\partial}{\partial y}\right)x_1 \approx |\nabla\times\mathbf{u_1}| \quad (5.41)$$

$$x_2 \approx \frac{1}{\alpha}(\nabla\cdot\mathbf{u_1})+\rho_1 \quad (5.42)$$

$$x_3 \approx -\frac{1}{\alpha}(\nabla\cdot\mathbf{u_1}). \quad (5.43)$$

From Equations 5.41-5.43, we see that the quantity x_1 is related to the curl of the velocity disturbance, and the quantities x_2 and x_3 are related to the compressibility of the system of SPPs.

We transform the solutions $\tilde{x}_i$ in space-time domain, and perform a stability analysis to identify behavioral parameters that lead to linearly stable solutions that do not grow as a function of time. To do this, an initial gaussian disturbance of the form $x_i(t=0) = \exp\left[-\kappa\left(x^2+y^2\right)\right], \kappa>0$, is applied, where $x_i \Leftrightarrow \tilde{x}_i$. The plot of $10\log_{10}(\max(|x_1(t=50\text{ s})|)/\max(|x_1(t=0\text{ s})|))$ as a function $\rho_0 L_x L_y$ for $u_0=v_0=0$ is shown in Figure 5-1. The amplitude of the disturbance x_1 after a long time ($t=50$ s) is lower than its initial amplitude for $\rho_0 L_x L_y > 1$, irrespective of the reaction time T of the boid. When $\rho_0 L_x L_y < 1$, the amplitude of x_1 at $t=50$ s grows much larger than the initial disturbance so that linear theory is no longer valid. Figure 5-1 also shows that the disturbance x_1 is damped at higher rates for lower reaction times T of the boid.

A similar analysis of x_2 (Figure 5-2) and x_3 (Figure 5-3) reveals that $\rho_0 L_x L_y > 1$ represents a criticality condition when disturbances do not grow over time and uniform motion is maintained in the SPP group. This criticality condition is not restricted to a Gaussian disturbance, and is found to hold even for an initial square disturbance (Appendix N).

For the simple case of $u_0=v_0=0$, it is also possible to arrive at the criticality condition ($\rho_0 L_x L_y$) analytically. Let us consider the general form of the solution in Equations 5.34-5.36:

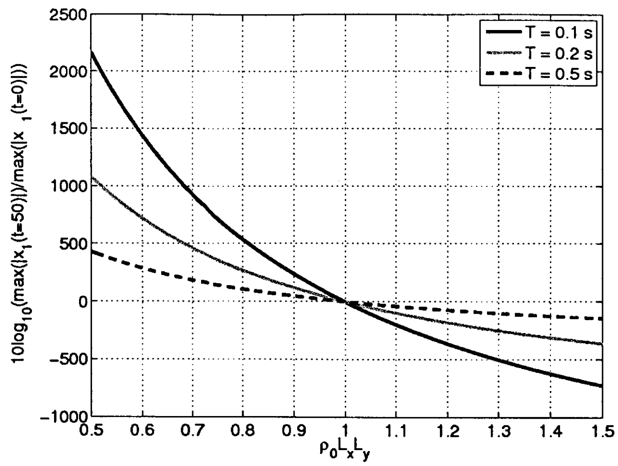

Figure 5-1: $10\log_{10}(\max(|x_1(t = 50s)|)/\max(|x_1(t = 0s)|)$ for $u_0 = v_0 = 0$ and for different reaction times $T = 0.1, 0.2, 0.5$ s. The amplitude of the disturbance x_1 after a large time ($t = 50$ s) is lower than its initial amplitude for a critical number of $\rho_0 L_x L_y > 1$, irrespective of the reaction time of the boid. In the sub-critical regime ($\rho_0 L_x L_y < 1$), the amplitude of the disturbance at 50 s has grown much larger than the initial initial amplitude such that the solution is no longer linearly stable and linear theory is no longer valid.

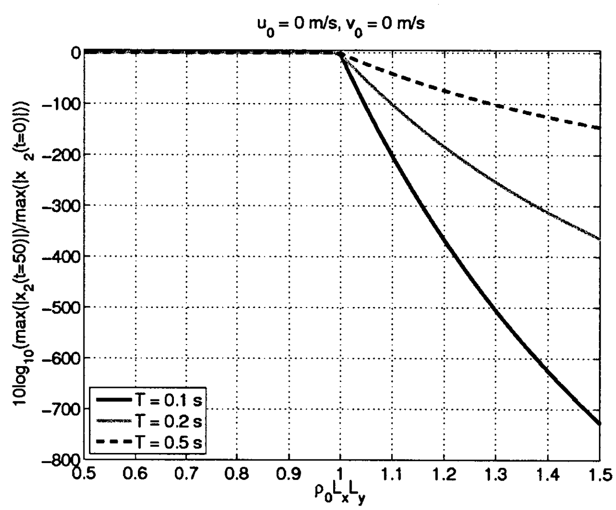

Figure 5-2: $10\log_{10}(\max(|x_2(t = 50s)|)/\max(|x_2(t = 0s)|)$ for $u_0 = v_0 = 0$ m/s and for different reaction times $T = 0.1, 0.2, 0.5$ s. The amplitude of the disturbance x_2 after a large time ($t = 50$ s) is lower than its initial amplitude for a critical number of $\rho_0 L_x L_y > 1$, irrespective of the reaction time of the boid.

$$\tilde{f}(k_x, k_y, t) = e^{-\lambda_i(k_x,k_y)t}\tilde{f}(k_x, k_y, t = 0), \tag{5.44}$$

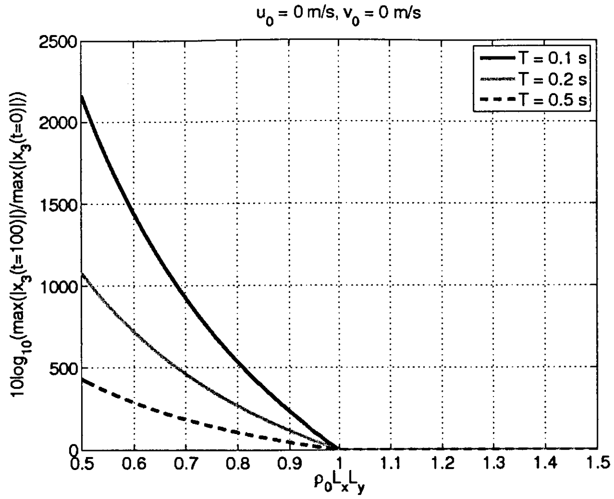

Figure 5-3: $10\log_{10}(\max(|x_3(t=50s)|)/\max(|x_3(t=0s)|)$ for $u_0 = v_0 = 0$ m/s and for different reaction times $T = 0.1, 0.2, 0.5$ s. The amplitude of the disturbance x_3 after a large time ($t = 50$ s) does not grow larger than its initial amplitude for a critical number of $\rho_0 L_x L_y > 1$, irrespective of the reaction time of the boid. In the sub-critical regime ($\rho_0 L_x L_y < 1$), the amplitude of the disturbance at 50 s has grown much larger than the initial initial amplitude such that the solution is no longer linearly stable and linear theory is no longer valid.

and let us also assume $\tilde{f}(k_x, k_y, t = 0) = 1$, for simplicity. From Parseval's theorem, we have

$$\begin{aligned}\int_{x=-\infty}^{\infty}\int_{y=-\infty}^{\infty} |f(x,y,t)|^2 \, \mathrm{d}x \, \mathrm{d}y &= \int_{k_x=-\infty}^{\infty}\int_{k_y=-\infty}^{\infty} \left|\tilde{f}(k_x,k_y,t)\right|^2 \, \mathrm{d}k_x \, \mathrm{d}k_y \\ &= \int_{k_x=-\infty}^{\infty}\int_{k_y=-\infty}^{\infty} \mathrm{e}^{-2\Re(\lambda_i(k_x,k_y))t} \, \mathrm{d}k_x \, \mathrm{d}k_y,\end{aligned} \tag{5.45}$$

where $\Re(\lambda)$ is the real part of λ. Let there exist a set of wavenumbers $\{k_x^s\} = [k_1, k_2]$ and $\{k_y^s\} = [k_3, k_4]$ where $\Re(\lambda_i(k_x^s, k_y^s)) < 0$. Then Equation 5.45 can be written as

$$\int_x \int_y |f(x,y,t)|^2 \, \mathrm{d}x \, \mathrm{d}y = \int_{k_x \notin k_x^s} \int_{k_y \notin k_y^s} \mathrm{e}^{-2\Re(\lambda_i(k_x,k_y))t} \, \mathrm{d}k_x \, \mathrm{d}k_y + \int_{k_x \in k_x^s} \int_{k_y \in k_y^s} \mathrm{e}^{-2\Re(\lambda_i(k_x,k_y))t} \, \mathrm{d}k_x \, \mathrm{d}k_y \quad (5.46)$$

Using the Mean Value Theorem for the second integral in Equation 5.46, there exists some $k_x^* \in k_x^s$ and $k_y^* \in k_y^s$ such that

$$\int_x \int_y |f(x,y,t)|^2 \, \mathrm{d}x \, \mathrm{d}y = \int_{k_x \notin k_x^s} \int_{k_y \notin k_y^s} \mathrm{e}^{-2\Re(\lambda_i(k_x,k_y))t} \, \mathrm{d}k_x \, \mathrm{d}k_y + \mathrm{e}^{-2\Re(\lambda_i(k_x^*,k_y^*))t} (k_2 - k_1)(k_4 - k_3). \quad (5.47)$$

Equation 5.47 shows that, for large t, the square integral of $f(x,y,t)$ will become exponentially large since $\Re(\lambda_i(k_x^*, k_y^*)) < 0$. If we are looking for square-integrable solutions for $f(x,y,t)$, then there can be no set where $\Re(\lambda_i(k_x^*, k_y^*)) < 0$. In other words, for all k_x, k_y, we require that $\Re(\lambda_i(k_x, k_y)) > 0$. Note that we have assumed that λ_i is an analytic function of k_x, k_y. The stability criteria will impose conditions on ρ_0 or the population density such that the disturbances are damped and linear stability is maintained. In the special case of $u_0, v_0 = 0$, the stability condition is merely $B(k_x, k_y) < 0$, for all k_x, k_y. From the expression for B in Equation 5.16, it is enough if we limit the maximum value of $B(k_x, k_y)$ to less than zero, which results in the simple linear-stability criterion:

$$\rho_0 L_x L_y > 1, \quad (5.48)$$

or

$$\rho_0 > \frac{1}{L_x L_y}. \quad (5.49)$$

For many species of animals, the length scale of perception and hence L_x, L_y is usually known, and so the criterion for linear stability specifies a critical population density above which disturbances are damped, and synchronous motion is maintained. Since $\rho_0 L_x L_y$ represents the total number of particles on average within the region of influence of any individual, the stability criterion merely states that disturbances get damped/do not grow and synchronous motion is maintained if there is at least one neighbour within the region of perception of each boid. The stability criterion $\rho_0 L_x L_y > 1$ can also be thought of as the condition when the regions of perception of two (or more) particles overlap so that each particle begins to influence the other.

5.5 Wave propagation within SPP groups

Consider the governing equations 5.30 -5.32 for $\tilde{x}_1, \tilde{x}_2$ and $\tilde{x}_3$

$$\frac{\partial \tilde{x}_i}{\partial t} + \lambda_i \tilde{x}_i = 0, \; i = 1, 2, 3. \tag{5.50}$$

Let the solution $\tilde{x}_i$ be given by

$$\tilde{x}_i = A_i(k_x, k_y) \, \mathrm{e}^{-j\omega_i t}, \tag{5.51}$$

where

$$A_i(k_x, k_y) = \tilde{x}_i(k_x, k_y, t = 0). \tag{5.52}$$

Using the solution in Equation 5.51 in Equation 5.50, we have

$$\lambda_i(k_x, k_y) = j\omega_i(k_x, k_y), \tag{5.53}$$

and the solution $x_i(x, y, t)$ can be written as

$$x_i(x,y,t) = \int_{k_x=-\infty}^{\infty}\int_{k_y=-\infty}^{\infty} \mathrm{e}^{-j\omega_i t}\,\mathrm{e}^{jk_x x}\,\mathrm{e}^{jk_y y}\tilde{x}_i(k_x,k_y,t=0)\,\mathrm{d}k_x\,\mathrm{d}k_y. \tag{5.54}$$

Let the initial disturbance be a narrow Gaussian pulse centered around $\mathbf{k_0} = (k_{x0}, k_{y0})$:

$$\tilde{x}_i(k_x,k_y,t=0) = \exp\left[-\kappa\left((k_x-k_{x0})^2+(k_y-k_{y0})^2\right)\right], \kappa > 0. \tag{5.55}$$

The frequency $\omega_i(k_x,k_y)$ can be expanded as a Taylor series around (k_{x0},k_{y0}) so that

$$\omega_i(k_x,k_y) = \omega_i(k_{x0},k_{y0}) + \left.\frac{\partial\omega_i}{\partial k_x}\right|_{k_{x0},k_{y0}}(k_x-k_{x0}) + \left.\frac{\partial\omega_i}{\partial k_y}\right|_{k_{x0},k_{y0}}(k_y-k_{y0}) + \text{ higher order terms} \tag{5.56}$$

We now define

$$\left.\frac{\partial\omega_i}{\partial k_x}\right|_{k_{x0},k_{y0}} \equiv c_{g,x,i} \tag{5.57}$$

$$\left.\frac{\partial\omega_i}{\partial k_y}\right|_{k_{x0},k_{y0}} \equiv c_{g,y,i}, \tag{5.58}$$

so that by neglecting higher order terms in the expansion of ω_i the solution $x_i(x,y,t)$ is given by

$$x_i(x,y,t) = \mathrm{e}^{-j(\omega_i(k_{x0},k_{y0})t-k_{x0}c_{g,x,i}t-k_{y0}c_{g,y,i}t)} \int_{k_x=-\infty}^{\infty} \mathrm{e}^{-\kappa(k_x-k_{x0})^2}\,\mathrm{e}^{jk_x(x-c_{g,x,i}t)}\,\mathrm{d}k_x \int_{k_y=-\infty}^{\infty} \mathrm{e}^{-\kappa(k_y-k_{y0})^2}\,\mathrm{e}^{jk_y(y-c_{g,y,i}t)}\,\mathrm{d}k_y. \tag{5.59}$$

$$= e^{-j(\omega_i(k_{x0},k_{y0})t - k_{x0}c_{g,x,i}t - k_{y0}c_{g,y,i}t)}$$

$$\frac{\pi}{\kappa}\exp\left[-\frac{(x - c_{g,x,i}t)^2}{4\kappa} - \frac{(y - c_{g,y,i}t)^2}{4\kappa}\right]. \quad (5.60)$$

Equation 5.60 represents a wave traveling with a group velocity of $\mathbf{c_{g,i}} = (c_{g,x,i}, c_{g,y,i}) = \left(\frac{\partial\omega_i}{\partial k_x}\Big|_{k_{x0},k_{y0}}, \frac{\partial\omega_i}{\partial k_y}\Big|_{k_{x0},k_{y0}}\right)$. Since x_1, x_2 and x_3 are linearly related to u_1, v_1 and ρ_1 (Equations 5.41, 5.42 and 5.43), we can conclude that u_1, v_1 and ρ_1 also travel as waves within SPP groups. Using Equations 5.53 and 5.33, we have the following dispersion relationships for the waves x_1, x_2 and x_3

$$\begin{Bmatrix} \omega_1 \\ \omega_2 \\ \omega_3 \end{Bmatrix} = \begin{Bmatrix} jB + (\mathbf{k}\cdot\mathbf{u_0}) \\ \frac{1}{2}\left(j\sqrt{B^2 - 6jB(\mathbf{k}\cdot\mathbf{u_0}) - (\mathbf{k}\cdot\mathbf{u_0})^2} + jB + 3(\mathbf{k}\cdot\mathbf{u_0})\right) \\ \frac{1}{2}\left(-j\sqrt{B^2 - 6jB(\mathbf{k}\cdot\mathbf{u_0}) - (\mathbf{k}\cdot\mathbf{u_0})^2} + jB - 3(\mathbf{k}\cdot\mathbf{u_0})\right) \end{Bmatrix} \quad (5.61)$$

For an initial pulse with $k_{x0} = k_{y0} = 0$, the group velocities in the x- and y-direction for x_1 are

$$c_{g,x,1} = \frac{\partial\omega_1}{\partial k_x}\Big|_{0,0} = j\frac{\partial B}{\partial k_x}\Big|_{0,0} + u_0 \quad (5.62)$$

$$c_{g,y,1} = \frac{\partial\omega_1}{\partial k_y}\Big|_{0,0} = j\frac{\partial B}{\partial k_y}\Big|_{0,0} + v_0. \quad (5.63)$$

The expression for the group speed of x_1 (Equations 5.62 and 5.63) clearly shows that x_1 propagates with a velocity of (u_0, v_0) (the real part of the group velocity), in agreement with simulations of $x_1(x, y, t)$ presented in Figure 5-4. Similarly consider initial Gaussian disturbances $\tilde{x}_2(t = 0)$ and $\tilde{x}_3(t = 0)$ centered around $k_x = k_y = 0$. Under a small wavenumber approximation, the x- and y-components of the group speed of x_2 are

$$c_{g,x,2} \approx \frac{j}{2}\frac{\partial B}{\partial k_x}\bigg|_{0,0} + 3u_0 \quad (5.64)$$

$$c_{g,y,2} \approx \frac{j}{2}\frac{\partial B}{\partial k_y}\bigg|_{0,0} + 3v_0, \quad (5.65)$$

and the the x- and y-components of the group speed of x_3 are

$$c_{g,x,3} \approx 0 \quad (5.66)$$

$$c_{g,y,3} \approx 0. \quad (5.67)$$

Taking the real part of the group speed of x_2, we see that x_2 is expected to travel at approximately three times the speed of the individual particles, in agreement with simulations of $x_2(x, y, t)$ in Figure 5-5. For small wavenumbers, the real part of the group speed of x_3 is approximately zero, and so we do not expect this mode to travel for low-wavenumber (or large spatial scale) disturbances. This again in agreement with simulations of $x_3(x, y, t)$ in Figure 5-6.

We have shown using both simulations and from theory that it is possible for disturbances to travel at speeds faster than the particle speeds within SPP groups. Such wave-like propagation of disturbances have been observed in nature as "density waves" in fish schools [203, 227] and bird flocks [98]. In all these cases, the speed of propagation of disturbances was greater than the normal speed of migration of the individuals.

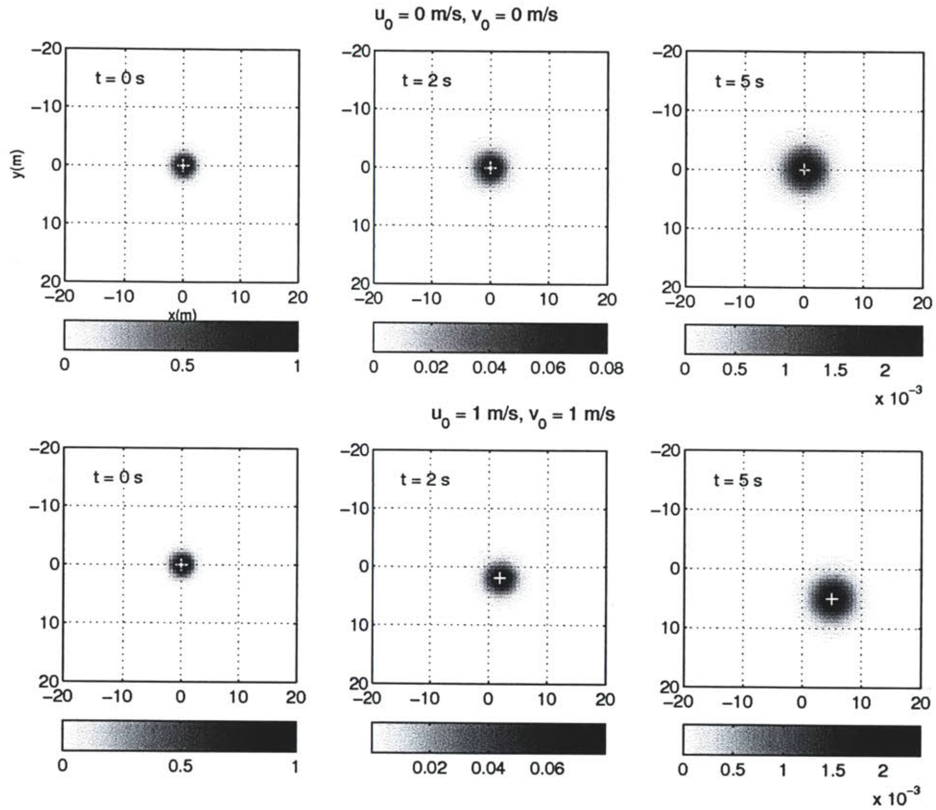

Figure 5-4: Images of $|x_1(x,y,t)|$ for different times $t = 0, 2, 5$ s and for $u_0 = v_0 = 0$ m/s (top row) and $u_0 = v_0 = 1$ m/s (bottom row). $\rho_0 L_x L_y = 2$ and reaction time $T = 0.5$ s. The white cross represents the location of the center of the disturbance (also the peak). The initial disturbance is of the form $\exp\left[-\kappa(x^2+y^2)\right], \kappa > 0$. For stationary groups ($u_0 = v_0 = 0$), the disturbance does not travel, but is exponentially damped. For non-zero SPP velocities, where $u_0, v_0 \neq 0$, the damped disturbance travels at the same speed of the particles. In this specific simulation for $u_0 = v_0 = 1$ m/s, the disturbance also travels at (1,1) m/s.

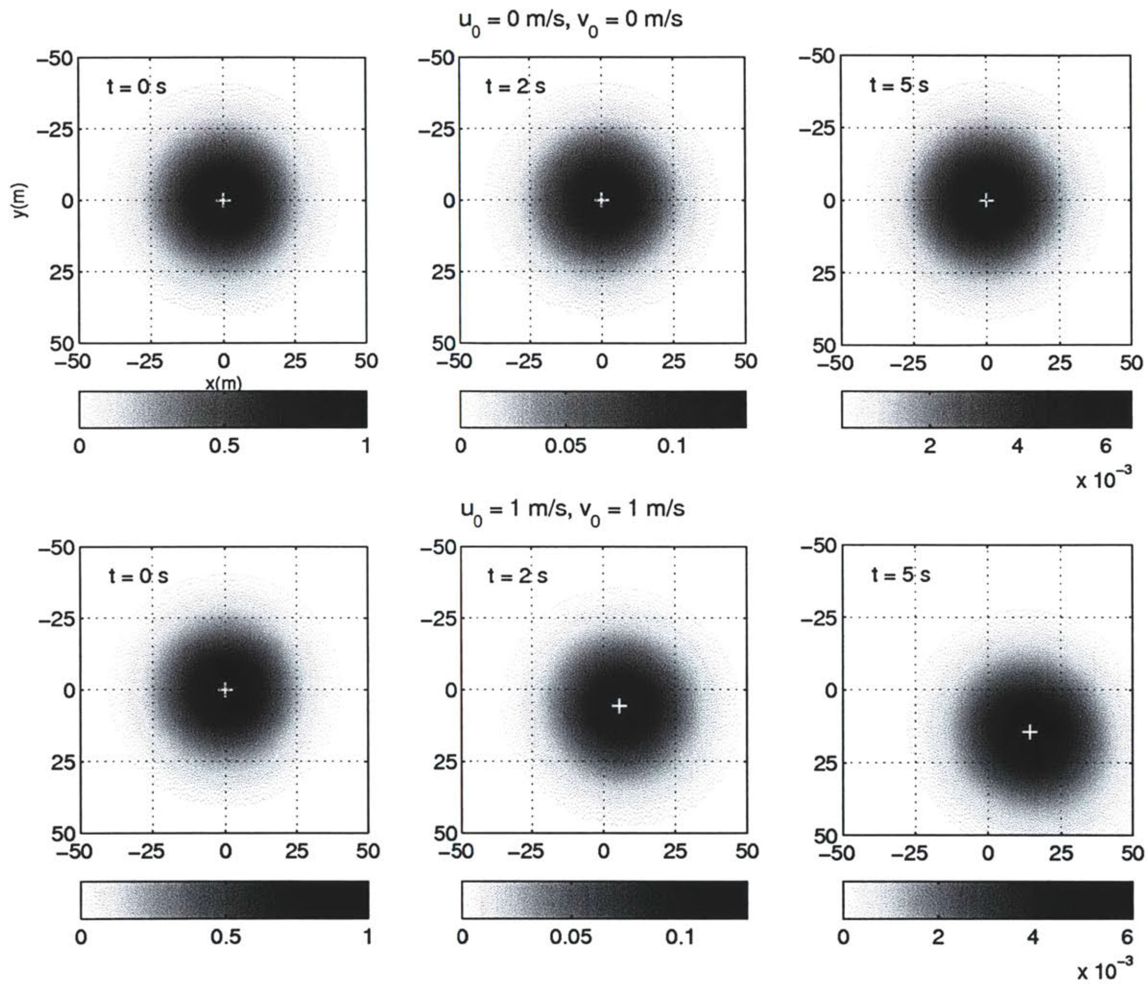

Figure 5-5: Images of $|x_2(x, y, t)|$ for different times $t = 0, 2, 5$ s and for $u_0 = v_0 = 0$ m/s (top row) and $u_0 = v_0 = 1$ m/s (bottom row). $\rho_0 L_x L_y = 2$ and reaction time $T = 0.5$ s. The white cross represents the location of the center of the disturbance (also the peak). The initial disturbance is of the form $\exp\left[-\kappa(x^2 + y^2)\right], \kappa > 0$. For stationary groups ($u_0 = v_0 = 0$), the disturbance does not travel, but is exponentially damped. For non-zero SPP velocities, where $u_0, v_0 \neq 0$, the damped disturbance travels at a speed greater than that of the particles. In this specific simulation for $u_0 = v_0 = 1$ m/s, the disturbance travels at $\approx$(3,3) m/s.

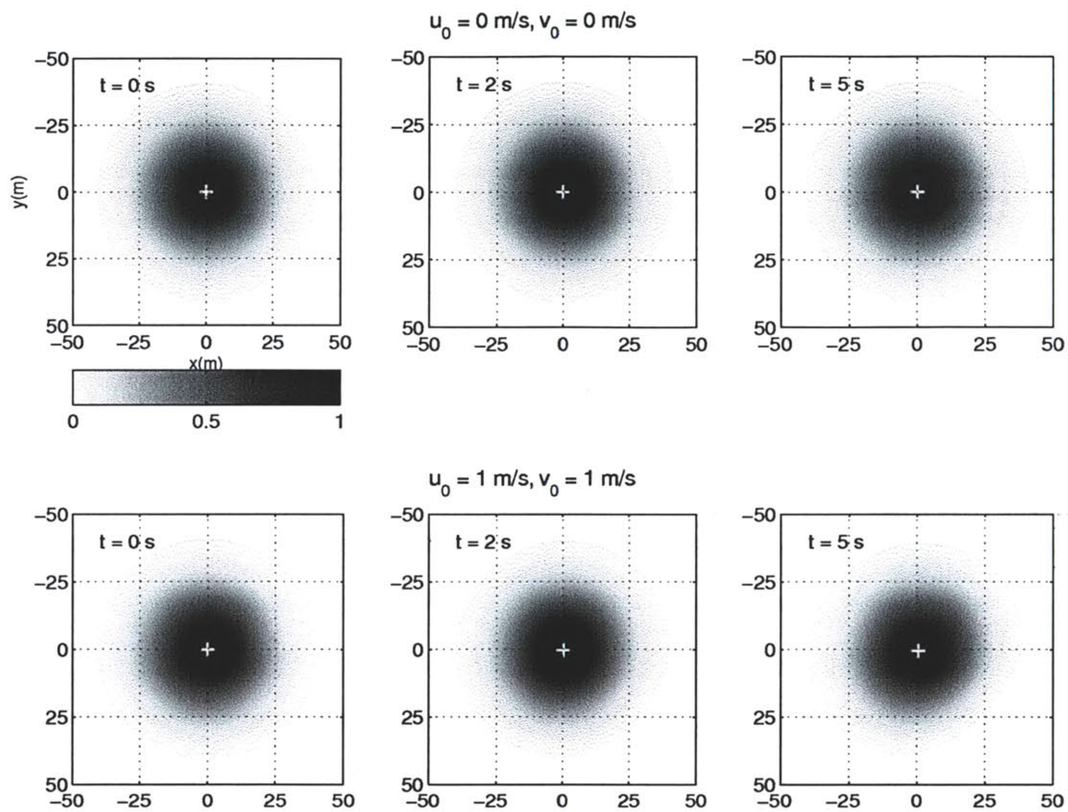

Figure 5-6: Images $|x_3(x, y, t)|$ for different times $t = 0, 2, 5$ s and for $u_0 = v_0 = 0$ m/s (top row) and $u_0 = v_0 = 1$ m/s (bottom row). $\rho_0 L_x L_y = 2$ and reaction time $T = 0.5$ s. The white cross represents the location of the center of the disturbance (also the peak). The initial disturbance is of the form $\exp\left[-\kappa(x^2 + y^2)\right], \kappa > 0$. For this initial disturbance and for both stationary groups ($u_0 = v_0 = 0$) as well as mobile groups, the disturbance does not travel, and remains more or less constant, as expected from Figure 5-3.

In Figures 5-4, 5-5 and 5-6, the propagation of x_1, x_2 and x_3 through the group is simulated, respectively. A post-critical scenario with $\rho_0 L_x L_y = 2$ is used and the reaction time of the individuals is assumed to be $T = 0.5$ s. For the case of stationary groups, where $u_0 = v_0 = 0$, none of the disturbances travel within the group (top rows of Figures 5-4, 5-5 and 5-6). Instead the disturbances diffuse slowly through the group. In the case of mobile groups, the results differ for x_1, x_2 and x_3. In the specific simulation for $u_0 = v_0 = 1$ m/s shown in Figure 5-4, disturbance x_1 travels at the same velocity as that of the particles. The disturbance also gets damped over time as its spreads through the group. The second disturbance x_2, however, travels at speeds much faster than that of the individuals. The magnitude of the disturbance also exponentially reduces as it spreads through the group. Interestingly, x_3 is undamped and does not travel through the group even for non-zero u_0, v_0 for the particular Gaussian initial disturbance chosen.

5.6 Discussion

The theoretical formulations in this paper are based on the assumption that individuals within a large group follow the simple behavioral model that each individual averages the velocity of its neighbours. The spatial spectrum of this averaging window is a key quantity in the behavioral term B in Equation 5.16. In the case of a uniform window, its spectrum is merely the products of two sinc terms in Equation 5.16.

There has been considerable research about individual behavioral rules different from the uniform velocity averaging rule used here. Refs. [112, 49] , for example, have reported the use of more complicated and possibly more realistic behavioral rules that include zones of orientation, attraction and repulsion, as well as blind zones [112]. Changing the individual behavioral model used in the theoretical formulation in Section 5.2.1 is simple. The behavioral model is constructed in space and its fourier transform replaces the sinc terms in Equation 5.16.

5.7 Conclusions

A continuum description of large groups of self-propelled particles (SPPs) is used to develop a fluid dynamic theory for describing collective behavior of animal groups. Starting from the simple behavioral rule that each individual picks the average velocity of all neighbours within its region of perception, we analytically showed that SPP groups behave as a fluid over spatial scales much larger than the mean spacing between individuals. We also analytically showed the existence of a critical population density where each particle needs at least one neighbor within its rgion of perception on average to sustain synchronous motion within the SPP group. It is shown that disturbances can propagate as waves within a group at speeds much higher than that of any individual. These findings may explain how rapid information transfer can occur within animal groups, which may ultimately help maintain long-range order. They also provide an analytic foundation for similar results obtained from numerical simulations, and laboratory and field experiments.

Chapter 6

Scattering from extended targets in range-dependent fluctuating ocean-waveguides with clutter, from theory and experiments

6.1 Introduction

Vertically extended air-filled tubular targets[159] are commonly used during acoustic experiments at sea [212]. They provide an important means of calibrating active sonar systems against full-field waveguide scattering models and for minimizing charting errors[212]. They also serve as a reference for determining the relative scattering strength from other objects of interest in the ocean due to their known high target strength. When modeling scattering from such air-filled extended targets in range- and depth-dependent fluctuating waveguides, it is not possible to make simplifying assumptions such as the target compactness assumption[211] of the Sonar Equation[258] or the iso-sound speed assumption[211] of the Ingenito Scattering model[113]. In this paper, a Greens' theorem-based full-field model that describes scattering from vertically extended tubular targets in range-dependent fluctuating ocean waveguides by taking into account nonuniform sound speed structure over the target's depth extent is shown to accurately describe the statistics of the targets' scattered field measured during three distinct field experiments.

Bistatic, long-range, low-frequency measurements of acoustic returns from vertically extended air-filled cylindrically-shaped targets were made during three field experiments sponsored by the Office of Naval Research (ONR). Two of these experiments were carried out in the New Jersey continental shelf region during May-June 2001 [212] and 2003 [158, 120] (NJ2001 and NJ2003), and the third experiment was carried out in Georges Bank during Sep-Oct 2006 [157, 89] (GOM2006). During all three experiments, Ocean Acoustic Waveguide Remote Sensing (OAWRS) systems[120, 89] were used to image passive acoustic targets, which were vertically suspended from the seafloor using floats and anchors, so that they occupied specified water depths. These man-made targets were manufactured by BBN Technologies[159] (Cambridge, MA) and consisted of 30-m long and 7-cm diameter air-filled tubular hoses made of gum rubber. The acoustic returns from these targets were measured across multiple frequency bands ranging from 415 Hz to 1325 Hz.

Besides man-made targets, target-like clutter were also imaged during all three experiments. Atlantic herring schools were found to be the primary cause of such target-like clutter imaged during the NJ2003 and GOM2006 experiments[120, 89]. While both fish schools and man-made targets have similar spatial characteristics and scattered intensity levels, the spectral dependence of acoustic returns from the man-made targets is shown to be very different from that of returns from fish schools, making them robustly distinguishable by multi-frequency measurements.

The target-scattered data from all three field experiments are also used to assess the performance of the Vertically Extended cylindrical Target Waveguide Scattering (VETWS) model[134] as well as other standard scattering models such as the sonar equation[258] and the Ingenito[113] scattering model. The means and variances of the acoustic field scattered by the man-made targets simulated using the VETWS model are shown to match (within 3 dB) the corresponding measured statistics in all three experiments considered in this paper. Sonar Equation estimates of mean scattered intensity from the targets lead to large errors, typically differing by up to an order of magnitude from both measurements and waveguide scattering theory. This is because the sonar equation approximation is not applicable to targets that are large compared to the acoustic wavelength in an ocean waveguide [211]. Using Ingenito's scattering model also leads to significant errors in estimating mean target-scattered intensity. This is because the experiments were conducted in range-dependent ocean environments with large variations in sound speed structure over the depth extent of the targets, scenarios that violate basic assumptions [113] of the Ingenito model.

The VETWS model can be applied to both pressure-release and penetrable cylindrical targets that are vertically extended in an ocean waveguide[134]. In this model, the scattered field in the vicinity of the target is expressed in terms of Hankel functions, whose coefficients are determined by matching appropriate boundary conditions on the surface of the target. By allowing the coefficients to vary with the depth of the target, the effects of incident field refraction are taken into account. While Ref. [134] provides an approximate numerical recipe to determine these coefficients, an alternative approach is used in this paper, by explicitly deriving their analytical expressions.

The arrival structure and dispersion of scattered acoustic returns from man-made targets is quantified by implementing the matched-filter [256, 137, 14]. By studying the effects of waveguide dispersion on the arrival structure of scattered returns, it is shown that the targets may appear in sonar imagery either as sharp, well localized returns with high signal-to-noise ratio (SNR) (> 10 dB) or as dispersed returns with low SNR. It is then important to have accurate knowledge of oceanography when trying to model scattering from such targets in continental shelf environments. Fluctuations in oceanography, such as the sound speed structure, are shown to affect the ability to localize the man-made targets in a waveguide. To account for the scintillation in the measured scattered intensity caused by fluctuations of the ocean waveguide, Monte-Carlo simulations of the scattered field are computed by implementing the full-field model in a range-dependent environment randomized by internal waves.

The three experimental scenarios where bi-static measurements of scattering from vertically extended air-filled cylindrical targets were made are described in the next section. In Sec. 6.3, the general characteristics of the target-scattered field from all three experiments, including spectral dependence of scattered returns, are described. Broad-spectrum measurements of the target scattered field are also shown to help distinguish such man-made targets from natural biological clutter such as fish schools that appear to be similar in single frequency long range sonar imagery. In Sec. 6.4, the theoretical approach and analytical formulation for scattering from the man-made targets are presented. In Section 6.5, comparisons are made of the measured statistics of target returns from all three experiments with (1) the Sonar Equation model, (2) the Ingenito scattering model and (3) the VETWS model. It is shown that both the sonar equation and the Ingenito scattering models lead to large errors (> 5 dB), while the full-field model is shown to be most accurate (errors < 3 dB) in describing the measured mean and standard deviation of the target-scattered levels.

6.2 Description of Field Experiments

6.2.1 The 2001 experiment of the ONR Geoclutter Program

The ONR-sponsored NJ2001 experiment that took place in the New Jersey continental shelf from April 17 to May 5, 2001, was designed to (1) study spatial and temporal variability of clutter in long-range active sonar, (2) identify dominant sources of clutter and understand their physical mechanisms, and (3) examine bistatic scattering characteristics of clutter[212]. Figure 6-1A and B show the bathymetry contours in the New Jersey continental shelf and the geometry of two tracks during the NJ2001 experiment, respectively. The experimental design consisted of a moored vertical source array, and a horizontal receiving array that was separately deployed allowing bistatic measurements of echo returns. Broadband Tukey-windowed linear frequency modulated (LFM) pulses 1s in duration and 50 Hz bandwidth were transmitted at frequencies centered at 375, 415, 750 and 1500 Hz. The study area represents a typical continental shelf environment with a fairly constant bathymetry but highly varied oceanography. Monitoring of physical oceanography was carried out concurrently with the acoustic sensing experiment. Measurements of water column temperature and salinity were taken regularly using expendable bathythermographs (XBT) and Conductivity, Temperature, Depth (CTD) sensors. The measured water column sound speed profiles are used as inputs in the modeling of the scattered returns from air-filled cylindrical targets.

6.2.2 The 2003 experiment of the ONR Geoclutter Program

The New Jersey continental shelf region was studied again during the NJ2003 experiment, which was designed to establish actual mechanisms of clutter and reverberation[80] including scattering from large fish shoals[158, 120] as well as calibrated air-filled targets. The geometry of two tracks during the experiment is shown in Figure 6-1C. During the experiment 1-s long LFM waveforms of 50-Hz bandwidth centered at 415, 950 and 1325 Hz were transmitted, enabling multi-spectral analysis of echo returns. Monitoring the physical oceanography occurred concurrently with the acoustic sensing experiment. Here XBT/CTD-based measurements of water column sound speed profiles are used to generate multiple realizations of a fluctuating ocean environment for monte-carlo modeling of the scattered returns from the air-filled cylindrical targets.

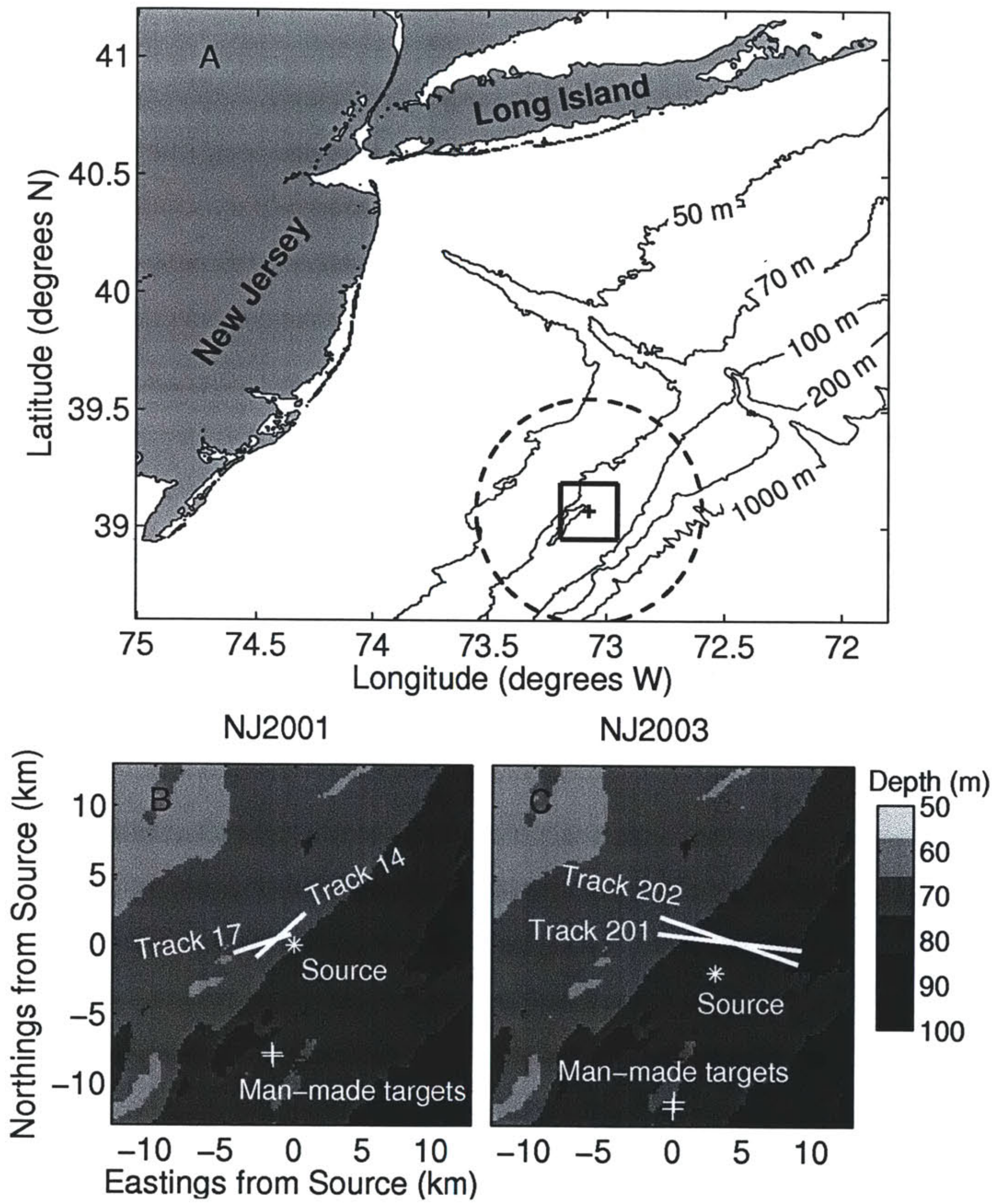

Figure 6-1: (**A**): Location of the NJ2001 and the NJ2003 experiments, off the coast of New Jersey. **Black dashed circle shows 60-km diameter areal imaging coverage in 40 s.** (**B,C**): Geometry of the experiments showing the location of the moored source, the targets, and 2 receiver tracks in each experiment from which measured target-scattered received levels are used for comparisons with models. The zoom area is shown as a black box in (A). The grayscale shows the relatively flat bathymetry in the region.

6.2.3 The 2006 experiment of the National Oceanographic Partnership Program (NOPP)

The NOPP-sponsored GOM2006 experiment that took place in the Gulf of Maine from Sep. 19 to Oct. 6, 2006, was designed to study the scattering characteristics and behavior[157] of Atlantic herring (*Clupea harengus*) through wide-area images of instantaneous scattered acoustic intensity levels[89]. Figure 6-2 shows the geometry of the experiment and bathymetry contours near Georges Bank, Gulf of Maine. The experimental design consisted of a moored vertical array and a horizontal receiving array that were separately deployed to allow bistatic measurements of echo returns. Broadband Tukey-windowed LFM pulses 1s in duration and 50 Hz bandwidth were transmitted at frequencies centered at 415, 735, 950 and 1125 Hz. The study area represents a complex continental shelf environment with highly variable bathymetry and oceanography. Concurrent measurements of water column temperature and salinity yielded a total of 186 water column sound speed profiles (SSPs) from the Georges Bank region[89] and the SSPs are used to generate fluctuating ocean realizations for monte-carlo modeling of scattered returns from the air-filled cylindrical targets.

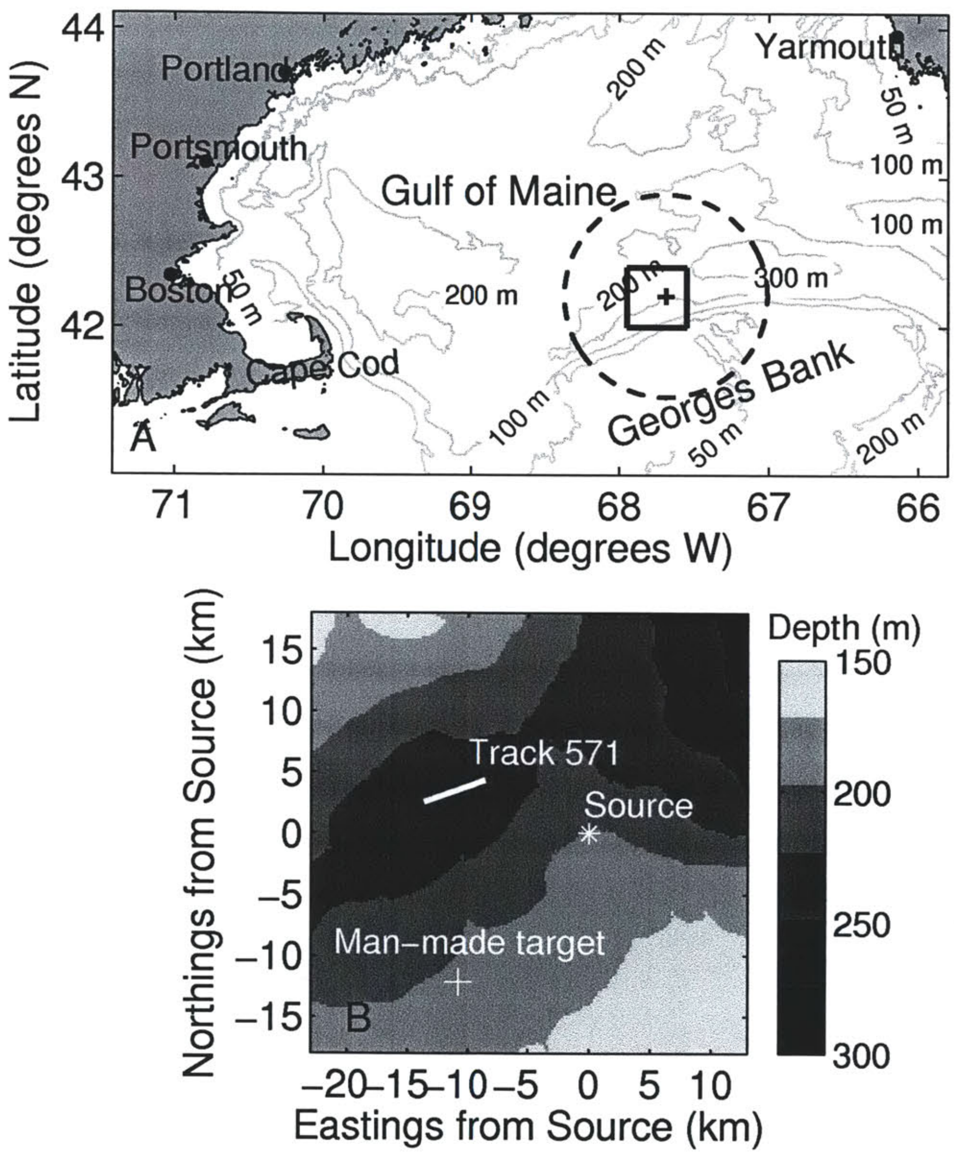

Figure 6-2: (**A**): Location of the GOM2006 experiment in the Gulf of Maine. Bathymetric contours are marked with grey lines. Black dashed circle shows 100-km areal imaging coverage in 75 seconds. (**B**): Geometry of the experiment showing the location of the moored source, the target, and the receiver track from which measured target-scattered received levels are used for comparisons with models. The zoom area is shown as a black box in the left figure. The grayscale shows the highly variable bathymetry in the region.

6.3 Distinguishing fish from man-made targets using multi-frequency measurements

Air-filled cylindrical targets were deployed in all three experiments, the NJ2001, NJ2003 and GOM2006, in order to (1) aid accurate charting of scattered returns onto a geographic grid [212, 120, 89] and (2) calibrate the data. Across these three experiments, a wide variety of scenarios with different source-target-receiver configurations in highly fluctuating ocean waveguides with varied bathymetry were explored.

In both the NJ2001 and NJ2003 experiments, the centers of the source and the receiver were located at depths of about 32 m and 30 m, respectively, in a water-column depth of roughly 70 m. Five targets, centered at water depths of about 44 m, were deployed during each of these two experiments, in water-column depths of roughly 80 m. In this paper, one target from each experiment (the southernmost target in Fig. 6-1B and C) is selected for data-model comparisons, based on (1) the target's clear visibility in the sonar image (i.e received acoustic intensity more than an order of magnitude above background reverberation levels, or SNR $\geq$ 10 dB) and (2) spatial isolation from other clutter features to ensure that the target-scattered returns are not contaminated with other clutter returns. These targets were typically 10 kilometers away from both the source and the receiver, as seen in Figs. 6-1B,C. Figure 6-3 shows the clear appearance of the targets in sonar imagery during both NJ2001 and NJ2003 experiments, respectively.

During the GOM2006 experiment, the source and receiver were located at depths of about 60 m and 105 m, respectively, in water-column depths ranging from 180-250 m. On Sep. 2, 2006, two air-filled cylindrical targets were deployed at selected locations shown in Fig. 6-2. The targets were centered at depths of 140 m and 180 m in a water-column depth of 200 m, and their distances from the source array were approximately 16 km and 15 km respectively. During the experiment, the 180-m deep target was often not clearly visible in OAWRS images, possibly because of target deflation due to the large hydrostatic pressure at such depths. In this paper, we consider the measurements of scattered intensity across different frequencies from

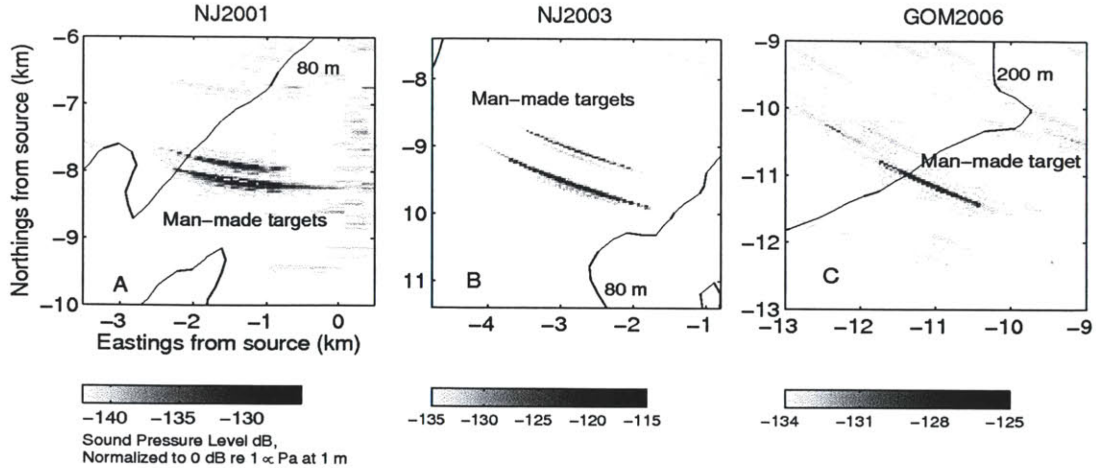

Figure 6-3: Discrete, consistent and strong acoustic returns from man-made targets were recorded during (A) NJ2001, (B) NJ2003 and (C) GOM2006. Examples of Ocean Acoustic Waveguide Remote Sensing (OAWRS) sound pressure-level (SPL) image, zoomed around the region of targets, normalized to 0 dB source-level, obtained on **(A)** May 1, 2001 at 10:58:15 GMT [212], **(B)** May 9, 2003 at 23:52:25 GMT and **(C)** October 2, 2006 at 23:10:00 GMT. A Linear Frequency modulated (LFM) 1-s long pulse with center frequency 415 Hz and bandwidth of 50 Hz was used to form the images. Black lines mark the 80-m isobath in (A) and (B) and the 200-m isobath in (C). The returns from man-made targets are at least an order of magnitude larger than returns from the background. The targets appear elongated in OAWRS imagery due to the different range- and azimuthal-resultions of the OAWRS receiving array. The range-resolution for the 50-Hz bandwidth source waveform used in all three experiments is ≈ 15 m [158]. The azimuthal resolution is range-dependent and is given by $R\alpha$, where R is the distance to the center of the receiving array and α is the angular resolution of the array at broadside given by $\alpha = \frac{\lambda}{L}$, where λ is the acoustic wavelength and L is the aperture length. At the target location, the azimuthal resolution for the OAWRS receiving array is ≈ 500 m.

the 140-m deep target, when SNR ≥ 10 dB.

In all three experiments, the targets appeared as either sharp, well-localized returns (Figs. 6-4D,E,F) or as weak, dispersed returns (Figs. 6-4G,H,I). Such changes in target-scattered field and arrival structure of target-scattered returns are caused by fluctuations in oceanography, as we show in Sec. 6.5 and in Appendix P. The targets are well-localized when most of the scattered acoustic energy is concentrated in the first few waveguide modes which combine constructively to form a sharp return with high SNR (Appendix P), such as the ones shown in Fig. 6-3. When the scattered acoustic energy is distributed across more waveguide modes, the later arrival of the higher order modes results in poorly localized, weak returns from the target (Appendix P).

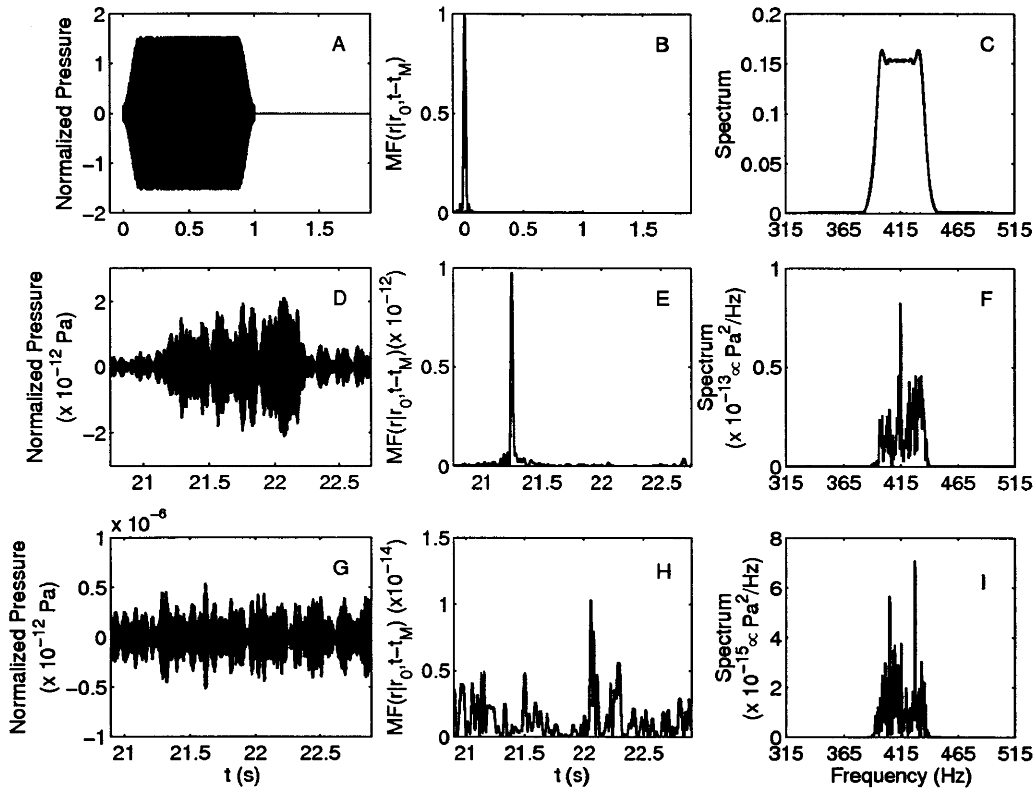

Figure 6-4: Examples of typical matched-filter output of man-made target-scattered data recorded during NJ2003. These examples are also representative of target-scattered returns observed during NJ2001 and GOM2006 experiments. Man-made targets usually show up as sharp well-localized returns after matched-filtering, but sometimes as weak, poorly localized returns due to waveguide dispersion. **(A,B,C)**: Transmitted Linear Frequency Modulated (LFM) signal envelope; Normalized matched-filter (MF) output of the LFM waveform; and signal spectrum. **(D,E,F)**: Example of envelope of received target-scattered signal before matched-filtering recorded on May 9, 2003 at 18:28:15 GMT; the MF output (computed using Equation 6.9) showing sharp, well localized target-return plotted as a function of two-way travel time; and frequency spectrum of the received signal in (D). **(G,H,I)**: Example of envelope of received target-scattered signal before matched-filtering recorded on May 9, 2003 at 18:31:35 GMT (3 minutes later than D), the MF output (computed using Equation 6.9) showing weak, dispersed, less well-localized target-return plotted as a function of two-way travel time, and frequency spectrum of the received signal in (G). Dispersed target returns were observed in roughly 25% of all target returns in NJ2003.

In wide-area OAWRS images, man-made targets often appeared similar to small fish schools. This is illustrated in Fig. 6-3(B), which shows a wide-area source-level-normalized sound pressure level (SPL) image for a 415 Hz source waveform, captured during NJ2003 on May 9. On this day, the presence of fish schools was confirmed by simultaneous in-situ measurements using a conventional fish finding sonar (CFFS)[158]. While returns from both man-made targets and fish schools appear similar at any one particular frequency, the availability of multi-spectral data enables the comparison of acoustic returns across multiple frequencies for spectral trends that can be used to discriminate man-made targets and fish.

The spectral dependence of scattering from fish has been extensively discussed for both the NJ2003[120] and GOM 2006[89] experiments. Based on in-situ CFFS and trawl measurements, Atlantic herring was found to be the major constituent of the fish schools imaged during both the experiments. The target strength of herring in both these experiments has been shown to increase as a function of OAWRS operating frequency[120, 89]. Since individual Atlantic herring are found to be acoustically compact (i.e swimbladder length $\ll$ acoustic wavelength) and to scatter incoherently from other shoaling herring in OAWRS imagery[120, 89], a Sonar Equation model was found to accurately describe scattering from herring schools, and was used to estimate their frequency-dependent target strength ($\widehat{TS}_{\text{fish}}$). The $\widehat{TS}_{\text{fish}}$ for both the NJ2003 and GOM2006 are shown in Figs. 6-5A and B, respectively.

The Sonar Equation, however, cannot be used to quantify scattering from non-compact targets in a waveguide, such as the air-filled cylindrical targets described in this paper[211]. To compare the frequency response of man-made targets with that of fish, we can still write an expression for a sonar-equation-derived target strength of the man-made target ($\widehat{TS}_{\text{tgt}}$). Such an estimated $\widehat{TS}_{\text{tgt}}$ is the target strength of an equivalent compact scatterer placed at the center of the man-made target, which gives rise to the same received scattered level as that of the man-made target.

The sonar-equation-derived $\widehat{TS}_{\text{tgt}}$ can be estimated from the data by

$$\widehat{TS}_{\text{tgt}} = \text{RL} - \text{SL} + 2\text{TL} \tag{6.1}$$

where RL is the measured (received) sound pressure level, SL is the known source level and 2TL is the two-way transmission loss averaged over the depth of the target. Transmission loss is computed using the parabolic equation based Range-dependent Acoustic Model (RAM)[45]. The mean and standard deviation of $\widehat{TS}_{\text{tgt}}$, shown in Fig. 6-5, are computed using several independent TS estimates across different frequencies. For comparison, the mean and standard deviation of the TS of fish ($\widehat{TS}_{\text{fish}}$) are also shown in the same figure.

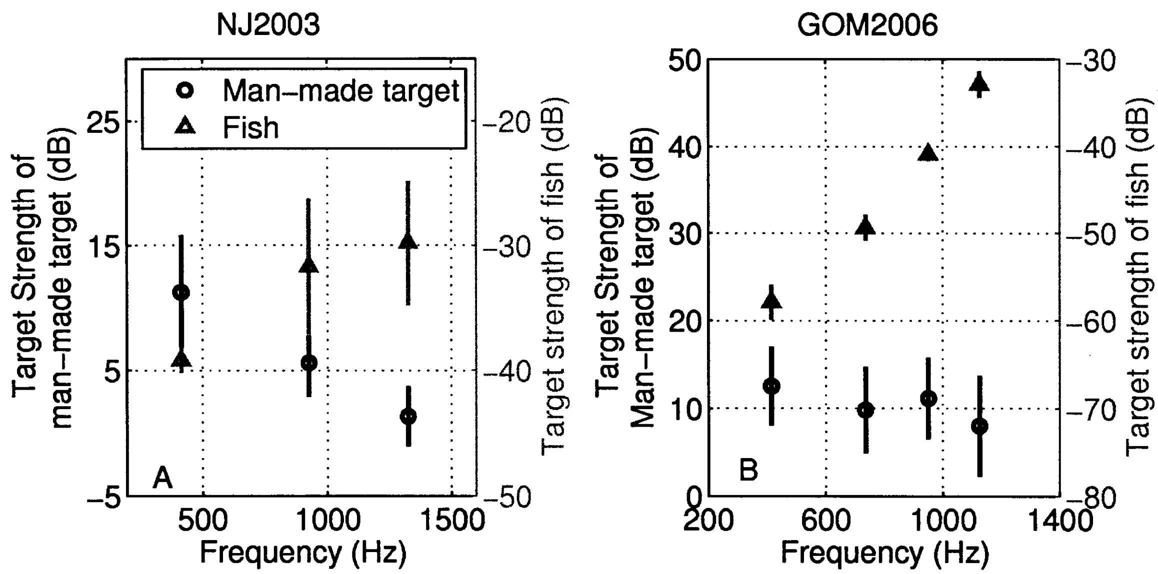

Figure 6-5: Sonar Equation-derived targets strengths of man-made targets vs fish ($\widehat{TS}_{\text{tgt}}$ vs $\widehat{TS}_{\text{fish}}$, Equation 6.1). The mean target strength of man-made targets (black dashed circles) and fish (gray triangles) show different trends as a function of frequency, and this difference in trend can be used to distinguish man-made targets from fish schools. **(A)** $\widehat{TS}_{\text{tgt}}$ vs $\widehat{TS}_{\text{fish}}$ measured on May 9, 2003, during NJ2003. Vertical bars are the standard deviations of the target strength estimates. A total of 85 transmissions from Track 201 were used for estimating $\widehat{TS}_{\text{tgt}}$ at 415 Hz. A total of 90 transmissions from track 202 were used for estimating $\widehat{TS}_{\text{tgt}}$ at 925 and 1325 Hz. To estimate $\widehat{TS}_{\text{fish}}$, data from both May 9 and May 14 were used as described in Ref. [120]. **(B)** $\widehat{TS}_{\text{tgt}}$ vs $\widehat{TS}_{\text{fish}}$ measured on Oct 2, 2006, during GOM2006. Vertical bars are standard deviations of the target strength estimates. A total of 20 transmissions from Track 571 were used for estimating $\widehat{TS}_{\text{tgt}}$ at each frequency shown. To estimate $\widehat{TS}_{\text{fish}}$, data from Oct 2 was used as described in Ref. [89].

The TS for fish increases as a function of frequency, as can be seen in Fig. 6-5. This is because the incident acoustic frequencies span the lower half of the resonance peak, where there is a sharp increase of TS for the fish imaged in both the New Jersey continental shelf during NJ2003 and the Gulf of Maine during GOM2006.[120, 89] In contrast, the TS of cylindrical targets are observed to follow the opposite trend as a function of frequency. This is because the expected resonance frequency for the extended targets is much lower (about 40-50 Hz) [153] than those for the fish. This difference in frequency response can be used to discern fish from man-made targets.

6.4 Theoretical Formulation

6.4.1 Problem Geometry

A target-centered cylindrical coordinate system is used (Fig. 6-6), where $\mathbf{r_t} = (a, \phi_t, z_t)$ is any point on the target's cylindrical surface with $0 \leq \phi_t \leq 2\pi$ and $-L/2 \leq z_t \leq L/2$. The total target length is L and the cylinder radius is a. The source is located at $\mathbf{r_0} = (\rho_0, \phi_0, z_0)$ and the receiver at $\mathbf{r} = (\rho, \phi, z)$. The bathymetry and oceanography are modeled as range-dependent.

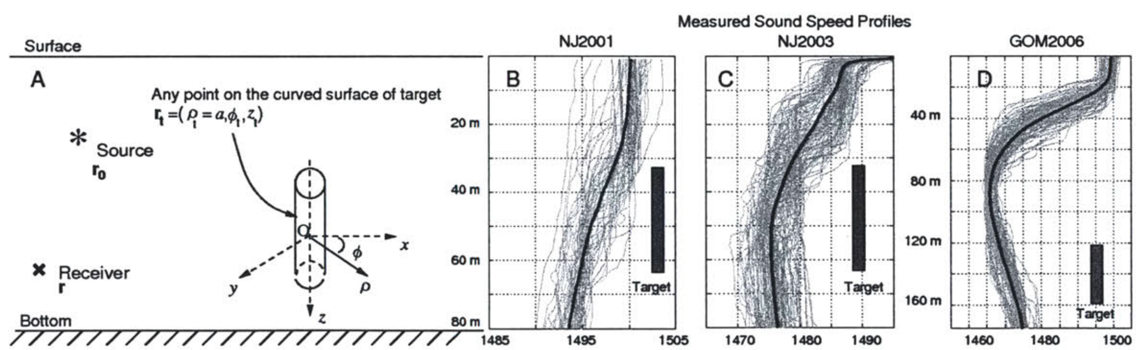

Figure 6-6: Geometry (not to scale) showing target-centered cylindrical coordinate system used in the Vertically Extended cylindrical Target Waveguide Scattering (VETWS) model. The cylinder has length L and radius a. The non-iso sound speed structure over the depth of the man-made extended target, measured during OAWRS 2001, OAWRS 2003 and OAWRS 2006 (gray lines) and their means (black lines) are shown to the right. The refraction of incident sound over the depth of the man-made target due to the depth-dependent sound speed structure is not taken into account by the Sonar equation or the Ingenito scattering models and leads to large errors when used to estimate target-scattered levels. The full-field Green's theorem-based VETWS model accounts for sound speed variations and accurately estimates mean target-scattered levels.

6.4.2 Theory

A Greens' Theorem approach[134] is used to calculate the scattered returns from vertically extended cylindrical targets in range-dependent ocean waveguides. The scattered pressure per Hertz at a particular frequency f at the receiver location is expressed as

$$P_{\text{scat}}(\mathbf{r}|\mathbf{r_0}, f) = -\oint_{S_t} \left[P(\mathbf{r_t}|\mathbf{r_0}, f)\nabla_t G(\mathbf{r}|\mathbf{r_t}, f) - \nabla_t P(\mathbf{r_t}|\mathbf{r_0}, f) G(\mathbf{r}|\mathbf{r_t}, f)\right] \cdot \mathbf{n_t}\, dS_t \quad (6.2)$$

where $P(\mathbf{r_t}|\mathbf{r_0}, f)$ is the total acoustic pressure per Hertz on target's surface, which is expressed as the sum of incident and scattered waves, $G(\mathbf{r}|\mathbf{r_t}, f)$ is the waveguide's Green function from any point on the target to the receiver, S_t is surface of the target and $\mathbf{n_t}$ is the normal to the target surface.

A pressure-release condition is assumed at the surface of the cylindrical target. The scattered field on the surface of the target can be expressed as a sum of weighted Hankel functions, as described in Ref. [134]. Hence, the scattered field at the receiver can be expressed as

$$\begin{aligned} P_{\text{scat}}(\mathbf{r}|\mathbf{r_0}, f) = &-\int_{z_t=-L/2}^{z_t=+L/2} \int_{\phi_t=0}^{2\pi} G(\mathbf{r}|\mathbf{r_t}, f) \frac{\partial P_{\text{inc}}(\mathbf{r_t}|\mathbf{r_0}, f)}{\partial \rho_t} a\, \mathrm{d}z_t\, \mathrm{d}\phi_t \\ &-\int_{z_t=-L/2}^{z_t=+L/2} \int_{\phi_t=0}^{2\pi} G(\mathbf{r}|\mathbf{r_t}, f) \sum_{n=0}^{\infty} A_n(z_t|\mathbf{r_0}, f) \cos(n\phi_t) \left[-k\mathrm{H}_{n+1}^{(1)}(ka) + \frac{n}{a}\mathrm{H}_n^{(1)}(ka)\right] a\, \mathrm{d}z_t\, \mathrm{d}\phi_t, \end{aligned} \quad (6.3)$$

where $P_{\text{inc}}(\mathbf{r_t}|\mathbf{r_0}, f)$ is the incident pressure on the target, $A_n(z_t|\mathbf{r_0}, f)$ are depth-dependent coefficients, $\mathrm{H}_n^{(1)}$ is the Hankel function of the first kind and n^{th} order, and $k = 2\pi f/c$ is the wavenumber.

The first integral in Equation 6.3 is evaluated numerically using an acoustic propagation model, such as RAM[45]. In order to solve the second integral, the coefficients A_n must be determined. While Ref. [134] provides an approximate numerical recipe to determine these coefficients, here analytical expressions are derived in Appendix O, which are then used in the scattering model.

6.5 Statistics of Measured and Simulated Scattered fields from Targets

6.5.1 Measured Returns from Passive Acoustic Targets

For each source transmission from location $\mathbf{r_0}$, the received acoustic pressure, p at time t and at hydrophone location $\mathbf{r}_h$ is first beamformed in azimuth. The beamformed result is given by

$$\Psi(\mathbf{r}|\mathbf{r_0}, t) = \frac{1}{N_h}\sum_{l=1}^{N_h} p(\mathbf{r}_{h,l}|\mathbf{r_0}, t + (l-1)\Delta) \tag{6.4}$$

where $\mathbf{r}$ is the center of the receiver array, $\mathbf{r}_{h,l}$ is the l^{th} hydrophone, N_h is the number of hydrophone elements in the receiver array and Δ is the time delay corresponding to the angle made by the man-made target to the receiver. The beamformed output, $\Psi(\mathbf{r}|\mathbf{r_0}, t)$, is Fourier transformed to obtain its complex spectral amplitude $\Phi(\mathbf{r}|\mathbf{r_0}, f)$ for frequency f, following the transform equation

$$\Phi(\mathbf{r}|\mathbf{r_0}, f) = \int_T \Psi(\mathbf{r}|\mathbf{r_0}, t)\ \mathrm{e}^{i2\pi ft}\mathrm{d}t, \tag{6.5}$$

where T is a time window containing the signal. The matched-filter [256, 137, 14] is then applied, which is given by

$$H(f|t_M) = KQ^*(f)\ \mathrm{e}^{i2\pi f t_M} \tag{6.6}$$

where t_M is the time delay of the matched-filter and K is the total energy in the input signal, given by

$$K = \left(\int |Q(f)|^2\ \mathrm{d}f\right)^{-1/2} \tag{6.7}$$

and $Q(f)$ is the source spectrum. The time-delay corresponds to two-way travel time from the source to the man-made target and back to the receiver. The time-dependent matched-filtered scattered return is then computed by Fourier synthesis as

$$\chi(\mathbf{r}|\mathbf{r_0}, t - t_M) = \int \Phi(\mathbf{r}|\mathbf{r_0}, f) H(f|t_M) \, \mathrm{d}f. \tag{6.8}$$

The maximum matched-filter output is then

$$\mathrm{MF}(\mathbf{r}|\mathbf{r_0}, t_M) = \max{}_t \left| \int_{f_i}^{f_f} \Phi(\mathbf{r}|\mathbf{r_0}, f) K Q^*(f) \, \mathrm{e}^{-i2\pi f(t-t_M)} \, \mathrm{d}f \right|^2. \tag{6.9}$$

For illustration the source signal characteristics for the NJ2003 experiment at a center frequency of 415 Hz are shown in Figs. 6-4A-C. Similar plots for the normalized transmitted signal amplitude (Fig. 6-4A), the corresponding matched filtered signal (Fig. 6-4B), and the signal spectrum (Fig. 6-4C) can also be obtained for the different transmitting frequencies used in all three experiments. The strong peak observed in the MF output corresponds to the direct arrival, which is accounted for by taking the maximum value of Eq. 6.9.

Figure 6-4E shows the MF output of the received signal for a target-receiver separation of 12.45 km, after waveguide propagation and scattering from targets, measured during NJ2003. The matched filter picks the true location of the target, shown as a sharp peak in Fig. 6-4E. However, the MF output of the scattered signal from the target is not always sharp, but were dispersed roughly 25% of the time in NJ2003 experiment for example, as illustrated in Fig. 6-4H in which a clear peak is not observed. This is due to waveguide dispersion, which causes higher order modes to arrive later at the receiver[14]. This effect is quantified by simulating the MF output for different oceanographic conditions in Appendix P.

After beamforming and matched filtering, the received pressure data is charted onto geographic space using the known source and receiver locations [155, 154, 212] to generate wide-area sonar images. Examples of images showing targets in NJ2001 and NJ2003 are shown in Figures 6-3(A) and 6-3(B), where the axes show the distance from the moored source, and the colorscale corresponds to the received normalized scattered pressure levels. In Figures 6-3(A) and 6-3(B), which correspond to a single transmission for the frequency band centered at 415 Hz, the targets are observed to stand 10 to 25 dB above the background reverberation.

The target-scattered levels are measured for two tracks on May 1, 2001, during the NJ2001 (Tracks 14 and 17), two tracks on May 9, 2003, during NJ2003 (Tracks 201 and 202) and one track on Oct 2, 2006, during GOM2006 experiment. These tracks, from each of the three experiments, are the ones in which the targets were most clearly observed in wide-area sonar images. It is also observed that the scattered returns fluctuate considerably from one transmission to the next, within each track. The mean target-scattered return for a particular track is computed as

$$\tilde{\mathcal{L}}_{\mathrm{meas}} = 10\log_{10}\left(\frac{\sum_{j=1}^{N} \mathrm{MF}(\mathbf{r_j}|\mathbf{r_0}, t_M)}{N}\right), \tag{6.10}$$

where N is the number of transmissions in the track. The log of measured target-scattered returns normalized by $\tilde{\mathcal{L}}_{\mathrm{meas}}$ (i.e $10\log_{10}(\mathrm{MF}(\mathbf{r_j}|\mathbf{r_0}, t_M)) - \tilde{\mathcal{L}}_{\mathrm{meas}}$) for all the three experiments are shown as black triangles in Figures 6-7,6-8 and 6-9, respectively. The fluctuation in measured target-scattered return is expected because the experiments were conducted in highly fluctuating waveguides where the acoustic field fluctuates according to Complex Circular Gaussian Random (CCGR) statistics [90, 23, 63, 152] due to the multi-modal or multipath nature of the combined propagation and scattering process. The instantaneous intensity I of a CCGR field follows the exponential distribution, while averaged intensity [90] and the log of averaged intensity [152] follow the gamma and exponential-gamma distributions, respectively, with first and second moments that can be analytically expressed in terms of sample size μ and expected intensity $\langle I \rangle$ [152]. The standard deviation of the log of averaged intensity from a CCGR field is given by [152]

$$\sigma = (10\log_{10}\mathrm{e})\sqrt{\zeta(2,\mu)} \tag{6.11}$$

where ζ is the Reimann zeta function. For $\mu = 1$ sample, the standard deviation is 5.6 dB. The number of degrees of freedom μ is expected to increase with the bandwidth of the transmitted signal and this decreases the standard deviation to approximately 3-4 dB[13], which is consistent with the experimentally measured standard deviation during the three experiments (Figs. 6-7-6-9). In order to account for the scintillation in measured scattered intensity, the VETWS model is extended to incorporate the waveguide randomness in the next sections and results of numerical simulations are compared to the experimental data.

6.5.2 Simulation of target scattered returns using VETWS

In this section the VETWS model is extended to calculate *broadband* scattered returns from targets in *fluctuating* continental shelf environments. Calculations are made for the different source signals centered at frequencies of 415 Hz, 735 Hz, 950 Hz, and 1125 Hz, which were used in the NJ2001, NJ2003 and GOM2006 experiments.

To compute the received scattered field from Eq. 6.3, the acoustic field incident on the target, $P_{\text{inc}}(\mathbf{r_t}|\mathbf{r_0}, f)$ and the waveguide Green function from the target to the receiver $G(\mathbf{r}|\mathbf{r_t}, f)$ are calculated using RAM[45]. Note that the coefficients $A_n(z_t|\mathbf{r_0}, f)$ can also be computed using $P_{\text{inc}}(\mathbf{r_t}|\mathbf{r_0}, f)$, as shown in Appendix O. The target-scattered field at the receiver (Eq. 6.3) depends on the cylindrical modes of oscillation of the target via A_n, H_n and H_{n+1}, where n denotes a particular harmonic. For the simulations, it is observed that the solution converges after summing only the first two harmonics ($n = 0, 1$). This is because the targets deployed in all three experiments have a radius that is much smaller than the acoustic wavelength for all the different frequencies used.

Source, receiver, and target center depths used in the model calculations for the different tracks in the three experiments are listed in Table 6.1. For both the New Jersey continental shelf and the Gulf of Maine, a sandy bottom with sound speed of 1700 m/s, density of 1.9 g/cm^3, and attenuation of 0.8 dB/λ [89, 80, 88], is used along with bathymetry and sound speed profiles measured during the experiments. For each receiver position $\mathbf{r_j}$ along a given track, M =20 Monte Carlo simulations of the target-scattered field are computed. In each simulation, the sound speed profile (SSP) is updated every 500 m[40] in range by randomly selecting an SSP from the measured list of profiles, and the acoustic forward propagation[14] is computed. The simulated matched-filtered output for each realization, n, and for each receiver location $\mathbf{r_j}$ is

$$\mathrm{SMF}^{(n)}(\mathbf{r_j}|\mathbf{r_0}, t_M) = \max{}_t \left| \int P^{(n)}_{\mathrm{scat}}(\mathbf{r_j}|\mathbf{r_0}, f) K Q^*(f)\ \mathrm{e}^{-i2\pi f(t-t_M)}\ \mathrm{d}f \right|^2. \qquad (6.12)$$

The average simulated matched-filter output for every receiver location $\mathbf{r_j}$ along a track is then computed as

$$\overline{\mathrm{SMF}(\mathbf{r_j})} = \frac{\sum_{n=1}^{M} \mathrm{SMF}^{(n)}(\mathbf{r_j}|\mathbf{r_0}, t = t_M)}{M}. \qquad (6.13)$$

The log of the mean simulated target-scattered return over an entire track is then computed by

$$\tilde{\mathcal{L}}_{\mathrm{VETWS}} = 10 \log_{10} \left(\frac{\sum_{j=1}^{N} \overline{\mathrm{SMF}(\mathbf{r_j})}}{N} \right) \qquad (6.14)$$

and the standard deviation is given by,

$$\sigma(\overline{\mathrm{SMF}(\mathbf{r_j})}) = \sqrt{\frac{1}{N} \sum_{j=1}^{N} \left(10 \log_{10} \overline{\mathrm{SMF}(\mathbf{r_j})} - \tilde{\mathcal{L}}_{\mathrm{VETWS}} \right)^2} \qquad (6.15)$$

where N is the number of transmissions per track. All average quantities are computed in the anitlog domain since a log-transformation introduces an inherent bias to each sample[152], which canot be removed by averaging the log-tranformed samples of the random variable. As in the case of the measured target-scattered returns, the randomization of the ocean waveguide and the use of broadband signals is expected to lead to an expected standard deviation of 3-4 dB for $\mathrm{SMF}^{(n)}(\mathbf{r_j}|\mathbf{r_0}, t_M)$ [14]. Averaging over 20 Monte-Carlo simulations is then expected to further reduce the standard deviation of $\overline{\mathrm{SMF}(\mathbf{r_j})}$ by $1/\sqrt{20}$, to ≈ 1 dB. This is consistent with numerical simulations of the VETWS-based target scattered returns in all three experiments (Figs. 6-7-6-9).

For all simulations of the target-scattered field, it was assumed that the air-filled cylindrical targets used during each field experiment remained vertical in the water column. However, this may not be the case as underwater currents may cause a target

Table 6.1: Parameters used for modeling target scattering

	ARE 2001	MAE 2003	GoM 2006
Source depth (m)	40	40	60
Receiver depth (m)	35	40	105
Target center depth (m)	44	44	140

to tilt. In Appendix R, it is shown that the effect of target tilt on the received target-scattered levels is not significant, since only weak underwater currents prevail in the shallow continental shelf environments where the three experiments were conducted.

6.5.3 Simulation of target scattered returns using the Sonar Equation and Ingenito scattering models

In order to implement the sonar equation and the Ingenito scattering models, the following scatter function for a pressure-release cylinder is used[260]:

$$S(\alpha,\beta;\alpha_i,\beta_i) = -\frac{kL}{\pi}\mathrm{sinc}\left[\frac{kL}{2}\left(\cos\alpha_i - \cos\alpha\right)\right]\sum_{m=0}^{\infty} B_m(-j)^m \cos\left(m\left[\beta-\beta_i\right]\right). \quad (6.16)$$

The sinc function in the above formula shows that the cylinder scatters like an array in the vertical, while in azimuth it scatters through cylindrical harmonics with amplitudes given by

$$B_m = -\epsilon_m j^m \frac{J_m(ka)}{H_m(ka)}. \quad (6.17)$$

In Eqs. 6.16 and 6.17, α and β are the elevation and azimuth angles of the scattered plane waves, α_i and β_i are the elevation and azimuth angles of the incident plane wave, ϵ_m is the Neumann number defined as $\epsilon_0 = 1$, and $\epsilon_m = 2$ for $m \neq 0$, and J_m is the Bessel function of first kind and order m.

The target-scattered level, according to a depth-averaged sonar equation model is given by

$$RL_{sonar} = SL + 2\overline{TL} + TS_{tgt} \quad (6.18)$$

where SL is the source-level, $2\overline{TL}$ is the two-way transmission loss averaged over the target depth, and TS is the target strength of the man-made target in the back-scatter direction, given by

$$TS_{tgt} = 10 \log_{10} \left| \frac{S(0, \pi; 0, 0)}{k} \right|^2 . \tag{6.19}$$

The transmission loss and target strengths are computed for the center-frequencies of the different source waveforms used in the field experiments. As in the case of simulations using the VETWS model, for every receiver location, $\mathbf{r}$, M =20 Monte-carlo simulations of RL_{sonar} are computed with the sound speed profile being randomized every 500 m in every simulation. The sound speed profiles are randomly selected from the list of measured profiles during each experiment. The target-scattered returns computed using the sonar equation model without any depth averaging of the TL are expected to have a standard deviation of $\sim 5.6\sqrt{2}$ dB, since each single-frequency one-way transmission is expected to have a standard deviation of 5.6 dB[63, 152] and forward and back propagation paths factor to a product of two CCGR variables. The averaging of the TL over the target depth and the averaging over 20 Monte-Carlo realizations are expected to reduce the standard deviation of RL_{sonar} from its theoretical expected value of $5.6\sqrt{2}$ dB, as is indeed found in simulations in Figs. 6-7-6-9.

To calculate the target-scattered levels using the Ingenito scattering model [113], the mode-shapes of the acoustic field are computed using KRAKEN normal-mode model [205] and the angle-dependent scatter-function in Eqn. 6.16 is used. For every receiver location $\mathbf{r}$, 20 monte-carlo simulations of the scattered intensity are performed. For each simulation, one range-independent sound speed profile from the measured profiles during each experiment is picked. The average bathymetry along the source-target-receiver propagation paths is used. The single-frequency scattered field computed using the Ingenito model is expected to follow CCGR statistics since it involves multipath acoustic propagation where scattering and propagation are combined in a double sum over the acoustic modes. Consequently, a 5.6 dB standard deviation is expected for the scattered returns for a single frequency signal. However, the use of multi-frequency signals along with Monte-Carlo averaging is expected to lead to smaller standard deviations of 3-4 dB [14, 152], as is seen from Figures 6-7-6-9.

6.5.4 Numerical Modeling and Experimental Data Comparisons

In this section results from numerical simulations using the VETWS model, the sonar equation model, and the Ingenito scattering model are compared with measured scattered returns from the air-filled cylindrical targets deployed during NJ2001, NJ2003 and the GOM2006 experiments.

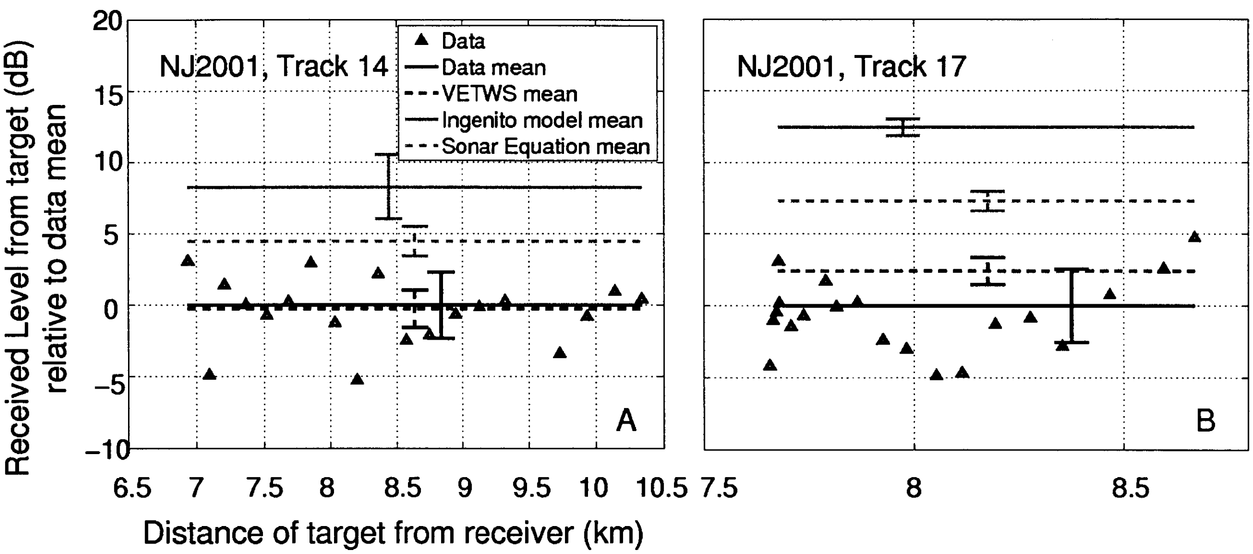

Figure 6-7: Comparison of man-made target-scattered levels modeled using the VETWS, Ingenito, and Sonar Equation models, relative to the mean scattered level measured during **(A)** Track 14 of NJ2001 and **(B)** Track 17 of NJ2001. The VETWS model-based mean target-scattered levels match the data to within 0.3 dB in Track 14 and to within 2 dB in Track 17, while both the Ingenito and Sonar Equation model means show large errors ($\geq$4.5 dB). The center frequency of the source is 415 Hz. Black triangles show the measured target-scattered levels for 19 transmissions made during Track 14 and 20 transmissions made during Track 17, relative to the mean measured level. The standard deviations (SD) of the data for both tracks are 2.5 dB, and are marked with solid black vertical lines. The SD of the simulated scattered levels using different models are computed based on Equations 6.14 and 6.15, and are (1) VETWS: 1.3 dB (Track 14) and 0.93 dB (Track 17); (2) Ingenito model: 2.26 dB (Track 14) and 0.6 dB (Track 17), and (3) Sonar Equation model: 1 dB (Track 14) and 0.7 dB (Track 17).

Figure 6-7 and shows the log of the measured target scattered returns normalized by $\tilde{\mathcal{L}}_{\text{meas}}$, for two distinct tracks (Tracks 14 and 17) on May 1, 2001, during the NJ2001 experiment. The log of the mean target-scattered returns computed using the three scattering models, normalized by $\tilde{\mathcal{L}}_{\text{meas}}$, are also shown in Figure 6-7. The VETWS-mean matches the data-mean to within 0.5 dB for Track 14 and to within 2 dB for Track 17. For both these tracks, the sonar equation model and the Ingenito scattering model overestimate the data-mean by approximately 5 dB and 10 dB, respectively, for both tracks.

A similar comparison is made in Figure 6-8 for two tracks on May 9, 2003, during the NJ2003 experiment, corresponding to two source waveforms centered at 415 Hz and 950 Hz. The results are similar to the comparison in Figure 6-7. The VETWS-mean matches the data-mean to within 0.1 dB for the 415 Hz centered source signal and to within 2 dB for the 950-Hz centered source signal. Again, both the sonar equation model and the Ingenito scattering model overestimate mean scattered levels by more than 5 dB.

During the GOM2006 experiment, four 50-Hz bandwidth LFM waveforms with center frequencies 415 Hz, 735 Hz, 950 Hz and 1125 Hz were transmitted during each track. The long inter-transmission time (75 s) and inter-leaving of frequencies leads to fewer data points available per waveform per track than in the NJ2001 and NJ2003 experiments. Figure 6-9 shows the log of the measured target scattered returns, with $\tilde{\mathcal{L}}_{\text{meas}}$ subtracted, for Track 571 on Oct 2, 2006, during the GOM2006 experiment, for all 4 waveforms transitted. The VETWS-mean matches the data-mean to within 0.5 dB for the 415-Hz and 735-Hz centered source signals and to within 3 dB for the 950-Hz and 1125-Hz centered source signals. The sonar equation model and the Ingenito scattering model overestimate the data by more than 4 dB.

6.6 Conclusion

Bistatic, long-range measurements of acoustic scattered returns from vertically extended, air-filled tubular targets were made during three distinct field experiments in fluctuating continental shelf environments. It is shown that Sonar Equation estimates of mean target-scattered intensity lead to large errors, differing by an order of magnitude from both the measurements and waveguide scattering theory. This is because

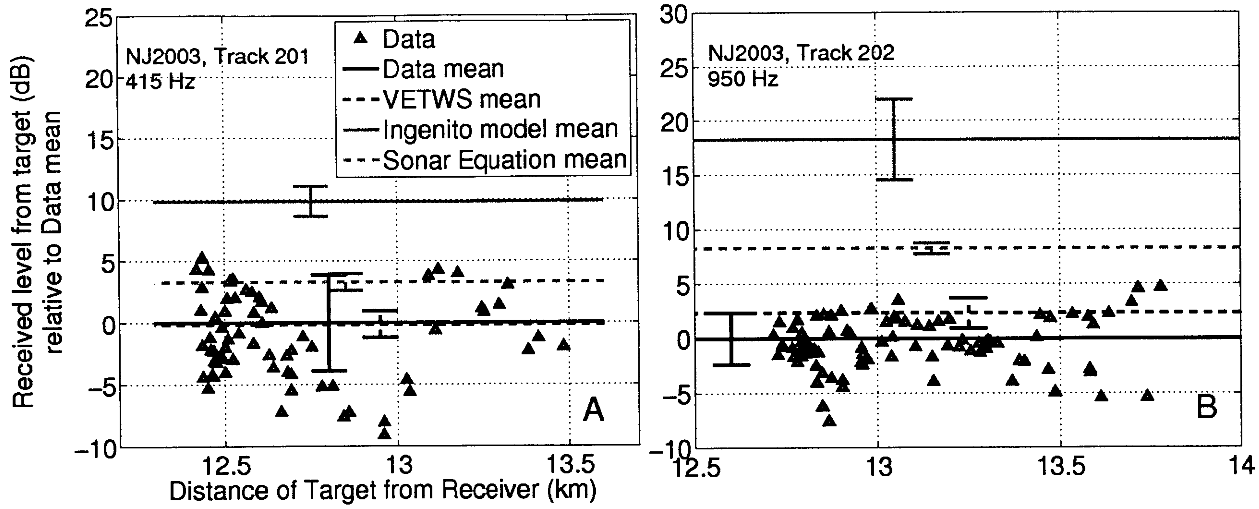

Figure 6-8: Comparison of man-made target-scattered levels modeled using the VETWS, Ingenito, and Sonar Equation models, relative to the mean scattered level measured during **(A)** Track 201 and **(B)** Track 202 of NJ2003. The center frequencies of the source are 415 Hz in Track 201 and 950 Hz in Track 202. The VETWS model-based mean target-scattered levels match the data to within 0.1 dB in Track 201 and 2 dB in Track 202, while both the Ingenito and Sonar Equation models show larger errors ($\geq$3.5 dB). Black triangles show the measured target-scattered levels for 89 transmissions made during Track 201 and 90 transmissions during Track 202, normalized to the mean measured scattered level. The standard deviations (SD) of the measurements and the simulated scattered levels using different models are marked with vertical lines and are (1) Data: 3.8 dB (Track 201) and 2.3 dB (Track 202), (2) VETWS: 1 dB (Track 201) and 1.3 dB (Track 202), (3) Ingenito model: 1.2 dB (Track 201) and 3.5 dB (Track 202), and (4) Sonar Equation model: 0.7 dB (Track 201) and 0.5 dB (Track 202).

the sonar equation approximation is not applicable to targets large compared to the acoustic wavelength in an ocean waveguide. The use of the Ingenito scattering model is also shown to lead to significant errors in estimating mean target-scattered intensity in the field experiments because they were conducted in range-dependent ocean environments with large variations in sound speed structure over the depth of the targets, scenarios that violate basic assumptions of the Ingenito model. A Greens' theorem based full-field model (VETWS) that describes scattering from vertically extended cylindrical targets in range-dependent ocean waveguides by taking into account nonuniform sound speed structure over the target's depth extent is shown to accurately describe the statistics of the targets' scattered field in all three field exper-

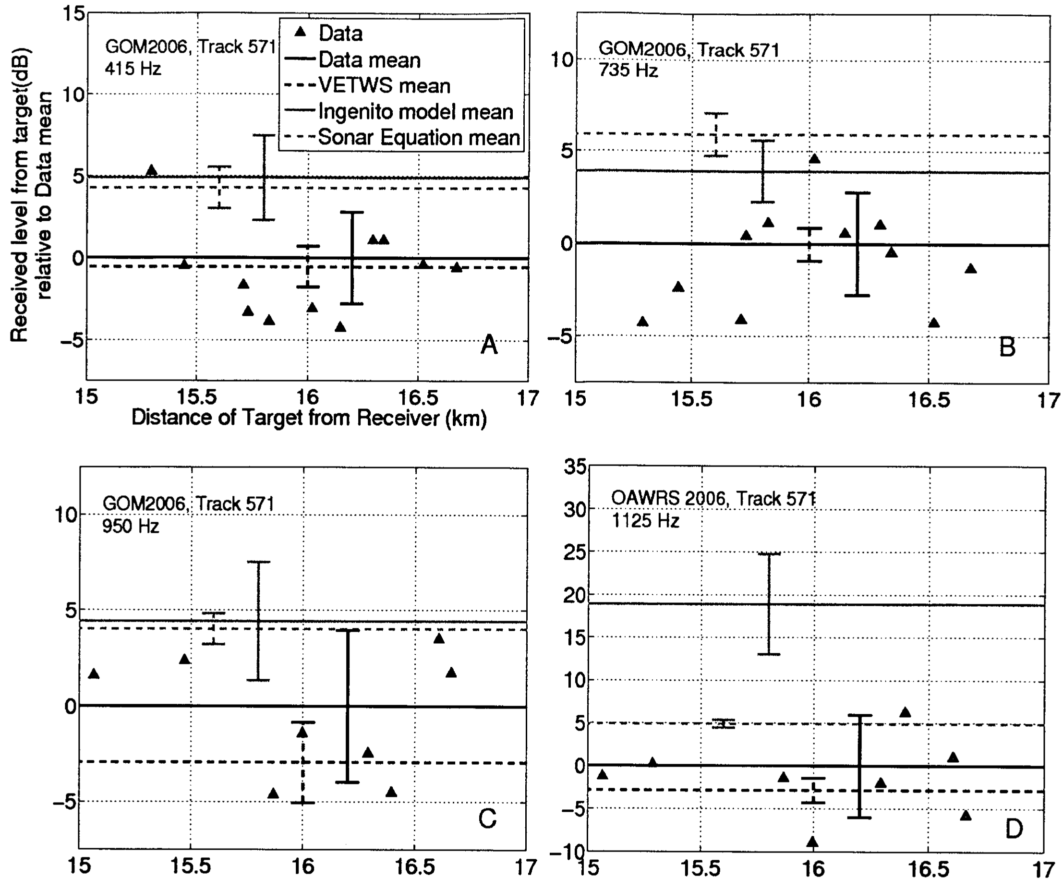

Figure 6-9: Comparison of man-made target-scattered levels modeled using the VETWS, Ingenito, and Sonar Equation models, relative to the mean scattered level measured during Track 571 of GOM2006 for different source center frequencies **(A)** 415 Hz, **(B)** 735 Hz, **(C)** 950 Hz and **(D)** 1125 Hz. The VETWS model-based mean target-scattered levels match the data to within 0.5 dB for (A) and (B) and to within 3 dB for (C) and (D), while both the Ingenito and Sonar Equation model means show errors $\geq$4 dB. Black triangles show the measured target-scattered levels for 10 transmissions when the targets were clearly visible (SNR>10 dB) during Track 571, normalized to the mean measured scattered level. Fewer transmissions were made per track per frequency during GOM2006 than in NJ2001 and NJ2003. The standard deviations (SD) of the measurements and the simulated scattered levels using different models are marked with vertical lines. For the different frequencies in (A-D), the SDs are respectively, (1) Data: 2.7 dB, 2.7 dB, 3.9 dB and 5.9 dB; (2) VETWS: 1.2 dB, 0.9 dB, 2 dB and 1.4 dB; (3) Ingenito model: 2.5 dB, 1.6 dB, 3 dB and 5.8 dB; and (4) Sonar Equation model: 1.2 dB, 1.1 dB, 0.8 dB and 0.4 dB.

iments. To account for the scintillation in the measured scattered intensity caused by fluctuations of the ocean waveguide, Monte-Carlo simulations of the scattered field are computed by implementing the full-field model in a range-dependent environment randomized by internal waves. Target-scattered returns are also shown to have a very different spectral dependence than that of returns from target-like clutter such as fish schools that plague long-range navy sonars operating in continental shelves, so that multi-frequency measurements may be used to distinguish fish from man-made targets.

Chapter 7

Remotely sensing tsunamis using infrasound in air and Rayleigh waves on the ground

Tsunamis are long-period (T $\sim$ 100 s), large-wavelength ($\geq$ 100 km) ocean surface gravity waves typically caused by submarine earthquakes or landslides that suddenly displace the ocean water-column [264]. Historically, large tsunamis have caused extensive loss of human lives and damage to property along the coastal regions of the world. For example, the Indian-Ocean Tsunami that occurred on December 26, 2004 caused over 350,000 fatalities [15] and an estimated economic loss of roughly 2 billion dollars [15] across India, Srilanka, Thailand and Indonesia.

Tsunamis are known to be silent-killers, since sufficient forewarning is usually unavailable before the wave closes in on the shore. The rise in sea level due to a tsunami in deep water, where these waves typically originate, is on the order of only few tens of centimeters [264], making them barely detectable by tidal guages. The U.S. has therefore deployed an extensive network of high-precision underwater pressure sensors in the Pacific Ocean that detect small changes in sea-surface elevation as part of the Pacific Tsunami Early Warning System [167]. Other oceans of the world are currently not monitored with similar underwater sensor networks due to the high development/maintenance costs [24], prompting the need to find alternate ways of remotely sensing tsunamis.

Recently, it has been suggested [199] that tsunamis could be a source of low-frequency sound that can be picked up thousands of kilometers away using shore-based pressure sensors long before the tsunami wave hits the shore. For example, during the Indian-Ocean tsunami event on December 26, 2004, an infrasound monitoring station at Diego Garcia, 2600 km away from the tsunami source, recorded high-intensity signals in the deep infrasound frequency regime (0.01 - 0.1 Hz) corresponding to propagation speeds of $\sim$ 300-400 m/s [199]. These signals were attributed to aero-acoustic waves from the tsunami, though the generation mechanism was unknown [199].

Here, we develop an analytical model for infrasound generation due to tsunamis, based on Greens theorem [171]. We propose an infrasound generation mechanism where the sea surface, under the action of the tsunami, acts as an acoustic source by generating mass flow into the atmosphere. Sound propagation from this source to a receiver, via an atmospheric waveguide, is modeled using normal-mode theory [124]. The analytical model is applied to quantify infrasound generated by the Indian-Ocean Tsunami. We show that the pressure level, frequency range and arrival time of the modeled infrasound signal match the corresponding signal characteristics measured by the infrasound monitoring station at Diego Garcia [199] during the tsunami event. The first tsunami-generated infrasound signals arrive at Diego Garcia roughly 2 hours after the earthquake, when the tsunami is still 1 hour 30 minutes away from the receiver on shore, making it feasible to use infrasound signals as precursors to tsunami arrival.

The possibility of remotely sensing tsunamis using seismic waves is examined by developing an analytical model for quantifying very low frequency (0.01-0.1 Hz) Rayleigh waves generated by a tsunami. Since tsunamis are very low frequency gravity waves in the ocean, their hydrodynamic pressure is not attenuated by depth of the ocean [180] and the seabottom is subject to low-frequency forcing as the tsunami wave passes over. The generation of Rayleigh waves due to such a low-frequency forcing of the seabottom is quantified by developing a full field model for compression and shear wave propagation in the seabed. The seismic model is then used to predict the vertical ground velocity at Diego Garcia Island caused by the 2004 Indian Ocean Tsunami. The amplitude of tsunami-induced vertical ground velocity is found to be highly sensitive to the compression and shear wave speeds in the sea-bottom. For reasonable values of these speeds, it is shown that the tsunami-induced vertical ground velocity amplitudes match measurements made in Diego Garcia. The Rayleigh waves are received at Diego Garcia several hours before the tsunami hits the shore, making tsunami-induced seismic waves a possible modality for remotely sensing tsunamis.

In the next section, we present the theoretical formulation of the air-borne infrasound generation model, followed by its application to the Indian-Ocean Tsunami in Section 7.2. The theoretical formulation of the tsunami-generated seismic wave model and its application to the Indian Ocean Tsunami are presented in Sections 7.3 and 7.4, respectively. The results of seismic modeling are presented and discussed in Section 7.5 .

7.1 Theoretical Formulation for aero-acoustic waves generated by a tsunami

We use a Cartesian coordinate system shown in Figure 7-1 to describe the tsunami propagation in the ocean. The ocean-air boundary is at $z = 0$. The atmosphere extends from $z = 0$ to $z = -200$ km, the ocean depth is assumed to be 4 km, and the seabottom for $z > 4$ km is assumed to be a half-space. The densities of air, water and the seabottom are 1 kg/m^3, 1000 kg/m^3 and 2000 kg/m^3, respectively. The sound speed in water (α_1) is 1500 m/s, the p-wave speed in the seabottom is $\alpha_2 = 2100$ m/s and the s-wave speed in the seabottom is $\beta_2 = 0.5\alpha_2 = 1050$ m/s (Section 7.3).

The sound speed in air is assumed to depend on the height as shown in Figure 7-1. The sound speed is approximately a constant for the first 100 km from the sealevel and then increases for heights greater than 100 km, in the Thermosphere [51]. Such a sound speed structure ensures that the atmosphere acts as a refractive waveguide and traps acoustic waves, resulting in efficient long-distance propagation over several hundreds of kilometers [196, 224, 200].

We now make the following simplifying assumptions about the geometry of tsunami propagation : (1) the tsunami propagates along the positive x-direction and has a simple support of length L_y in the y-direction, and (2) the tsunami propagates with a constant velocity given by [180]

$$c_w = \sqrt{gd} \tag{7.1}$$

where d is the water depth and g is the acceleration due to gravity. Both are realistic assumptions because, (1) tsunamis are often caused by elongated undersea faults that effectively beam the tsunami in a particular direction, thereby restricting their spatial extent in the direction normal to the direction of propagation, and (2) the water depth in the deep ocean is more or less constant (≈ 4 km) so that the speed of propagation is also constant.

Under these simplifying assumptions, the vertical velocity of the ocean surface due to the tsunami at any point $x_0, y_0)$ at time t is given by

$$v(x_0, y_0, t) = v\left(t - \frac{x_0}{c_w}\right) W(y_0) \tag{7.2}$$

where W is a spatial window in the y-direction given by

$$W(y_0) = \begin{cases} 1, & \text{for } \frac{-L_y}{2} \leq y_0 \leq \frac{L_y}{2} \\ 0, & \text{otherwise.} \end{cases} \tag{7.3}$$

We use Greens theorem [171] to quantify tsunami sound generation and propagation in the atmosphere. The air-water boundary is modeled as a rigid boundary, parts of which move up and down as the tsunami passes by. This problem is analogous to that of finding the acoustic pressure due to a moving piston. The total acoustic pressure $\tilde{p}_\omega(\mathbf{r})$ at any receiver $\mathbf{r} = (x, y)$ is given by [215, 25, 171]

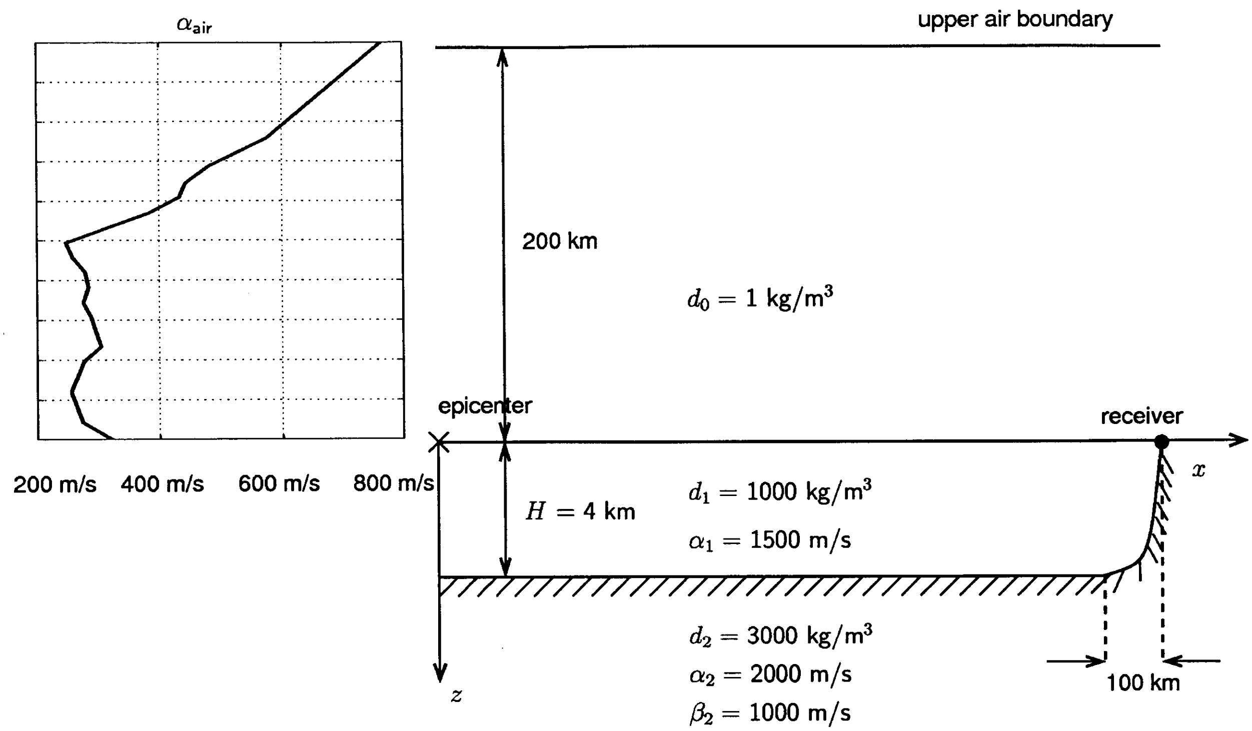

Figure 7-1: The geometry of the tsunami sound and seismics wave generation problem. For the aero-acoustics problem, the origin is assumed to be at the epicenter marked with a cross in the figure. For the seismics problem, the origin is at the interface between water and seabottom, directly below the epicenter. The sound speed in air is assumed to vary with height as described by the profile shown on the left. The sound speed is assumed to be constant in both the water and the seabottom.

$$\tilde{p}_\omega(\mathbf{r}) = \int_{x_0}\int_{y_0} G_\omega(\mathbf{r}|\mathbf{r_0})\,\frac{\partial}{\partial n_0}\tilde{p}_\omega(\mathbf{r_0})\,\mathrm{d}S_0. \tag{7.4}$$

where ω is the angular frequency, $\mathbf{r_0} = (x_0, y_0)$ is any point on the integration surface that spans the entire sea surface area over which the tsunami is present (the source region), n_0 is the normal to the surface, $G_\omega(\mathbf{r}|\mathbf{r_0})$ is the Greens function that describes propagation from any point in the source region to the receiver at $\mathbf{r}$, $\tilde{p}_\omega(\mathbf{r_0})$ is the total acoustic pressure at any point on the source region and the area element $\mathrm{d}S_0$ is given by $\mathrm{d}S_0 = \mathrm{d}x_0\mathrm{d}y_0$.

The Greens' function for this problem, $G_\omega(\mathbf{r}|\mathbf{r_0})$, is computed using a normal modes approach [124], and is shown in Figure 7-2 for a 0.1 Hz source frequency and a source location at the air-sea interface. To evaluate Equation 7.4, the normal derivative of the total pressure on the sea-surface needs to be computed.

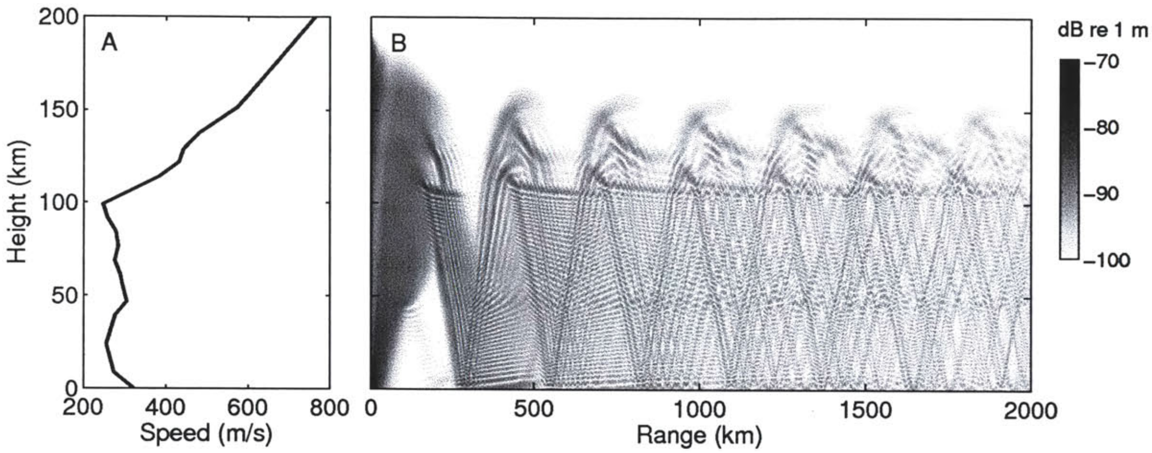

Figure 7-2: **(A)** Sound speed in air as a function of elevation from the ground ($z = 0$).**(B)** $10\log_{10}(|G|)$ where G is the Greens function for a source near the ground for 0.1 Hz. The KRAKEN normal mode program [205] is used for computing the Greens function. To prevent reflections from the waveguide boundary at $z = -200$ km, an artificial attenuating layer is used in the top 50 km, following the procedure described in [84]. The sharp increase in sound speed after 100 km in (A) causes sound rays to refract back into the ground. The resulting transmission loss is much lower than in free space, making the atmosphere an efficient channel for low frequency acoustic wave propagation.

7.1.1 The normal derivative of total pressure

Since the normal particle velocity is continuous across the air-water boundary, the gradient of the total acoustic pressure at any point $\mathbf{r_0} = (\rho_0, \theta_0)$ in the source region can be written as

$$\nabla p(\mathbf{r_0}, t) = -d_0 \frac{\partial \mathbf{u}(\mathbf{r_0}, t)}{\partial t} \tag{7.5}$$

where d_0 is the density of air and $\mathbf{u} = (u, v)$ is the particle velocity at the air-water interface. We assume that the normal to the surface (n_0) is approximately in the $-z$ direction so that

$$\frac{\partial p(\mathbf{r_0}, t)}{\partial n_0} \approx -\frac{\partial p(\mathbf{r_0}, t)}{\partial z} = d_0 \frac{\partial v(\mathbf{r_0}, t)}{\partial t}. \tag{7.6}$$

Fourier transform of Equation 7.6 yields

$$\frac{\partial \tilde{p}_\omega(\mathbf{r_0})}{\partial n_0} = i\omega d_0 \tilde{v}(\mathbf{r_0}, \omega) \tag{7.7}$$

where $\tilde{v}$ is the Fourier transform of $v(t, \rho_0)$ given by

$$\begin{aligned} \tilde{v}(\mathbf{r_0}, \omega) &= \int_{-\infty}^{\infty} \mathrm{e}^{-i\omega t} v(x_0, y_0, t) \mathrm{d}t \\ &= \mathrm{e}^{-i\omega x_0/c_w} W(y_0)\, \tilde{v}(\omega) \end{aligned} \tag{7.8}$$

Equation 7.8 follows from Equation 7.2 and the time shift property of the Fourier transform.

7.2 Application to the 2004 Indian Ocean Tsunami

On December 26, 2004, a powerful underwater earthquake (M 9.1) occured off the Andaman and Sumatran Islands and unleashed a powerful tsunami that spread across the Bay of Bengal before striking the Indian subcontinent and Srilanka [136]. Infrasound signals from both the earthquake and the tsunami were recorded at stations in

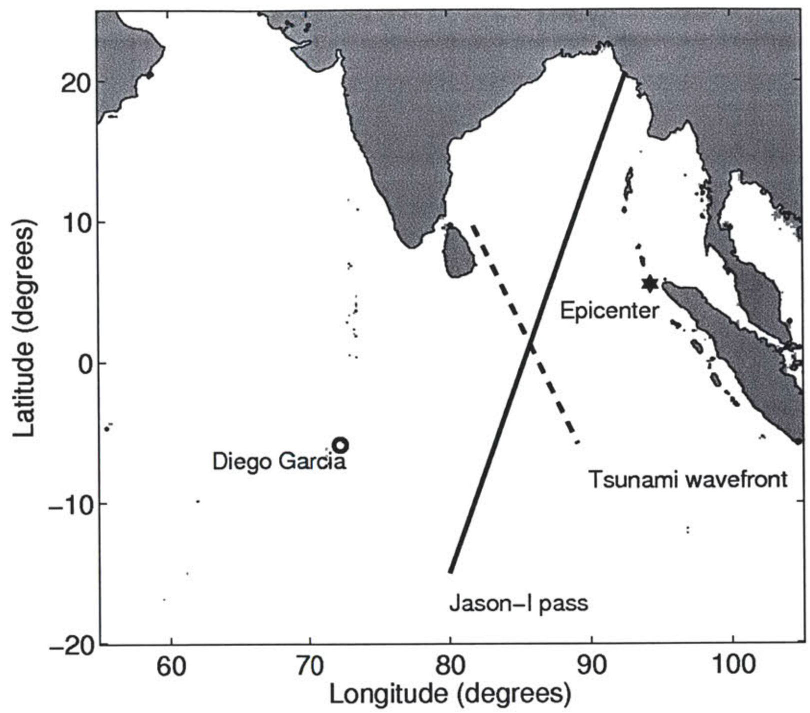

Figure 7-3: Geographic location of the epicenter (star) and the infrasound station (circle). The dotted line is the tsunami wavefront roughly two hours after the earthquake. The solid line is the concurrent altimeter satellite (Jason-I) pass.

Srilanka and in the Indian Ocean. These stations belong to the International Monitoring System (IMS) set up to observe seismic activities as part of the Comprehensive Test Ban Treaty. Infrasound data from one of these stations at Diego Garcia in the Indian Ocean (Figure 7-3) reportedly shows evidence of tsunami-generated infrasound [199], though the generation mechanism is not known.

In this section, we compare the tsunami-generated infrasound measured at Diego Garcia with results of the model developed in Section 7.1. We show that there is a good match in frequency content, time variation and the pressure level of the measured and modeled signals.

7.2.1 Tsunami-generated acoustic pressure

Using Equations 7.4, 7.7 and 7.8 the total tsunami-generated acoustic pressure at the receiver is

$$\tilde{p}\left(\mathbf{r},\omega\right) = \int_{x_0=-\infty}^{\infty} \int_{y_0=-L_y/2}^{L_y/2} i\omega d_0 \tilde{v}(\omega)\ \mathrm{e}^{-i\omega x_0/c_w} G_\omega(\mathbf{r}|\mathbf{r_0})\ \mathrm{d}x_0\ \mathrm{d}y_0, \tag{7.9}$$

The total acoustic pressure from the tsunami depends on the mass flow of air, via the $\tilde{v}(\omega)$ term. This term acts as the "source spectrum" that determines the frequency range of the received signal. The contributions from each point (x_0, y_0) in the source region are weighed by (1) a phase term $\mathrm{e}^{-j\omega x_0/c_w}$ that accounts for the motion of the tsunami and (2) the Greens function $G_\omega(\mathbf{r}|\mathbf{r_0})$, which accounts for the travel time to the receiver. In order to evaluate Equation 7.9, we need the sea-surface vertical velocity spectrum $\tilde{v}(\omega)$, which can be obtained from the sea-surface displacement. For our simulations, we use $L_y = 1000$ km, based on observations of the spatial extent of the 2004 Indian Ocean Tsunami [1].

If we further assume that the source region defined by the space-time surface displacement due to the tsunami has compact spatial support given by $-L_x/2 \leq x_0 \leq L_x/2$, which is propagating and evolving, then for a receiver in the far-field of the tsunami source region when $\sqrt{x^2+y^2} \gg (L_x^2 + L_y^2)/\lambda$, where λ is the acoustic wavelength, and in free-space, Equation 7.9 can be simplified to

$$\tilde{p}\left(\mathbf{r},\omega\right) \approx 2i\omega d_0 \tilde{v}(\omega) \frac{\mathrm{e}^{ikr}}{4\pi r}\ L_x L_y\ \mathrm{sinc}\left(\frac{(k_x - k_w)L_x}{2}\right)\ \mathrm{sinc}\left(\frac{k_y L_y}{2}\right), \tag{7.10}$$

where $r = \sqrt{x^2+y^2}$ is the range to the receiver, $k_w = \omega/c_w$ is the wavenumber of the surface-traveling tsunami, $k_x = k\cos\Theta$ is the projection of the acoustic wavenumber in the x-direction, $k_y = k\sin\Theta$ is the projection of the wavenumber in the y-direction, and $\Theta = \tan^{-1}\left(\frac{y}{x}\right)$ and is the angle subtended by the receiver at the center of the source region. When the receiver is in the far-field of the source region, the acoustic pressure has a sinc-like beampattern due to integration over finite spatial windows in the x- and y-directions.

If instead of the free-space Green's function we use the range-independent atmospheric waveguide Green's function for a source and a receiver at the air-sea interface

$$G(\mathbf{r}|\mathbf{r_0}) = \frac{id_0}{\sqrt{8\pi|\mathbf{r}-\mathbf{r_0}|}}\, \mathrm{e}^{-i\pi/4} \sum_n \frac{u_n(z_0=0)u_n(z=0)}{\sqrt{\xi_n}}\, \mathrm{e}^{i\xi_n|\mathbf{r}-\mathbf{r_0}|}, \tag{7.11}$$

where $u_n(z)$ is the n^{th} mode shape and ξ is the horizontal wavenumber, z_0 is the source depth and z is the receiver depth, then in the far-field, the total acoustic pressure is given by

$$\tilde{p}\,(\mathbf{r},\omega) \approx -\omega d_0^2 \tilde{v}(\omega)\ \mathrm{e}^{-i\pi/4} \sum_n \frac{u_n(0)^2}{\sqrt{8\pi\xi_n r}} \mathrm{e}^{i\xi_n r}\ L_x L_y \\ \operatorname{sinc}\left(\frac{(\xi_n\cos\Theta - k_w)L_x}{2}\right)\ \operatorname{sinc}\left(\frac{\xi_n\sin\Theta L_y}{2}\right). \tag{7.12}$$

For the simulations used in the paper, the far-field approximation is not used and the integration over the tsunami source region is explicitly computed.

7.2.2 Vertical velocity of the sea-surface due to the tsunami

The 2004 Indian-Ocean Tsunami was observed by four satellite altimeters flying at the time of the event [1]. Figure 7-4A shows the spatial profile of the ocean surface displacement measured by one of the satellites, Jason-I, which overflew the tsunami (solid line in Figure 7-3) two hours after the earthquake. We used this profile to compute the vertical velocity of the ocean surface, $v(t)$ (Figure 7-4B) and its Fourier transform $\tilde{v}(\omega)$ (Figure 7-4C). Here we have assumed that (1) the tsunami is non-dispersive, i.e the same waveform in Figure 7-4A is preserved as the tsunami propagates away from the source and (2) the phase speed (c_w) is constant, and is approximately $\sqrt{9.81 \times 4000} \approx 200$ m/s. Both these assumptions are valid as long as the tsunami is in the deep ocean, where the water depth is more of less constant [180].

Once the tsunami reaches the continental shelf, the water depth and consequently c_w decreases according to Equation 7.1. The spectrum of the vertical sea-surface velocity (Figure 7-4C) shows that most of the acoustic energy received is expected to be in the deep infrasound regime (f <0.1 Hz).

7.2.3 Comparison of modeled and measured infrasound signals from the Indian Ocean Tsunami

Under the assumptions stated in Sections 7.1 and 7.2.2, we apply Equation 7.9 to compute the total tsunami-induced acoustic pressure at a receiver located at Diego Garcia. The origin of the coordinate system is placed at the epicenter of the earthquake, which is also assumed to be the source point of the tsunami.

The spectrum of the modeled received signal (Figure 7-5A) shows that most of the acoustic energy is concentrated in the deep infrasound frequency regime (0.01-0.1 Hz). This is in good agreement with the frequency range of the measured tsunami infrasound signal reported by [199]. Reconstruction of the received pressure time series from the frequency spectrum shows that (1) the maximum pressure magnitude of ≈ 0.5 Pa shown in Figure 7-5B matches the value reported by [199] and (2) the time of first arrival occurs roughly 2 hours after the earthquake, again in good agreement with the time series reported in Figure 1A by [199]. The power-spectral density of the tsunami-generated infrasound signals are also found to be upto two orders of magnitude higher than those of prevalent ambient noise, as can be seen from Figure 7-6. The ambient noise was recorded in four different stations in different regions of the world by infrasound stations part of the Comprehensive Test Ban Treaty (CTBT) monitoring. [199]

The first strong aero-acoustic signals from the tsunami arrive roughly 2 hours after the earthquake, when the tsunami is still about 1 hour 30 min away from the receiver on shore, making it feasible to use infrasound signals in early-warning systems. The proposed aero-acoustic model makes use of the assumption that c_w, the speed of tsunami propagation in the ocean, is a constant. This assumption holds in the deep

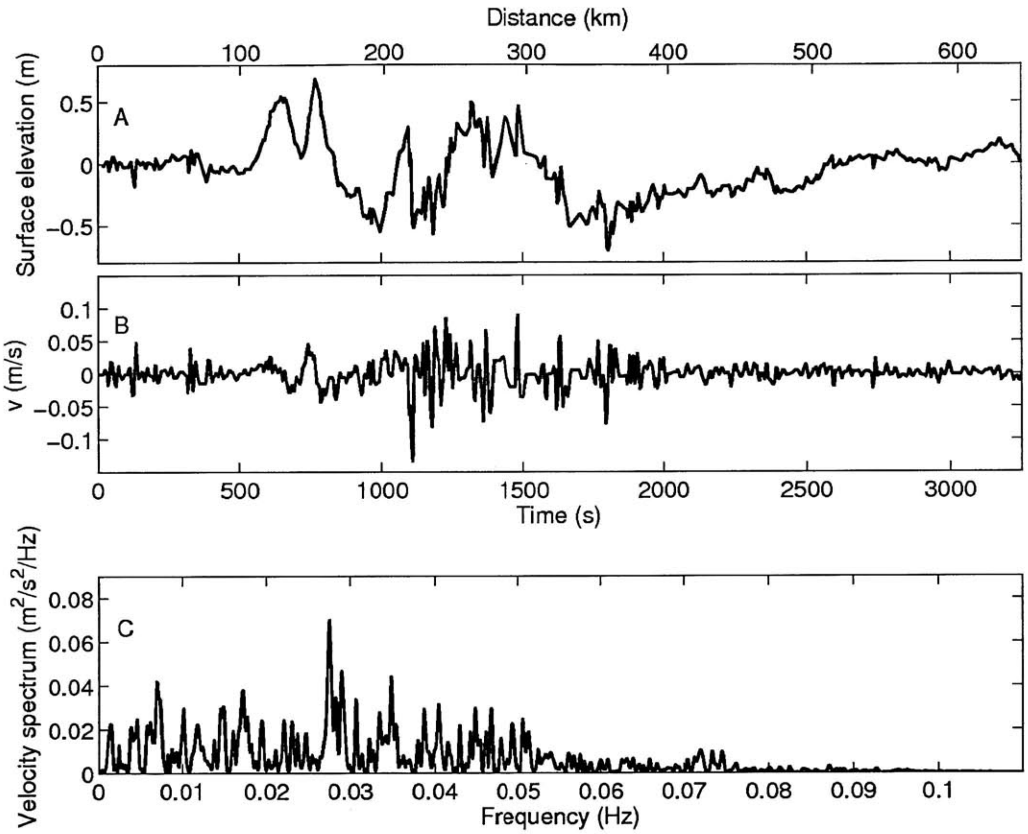

Figure 7-4: **(A)** Sea surface elevation measured by Jason-I projected along the radial joining the epicenter and the receiver at Diego Garcia in Figure 7-3. The surface elevation is first measured as a function of radial distance and then converted to a function of time using a constant phase speed of $c_w = \sqrt{gd} \approx 200$ m/s. **(B)** Vertical velocity of the sea surface at any point as the tsunami profile in (A) passes over that point. The vertical velocity is a measure of the mass flow into the atmosphere caused by the tsunami and is the source of tsunami infrasound. **(C)** The spectrum of the time signal in (B) showing most of the energy of the tsunami source in the deep infrasound frequency regime of less than 0.1 Hz.

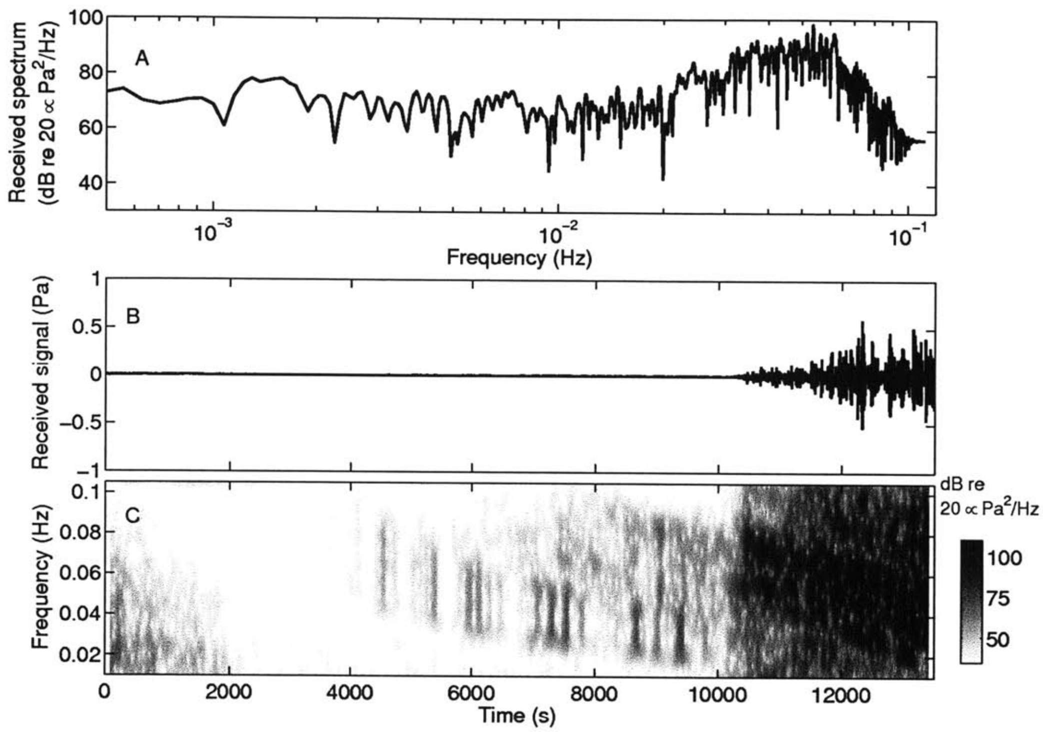

Figure 7-5: **(A)** Modeled spectrum of the acoustic pressure received at Diego Garcia due to a propagating Tsunami. Most of the received acoustic energy is in the infrasonic frequency regime. **(B)** Modeled received signal in time. The earthquake is assumed to occur at $t = 0$ s. **(C)** Power spectral density of the time series in (B) again showing that most of the energy in the tsunami-generated infrasound is concentrated below 0.1 Hz. The first strong tsunami signal is predicted to arrive approximately 2 hours after the earthquake, giving an average speed of propagation of 380 m/s. This speed is approximately 1.9 times that of the tsunami's 200 m/s propagation speed, and so the infrasound signal arrives approximately 1 h 30 m before the tsunami reaches the shore. The time of first arrival of the tsunami signal matches the measurements made in Diego Garcia.

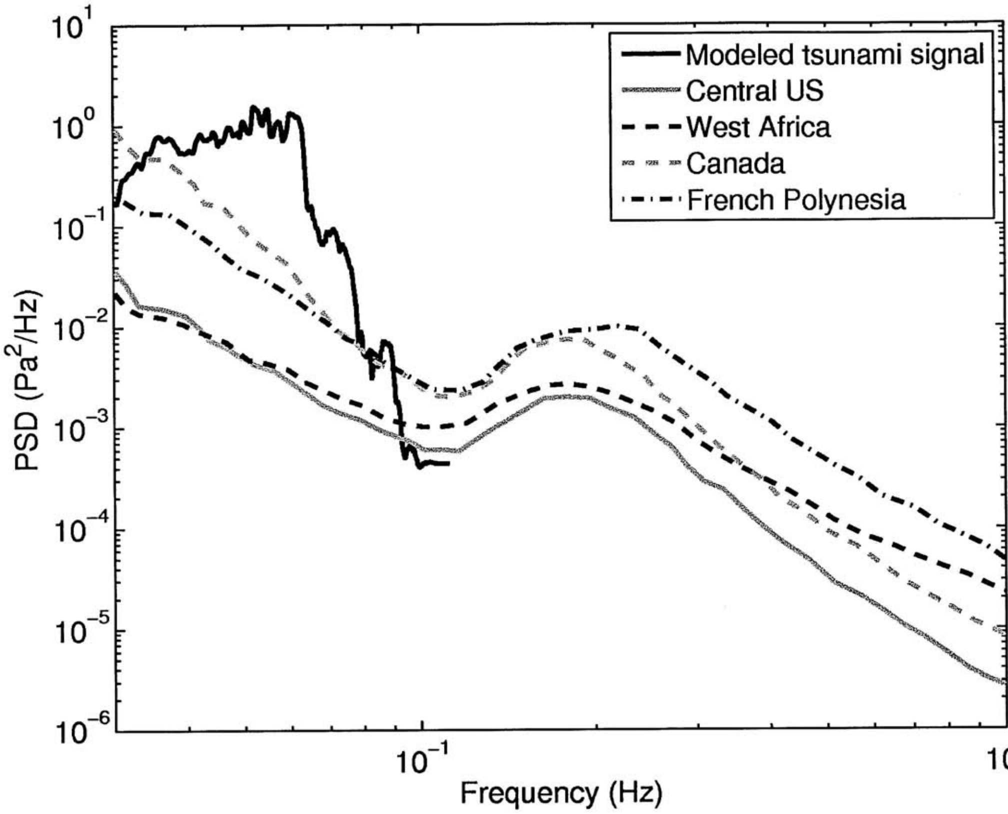

Figure 7-6: Comparison of the modeled power spectral density of the tsunami with prevalent average background noise recorded in 4 different places around the world recorded by infrasound stations part of CTBT monitoring [199]. The tsunami-generated signal stands above the background noise for frequencies less than 0.1 Hz. The tsunami signal is not simulated for frequencies above 0.1 Hz, since most of the acoustic energy lies at frequencies below 0.1 Hz.

ocean, where the water depth and consequently c_w is more or less constant. As the tsunami enters the continental shelf, however, the water depth and and so the tsunami propagation speed decreases. Simultaneously, the tsunami wavelength decreases and its waveheight increases. It is then expected that the sound pressure levels of the signals increase. However, these changes take place very near the shore (< 100 km), at distances much smaller when compared to the total distance traveled by the tsunami (> 2500 km). The results presented in Figure 7-5 do not account for such changes close to the shore. These results, however, are expected to change only for times $>$ 12000 s, just before the tsunami hits the shore.

The calculations made in this chapter also assume that the sound speed profile in air is range-independent. The sound speed structure in air is, in fact, a strong function of the wind speed and direction[51]. The range-dependence of the sound speed structure also means that 3D calculations of the Greens function in air have to be made to take into account any 3D refraction of sound. This is especially true for the particular problem discussed in this chapter, where the tsunami-source is in the Northern Hemisphere and the receiver is in the Southern Hemisphere (Fig. 7-3) and the prevailing trade-winds change direction across the Equator. Such refraction of sound may lead to an apparent change in direction of infrasound arrivals at the receiver.

7.3 Theoretical formulation for seismic waves generated by tsunami

In this section, we derive an analytical expression for the vertical displacement at any point on a fluid-solid interface when the interface is subject to a point impulsive load. We then use this expression to compute the vertical displacement of the ground expected at Diego Garcia due to the hydrodynamic pressure exerted by the tsunami on the seabottom.

Consider a fluid-half-space solid system as shown in Figure 7-1. The fluid (seawater) is given by $-H < z < 0$ and the solid (seabottom) is given by $z > 0$. The density of the fluid and the p-wave speed are d_1 and α_1, respectively. The density of the solid is d_2, the p-wave speed is α_2 and the s-wave speed is β_2. Since the interface is subject to a normal point force, the wavemotion in both the fluid and the solid is axially symmetric about the point of application of the force, and cylindrical coordinates (ρ,θ,z) are employed. The origin is located at the load point on the interface. We will first derive expressions assuming H as a constant over range, and then extend the results to slowly varying H.

7.3.1 Governing equations

The displacement potentials are ϕ_1 in the fluid and ϕ_2 and ψ_2 in the solid, so that the governing equations are [274]

$$\frac{\partial^2 \phi_1}{\partial \rho^2} + \frac{1}{\rho}\frac{\partial \phi_1}{\partial \rho} + \frac{\partial^2 \phi_1}{\partial z^2} = \frac{1}{\alpha_1^2}\ddot{\phi}_1 \tag{7.13}$$

$$\frac{\partial^2 \phi_2}{\partial \rho^2} + \frac{1}{\rho}\frac{\partial \phi_2}{\partial \rho} + \frac{\partial^2 \phi_2}{\partial z^2} = \frac{1}{\alpha_2^2}\ddot{\phi}_2 \tag{7.14}$$

$$\frac{\partial^2 \psi_2}{\partial \rho^2} + \frac{1}{\rho}\frac{\partial \psi_2}{\partial \rho} + \frac{\partial^2 \psi_2}{\partial z^2} - \frac{\psi_2}{\rho^2} = \frac{1}{\beta_2^2}\ddot{\psi}_2 \tag{7.15}$$

The double dots represent double derivatives with respect to time. The displacements in the fluid are given by

$$u_1 = \frac{\partial \phi_1}{\partial \rho},\ w_1 = \frac{\partial \phi_1}{\partial z} \tag{7.16}$$

and the displacements in the solid are given by

$$u_2 = \frac{\partial \phi_2}{\partial \rho} - \frac{\partial \psi_2}{\partial z},\ w_2 = \frac{\partial \phi_2}{\partial z} + \frac{1}{\rho}\frac{\partial (\rho\psi_2)}{\partial \rho}. \tag{7.17}$$

7.3.2 Boundary conditions

A point load is applied at the origin and is given by $A(t)\delta(\rho)/2\pi\rho$. The shear stress at the interface is zero (ideal fluid) while there is continuity of the normal displacements and normal stresses in the fluid and solid. Since the fluid layer is of finite thickness H, the normal stress at the top of the fluid layer is assumed to be zero ("pressure-release" surface).

The boundary conditions are then

$$w_1\big|_{z=0} = w_2\big|_{z=0} \tag{7.18}$$

$$\sigma_{zz,2}\big|_{z=0} = \sigma_{zz,1}\big|_{z=0} - A(t)\frac{\delta(\rho)}{2\pi\rho} \tag{7.19}$$

$$\sigma_{zz,1}\big|_{z=-H} = 0 \tag{7.20}$$

$$\sigma_{z\rho,2}\big|_{z=0} = \sigma_{z\rho,1}\big|_{z=0} = 0. \tag{7.21}$$

7.3.3 Integral transforms of the governing equations

The solution for the governing equations (Eqs. 7.13,7.14,7.15) are obtained using the Fourier and Hankel tranforms defined by

$$\tilde{f}(\omega) = \int_{-\infty}^{\infty} f(t)\ \mathrm{e}^{-i\omega t}\ \mathrm{d}t, \text{ and} \tag{7.22}$$

$$f^{H_n}(\xi) = \int_0^{\infty} f(\rho) J_n(\xi\rho)\rho\ \mathrm{d}\rho, \tag{7.23}$$

respectively. Applying these transforms to Eq. 7.13 yields

$$\begin{aligned}
-\xi^2 \tilde{\phi}_1{}^{H_0} + \frac{\partial^2 \tilde{\phi}_1{}^{H_0}}{\partial z^2} &= -\frac{\omega^2}{\alpha_1^2}\tilde{\phi}_1{}^{H_0} \\
\Rightarrow \frac{\partial^2 \tilde{\phi}_1{}^{H_0}}{\partial z^2} &= \left(\xi^2 - \frac{\omega^2}{\alpha_1^2}\right)\tilde{\phi}_1{}^{H_0} \\
\Rightarrow \frac{\partial^2 \tilde{\phi}_1{}^{H_0}}{\partial z^2} &= \gamma^2 \tilde{\phi}_1{}^{H_0}
\end{aligned} \tag{7.24}$$

where $\gamma^2 = \left(\xi^2 - \frac{\omega^2}{\alpha_1^2}\right)$. Similarly, Eqs. 7.14 and 7.15 are transformed to

$$\frac{\partial^2 \tilde{\phi_2}^{H_0}}{\partial z^2} = \eta^2 \tilde{\phi_2}^{H_0}, \text{ and} \tag{7.25}$$

$$\frac{\partial^2 \tilde{\psi_2}^{H_1}}{\partial z^2} = \chi^2 \tilde{\psi_2}^{H_1}, \tag{7.26}$$

respectively, where $\eta^2 = \left(\xi^2 - \frac{\omega^2}{\alpha_2^2}\right)$ and $\chi^2 = \left(\xi^2 - \frac{\omega^2}{\beta_2^2}\right)$.

The solutions to Eqs. 7.24, 7.25 and 7.26 are

$$\tilde{\phi_1}^{H_0} = \Phi_1^{(1)}(\xi,\omega)\ \mathrm{e}^{\gamma z} + \Phi_1^{(2)}(\xi,\omega)\ \mathrm{e}^{-\gamma z} \tag{7.27}$$

$$\tilde{\phi_2}^{H_0} = \Phi_2(\xi,\omega)\ \mathrm{e}^{-\eta z} \tag{7.28}$$

$$\tilde{\psi_2}^{H_1} = \Psi_2(\xi,\omega)\ \mathrm{e}^{-\chi z}. \tag{7.29}$$

Note that in the solid, only terms that lead to finite values for $|z| \to \infty$ are chosen.

The displacements and stresses in the fluid and solid are also transformed so that

$$\tilde{u_1}^{H_1} = -\xi \tilde{\phi_1}^{H_0} \tag{7.30}$$

$$\tilde{w_1}^{H_0} = \frac{\partial \tilde{\phi_1}^{H_0}}{\partial z} \tag{7.31}$$

$$\tilde{u_2}^{H_1} = -\frac{\partial \tilde{\psi_2}^{H_1}}{\partial z} - \xi \tilde{\phi_2}^{H_0} \tag{7.32}$$

$$\tilde{w_2}^{H_0} = \frac{\partial \tilde{\phi_2}^{H_0}}{\partial z} + \xi \tilde{\psi_2}^{H_1} \tag{7.33}$$

$$\tilde{\sigma}_{zz,2}^{H_0} = \mu \left[\left(\xi^2 + \chi^2\right) \tilde{\phi_2}^{H_0} + 2\xi \frac{\partial \tilde{\psi_2}^{H_1}}{\partial z} \right] \tag{7.34}$$

$$\tilde{\sigma}_{z\rho,2}^{H_1} = -\mu \left[2\xi \frac{\partial \tilde{\phi_2}^{H_0}}{\partial z} + \left(\xi^2 + \chi^2\right) \tilde{\psi_2}^{H_1} \right], \tag{7.35}$$

where μ is Lamé's constant for the solid such that $\beta_2 = \sqrt{\mu/d_2}$. The transformed boundary conditions are

$$
\begin{aligned}
\tilde{w_1}^{H_0} &= \tilde{w_2}^{H_0} && (7.36)\\
\tilde{\sigma}^{H_0}_{zz,2}|_{z=0} &= \tilde{\sigma}^{H_0}_{zz,1}|_{z=0} - \frac{\tilde{A}(\omega)}{2\pi} && (7.37)\\
\tilde{\sigma}^{H_0}_{zz,1}|_{z=-H} &= 0 && (7.38)\\
\tilde{\sigma}^{H_1}_{z\rho,2}|_{z=0} = \tilde{\sigma}^{H_1}_{z\rho,2}|_{z=0} &= 0.. && (7.39)
\end{aligned}
$$

7.3.4 Vertical displacement of the fluid-solid interface

Boundary conditions 7.36-7.39 lead to the following set of linear equations for the coeffecients in Eqs. 7.27-7.29:

$$
\begin{aligned}
\gamma\Phi_1^{(1)} - \gamma\Phi_1^{(2)} + \eta\Phi_2 - \xi\Psi_2 &= 0 && (7.40)\\
d_1\omega^2\Phi_1^{(1)} + d_1\omega^2\Phi_1^{(2)} + \mu\left(\xi^2+\chi^2\right)\Phi_2 - 2\mu\xi\chi\Psi_2 &= -\frac{\tilde{A}}{2\pi} && (7.41)\\
e^{-\gamma H}\Phi_1^{(1)} + e^{\gamma H}\Phi_1^{(2)} &= 0 && (7.42)\\
-2\xi\eta\Phi_2 + \left(\xi^2+\chi^2\right)\Psi_2 &= 0, && (7.43)
\end{aligned}
$$

and the coeffecients are given by

$$
\begin{aligned}
\Phi_1^{(1)} &= \frac{\tilde{A}}{2\pi}\frac{\eta\,(\xi^2-\chi^2)\ e^{\gamma H}}{\Gamma(\xi,\omega)}\\
\Phi_1^{(2)} &= -\frac{\tilde{A}}{2\pi}\frac{\eta\,(\xi^2-\chi^2)\ e^{-\gamma H}}{\Gamma(\xi,\omega)}\\
\Phi_2 &= \frac{\tilde{A}}{2\pi}\frac{2\gamma\,(\xi^2+\chi^2)\cosh(\gamma H)}{\Gamma(\xi,\omega)}\\
\Psi_2 &= \frac{\tilde{A}}{2\pi}\frac{4\eta\xi\cosh(\gamma H)}{\Gamma(\xi,\omega)}
\end{aligned}
$$

where

$$
\Gamma(\xi,\omega) = \left[8\eta\chi\xi^2 - 2\xi^4 - 4\xi^2\chi^2 - 2\chi^4\right]\gamma\mu\cosh(\gamma H) + \left[2\eta d_1\omega^2\left(\chi^2-\xi^2\right)\right]\sinh(\gamma H). \qquad (7.44)
$$

The vertical displacement of the solid-fluid interface is then computed from Eq. 7.31 as

$$\begin{aligned}
\left.\tilde{w}_1^{H_0}\right|_{z=0} &= \left.\frac{\partial \tilde{\phi}_1^{H_0}}{\partial z}\right|_{z=0} \\
&= \gamma\Phi_1^{(1)} - \gamma\Phi_1^{(2)} \\
&= \frac{\tilde{A}}{2\pi}\frac{2\gamma\eta\,(\xi^2-\chi^2)\cosh(\gamma H)}{\Gamma(\xi,\omega)}.
\end{aligned} \tag{7.45}$$

Applying the inverse Hankel transform to Eq. 7.45, we have

$$\tilde{w}_1(\rho,\omega) = \frac{\tilde{A}}{2\pi}\int_0^\infty \frac{2\gamma\eta\,(\xi^2-\chi^2)\cosh(\gamma H)}{\Gamma(\xi,\omega)} J_0(\xi\rho)\xi\,\mathrm{d}\xi \tag{7.46}$$

$$= \frac{\tilde{A}}{2\pi}\int_0^\infty \frac{J_0(\xi\rho)\xi}{\mathcal{S}(\xi,\omega)}\,\mathrm{d}\xi, \tag{7.47}$$

where

$$\mathcal{S}(\xi,\omega) = \frac{\mu\,(4\eta\chi\xi^2-\xi^4-2\xi^2\chi^2-\chi^4)}{\eta\,(\xi^2-\chi^2)} - \frac{d_1\omega^2\tanh(\gamma H)}{\gamma}. \tag{7.48}$$

The integrand in Eq. 7.47 has a singularity whenever $\mathcal{S}(\xi,\omega)$ is zero and in order to evaluate the integral, it is convenient to consider the analytical continuation of the integrand in the complex plane. The resulting complex integral is evaluated by contour integration as described by [2], and is given by $-2\pi i$ times the sum of the residues of the integrand:

$$\tilde{w}_1(\rho,\omega) = -i\tilde{A}\sqrt{\frac{1}{2\pi\rho}}\,\mathrm{e}^{i\frac{\pi}{4}}\sum_{n=1}^{N}\frac{\sqrt{\xi_n}\,\mathrm{e}^{-i\xi_n\rho}}{\left.\frac{\partial\mathcal{S}(\xi,\omega)}{\partial\xi}\right|_{\xi=\xi_n}} \tag{7.49}$$

where, ξ_n, $n = 1, 2, .., N$ are the zeros of $\mathcal{S}(\xi,\omega)$ defined in Eq. 7.48. Here, we have used the fact that

$$J_0(\xi\rho) = \frac{1}{2}\left(H_0^{(1)}(\xi\rho) + H_0^{(2)}(\xi\rho)\right) \tag{7.50}$$

and the asymptotic forms of $H_0^{(1)}$ and $H_0^{(2)}$ for large arguments:

$$H_0^{(1)}(x) \sim \sqrt{\frac{2}{\pi x}}\, \mathrm{e}^{i\left(x-\frac{\pi}{4}\right)},\; H_0^{(2)}(x) \sim \sqrt{\frac{2}{\pi x}}\, \mathrm{e}^{-i\left(x-\frac{\pi}{4}\right)}. \tag{7.51}$$

Equation 7.49 holds under the assumption of constant H. If the bathymetry varies slowly with range, as is the case with a receiver on land, then the poles ξ_n are also range-dependent and an adiabatic approximation [272] is used:

$$\tilde{w}_1(\rho,\omega) = -i\tilde{A}\sqrt{\frac{1}{2\pi\rho}}\, \mathrm{e}^{i\frac{\pi}{4}} \sum_{n=1}^{N} \frac{\sqrt{\xi_n(\rho)}\, \mathrm{e}^{-i\int_0^{\rho} \xi_n(\rho')\, \mathrm{d}\rho'}}{\left.\frac{\partial S(\xi,\omega)}{\partial \xi}\right|_{\xi=\xi_n(\rho)}}. \tag{7.52}$$

7.4 Seismic waves generated by the 2004 Indian Ocean Tsunami

During the Indian Ocean tsunami event on December 25, 2004, the ground displacement due to the Sumatran Earthquake was recorded at the Diego Garcia seismic station in the Indian Ocean (Figure 7-3). In this section, we model the vertical velocity of the ground at a receiver in Diego Garcia due to a moving tsunami using Equation 7.49, and compare the model with measurements.

We will revert to the Cartesian coordinate system used in infrasound formulation to compute the vertical displacement of the ground due to the tsunami. The vertical displacement at a receiver at (x, y) due to a source at (x_0, y_0) is given by (Equation 7.52)

$$\begin{aligned} \tilde{w}_1(x,y|x_0,y_0;\omega) &= -i\tilde{A}\sqrt{\frac{1}{2\pi D(x,y|x_0,y_0)}}\, \mathrm{e}^{i\frac{\pi}{4}} \sum_{n=1}^{N} \frac{\sqrt{\xi_n(D)}\, \mathrm{e}^{-i\int_0^{D} \xi_n(D')\, \mathrm{d}D'}}{\left.\frac{\partial S(\xi,\omega)}{\partial \xi}\right|_{\xi=\xi_n(D)}} && (7.53) \\ &= \tilde{A}\tilde{w}_1^G(x,y|x_0,y_0;\omega) && (7.54) \end{aligned}$$

where $D(x,y|x_0,y_0) = \sqrt{(x-x_0)^2 + (y-y_0)^2}$ is the distance between the source and receiver, $\tilde{w}_1^G(x,y|x_0,y_0;\omega)$ acts as the "Greens function" for the vertical displacement for unit force at the source point, and $\tilde{A}$ is the Fourier transform of the total force acting on the seabottom due to the tsunami, which can be obtained from linear hydrodynamics theory [180]. It can be shown that if the wave height of the tsunami at any point ρ_0 is given by

$$Z(x_0, y_0, t) = Z\left(t - \frac{x_0}{c_w}\right) W(y_0), \tag{7.55}$$

where c_w is the speed of propagation of the tsunami and W is the window function defined in Equation 7.3, then the total force acting on an area element on the seabottom is given by

$$\tilde{A} = d_1 g \frac{\tilde{Z}(\omega)\ \mathrm{e}^{-i\omega x_0/c_w}}{\cosh(\frac{\omega H}{c_w})} W(y_0)\ \mathrm{d}x_0\ \mathrm{d}y_0, \tag{7.56}$$

where H is the total water depth, and g is the acceleration due to gravity.

The total vertical velocity ($\tilde{v}_1$) of the ground is obtained by integrating over the contributions from all source regions and by using Equations 7.54 and 7.56

$$\tilde{v}_1(,t) = \int_{x_0=-\infty}^{\infty} \int_{y_0=-L_y/2}^{L_y/2} i\omega d_1 g \frac{\tilde{Z}(\omega)\ \mathrm{e}^{-i\omega x_0/c_w}}{\cosh(\frac{\omega H}{c_w})} \tilde{w}_1^G(x, y|x_0, y_0; \omega)\ \mathrm{d}x_0\ \mathrm{d}y_0. \tag{7.57}$$

For the calculation of $\tilde{w}_1^G(\rho|\rho_0, \theta_0; \omega)$, the following parameters were used: $\alpha_1 = 1500$ m/s, $d_1 = 1025$ kg/m^3, $d_2 = 2000$ kg/m^3 [242], and $L_y = 1000$ km. The wave height spectrum $\tilde{Z}(\omega)$ is computed from the time series of waveheight shown in Figure 7-4A. The vertical velocity of the ground is computed for different values of p-wave speeds (α_2) ranging from 1700 to 2500 m/s. The s-wave speed (β_2) is assumed to be $0.5\alpha_2$ [4].

7.5 Results and Discussion

The spectrum of the modeled received signal for $\alpha_2 = 2100$ m/s and $\beta_2 = 1050$ m/s shows most of the acoustic energy is in the frequency range of 0.01 and 0.03 Hz (Figure 7-7A). The time series of the vertical velocity and its spectrogram (Figures 7-7B,C) shows that the first arrival time corresponds to a wave speed of $\sim$ 800 m/s. This speed is much lower than the p-wave speeds in the seabottom and water, consistent with expected the propagation speed of Rayleigh waves [69, 4] that propagate along the water-seabed interface. The radial wavenumber of propagation of this wave corresponds to the zeros of Equation 7.48. The Rayleigh wave speed is still much larger than the tsunami propagation speed, so that these waves can be interpreted as precursors for use in tsunami early warning systems.

The ground displacement due to both the Sumatran-Andaman Earthquake and the associated Indian Ocean Tsunami was measured by seismometers in Diego Garcia Island in the Indian Ocean [266]. Any comparison between the measurement at Diego Garcia and the prediction of the model is meaningful only under the assumption that the tsunami-induced ground motion dominates earthquake-induced ground motion in the frequency regime of interest (0.01-0.1 Hz). If this assumption holds, we find that by using a p-wave speed of $\alpha_2 = 2100$ m/s and an s-wave speed of $\beta_2 = 1050$ m/s, there is a good match between modeled and measured vertical ground velocities [266] for times > 6000 s after the earthquake. These values of α_2 and β_2 fall within past estimates of p-wave and s-wave speeds in the Indian Ocean basin region [242].

In the absence of any knowledge of the p-wave and s-wave speeds in the seabottom, the modeled results should be interpreted as an upper bound on the tsunami-induced ground vertical velocity, given the measurements in Diego Garcia. For example, lowering the choice of p-wave speed from 2100 m/s to 1700 m/s increases the maximum tsunami-induced vertical ground velocity by a factor of 2 (Figure 7-8). This if found to be in disagreement with the measurements made in Diego Garcia. The minimum p-wave speed used in the model is then restricted to $\alpha_2 = 2100$ m/s. If the earthquake-induced vertical velocity is assumed to dominate the tsunami-induced velocities, then any p-wave speed higher than 2100 m/s may be chosen in the model. For example, by increasing the p-wave speed from 2100 m/s to 3000 m/s, the maximum tsunami-induced vertical ground velocity reduces by a factor of 4 (Figure 7-8). This would mean that the earthquake-induced vertical ground velocity is 4 times larger than the tsunami-induced vertical ground velocity.

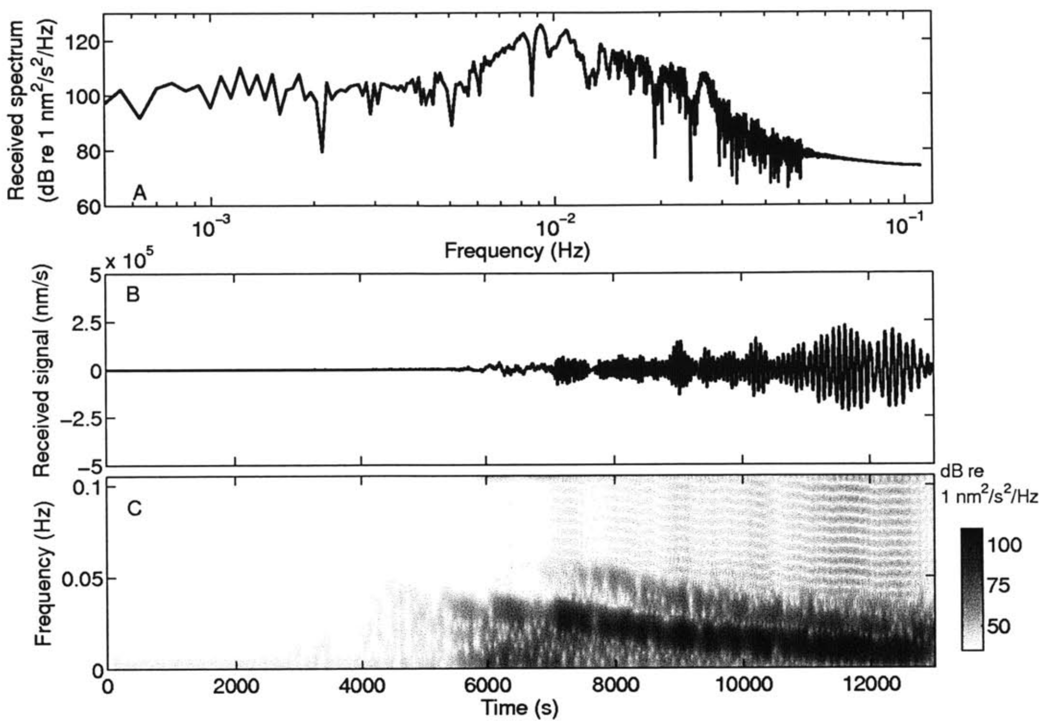

Figure 7-7: **(A)** Modeled spectrum of the tsunami-induced vertical ground displacement received at Diego Garcia. Most of the signal energy is at frequencies less than 0.03 Hz. **(B)** Modeled time series of tsunami-generated vertical velocity showing the arrival structure at Diego Garcia. The maximum amplitude of the tsunami signal, which arrives approximately 2 hours after the earthquake, is comparable to the maximum amplitude of ground motion measured at Diego Garcia [266] during the same time. A p-wave speed of $\alpha_2 = 2100$ m/s and an s-wave speed of $\beta_2 = 1050$ m/s were used to simulate the vertical ground veocity. **(C)** Power spectral density of the time series in (B) again showing that most of the energy in the tsunami-generated infrasound is concentrated below 0.1 Hz. The first strong tsunami signal is predicted to arrive approximately 1.5 hours after the earthquake, giving an average speed of propagation of 800 m/s. This speed is approximately 4 times that of the tsunami's 200 m/s propagation speed, and so the infrasound signal arrives approximately 3 hours before the tsunami hits the shore.

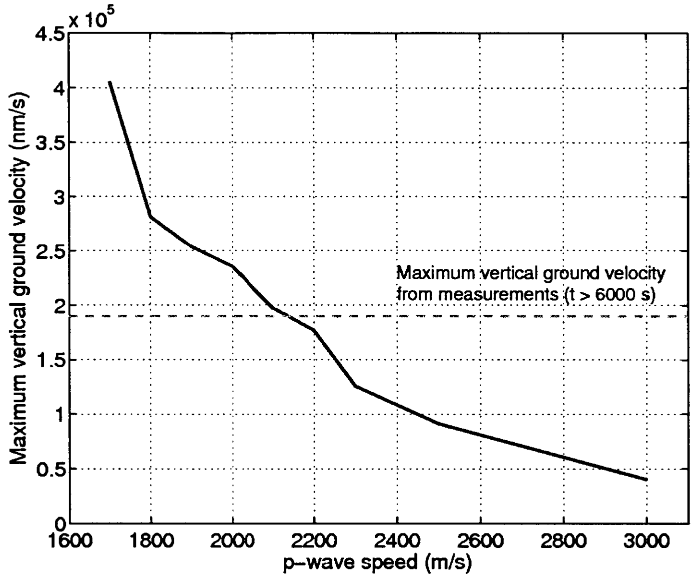

Figure 7-8: The maximum vertical ground velocity at Diego Garcia computed using the model in Section 7.3 for different values of p-wave speed α_2. An s-wave speed of $\beta_2 = 0.5\alpha_2$ is assumed. The vertical ground velocity is sensitive to the choice of α_2. The gray line is the maximum vertical ground velocity measured during the earthquake for t > 6000 s. For a p-wave speeed of $\alpha_2 = 2100$ m/s and an s-wave speed of $\beta_2 = 1050$ m/s, there is a good match between the data and modeled vertical velocities. If the earthquake-induced vertical ground velocity dominates the tsunami-induced signals, then any value of α_2 greater than 2100 m/s may be used in the model.

7.6 Conclusions

In this chapter, we suggest a mechanism for infrasound generation by tsunamis, where the rate of change of mass flow of air due to tsunami motion acts as the acoustic source term. Based on this mechanism, some simplifying assumptions about the geometry of tsunami propagation, and the Greens theorem, we develop an analytical model to quantify infrasound signals generated by a tsunami located hundreds of kilometers away from a receiver. The analytical model is applied to the Indian Ocean Tsunami that occurred on December 26, 2004. The pressure level, frequency range and arrival time of the modeled infrasound signal are shown to match the corresponding signal characteristics measured by infrasound monitoring stations during the tsunami event. We also show that the air-borne infrasound signals travel faster than the tsunami and so these signals measured using land-based sensors can potentially be used to remotely sense tsunamis and provide sufficient warning before the tsunami hits shore.

The possibility of remotely sensing tsunamis using seismic waves is also examined by developing an analytical model for quantifying very low frequency (0.01-0.1 Hz) Rayleigh waves generated by a tsunami. The generation of Rayleigh waves due to the low-frequency forcing of the seabottom due to a tsunami is quantified by developing a full field model for compression and shear wave propagation in the seabottom in the presence of a finite-thickness ocean layer. The seismic model is then used to predict the vertical ground velocity at Diego Garcia Island caused by the 2004 Indian Ocean Tsunami. The amplitude of tsunami-induced vertical ground velocity is found to be highly sensitive to the compression and shear wave speeds in the sea-bottom. For reasonable values of these speeds (compression speed of 2000 m/s and shear wave speed of 1050 m/s), it is shown that the tsunami-induced vertical ground velocity amplitudes match measurements made in Diego Garcia, under the assumption that earthquake-induced ground motion does not mask tsunami-induced ground motion for times $>$ 1.5 hours after the arthquake. The tsunami-induced Rayleigh waves are received at Diego Garcia several hours before the tsunami hits the shore, making tsunami-induced seismic waves a possible modality for remotely sensing tsunamis.

Chapter 8

Conclusions

In this thesis, we presented a number of recent findings in marine ecology related to the behavior of vast oceanic fish shoals that were made possible by the Ocean Acoustic Waveguide Remote Sensing (OAWRS) technique. The OAWRS system is capable of instantaneously imaging and continuously monitoring fish populations over continental shelf-scale areas, spanning thousands of square kilometers. Here, we showed how OAWRS can be used to quantify the acoustic scattering response of fish and remotely infer their physiological characteristics to enable species classification. We also showed that OAWRS can be used in a variety of oceanic ecosystems around the world to study many ecologically important fish species such as Alaskan Pollock, Peruvian Anchovy, Barents Sea capelin, Southern blue whiting, Argentine hake and Atlantic bluefin tuna.

Fish population density images from two field experiments demonstrating the remote-sensing capabilities of OAWRS were used to quantify fish shoaling behavior over continental shelf-scale areas. Observations of fish shoals made during the OAWRS 2003 experiment in the New Jersey strataform were used to quantify (1) inter-shoal dynamics such as coalescence of fish groups over tens of kilometers, (2) fish mass flow between different parts of a large shoal and (3) the stresses acting on large fish shoals. To do this, a novel Minimum Energy Flow (MEF) method was developed and applied to extract velocity and force fields driving motion from time-varying density images describing compressible or incompressible motion, such as OAWRS fish population density images.

Observations of fish shoals during the OAWRS 2006 experiment in the Georges Bank were used to confirm general theoretical predictions on group behavior believed to apply in nature irrespective of animal species. By quantifying the formation processes of vast oceanic fish shoals during spawning, it was shown that (1) a rapid transition from disordered to highly synchronized behavior occurs as population density reaches a critical value; (2) organized group migration occurs after this transition; and (3) small sets of leaders significantly influence the actions of much larger groups.

Many species of animals including fish, birds, insects and other self-propelled particles (SPPs) are known to form groups that move in an organized fashion. A fluid dynamic theory was developed to describe collective behavior of animal groups. Starting from the simple behavioral rule that each individual picks the average velocity of all neighbours within its region of perception, we analytically showed that SPP groups behave as a fluid over spatial scales much larger than the mean spacing between individuals. We also analytically showed the existence of a critical population density where each particle needs at least one neighbor within its rgion of perception on average to sustain synchronous motion within the SPP group. It was shown that disturbances can propagate as waves within a group at speeds much higher than that of any individual. These findings may explain how rapid information transfer can occur within animal groups, which may ultimately help maintain long-range order. They also provide an analytic foundation for similar results obtained from numerical simulations, and laboratory and field experiments.

Scattering from extended targets in range-dependent fluctuating ocean waveguides was then studied using bistatic, long-range measurements of acoustic scattered returns from vertically extended, air-filled cylindrical targets made during three distinct OAWRS field experiments. It was shown that Sonar Equation estimates of mean target-scattered intensity lead to large errors, differing by an order of magnitude from both the measurements and waveguide scattering theory. This is because the sonar equation approximation is not applicable to targets large compared to the acoustic wavelength in an ocean waveguide. The use of the Ingenito scattering model was also shown to lead to significant errors in estimating mean target-scattered intensity in the field experiments because they were conducted in range-dependent ocean environments with large variations in sound speed structure over the depth of the targets, scenarios that violate basic assumptions of the Ingenito model. A Greens' theorem based full-field model that describes scattering from vertically extended cylindrical targets in range-dependent ocean waveguides by taking into account nonuniform sound speed structure over the target's depth extent was shown to accurately describe the statistics of the targets' scattered field in all three field experiments. To account for the scintillation in the measured scattered intensity caused by fluctuations of the ocean waveguide, Monte-Carlo simulations of the scattered field were computed by implementing the full-field model in a range-dependent environment randomized by internal waves. Furthermore, the target-scattered returns were shown to have a very different spectral dependence than that of returns from target-like clutter such as fish schools that plague long-range navy sonars operating in continental shelves, so that multi-frequency measurements can be used to distinguish fish from man-made targets.

Measurements of infrasound made during the 2004 Indian Ocean Tsunami event have suggested that large-scale tsunamis may produce deep-infrasonic signals that travel thousands of kilometers in the atmosphere. In this thesis, we presented an analytical model to describe air-borne infrasound generation by tsunamis and show that the mass flow of air caused by changes in sea-level due to a passing tsunami can generate infrasound. The analytical model was then used to quantify deep infrasound (0.01-0.1 Hz) generated by the 2004 Indian Ocean Tsunami, which was shown to be of sufficient amplitude to be picked up thousands of kilometers away, at Diego Garcia island in the Indian Ocean. The pressure level, frequency range and arrival time of the modeled infrasound signal match the corresponding characteristics of the signal measured by an infrasound monitoring station at Diego Garcia Island during the tsunami event. The air-borne acoustic signals are received at Diego Garcia 1 hour and 30 min before the tsunami hits the shore, making it feasible to use infrasound for remotely sensing tsunamis and providing sufficient early warning. The possibility of detecting tsunamis via seismic means was also examined by developing an analytical model for quantifying very low frequency (0.01-0.1 Hz) Rayleigh waves generated by a tsunami. We used the seismic model to predict the Rayleigh wave-induced vertical ground velocity at Diego Garcia Island caused by the Indian Ocean Tsunami. The amplitude of tsunami-induced vertical ground velocity was found to be sensitive to the compression and shear wave speeds in the sea-bottom. For reasonable values of these speeds, it was shown that the tsunami-induced vertical ground velocity amplitudes match measurements made in Diego Garcia. The Rayleigh waves are received at Diego Garcia several hours before the tsunami hits the shore, making tsunami-induced seismic waves a possible modality for remotely sensing tsunamis.

Appendix A

Experimental and theoretical statistics of OAWRS intensity images

In the Ocean Acoustic Waveguide Remote Sensing (OAWRS) experiments of 2003 and 2006 [158, 157] acoustic returns measured by OAWRS were found to obey circular complex Gaussian random (CCGR; [90] field fluctuations following theory [23, 63, 152, 158, 157] and many previous ocean acoustic experiments [64, 145, 75, 213, 13, 243]. The instantaneous intensity I of a CCGR field follows the exponential distribution, while averaged intensity [90] and the log of averaged intensity [152] follow the gamma and exponential-gamma distributions, respectively, with first and second moments that can be analytically expressed in terms of sample size μ and expected intensity I [152]. The standard deviation (SD) of the log of averaged intensity from a CCGR field is

$$\sigma = (10 \log_{10} \mathrm{e}) \sqrt{\zeta(2, \mu)} \tag{A.1}$$

where ζ is Riemann's zeta function, and is approximately given by $\sigma = 4.34\sqrt{1/\mu}$, for $\mu > 3$ [152] so that stationary averaging over μ independent samples asymptotically reduces the SD by $\sqrt{\mu}$, a fact that is exploited in most imaging systems which employ

CCGR fields, including OAWRS, to obtain low-variance images.

In the OAWRS 2003 experiment, the empirically determined SD of the log of averaged intensity from OAWRS imagery is on the order of 1 dB at a given OAWRS pixel. For example, a ~1.3 dB SD is measured for the log of averaged intensity at any pixel, as shown in Fig. A-1A where no large fish groups are present and the scattered returns leading to the observed intensity measurements are consistent with returns from the seafloor. The same ~1.3 dB SD is also measured for OAWRS imaging of a large fish shoal (Fig. A-1B,C). In both cases, the low SD are the result of 10 sample (5 temporal, 2 range) averaging, and closely follow the 1.4 dB theoretically expected from Eq. A.1, as has been noted by Makris et al. [158]. The ~20 dB contrast between fish shoals and background seafloor scattering (Fig. A-1) is much larger than the ~1.3 dB SD, which is low enough to make details in shoal morphology discernable. Log-transformed intensity is used to present OAWRS imagery data since pattern recognition in intensity images formed from CCGR field data is optimized by matching in the log domain where noise is signal-independent and the variance is stabilized [151] by homomorphic transformation. Similar SD for the log of measured intensity in the OAWRS 2006 experiment were obtained by stationary averaging [157]. In the OAWRS 2003 and 2006 experiments, averaged intensity returns from the seafloor exhibited a trend of smooth decay with range (Fig. A-1, Fig. S5 in Ref. [157] following theoretical expectations for uniformly distributed waveguide scatterers [35, 66, 156] and many measurements of seafloor reverberation and transmission in the ocean [35, 154, 231, 99, 104, 208, 213, 13, 157]. The smooth trend is expected because the many independent modal contributions from random propagation and scattering that lead to CCGR field statistics by the central limit theorem (CLT) also lead to a lack of coherent modal interference structure [35, 66, 156, 40, 213, 158, 41]. Randomization of the acoustic field arises from both fluctuations in the water column due to diverse phenomena such as internal waves, eddies, turbulence, boundary roughness at the sea surface and seafloor, as well as fluctuations in the properties of scatterers such as position, aspect and composition.

The instantaneous intensity of conventional fish-finding sonar (CFFS) returns from

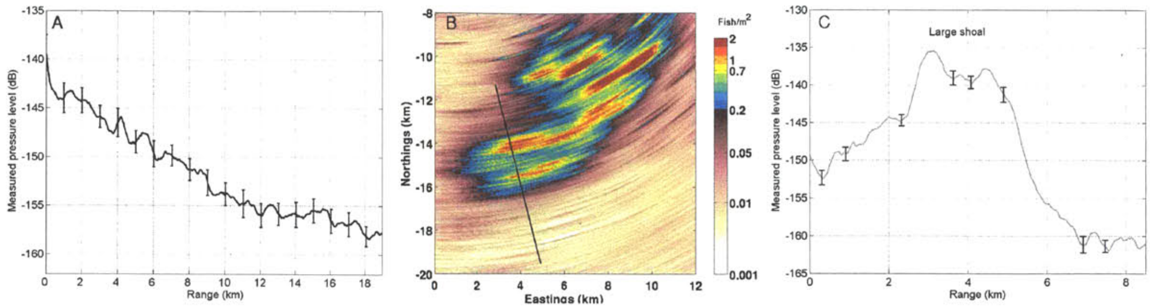

Figure A-1: **(A)** Averaged intensity measured by OAWRS in the absence of prominent fish shoals, normalized to unit source power, from the OAWRS 2003 survey shows a trend of smooth decay with range. Returns are consistent with scattering from the seafloor. Error bars = experimentally determined SD of ~1.3 dB for the standard 10 sample (5-ping and 2-range-cell) intensity average employed in OAWRS 2003. **(B)** Instantaneous OAWRS image of fish population density showing a large fish shoal (10:25 h Eastern daylight time [EDT]; May 14, 2003). Solid black line = transect through the shoal along which averaged intensity is shown in (A). This image is typical of thousands collected during the 2003 OAWRS survey [153]. **(C)** Averaged intensity measured by OAWRS along the transect through a large fish shoal in (B), with experimentally determined SD of ~1.3 dB

fish vary significantly as a function of fish aspect and also follow CCGR statistics [56] as a consequence of the CLT [43]. It has also been noted [152] that as a consequence of the CLT, the same CCGR field, averaged intensity and log averaged intensity statistics are found in CFFS scattering from fish and in ocean-acoustic waveguide transmission scintillation, where stationary averaging is typically needed in all cases to produce low variance images. The 5.6 dB instantaneous intensity SD, for example, is often too high for many imaging applications and is typically reduced by stationary averaging [152].

Appendix B

Expected intensity in OAWRS imaging of fish groups

The expected square magnitude of the field, $\left\langle |\phi_s(\rho_C)|^2 \right\rangle$, proportional to instantaneous intensity, scattered from N independent and identically distributed fish with random position, orientation and scattering properties within the OAWRS resolution footprint of area $A(\rho_C)$, centered at horizontal location ρ_C can be expressed as [14]

$$10\log_{10}\left\langle |\phi_s(\rho_C)|^2 \right\rangle = SL + TLA(\rho_C, z_0, H) + 10\log_{10}\left\langle \left| \frac{S(f)}{k} \right|^2 \right\rangle + 10\log_{10}\langle n_a \rangle \quad \text{(B.1)}$$

where SL is the source level normalization, TLA is a transmission loss area term describing the expected second moment of depth averaged propagation to and from the fish layer integrated over the resolution footprint of the OAWRS system, $S(f)$ is the random scatter function of a fish in the group, k is the acoustic wavenumber, and $\langle n_a \rangle = N/A(\rho_C)$ is the expected areal fish density within the spatially varying resolution footprint.

The third term on the right hand side of Eq. B.1 is defined as the target strength (TS) corresponding to the expected scattering cross section of a fish in the group. The TLA term, a function of center depth z_0 and thickness of the fish layer H, can be expressed as

$$TLA\left(\rho_C, z_0, H\right) = 10\log_{10}\chi\left(\rho_C, z_0, H\right) \tag{B.2}$$

$$\begin{aligned}\chi\left(\rho_C, z_0, H\right) = \int_{A(\rho_C)} A(\rho_C) \int_{z_S=z_0-H/2}^{z_S=z_0+H/2} \iint_{c(\mathbf{r_w}),d(\mathbf{r_w})} (4\pi)^4 \times \\ \left|G\left(\mathbf{r}|\rho_S, z_S; f, c(\mathbf{r_w}), d(\mathbf{r_w})\right) G\left(\rho_S, z_S|\mathbf{r_0}; f, c(\mathbf{r_w}), d(\mathbf{r_w})\right)\right|^2 \times \\ P\left(c(\mathbf{r_w}), d(\mathbf{r_w})\right) P(\rho_S, z_S)\ \mathrm{d}z_S\ \mathrm{d}^2\rho_S\ \mathrm{d}c(\mathbf{r_w})\ \mathrm{d}d(\mathbf{r_w})\end{aligned} \tag{B.3}$$

where $G\left(\mathbf{r}|\rho_S, z_S; f, c(\mathbf{r_w}), d(\mathbf{r_w})\right)$ and $G\left(\rho_S, z_S|\mathbf{r_0}; f, c(\mathbf{r_w}), d(\mathbf{r_w})\right)$ are Green functions describing random waveguide propagation to and from the fish, $P\left(c(\mathbf{r_w}), d(\mathbf{r_w})\right)$ is the joint probability distribution of sound speed c and seawater density d in the water column at any point $\mathbf{r_w}$ in the propagation path and $P(\rho_S, z_S)$ is the probability of finding a fish at (ρ_S, z_S). For a uniform distribution of fish within the OAWRS resolution footprint $P(\rho_S, z_S) = \frac{1}{HA(\rho_C)}$, so that

$$\begin{aligned}\chi\left(\rho_C, z_0, H\right) = \int_{A(\rho_C)} H \int_{z_S=z_0-H/2}^{z_S=z_0+H/2} (4\pi)^4 \left\langle \left|G\left(\mathbf{r}|\rho_S, z_S; f, c(\mathbf{r_w}), d(\mathbf{r_w})\right)\right.\right. \\ \left.\left. G\left(\rho_S, z_S|\mathbf{r_0}; f, c(\mathbf{r_w}), d(\mathbf{r_w})\right)\right|^2 \middle| \rho_S, z_S\right\rangle\ \mathrm{d}z_S\ \mathrm{d}^2\rho_S\end{aligned} \tag{B.4}$$

where the conditional expectation is over the water column sound speed and density random variables.

Appendix C

Transmission loss over the OAWRS resolution footprint

The transmission loss area (TLA) term in Eq. B.1 is computed using the US Navy standard range-dependent acoustic model (RAM) [45] in conjunction with measured oceanographic data including sound speed of the water column and sediment, sediment density and attenuation, and bathymetry.

The TLA computed for all the environments considered in this paper are displayed in Fig. C-1A,B and show the trend of smooth decay with range expected from theory [35, 66, 156, 40], measured seafloor reverberation [Fig. A-1], [80] and past experiments [145, 75, 212, 243]. They also exhibit low SDs of ~1 to 1.5 dB over expected fish shoal depths (Table 1).

To determine TLA, the Green functions in Eq. B.3 are computed with the RAM parabolic equation model [45, 124] for an ocean-acoustic waveguide. The conditional expectation value in Eq. B.3 is determined by averaging 100 Monte-Carlo realizations, where the Green functions are computed along the entire propagation path in range and depth for each realization.

Each Monte-Carlo realization itself employs a different sound speed depth profile every 500 m [40, 13] along the propagation path. Measured sound speed profiles from the OAWRS 2003 experiment (Fig. C-1C) are used to generate TLA in Fig. C-1A, and from the Argo Database [58] (Fig. C-1D) to generate TLA in Fig. C-1B. The SD of TLA over a depth layer H, is defined as

$$\sigma\left(TLA\right) = \sqrt{\frac{1}{H}\int_{z_S=z_0-H/2}^{z_S=z_0+H/2} \left(TLA_0(z) - TLA(H, z_0)\right)^2 \, \mathrm{d}z} \tag{C.1}$$

where

$$TLA_0(z) = 10\log_{10}\int_{A(\rho_C)} (4\pi)^4 \langle |G(\mathbf{r}|\rho_S, z; f, c(\mathbf{r_w}), d(\mathbf{r_w})) \\ G(\rho_S, z|\mathbf{r_0}; f, c(\mathbf{r_w}), d(\mathbf{r_w}))|^2 \,|\rho_S, z\rangle \, \mathrm{d}^2\rho_S \tag{C.2}$$

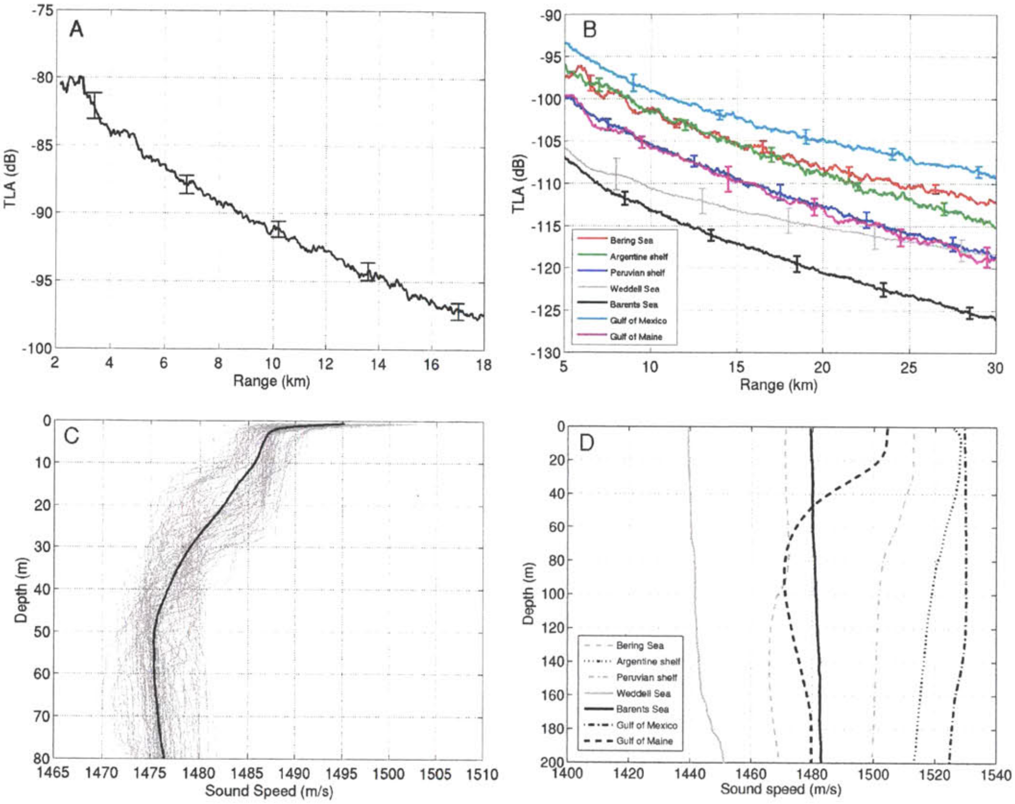

Figure C-1: **(A)** Expected 2-way transmission loss area term (TLA) computed by Monte-Carlo simulation for the OAWRS 2003 experimental environment (continental shelf south of Long Island, NY), for $H = 30$ m and $z_0 = 65$ m where fish shoals were observed by CFFS. Error bars show the TLA SD (σ) of 1 to 1.5 dB over the depths of this fish shoal layer. **(B)** Expected 2-way TLA for the environments considered in "Potential ecosystem exploration" in Chapter 2. For each environment, the mean TLA is computed by averaging over the expected fish shoal depth (Table 1). Error bars indicate the SD in TLA over these depths. The water depths in the different environments are (1) 150 m for Bering Sea, Gulf of Mexico, Peru, Barents Sea, (2) 180 m for Gulf of Maine, and (3) 200 m for Argentina, Antarctica. (c) Sound speed profiles measured during the OAWRS 2003 survey in the continental shelf south of Long Island, NY, and used to compute TLA in (A). **(D)** Measured sound speed profiles for various continental shelf environments [58] used to compute TLA in (B). The environments span the canonical cases of upward refracting (Antarctic), well-mixed (Gulf of Mexico), downward refracting (Peru), and a deep water sound speed minimum (Gulf of Maine).

Appendix D

Empirical estimation of target strength and areal population density from OAWRS data

The target strength (TS) at OAWRS frequencies, $\mathrm{TS}_{\mathrm{OAWRS}}$, is estimated using (1) OAWRS measurements of averaged intensity, (2) modeled TLA, and (3) simultaneous CFFS measurements of number density. Stationary averaging is then employed over hundreds of OAWRS and CFFS samples to obtain a low-variance $\mathrm{TS}_{\mathrm{OAWRS}}$ estimate, using OAWRS fish population density maps such as those shown in Figs. 2-2 and A-1B.

The maximum likelihood estimate (MLE)

$$\widehat{\mathrm{TS}}_{\mathrm{OAWRS}}(\rho_S, f) = 10\log_{10}\left|\frac{\widehat{S(f)}}{k}\right|^2 =$$
$$10\log_{10}\left|\widehat{\phi_s}(\rho_S, f)\right|^2 - 10\log_{10}\hat{\chi}\left(\rho_C, z_0, H, f\right) - 10\log_{10}\widehat{n_a}(\rho_C) - \mathrm{SL} \quad \text{(D.1)}$$

is obtained from invariance of the MLE [133] as prescribed by evaluation of parameters at their corresponding MLEs in Eq. B.1. While the first 2 terms on the right hand side of Eq. D.1 are estimated from OAWRS measurements of averaged intensity (Appendix A) and modeled TLA (Appendix C), respectively, the areal fish number density n_a is estimated from simultaneous CFFS measurements as

$$10\log_{10}\widehat{n_a}(\rho_C) = \widehat{SS}_C(\rho_C) - \widehat{\mathrm{TS}}_C \tag{D.2}$$

where SS_C is CFFS-measured scattering strength and TS_C is the target strength of an individual fish at the CFFS operating frequency.

Table D.1: Standard Deviation (SD) of different terms on the right hand side of Eqs. D.1 and D.2 before and after stationary averaging over OAWRS pixels (n=181). Note that SD of the target strength estimate $\widehat{\mathrm{TS}}_C$ is not affected by averaging over OAWRS data.

Terms in Eqs. D.1 & D.2	SD per OAWRS pixel (dB)	SD after stationary averaging
$10\log_{10}\left\|\widehat{\phi_s}(\rho_S, f)\right\|^2$	1.3	0.09
$10\log_{10}\hat{\chi}(\rho_C, z_0, H, f)$	0.5 to 1	0.07
$\widehat{SS}_C(\rho_C)$	1.5	1.1
$\widehat{\mathrm{TS}}_C$	0.65	0.65
$\widehat{\mathrm{TS}}_{\mathrm{OAWRS}}$	2.3	0.67

We now explain how the SD of the fish target strength estimate at 415 Hz from OAWRS 2003 data shown in Fig. 2-5 was determined and how it is consistent with theory and other measurements. At a given OAWRS 2003 pixel, the variance (i.e. SD^2) of $\widehat{\mathrm{TS}}_{\mathrm{OAWRS}}$ is the sum of the variances of each term on the right hand side of Eq. D.1, given their independence. For the first 2 terms,$10\log_{10}\left|\widehat{\phi_s}(\rho_S, f)\right|^2$ and $10\log_{10}\hat{\chi}(\rho_C, z_0, H, f)$, the SD are 1.3 dB (Appendix A) and 1 dB (Appendix C), respectively. The variance of the third term, $10\log_{10}\widehat{n_a}(\rho_C)$, is the sum of the variances of $\widehat{SS}_C$ and $\widehat{\mathrm{TS}}_C$, given the independence of the terms in Eq. D.2. The SD of $\widehat{SS}_C$ and $\widehat{\mathrm{TS}}_C$ are 1.5 dB and 0.65 dB per OAWRS pixel, respectively, from CFFS measurements made during the OAWRS 2003 experiment. The resulting SD of $\widehat{\mathrm{TS}}_{\mathrm{OAWRS}}$, per OAWRS pixel, is then 2.3 dB.

Estimates of $\mathrm{TS}_{\mathrm{OAWRS}}$ based on many independent OAWRS pixels within regions of statistically stationary fish populations are then averaged to reduce the SD. During the OAWRS 2003 experiment, both OAWRS and CFFS co-registered many fish shoals with statistically stationary populations, such as the one shown in Fig. A-1. The SD of all the terms on the right hand side of Eqs. D.1 and D.2 after stationary averaging over

181 OAWRS samples, obtained within such stationary populations, are summarized in Table D.1. Note that the SD of $\widehat{\mathrm{TS}}_C$ cannot be reduced by averaging OAWRS data because it is assumed not to vary across OAWRS samples. After stationary averaging, the theoretical and empirical SD of 0.67 dB (Table D.1) for $\widehat{\mathrm{TS}}_{\mathrm{OAWRS}}$ agrees well with the empirically determined value of 0.7 dB shown in Table D.2 and Fig. 2-5.

To estimate OAWRS areal number densities over the wide areas shown in Figs. 2-3 and A-1B, Eq. B.1 is again employed by now grouping together all terms except $10\log_{10}\widehat{n_a}(\rho_C)$, and using the empirically estimated $\mathrm{TS}_{\mathrm{OAWRS}}$. Extrapolating $\widehat{\mathrm{TS}}_{\mathrm{OAWRS}}$ in an OAWRS image to spatial locations where there are no CFFS measurements is valid when the fish obey stationary random processes in their spatial distribution and scattering properties. The variance of the OAWRS areal number density, at any given OAWRS pixel, is the sum of the variances of $10\log_{10}\left|\widehat{\phi_s}(\rho_S, f)\right|^2$, and $10\log_{10}\hat{\chi}\left(\rho_C, z_0, H, f\right)$. Using the SD in Tables E1 and E2, OAWRS 2003 estimates of number density then have a SD of 1.5 dB for statistically stationary fish populations.

Table D.2: Empirically estimated target strength (TS) at 415 Hz for OAWRS 2003 experiment. Six transects through statistically stationary fish populations co-registered by OAWRS and CFFS are used to compute the least squares estimate (effectively same as MLE for the given data) and standard deviation of $\widehat{\mathrm{TS}}_{\mathrm{OAWRS}}$. n_v =number density. EDT=Eastern Daylight Time.

Day (May 2003)	Time (EDT)	Transect length through shoal (m)	Average n_v (CFFS) fish/m^3	No. of independent samples (n)	Least squares $\widehat{\mathrm{TS}}_{\mathrm{OAWRS}}$ (dB re 1 m^2 at 415 Hz)
14	12:17	3000	0.04	85	-39.7
14	14:03	3500	0.03	59	-40.1
15	10:08	210	0.02	12	-40.3
15	11:19	105	0.02	6	-40.3
15	12:20	87	0.02	2	-39.8
15	13:19	306	0.02	17	-39.8
				Mean $\widehat{\mathrm{TS}}_{\mathrm{OAWRS}}$	-40.0
				SD $\widehat{\mathrm{TS}}_{\mathrm{OAWRS}}$	0.7

Appendix E

Signal to noise ratio in OAWRS intensity images

The signal to noise ratio (SNR) in OAWRS images is the ratio of the expected scattered intensity from fish to that from the seafloor

$$\mathrm{SNR} = 10 \log_{10} \frac{\left\langle |\phi_S|^2_{\text{fish}} \right\rangle}{\left\langle |\phi_S|^2_{\text{bottom}} \right\rangle} \tag{E.1}$$

Expressions for the second moment of the scattered field from fish groups, $\left\langle |\phi_S|^2_{\text{fish}} \right\rangle$, proportional to the expected scattered intensity, appear in Appendix B. The second moment of the scattered field from the seabottom, $\left\langle |\phi_S|^2_{\text{bottom}} \right\rangle$, depends on seafloor scattering properties. Seafloor scattering has been studied extensively since World War II, and empirical models have been used to describe various field measurements [258]. For most seabottom types, including sand, silt and rocky bottoms, little or no frequency dependence has been measured in seafloor scattering strength over the OAWRS frequencies considered here [258]. Seafloor scattering properties measured recently [80] are used for all continental shelves considered here for a typical sandy bottom. The seafloor returns for all the environments discussed in "Potential ecosystem exploration" section in Chpater 2 are computed by using the scattering model developed in Ref. [80].

Appendix F

Predicting fish TS at low frequencies and estimating physiological parameters from measured TS

The target strength (TS) of pelagic fish with swimbladders has been studied in detail at the frequencies of conventional fish finding sonar (CFFS; 10 kHz to ~200 kHz) both experimentally and with theoretical models. In this regime, several empirical models relating TS to fish length are available [140, 162, 190, 130, 197]. In contrast, limited fish TS data have been collected at lower frequencies (0.01 to 1 kHz) where OAWRS typically operates and swimbladder resonance is found in many species. Indeed OAWRS is among the first systems to provide data at frequencies ≤ 1 kHz, where many strong variations in scattering are expected due to swimbladder resonance according to various models [141, 142]. At such low frequencies, swimbladder scattering becomes effectively omnidirectional so that TS becomes

$$\mathrm{TS} = 10 \log_{10} \left(\frac{\Sigma}{4\pi} \right) \tag{F.1}$$

and the total scattering cross section Σ is directly proportional to the square magnitude of the fish scatter function $S(f)$ and the acoustic wave number via

$$\Sigma = 4\pi \left| \frac{S(f)}{k} \right|^2 \tag{F.2}$$

which depends on swimbladder shape and material properties of the surrounding fish. According to Love's model [141], a US Navy standard, the backscattering cross section, related to the total scattering cross section by $\Sigma_{\text{BS}} = \Sigma/4\pi$, is given by

$$\Sigma_{\text{BS}} = \frac{r^2}{\frac{f_0^2}{f^2}\eta^{-2} + \left(\frac{f_0^2}{f^2} - 1\right)^2} \tag{F.3}$$

where r is the equivalent swimbladder radius (m), f is the insonifying frequency (Hz), f_0 is the swimbladder's resonance frequency (Hz), and η is a dimensionless damping factor. For swimbladders that can be approximated as prolate spheroids, the resonance frequency is given by

$$f_0 = \kappa \frac{1}{2\pi r} \sqrt{\frac{3\gamma P}{d_f}} \tag{F.4}$$

where κ is the dimensionless swimbladder correction factor that Weston [267] obtained using Strasberg's solution for scattering from an oblate spheroid [237], $\gamma = 1.4$ is the ratio of the specific heats of air, P is the ambient pressure (Pa), and d_f is the fish flesh density (kg/m^3) (e.g. for Atlantic herring d_f = 1071 kg/m^3; [176]). The damping factor η is obtained from

$$\frac{1}{\eta} = \frac{2\pi r f^2}{f_0 c} + \frac{\xi}{\pi r^2 f_0 d_f} \tag{F.5}$$

where c is the speed of sound in water (m/s) and ξ is the viscosity of the fish flesh (Pa s) (e.g. empirical value for Atlantic herring: $\xi = 50$ Pa s; [176]).

The swimbladder correction term [267] is

$$\kappa = \frac{\sqrt{2}\,(1-\epsilon^2)^{1/4}}{\epsilon^{1/3}} \left\{ \ln\left[\frac{1+\sqrt{1-\epsilon^2}}{1-\sqrt{1-\epsilon^2}} \right] \right\}^{-1/2} \tag{F.6}$$

where the eccentricity ϵ is the ratio of the minor to major axis of a prolate spheroid.

The volume of the swimbladder is assumed to follow Boyle's Law so that

$$P_0 V_0 = P_z V_z \tag{F.7}$$

where (P_0, V_0) are the ambient pressure and volume at zero depth, and (P_z, V_z) are the pressure and volume at any depth z. For a prolate spheroid, volume is related to the semimajor axis a and semi-minor axis b by

$$V(z) = \frac{4}{3}\pi a^2(z) b \tag{F.8}$$

Fish TS is then modeled (Figs. 2-5, 2-6, 2-8, 2-10, 2-12, 2-14, and 2-16) by assuming the prolate spheroid swimbladder has a major axis that is a constant percentage of total fish length, usually 26 to 33% [91, 176]. Swimbladder volume is assumed to only change through variation in minor axis [27, 189, 190] due to physical constraints in fish anatomy. Given fish length and depth distribution, target strength can be parameterized by a single parameter, swimbladder volume or equivalently neutral buoyancy depth. For OAWRS 2003 analysis, fish length distributions were determined from overnight in situ measurements of individual fish. Measurements were made by CFFS at 38 kHz in the vicinity of the shoals imaged earlier the same day. These TS measurements were then used to calculate the fish mean length, which was found to be approximately 28.6 cm within the OAWRS imaged shoals [162]. Fish depth distribution was also determined from CFFS echograms. For OAWRS 2006, fish length distributions and swimbladder geometries were also obtained from concurrent trawl samples.

The expansion ratio of the minor axis at the surface, $a(0)/a(z_{nb})$, is shown in Fig. F-1 for a range of neutral buoyancy depths z_{nb} typical of physostome fish. For example, a physostome at the surface would have to take in an amount of air corresponding to a doubling of its swimbladder minor axis to achieve neutral buoyancy at a depth of 30 m. However, neutral buoyancy in physostomes occurs down to 60 m depth [248] for which gulping of air is an unlikely mechanism. The neutral buoyancy depth of 78 m, which we obtain by fitting the OAWRS 2003 data with the Love model (Fig. 2-5), suggests that physostome fish such as herring should have mechanisms either for building up gas in their swimbladder, e.g. gas-producing bacteria in their digestive tract, or for damping which lower and spread the resonance and have shallower neutral buoyancy depth.

A shoal will host herring of variable satiety since swimbladder gas content will vary from diffusive loss or gas-production gain mechanisms so that a system making measurements only above 1.0 kHz would not likely be able to determine the corresponding distribution of neutral buoyancy depths within a shoal. Measurements over a range of frequencies at and below resonance for all physiologically plausible neutral buoyancy depths would be necessary.

The TS corresponding to the average scattering cross section of an individual fish at OAWRS operating frequencies is obtained by calibrating OAWRS fish population densities to those calculated from simultaneous in situ CFFS measurements at the spatial locations where simultaneous data in shoals is available (Appendix D). OAWRS TS estimation also requires compensating the received sound pressure-levels for (1) 2-way transmission loss in the range-dependent continental-shelf waveguide; (2) the spatially varying resolution footprint of the OAWRS sourcereceiver system; and (3) source power [158, 13].

For useful concepts about scattering at, or near, swimbladder resonance see Ref. [178] (salmon), Ref. [142] (blue whiting), Ref. [177] (Pacific hake) and Ref. [176] (Atlantic herring), where scattering responses of fish at 100 Hz to 5000 Hz were fit to Love's model.

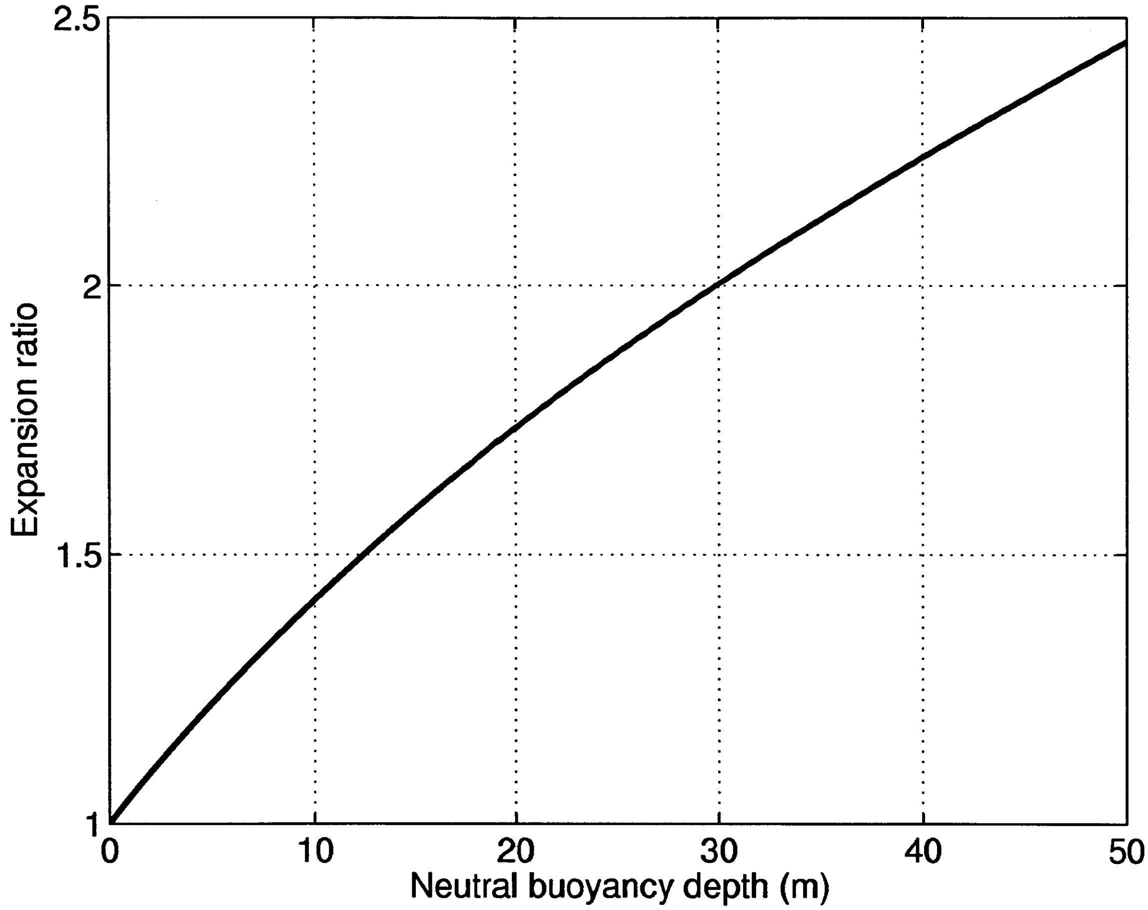

Figure F-1: Expansion ratio of the swimbladder minor axis at the surface as a function of neutral buoyancy depth

Appendix G

Comparison of MEF with the method proposed by Wildes et al.

Here we compare the performance of MEF and the method proposed by Wildes et al. [270], in recovering motion involving large changes in velocity over space. As mentioned in Section 3.2, we expect the latter to "smooth out" large variations, and the former to preserve these variations. For flows that involve small variations in velocity over space, both these methods are expected to perform equally well.

In this section, we quantify the ability of both methods to recover an idealization of a Kármán vortex street [20], which is a good example of a flow with large spatial gradients in velocity, as illustrated in Figure G-1. Such a repeating pattern of swirling vortices is caused by the unsteady separation of flow of a fluid over bluff bodies [20]. Accurately quantifying vortices is important in many fields such as medical imaging of blood flow using MRI where the presence of vortices, for example, indicates blockages of arteries [220]. Here, we have idealized each vortex in Fig. G-1 as a "Lamb-Oseen vortex" [223], which models a line vortex that decays due to viscosity. The tangential velocity of the vortex is given as a function of radius r :

$$V_\theta(r) \quad = \quad (V_{\theta,\mathrm{max}}) \left(1 + \frac{0.5}{\alpha}\right) \frac{r_c}{r} \left[1 - \exp\left(-\frac{\alpha r^2}{r_c^2}\right)\right] \tag{G.1}$$

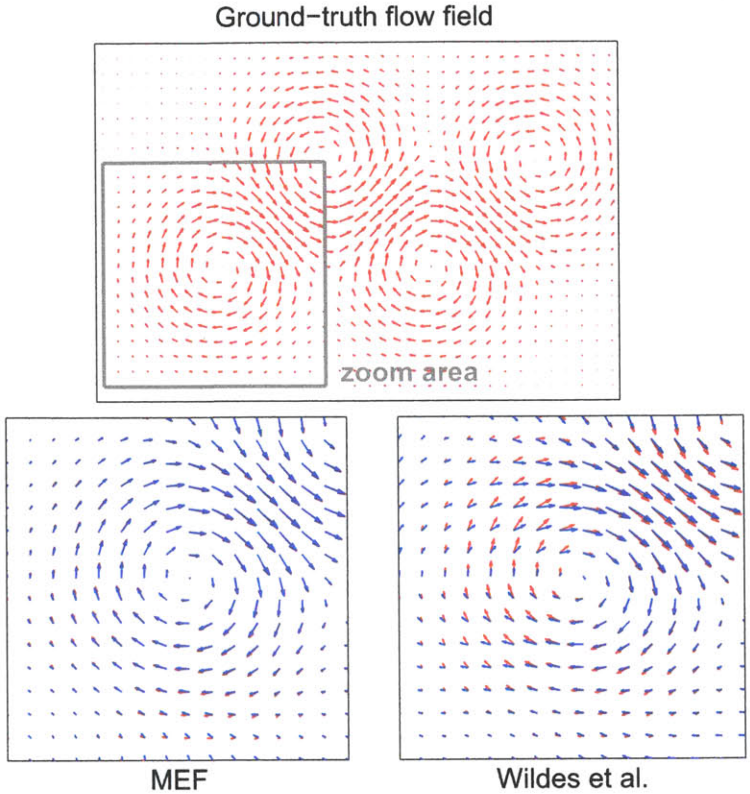

Figure G-1: Comparison of MEF and the method proposed in Ref. [270]. (**A**) Ground-truth flow field - an idealization of a von-Kármán vortex street. (**B**) Comparison between MEF-estimated (blue) and ground-truth mass flows in the zoom region shown in (A). The vectors lie almost on top of each other and the maximum error is ~ 10 %. (**C**) Comparison between flow vectors estimated using the method proposed by Wildes et al. (blue arrows) and the ground-truth vectors (red arrows). There is significant error ($\sim$ 30-40 %) in the estimated vectors.

where $V_{\theta,\text{max}}$ is the peak tangential velocity, α is a viscosity-dependent constant and r_c is the core radius of the vortex. In this example, we have chosen $V_{\theta,\text{max}} = 1$, $\alpha = 1.26$ [60], $r_c = 10$ for each vortex shown in Figure G-1.

In the example we have chosen, the MEF technique recovers the motion to within 10% accuracy except in regions of very low velocity, as can be seen from Figure G-1. This contrasts with the method proposed by Wildes et al., where errors are high (30-40%) even in regions of high velocity (Figure G-1) and shows that the "unsmoothness of flow" criterion chosen in Ref. [270] distorts the flow field in order to make it vary more smoothly than in the actual flow.

Corpetti et al. have employed a more complicated "div-curl minimization" technique [47] to preserve vortices in the flow field, rather than the Principle of Least Action used here. They report errors on the order of 10% [47] when recovering vortices in fluid flow, as we find here for the simpler MEF approach.

Appendix H

Discretization and numerical implementation of MEF

In order to solve Equations 3.8 and 3.9 numerically on a discrete grid, we employ a finite difference method to approximate the partial derivatives.

For this purpose, we use the following "computational stencils:"

$$(\bar{u}_{xx})_{i,j} = \frac{\bar{u}_{i,j+1} - 2\bar{u}_{i,j} + \bar{u}_{i,j-1}}{\epsilon^2} \tag{H.1}$$

$$(\bar{u}_{xy})_{i,j} = \frac{\bar{u}_{i+1,j+1} - \bar{u}_{i-1,j+1} - \bar{u}_{i+1,j-1} + \bar{u}_{i-1,j-1}}{4\epsilon^2} \tag{H.2}$$

$$(\bar{v}_{yy})_{i,j} = \frac{\bar{v}_{i+1,j} - 2\bar{v}_{i,j} + \bar{v}_{i-1,j}}{\epsilon^2} \tag{H.3}$$

$$(\bar{v}_{xy})_{i,j} = \frac{\bar{v}_{i+1,j+1} - \bar{v}_{i-1,j+1} - \bar{v}_{i+1,j-1} + \bar{v}_{i-1,j-1}}{4\epsilon^2} \tag{H.4}$$

where the subscripts i and j are *row* and *column* indices respectively and ϵ is the grid interval.

Replacing the spatial partial derivatives in Equations 3.8 and 3.9 with finite differences and grouping the terms in $\bar{u}_{i,j}$ and $\bar{v}_{i,j}$, we obtain

$$\left(\frac{\lambda}{\rho_{i,j}} + \frac{2}{\epsilon^2}\right)\bar{u}_{i,j} = (\rho_{tx})_{i,j} + \frac{\bar{u}_{i,j-1} + \bar{u}_{i,j+1}}{\epsilon^2} + (\bar{v}_{xy})_{i,j} \tag{H.5}$$

$$\left(\frac{\lambda}{\rho_{i,j}} + \frac{2}{\epsilon^2}\right)\bar{v}_{i,j} = (\rho_{ty})_{i,j} + \frac{\bar{v}_{i-1,j} + \bar{v}_{i+1,j}}{\epsilon^2} + (\bar{u}_{xy})_{i,j} \tag{H.6}$$

Based on equations H.5 and H.6, we suggest an iterative algorithm

$$\left(\frac{\lambda}{\rho_{i,j}} + \frac{2}{\epsilon^2}\right)\bar{u}_{i,j}^{(n+1)} = (\rho_{tx})_{i,j} + \frac{\bar{u}_{i,j-1}^{(n)} + \bar{u}_{i,j+1}^{(n)}}{\epsilon^2} + (\bar{v}_{xy})_{i,j}^{(n)} \tag{H.7}$$

$$\left(\frac{\lambda}{\rho_{i,j}} + \frac{2}{\epsilon^2}\right)\bar{v}_{i,j}^{(n+1)} = (\rho_{ty})_{i,j} + \frac{\bar{v}_{i-1,j}^{(n)} + \bar{v}_{i+1,j}^{(n)}}{\epsilon^2} + (\bar{u}_{xy})_{i,j}^{(n)} \tag{H.8}$$

where the superscripts $(n+1)$ and (n) represent the iteration numbers.

Appendix I

Solving for pressure and force field

In order to solve Equations 3.14 and 3.15, we rewrite them as

$$(f_1)_{yy} = g(x,y,t) + (f_2)_{xy} \tag{I.1}$$

$$(f_2)_{xx} = h(x,y,t) + (f_1)_{xy} \tag{I.2}$$

We now write the spatial derivatives of f_1 and f_2 at each pixel (i,j) using finite differences as

$$((f_1)_{yy})_{i,j} = \frac{(f_1)_{i+1,j} + (f_1)_{i-1,j} - (2f_1)_{i,j}}{\epsilon^2} \tag{I.3}$$

$$((f_1)_{xy})_{i,j} = \frac{(f_1)_{i+1,j+1} + (f_1)_{i-1,j-1} - (f_1)_{i+1,j-1} - (f_1)_{i-1,j+1}}{4\epsilon^2} \tag{I.4}$$

$$((f_2)_{xx})_{i,j} = \frac{(f_2)_{i,j+1} + (f_2)_{i,j-1} - (2f_2)_{i,j}}{\epsilon^2} \tag{I.5}$$

$$((f_2)_{xy})_{i,j} = \frac{(f_2)_{i+1,j+1} + (f_2)_{i-1,j-1} - (f_2)_{i+1,j-1} - (f_2)_{i-1,j+1}}{4\epsilon^2}. \tag{I.6}$$

Based on the above finite difference scheme, we suggest the following iterative procedure

$$(f_1)_{i,j}^{(n+1)} = {}_y\bar{f}_1^{(n)} - \frac{\epsilon^2\left[g_{i,j} + ((f_2)_{xy})_{i,j}^{(n)}\right]}{2} \tag{I.7}$$

$$(f_2)_{i,j}^{(n+1)} = {}_x\bar{f}_2^{(n)} - \frac{\epsilon^2\left[h_{i,j} + ((f_1)_{xy})_{i,j}^{(n)}\right]}{2} \tag{I.8}$$

where

$$_y\bar{f}_1 = \frac{(f_1)_{i+1,j} + (f_1)_{i-1,j}}{2} \tag{I.9}$$

$$_x\bar{f}_2 = \frac{(f_2)_{i,j+1} + (f_2)_{i,j-1}}{2}. \tag{I.10}$$

and n is the iteration number.

Similarly, we rewrite Eq. 3.19 as

$$\nabla^2 p = l(x,y,t) \tag{I.11}$$

and

$$\nabla^2 p_{i,j} = 4\frac{\bar{p}_{i,j} - p_{i,j}}{\epsilon^2} \tag{I.12}$$

where

$$\bar{p}_{i,j} = \frac{p_{i+1,j} + p_{i-1,j} + p_{i,j+1} + p_{i,j-1}}{4}. \tag{I.13}$$

We then suggest the following iterative procedure

$$p_{i,j}^{(n+1)} = \bar{p}_{i,j}^{(n)} - \frac{\epsilon^2 l_{i,j}}{4} \tag{I.14}$$

where n is the iteration number.

Appendix J

Computing ground-truth and MEF velocities and pressures for synthetic image sequences

The following algorithm is followed for computing the ground-truth flow field in Figure 3-3 :

Step 1

Use $\rho^{(1)}$ and $\rho^{(2)}$ along with Equations 3.8 and 3.9 to find $\left(\bar{u}^{(1)}, \bar{v}^{(1)}\right)$. We will assume this to be our ground-truth flow, $\left(\bar{u}_{\text{gt}}^{(1)}, \bar{v}_{\text{gt}}^{(1)}\right)$. Superscripts indicate time-steps.

Step 2

Use $\rho^{(2)}$ and $\rho^{(3)}$ along with Equations 3.8 and 3.9 to find $\left(\bar{u}_{\text{gt}}^{(2)}, \bar{v}_{\text{gt}}^{(2)}\right)$.

Step 3

Use Equation 3.1, $\left(\bar{u}_{\text{gt}}^{(1)}, \bar{v}_{\text{gt}}^{(1)}\right)$, and $\rho^{(1)}$ to compute $\rho^{*(2)}$. Similarly use $\left(\bar{u}_{\text{gt}}^{(2)}, \bar{v}_{\text{gt}}^{(2)}\right)$ and $\rho^{*(2)}$ to compute $\rho^{*(3)}$

Step 4

Compute MEF flow rates, $\left(\bar{u}_{\text{MEF}}^{(1)}, \bar{v}_{\text{MEF}}^{(1)}\right)$ and $\left(\bar{u}_{\text{MEF}}^{(2)}, \bar{v}_{\text{MEF}}^{(2)}\right)$, using density pairs $\left(\rho^{(1)}, \rho^{*(2)}\right)$ and $\left(\rho^{*(2)}, \rho^{*(3)}\right)$ respectively, and Equations 3.8 and 3.9.

Step 5

Use $\left(\bar{u}_{\mathrm{gt}}^{(1)}, \bar{v}_{\mathrm{gt}}^{(1)}\right)$ and $\left(\bar{u}_{\mathrm{gt}}^{(2)}, \bar{v}_{\mathrm{gt}}^{(2)}\right)$ in Equations 3.11 and 3.12 to compute the ground-truth pressure. Assume there is no external forcing.

Step 6

Use $\left(\bar{u}_{\mathrm{MEF}}^{(1)}, \bar{v}_{\mathrm{MEF}}^{(1)}\right)$ and $\left(\bar{u}_{\mathrm{MEF}}^{(2)}, \bar{v}_{\mathrm{MEF}}^{(2)}\right)$ in Equations 3.11 and 3.12 to compute the MEF pressure. Assume there is no external forcing.

Appendix K

Shoal formation during one week of Experiments in Gulf of Maine

The overall process of rapid shoal formation, triggered by attainment of a critical density of 0.2 fish/m^2 near sunset, followed by migration towards spawning grounds, is found to describe a regular diurnal pattern. The pattern was observed on 7 of 7 days in the central region of Georges Bank's northern flank during the herring spawning period, and defined the dominant behavior observed there. In this central region, of the highest historical spawning populations (Fig. 4-4E), OAWRS sampling of the shoal formation process was relatively complete on 5 days, September 28, 29, October 1-3, and fragmentary on 2 days, September 30, Oct 5, due to severe autumn weather or logistical constraints at sea. The diurnal shoal formation pattern was also observed by OAWRS at the south western end of Georges Bank's northern flank on September 26, 27, but mixed with apparent eastward migrations of preexisting shoals in the daytime and at night. Later observations at this southwestern extremity on October 4 revealed little activity, suggesting the herring observed there earlier had migrated eastwards.

Documentation of the shoal formation process for the 5 days in the central region of Georges Bank's northern flank when OAWRS sampling was relatively complete appears in Figs. 4-1 to 4-4 for October 3 and September 29, Figs. K-1 to K-4 for September 28-29 and October 1-2, and Movie S1 of Ref.[157] for October 3. Shoal forming convergence waves, traveling at speeds much greater than herring groups swim, consistently appeared near sunset when a critical density of 0.2 fish/m^2 was attained. This was followed by much slower southern migrations consistent with herring group swimming speeds, as shown in Fig. 4-3 and Figs. K-1- K-4. The waves originated within favored bathymetric contours (160-190 m) from small catalyzing clusters, which acted as sources, and tended to propagate along these contours. This led to the formation of large shoals which often extended for tens of kilometers along the northern flank of Georges Bank as shown in Figs. 4-1 to 4-4. The observed shoal forming waves arose from sequences of local synchronous convergence actions and reactions by members of the shoal, which define propagating compressional waves in a medium of variable density [216]. Such waves have been theoretically predicted to exist in large animal groups [253]. Compressional waves in fish shoals require the propagation of changes in population density and so are inherently different from turning waves [210] which only require the propagation of changes in fish orientation. Our observations show that a small group of leaders initiated shoal formation. Since migration typically occurred sometime after the shoals had already developed, it is not clear that the same leaders responsible for shoal initiation were also responsible for choosing a migration direction. The fact that all migrations were directed towards the spawning ground, however, indicates that the shoal migration directions were not random but were strongly influenced by synchronous spawning behavior.

Population density versus time as shown in Figs. 4-3B-C, K-1D-F, K-2D, K-3B, K-4D-E, is the spatial average over a 0.6 km by 0.6 km patch around the region where the shoal initiates in OAWRS imagery. The two solid lines in these figures, whose slopes indicate the rate of change of population density before and after the transition, are the linear least square fits to data points they span. The slopes before a critical density of 0.2 fish/m^2 is attained are consistently orders of magnitude smaller than those after it is attained. Intersection of these least square lines before and after the transition consistently occurs at 0.2 fish/m^2 when rounded to the nearest tenth. The shoal lengths of Figs. 4-3A, K-1C, K-2C, K-3A, K-4C, were determined from OAWRS imagery by finding the major axis extent of population density features exceeding 0.2 fish/m^2. The migration distances of southern shoal edges were determined by segmenting the shoal edges with a 0.2 fish/m^2 threshold and estimating the mean location of this edge for a given shoal from OAWRS imagery. The lines shown for shoals lengths during formation and migration distances are linear least square fits to the data points of corresponding color.

Our autumn 2006 OAWRS experiment in the Gulf of Maine and Georges Bank employed four research vessels, the RV Oceanus which towed the OAWRS receiving array and collected OAWRS data, the RV Endeavor from which the OAWRS source array was deployed in either moored or drift mode, the RV Hugh Sharp which collected CFFS data, and the RV Delaware II which collected CFFS and trawl data. The RV Delaware II also conducted the National Marine Fisheries Service Annual Fall Herring Survey with traditional methods for measuring the distribution, abundance and behavior of oceanic fish populations [77, 170, 83, 202]. The beamwidth of the CFFS used by RV Hugh Sharp in our field experiment was 7.0° at 38 kHz, which yields a 20 m diameter resolution footprint at 160-m depth where many of the fish groups we imaged were concentrated, while that for the RV Delaware II was 12.0° at 38 kHz (Fig. 4-2A-B) which leads to a 33 m diameter resolution footprint at 160-m depth.

We used the same OAWRS imaging system described in Ref. [158] for all OAWRS measurements presented here, which are the scattered returns of linear frequency modulated (LFM) source waveform transmissions of 50 Hz bandwidth and 1 second duration centered at 950 Hz. Scattered returns at the receiver were beamformed and match filtered leading to a range resolution of 15 m. OAWRS azimuthal resolution in radians varies as the acoustic wavelength λ (1.55 m) divided by the projected array length L$\cos\theta$, where L is the full array length (47.25 m) and the azimuth angle θ is zero at broadside, which is normal to the array axis. While 1 second transmissions were sent every 75 seconds at various non-overlapping frequencies to enable imaging over a 100 km diameter, consecutive LFM transmissions centered at 950 Hz were typically sent only every 150 seconds. All OAWRS images presented here are the averaged returns of 3 consecutive 950 Hz LFM transmissions and two consecutive

15-m range cells to obtain intensity averaged with at least 6 independent samples at each pixel of 30-m dimension. Scattering strength [258] was obtained by correcting the measured beamformed and match filtered pressure level for transmitted level, array beampattern and two-way transmission loss [40, 13] which was determined by parabolic equation modeling [158, 13]. OAWRS incident signals were at least 3 orders of magnitude less intense than those of the CFFS. Population density was estimated from scattering strength by determining the mean fish scattering cross section at the OAWRS frequency necessary for OAWRS and CFFS population densities to match over regions where simultaneous measurements of statistically stationary fish populations were available [158].

An example of the measured pressure level of scattered returns after beamforming and match filtering appears in Fig. K-5A, which is the same data as that presented in Fig. 4-1G before conversion to fish population density. The lack of apparent speckle noise fluctuations in these images is a result of (i) our standard 6-sample intensity average, and (ii) inherent variance reduction from application of the matched filter to fluctuating signals received in an ocean waveguide [13]. The mean measured pressure level along the transect shown in Fig. K-5A appears in Fig. K-5B with experimentally determined standard deviations for our standard 6-sample (3-ping and 2-range-cell) intensity average. These measured standard deviations range from 1.1 to 1.6 dB as shown in Fig. K-5B or 29% to 45% of our standard 6-sample-averaged OAWRS intensity data. These measured standard deviations are consistent with the theory and previous measurements of received circular complex Gaussian field data [158, 90, 152, 151, 154, 212] after matched filtering and intensity averaging [14]. The expected two-way transmission loss (TL) along the Fig. K-5A transect is shown in Fig K-5C, determined from parabolic equation based Monte Carlo modeling with measured bathymetry and oceanography. It is dominated by the two-way cylindrical spreading loss of a waveguide and has small variation over the depths where fish shoals were observed by CFFS (Fig. 4-2). The mean two way TL trend is consistent with that of our measured pressure level in Figs. K-5B where large fish shoals are not found, i.e. ranges other than 9.5-13 km. Statistical analysis of our experimental data shows that the stationary averaging we employed leads to a standard deviation per pixel in the OAWRS population density estimates presented of roughly 1-2 dB in regions where shoal populations follow a stationary random process in space and time consistent with that determined by the simultaneous CFFS measurements needed to determine the expected fish scattering cross-section at OAWRS frequencies. This standard deviation is due to the combined effects of received field fluctuation from transmission, scattering, and source level calibration. We were not able to convert scattering strength to fish population density for the fish groups observed in regions shallower than the 100-m bathymetric contour due to lack of corresponding CFFS measurements of fish depth distributions and population densities in those regions. Fig. 4-4A-D is left in terms of scattering strength because much of the population observed has migrated to depths shallower than 100 m.

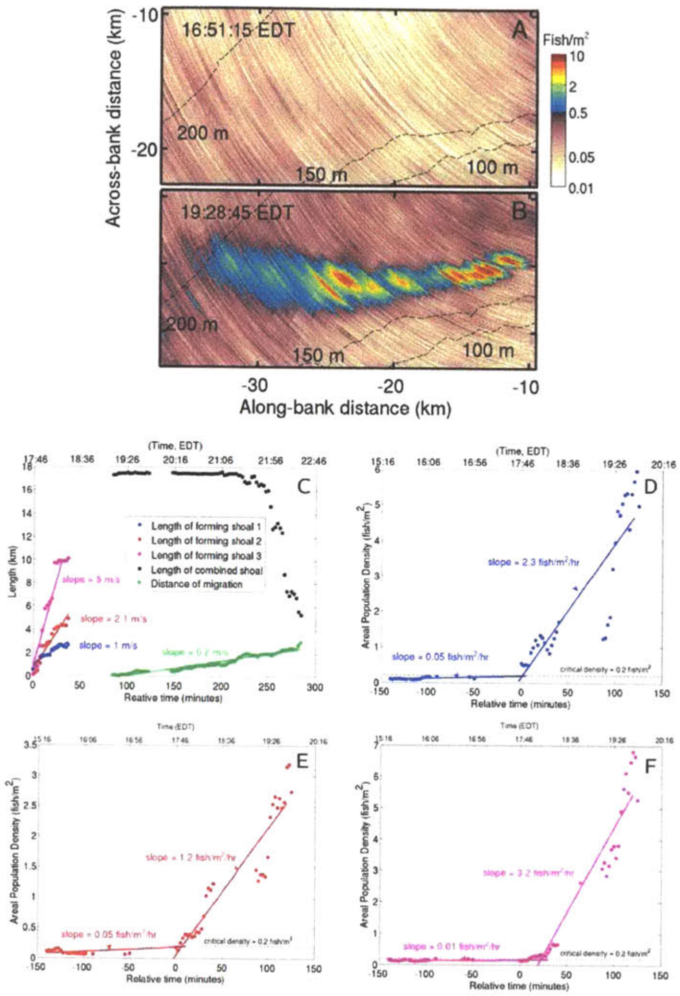

Figure K-1: **(A-B)** OAWRS areal density (fish/m^2) on 2 Oct. 2006 illustrates shoal emergence near sunset, which was at 18:10 EDT. The origin of the coordinate system is at the source location 42.2089°N, 67.6892°W. Spatial location of region imaged is shown in Fig. K-6. **(C)** Shoal length (major axis) and migration distance versus time, including growth and migration speeds on the evening of Oct 2, 2006 from OAWRS imagery data. Shoal 1 (blue) initiates at (-12,-15), Shoal 2 (red) at (-27,-16) and Shoal 3 (magenta) at (-19,-16) in (along-bank, across-bank) coordinates of Fig S1A-B at 17:46 EDT. Magenta, red and blue solid lines are linear best fits for the data points, with slopes indicating shoal forming wave speeds. Shoals 1, 2 and 3 combine between 18:30 EDT and 19:00 EDT. Migration distance of combined shoal southern edge (green points) towards spawning area. Green solid line is linear best fit with slope indicating migration speed. **(D-F)** Mean areal population density versus time for Shoal 1 (blue data), 2 (red data) and 3 (magenta data) over respective 600 m $\times$ 600 m areas about their initiation coordinates from OAWRS imagery. Slow growth in population density before critical density is attained at 17:46 EDT. Immediately afterward density increases rapidly and shoal forming wave initiates.

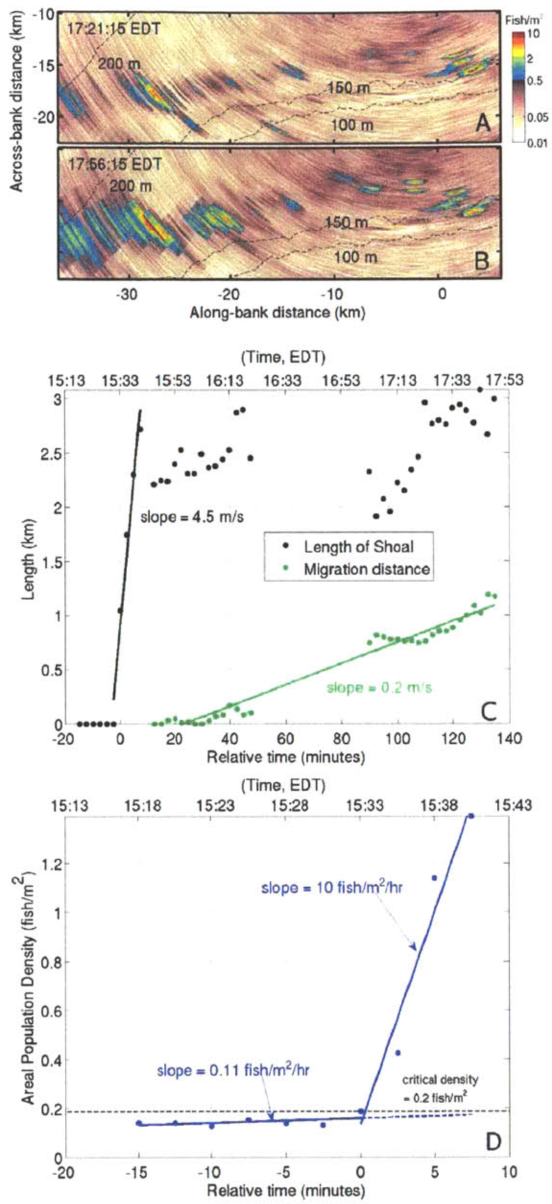

Figure K-2: **(A-B)** OAWRS areal density (fish/m^2) on 1 Oct. 2006 illustrates sparse shoal emergence near sunset, which was at 18:11 EDT. The origin of the coordinate system is at the source location 42.2089°N, 67.6892°W. **(C)** Shoal length (major axis) and migration distance versus time, including growth and migration speeds on the evening of Oct. 1, 2006 from OAWRS imagery data. Shoal initiates at (2,-12) in (along-bank, across-bank) coordinates of Fig. K-2A-B at 15:33 EDT. Black solid line is linear best fit for the data points with slope indicating shoal forming wave speed. Migration distance of the shoal's southern edge (green points) towards spawning area. Green solid line is linear best fit with slope indicating migration speed. **(D)** Mean areal population density of the shoal versus time over a 600 m $\times$ 600 m area about its initiation coordinates from OAWRS imagery. Slow growth in population density before critical density is attained at 15:33 EDT. Immediately afterward density increases rapidly and shoal forming wave initiates.

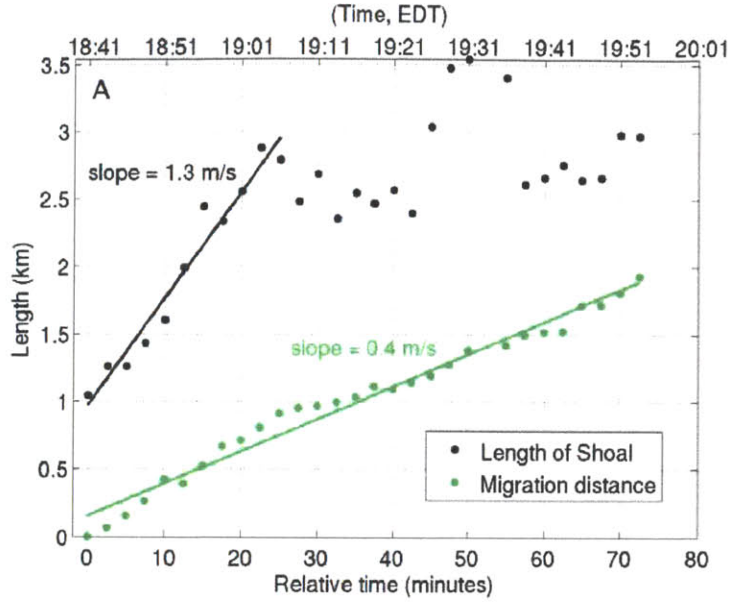

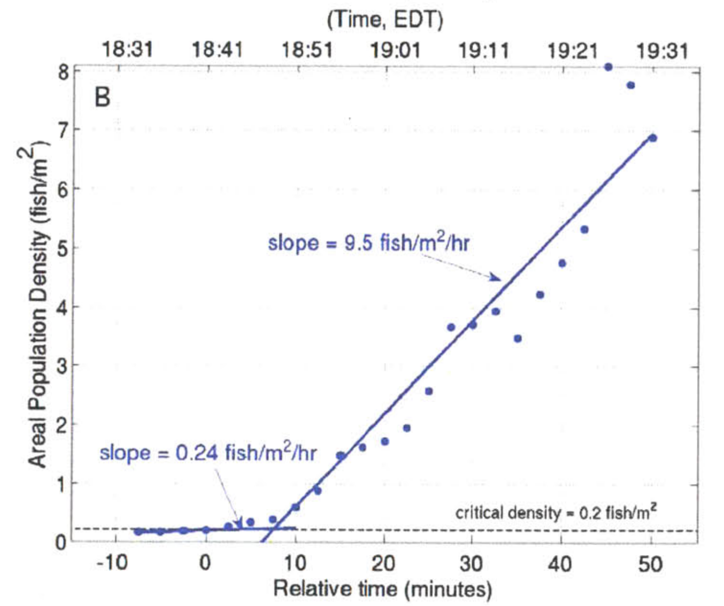

Figure K-3: **(A)** Shoal length (major axis) and migration distance versus time, including growth and migration speeds on the evening of Sept. 29, 2006 from OAWRS imagery data. Shoal initiation was missed due to a data gap. An already initiated shoal of 1 km length passes through (5,-12) in (along-bank, across-bank) coordinates of Fig. 4-4A-D at zero relative time and continues to grow. Black solid line is linear best fit for the data points with slope indicating shoal forming wave speed. Migration distance of the shoal's southern edge (green points) towards spawning area. Green solid line is linear best fit with slope indicating migration speed. (B) Mean areal population density of the shoal versus time over a 600 m $\times$ 600 m area about its southern edge. Slow growth in population density before critical density is attained at 18:51 EDT. Immediately afterward density increases rapidly as shoal forming wave propagates through.

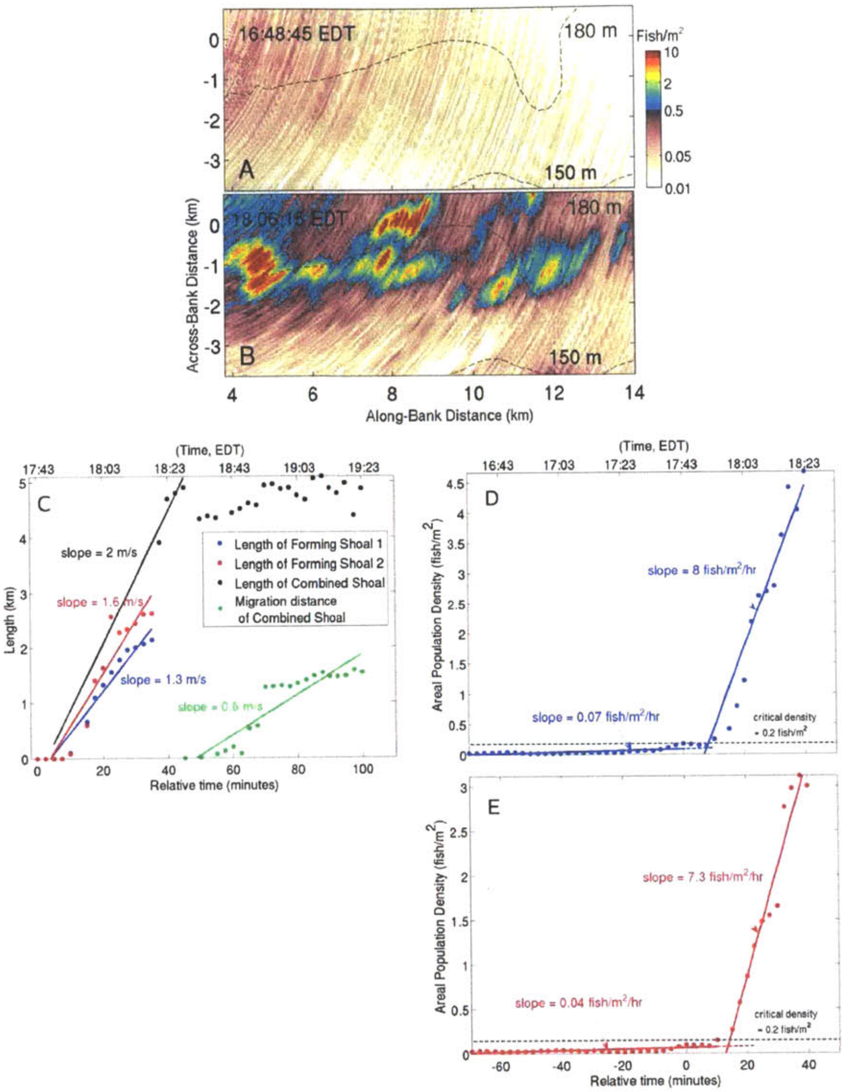

Figure K-4: **(A-B)** OAWRS areal density (fish/m^2) on 28 Sept. 2006 illustrates shoal emergence near sunset, which was at 18:17 EDT. The origin of the coordinate system is at the source location 41.9397°N, 68.1°W. (C) Shoal length (major axis) and migration distance versus time, including growth and migration speeds on the evening of Sept. 28, 2006 from OAWRS imagery data. Shoal 1 (blue) initiates at (10.5,-2) and Shoal 2 (red) at (12,-1.5) in (along-bank, across-bank) coordinates of Fig. K-4A-B at 17:43 EDT. Red and blue solid lines are linear best fits for the data points, with slopes indicating shoal forming wave speeds. Shoals 1 and 2 combine at 18:19 EDT. Migration distance of combined shoal southern edge (green points) towards spawning area. Green solid line is linear best fit with slope indicating migration speed. **(D-E)** Mean areal population density versus time for Shoal 1 (blue data) and 2 (red data) over respective 600 m $\times$ 600 m areas about their initiation coordinates from OAWRS imagery. Slow growth in population density before critical density is attained at 17:43 EDT. Immediately afterward density increases rapidly and shoal forming wave initiates.

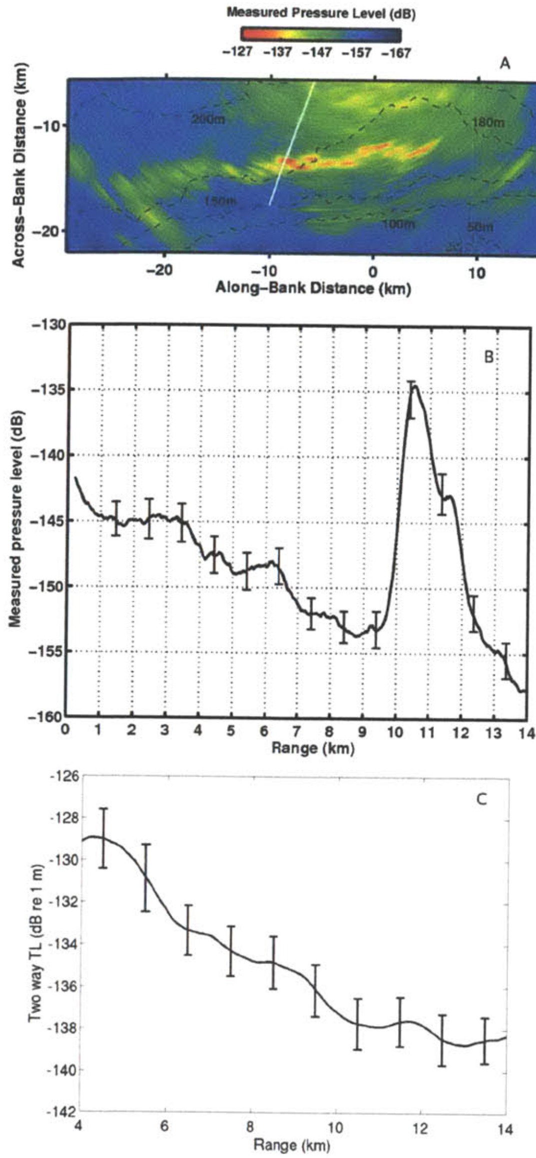

Figure K-5: **(A)** Measured pressure level of scattered returns after beamforming and match filtering in dB re 1 m, normalized to unit source power. Same data as that presented in Fig. 4-1G before conversion to fish population density, with our standard 6- sample (3-ping and 2-range-cell) intensity average. (B) Mean measured pressure level along the transect in Fig. K-5A appears with experimentally determined standard deviations for our standard 6-sample (3-ping and 2-range-cell) intensity average. **(C)** Expected two way transmission loss (TL) along transect in (A) for depth-averaged intensity within 40 m of the seafloor where fish shoals were observed by CFFS (Fig. 4-2). Computed by parabolic equation-based Monte Carlo modeling [13] with measured bathymetry and oceanography. The trend is dominated by two-way cylindrical spreading. Error bars show roughly 1 dB standard deviation of 40-m depth average at given ranges indicating low variation in expected 2-way TL over fish shoal depths observed in Fig. 4-2.

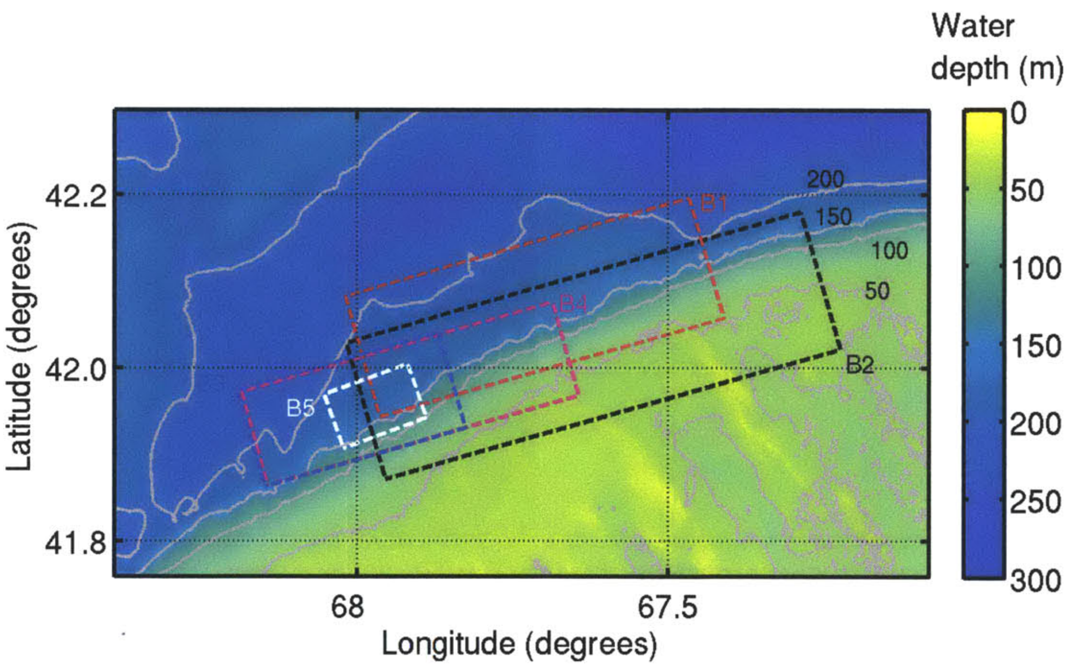

Figure K-6: Georges Bank bathymetry in the region of the OAWRS images shown in Figs. K-1- K-4. Boxes B1 and B2 are regions shown in Fig. 4-1G-L and Fig. 4-4A-D, respectively. Boxes B3, B4 and B5 are regions shown in Figs. K-1A-B, K-2A-B and K-4A-B respectively.

Appendix L

Linear extension of the discrete-time behavioral rule to a continuous-time system

For the average velocity field considered in our analysis, the individual behavioral rule can be written as a convolution of the total velocity $\mathbf{u} = (u, v)$ with a window function:

$$\mathbf{u}(x, y, t+T) = \left[\sum_i \delta(x - x_i(t+T))\delta(y - y_i(t+T))\mathbf{u}_i(t)\right] * W_{sm2}(x, y) \\ * \left[\frac{\Gamma(x, y, L_x, L_y)}{\rho_0 L_x L_y}\right] \quad \text{(L.1)}$$

where Γ is the normalized rectangle function defined in 5.10, and $T > 0$ is the reaction time of each boid. In order to extend the behavioral rule to a continuous sytem, we need to define the velocity evolution for any intermediate time $t + \Delta t$, where $0 \leq \Delta t \leq T$. To do this, we will assume that the velocity changes *linearly* from $\mathbf{u}(x, y, t)$ to $\mathbf{u}(x, y, t+T)$, so that

$$\mathbf{u}(x,y,t+\Delta t) \quad = \quad \mathbf{u}(x,y,t) + \frac{\Delta t}{T}\left[\mathbf{u}(x,y,t+T) - \mathbf{u}(x,y,t)\right]. \tag{L.2}$$

We now try to represent the left hand side of Equation L.2 as a convolution with a window function. Since the right hand side of Equation L.2 is a linear function of Δt, the window function is also assumed to linearly depend of Δt and is represented by $a(x,y) + \frac{\Delta t}{T}b(x,y)$, so that

$$\mathbf{u}(x,y,t+\Delta t) = \left[\sum_i \delta(x - x_i(t+\Delta t))\delta(y - y_i(t+\Delta t))\mathbf{u}_i(t)\right] * \\ \left[a(x,y) + \frac{\Delta t}{T}b(x,y)\right] * W_{sm2}(x,y) \tag{L.3}$$

where a and b are found by matching the initial and final values of $\mathbf{u}$. For $\Delta t = 0$, and using Equations L.2 and L.3 we have

$$\mathbf{u}(x,y,t) \quad = \quad \left[\sum_i \delta(x - x_i(t))\delta(y - y_i(t))\mathbf{u}_i(t)\right] * [a(x,y)] * W_{sm2}(x,y). \tag{L.4}$$

Comparing Equations L.4 and 5.2, we have

$$a(x,y) \quad = \quad \delta(x)\delta(y). \tag{L.5}$$

For $\Delta t = T$, we have

$$\mathbf{u}(x,y,t+T) = \left[\sum_i \delta(x - x_i(t+T))\delta(y - y_i(t+T))\mathbf{u}_i(t)\right] * \\ [a(x,y) + b(x,y)] * W_{sm2}(x,y). \tag{L.6}$$

Comparing Equations L.6 and L.1, we have

$$a(x,y) + b(x,y) = \frac{\Gamma(x,y,L_x,L_y)}{\rho_0 L_x L_y} \tag{L.7}$$

$$\Rightarrow b(x,y) = \frac{\Gamma(x,y,L_x,L_y)}{\rho_0 L_x L_y} - \delta(x)\delta(y). \tag{L.8}$$

Substituting Equations L.5 and L.8 into Equation L.3, we have

$$\mathbf{u}(x,y,t+\Delta t) = \left[\sum_i \delta(x - x_i(t+\Delta t))\delta(y - y_i(t+\Delta t))\mathbf{u}_i(t)\right] * \left[\delta(x)\delta(y) + \frac{\Delta t}{T}\left(\frac{\Gamma(x,y,L_x,L_y)}{\rho_0 L_x L_y} - \delta(x)\delta(y)\right)\right] * W_{sm2}(x,y). \tag{L.9}$$

Appendix M

Decoupled governing equations for the SPP group

The square matrix $[M]$ in Equation 5.27 can be written as

$$[M] \;=\; [S]\,[\Lambda]\,[S]^{-1}, \tag{M.1}$$

where

$$[\Lambda] \;=\; \begin{bmatrix} \lambda_1 & 0 & 0 \\ 0 & \lambda_2 & 0 \\ 0 & 0 & \lambda_3 \end{bmatrix}, \text{ and} \tag{M.2}$$

$$[S] \;=\; \begin{bmatrix} \bar{e}_1 & \bar{e}_2 & \bar{e}_3 \end{bmatrix}. \tag{M.3}$$

Pre-multiplying both sides of Equation 5.27 with $[S]^{-1}$, we have

$$\frac{\partial}{\partial t}\left\{[S]^{-1}\{\bar{a}\}\right\} + [\Lambda]\left\{[S]^{-1}\{\bar{a}\}\right\} \;=\; 0. \tag{M.4}$$

We now define the transformation

$$\left\{\begin{array}{c}\tilde{x}_1\\ \tilde{x}_2\\ \tilde{x}_3\end{array}\right\} \equiv \left\{[S]^{-1}\{\bar{a}\}\right\} \tag{M.5}$$

and substitute in Equation M.4 so that

$$\frac{\partial}{\partial t}\left\{\begin{array}{c}\tilde{x}_1\\ \tilde{x}_2\\ \tilde{x}_3\end{array}\right\} + \begin{bmatrix}\lambda_1 & 0 & 0\\ 0 & \lambda_2 & 0\\ 0 & 0 & \lambda_3\end{bmatrix}\left\{\begin{array}{c}\tilde{x}_1\\ \tilde{x}_2\\ \tilde{x}_3\end{array}\right\}. \tag{M.6}$$

Equation M.6 represents the following set of decoupled equations in the transformed variables $(\tilde{x}_1, \tilde{x}_2, \tilde{x}_3)$:

$$\frac{\partial \tilde{x}_1}{\partial t} + \lambda_1 \tilde{x}_1 = 0 \tag{M.7}$$

$$\frac{\partial \tilde{x}_2}{\partial t} + \lambda_2 \tilde{x}_2 = 0 \tag{M.8}$$

$$\frac{\partial \tilde{x}_3}{\partial t} + \lambda_3 \tilde{x}_3 = 0. \tag{M.9}$$

The general solution for these equations are given by

$$\tilde{x}_1 = \mathrm{e}^{-\lambda_1 t}\tilde{x}_1(t=0) \tag{M.10}$$

$$\tilde{x}_2 = \mathrm{e}^{-\lambda_2 t}\tilde{x}_2(t=0) \tag{M.11}$$

$$\tilde{x}_3 = \mathrm{e}^{-\lambda_3 t}\tilde{x}_3(t=0). \tag{M.12}$$

Appendix N

Critical population density for an initial square-pulse disturbance

The calculations for critical density for an intial Gaussian disturbance in Section 5.4 are repeated here for an initial square-pulse disturbance given by

$$x_i(x, y, t = 0) = \begin{cases} 1, & \text{for } |x|, |y| < 1, \\ 0, & \text{otherwise.} \end{cases} \tag{N.1}$$

The same criticality condition of $\rho_0 L_x L_y > 1$ is seen for linearly stable solutions in x_1, x_2 and x_3.

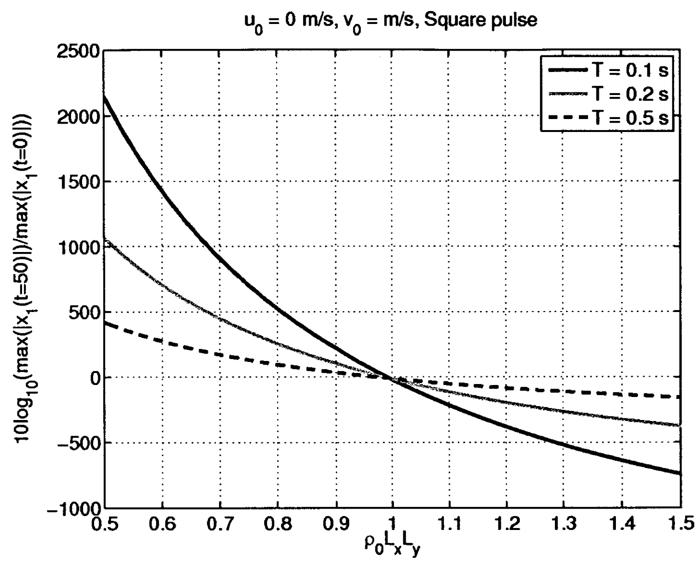

Figure N-1: $10\log_{10}(\max(|x_1(t = 50s)|)/\max(|x_1(t = 0s)|)$ for $u_0 = v_0 = 0$ and for different reaction times $T = 0.1, 0.2, 0.5$ s. The initial disturbance is square-shaped (Equation N.1) and centered at (0,0). The amplitude of the disturbance x_1 after a large time ($t = 50$ s) is lower than its initial amplitude for a critical number of $\rho_0 L_x L_y > 1$, irrespective of the reaction time of the boid. In the sub-critical regime ($\rho_0 L_x L_y < 1$), the amplitude of the disturbance at 50 s has grown much larger than the initial initial amplitude such that the solution is no longer linearly stable and linear theory is no longer valid. The same criticality condition is found to hold for an initial Gaussian disturbance as well.

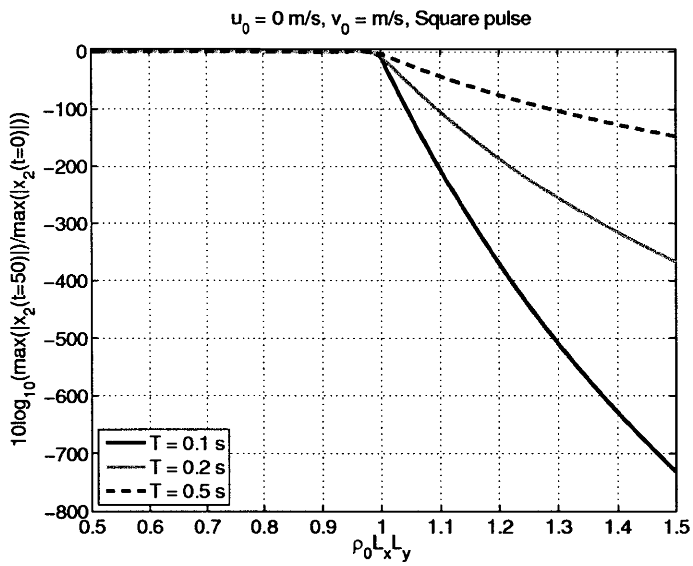

Figure N-2: $10\log_{10}(\max(|x_2(t = 50s)|)/\max(|x_2(t = 0s)|)$ for $u_0 = v_0 = 0$ and for different reaction times $T = 0.1, 0.2, 0.5$ s. The initial disturbance is square-shaped (Equation N.1) and centered at (0,0). The amplitude of the disturbance x_2 after a large time ($t = 50$ s) is lower than its initial amplitude for a critical number of $\rho_0 L_x L_y > 1$, irrespective of the reaction time of the boid. The same criticality condition is found to hold for an initial Gaussian disturbance as well.

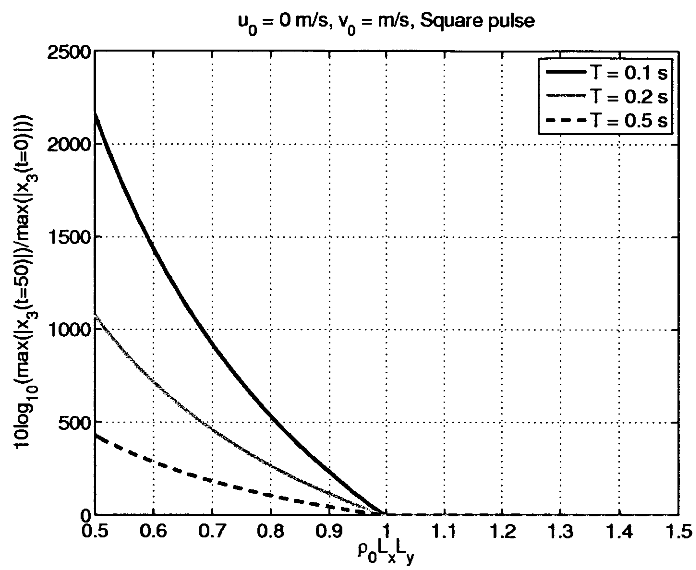

Figure N-3: $10\log_{10}(\max(|x_3(t=50s)|)/\max(|x_3(t=0s)|)$ for $u_0 = v_0 = 0$ and for different reaction times $T = 0.1, 0.2, 0.5$ s. The initial disturbance is square-shaped (Equation N.1) and centered at (0,0). The amplitude of the disturbance x_2 after a large time ($t = 50$ s) does not grow larger than its initial amplitude for a critical number of $\rho_0 L_x L_y > 1$, irrespective of the reaction time of the boid. In the sub-critical regime ($\rho_0 L_x L_y < 1$), the amplitude of the disturbance at 50 s has grown much larger than the initial initial amplitude such that the solution is no longer linearly stable and linear theory is no longer valid. The same criticality condition is found to hold for an initial Gaussian disturbance as well.

Appendix O

Alternate Method for Computing Coefficients A_n

In Ref. [134], the coefficients $A_n(z_t|\mathbf{r_0}, f)$ were estimated using a least squares approach. Here, we obtain exact analytic expressions for the coefficients by exploiting the orthogonality property of the cylindrical modes. From Equation 3 in Ref. [134],

$$P_{\text{scat}}(\rho_t = a, \phi_t, z_t|\mathbf{r_0}, f) = \sum_{n=0}^{\infty} A_n(z_t|\mathbf{r_0}, f)\ \mathrm{H}_n^{(1)}(ka)\ \cos(n\phi_t). \tag{O.1}$$

For a pressure release target the total pressure on its surface is zero and so,

$$P_{\text{scat}}(\rho_t = a, \phi_t, z_t|\mathbf{r_0}, f) = -P_{\text{inc}}(\rho_t = a, \phi_t, z_t|\mathbf{r_0}, f) \tag{O.2}$$

Multiplying both sides by $\cos(m\phi_t)$ and integrating over ϕ_t,

$$\int_{\phi_t=0}^{2\pi} \sum_{n=0}^{\infty} A_n(z_t|\mathbf{r_0}, f)\ \mathrm{H}_n^{(1)}(ka)\ \cos(n\phi_t)\ \cos(m\phi_t)\ \mathrm{d}\phi_t =$$

$$- \int_{\phi_t=0}^{2\pi} P_{\text{inc}}(a, \phi_t, z_t|\mathbf{r_0}, f)\ \cos(m\phi_t)\ \mathrm{d}\phi_t. \tag{O.3}$$

But,

$$\int_{\phi_t=0}^{2\pi} \cos(n\phi_t)\,\cos(m\phi_t)\,\mathrm{d}\phi_t = 0,\ n \neq m$$
$$= \pi,\ n = m \neq 0$$
$$= 2\pi,\ n = m = 0. \tag{O.4}$$

Thus,

$$A_m(z_t|\mathbf{r_0}, f) = \begin{cases} \dfrac{-\int_{\phi_t=0}^{2\pi} P_{\mathrm{inc}}(a,\phi_t,z_t|\mathbf{r_0},f)\,\cos(m\phi_t)\,\mathrm{d}\phi_t}{\pi \mathrm{H}_m^{(1)}(ka)}, & m \neq 0 \\ \dfrac{-\int_{\phi_t=0}^{2\pi} P_{\mathrm{inc}}(a,\phi_t,z_t|\mathbf{r_0},f)\,\mathrm{d}\phi_t}{2\pi \mathrm{H}_0^{(1)}(ka)}, & m = 0. \end{cases} \tag{O.5}$$

Appendix P

Effect of oceanography on arrival structure of target scattered returns

Acoustic returns from targets are either sharp and well-localized or dispersed in sonar imagery (Figure 6-4). It is shown that changes in oceanography, such as the sound speed structure in the water column can cause dispersion in target returns.

The example of target scattering in the New Jersey continental shelf, shown in Figure 6-4D-I, is considered to simulate the matched filter output for different oceanographic conditions. Figure P-1A shows the SMF output (Equation 6.12) for one particular measured sound speed profile (SSPs) used as input in the simulation, where the target is predicted to show up as a sharp, well-localized return. The modal contribution to the total SMF output, also shown in the figure, indicates that most of the energy is concentrated in the first few modes. This figure is comparable with Figure 6-4E, which shows one measured MF output (Equation 6.9) during Track 201 of OAWRS 2003. By using a different SSP, however, the SMF output in Figure P-1B shows a dispersed arrival structure with the acoustic energy being distributed over more number of modes than in Figure P-1A, and is comparable to Figure 6-4H. The significant contributions from higher order modes that arrive later implies that the target appears weaker and poorly-localized in sonar imagery.

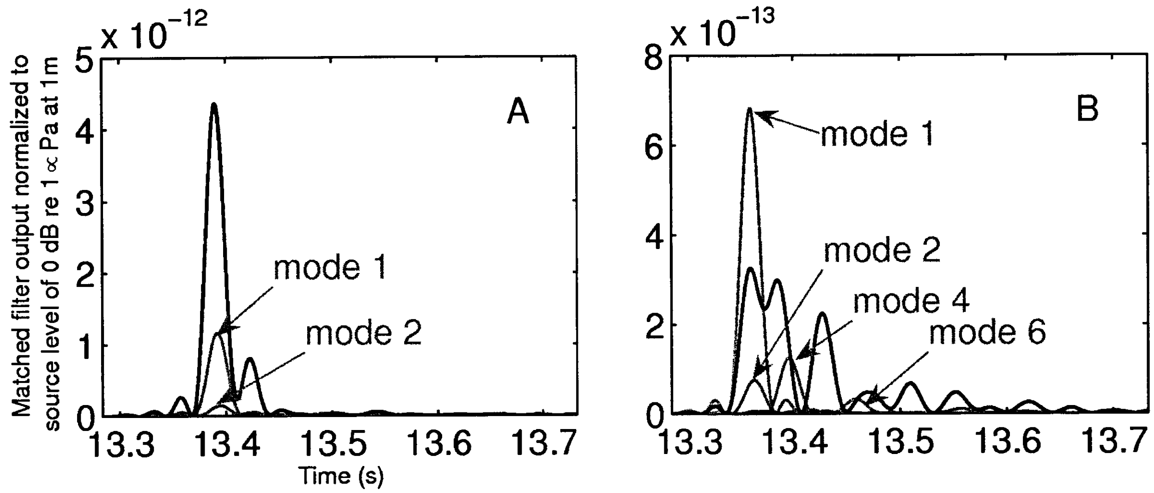

Figure P-1: Scattering from man-made, air-filled cylindrical targets simulated using the VETWS model for different oceanographic conditions in the New Jersey environment. Targets can appear either as strong, well-localized returns or weak, poorly-localized returns after matched-filtering, due to modal dispersion in the ocean waveguide. The Greens' function used in the VETWS model is computed using the KRAKEN normal-mode propagation model. The different dominant acoustic modes are marked in gray. The modes combine either constructively or destructively to form the total scattered return, which is marked in black. (**A**) Example of sharp, well-localized return from target with most of the scattered energy concentrated in the first 2 modes. The first 2 modes have very similar propagation speeds and so arrive almost at the same time at the receiver, resulting in good localization of the man-made target. (**B**) Example of dispersed return from target with scattered energy distributed across more modes than in (A). The same source-receiver-target geometry of (A) was used, but with a different sound speed profile. The higher order modes have lower horizontal propagation speeds and so arrive later at the receiver. The dispersion results in weaker and poorly-localized returns from the man-made target.

Appendix Q

Small Radius Approximation

Computing $P_{\mathrm{inc}}(\mathbf{r_t}|\mathbf{r_0}, f)$ and $G(\mathbf{r}|\mathbf{r}_{\mathrm{t}}, f)$ in Equation 6.3 for every point on the surface of the vertically extended targets, for every single frequency and for every Monte-Carlo realization of the fluctuating ocean environment may be computationally intensive. Here, we present some simplifications to Equation 6.3, based on two assumptions, (1) the far-field assumption and (2) small-radius assumption.

When $\rho_0 \gg \rho_t$, the waveguide Green's function from the source to any point on the target can be written as

$$G(\rho_t, z_t, \phi_t|\mathbf{r_0}; f) = \frac{i}{d(z_0)\sqrt{8\pi\rho_0}} \mathrm{e}^{-i\pi/4} \sum_{n=1}^{\infty} \psi_n(z_0)\psi_n(z_t) \frac{\mathrm{e}^{i\xi_n\rho_0}\mathrm{e}^{i\xi_n\rho_t\cos\phi_t}}{\sqrt{\xi_n}} \tag{Q.1}$$

where ψ_n is the n^{th} mode shape, ξ_n is the horizontal component of the wavenumber vector for the n^{th} mode. The expression above can be written as

$$G(\rho_t, z_t, \phi_t|\mathbf{r_0}; f) = \sum_{n=1}^{\infty} T_n\left(\mathbf{r_0}\right) \psi_n(z_t) \mathrm{e}^{i\xi_n\rho_t\cos\phi_t} \tag{Q.2}$$

where

$$T_n\left(\mathbf{r_0}\right) = \frac{i}{d(z_0)\sqrt{8\pi\xi_n\rho_0}} \psi_n(z_0) \mathrm{e}^{i(\xi_n\rho_0 - \pi/4)}. \tag{Q.3}$$

Since $P_{\text{inc}}(\mathbf{r_t}|\mathbf{r_0}, f) = 4\pi \times G(\rho_t, z_t, \phi_t|\mathbf{r_0}; f)$, we have

$$P_{\text{inc}}(\mathbf{r_t}|\mathbf{r_0}, f) = 4\pi \sum_{n=1}^{\infty} T_n\left(\mathbf{r_0}\right) \psi_n(z_t) \mathrm{e}^{i\xi_n \rho_t \cos\phi_t} \qquad \text{(Q.4)}$$

$$\left.\frac{\partial P_{\text{inc}}(\mathbf{r_t}|\mathbf{r_0})}{\partial \rho_t}\right|_{\rho_t=a} = (4\pi i) \sum_{n=1}^{\infty} \xi_n \cos\phi_t T_n\left(\mathbf{r_0}\right) \psi_n(z_t) \mathrm{e}^{i\xi_n a \cos\phi_t} \qquad \text{(Q.5)}$$

Similarly, the waveguide Green's function from any point on the target to the receiver is given by

$$G(\mathbf{r}|\rho_t, z_t, \phi_t; f) = \sum_{m=1}^{\infty} V_m\left(\mathbf{r}\right) \varphi_m(z_t) \mathrm{e}^{i\xi'_m a \cos\phi_t} \qquad \text{(Q.6)}$$

where

$$V_m\left(\mathbf{r}\right) = \frac{i}{d(0)\sqrt{8\pi\xi'_m \rho}} \varphi_m(z) \mathrm{e}^{i(\xi'_m \rho - \pi/4)}. \qquad \text{(Q.7)}$$

Q.1 The first integral (I_1) in Equation 6.3

Using Equations Q.5 and Q.6 in the first integral (I_1) of Equation 6.3, we have

$$\mathrm{I}_1 = P^{(1)}_{scat}(\mathbf{r}|\mathbf{r_0}, f) =$$
$$-(4\pi i) \sum_{n=1}^{\infty} \sum_{m=1}^{\infty} (\xi_n a) T_n\left(\mathbf{r_0}\right) V_m\left(\mathbf{r}\right) \int_{z_t=-L/2}^{z_t=+L/2} \psi_n(z_t)\varphi_m(z_t) \mathrm{d}z_t \int_{\phi_t=0}^{2\pi} \mathrm{e}^{i(\xi_n+\xi'_m) a \cos\phi_t} \cos\phi_t \mathrm{d}\phi_t \qquad \text{(Q.8)}$$

For $(\xi_n + \xi'_m)\, a \ll 1$ (i.e small-radius approximation), we have

$$\mathrm{I}_1 = P^{(1)}_{scat}(\mathbf{r}|\mathbf{r_0}, f) \approx -(4\pi i) \sum_{n=1}^{\infty} \sum_{m=1}^{\infty} (\xi_n a) T_n\left(\mathbf{r_0}\right) V_m\left(\mathbf{r}\right) \int_{z_t=-L/2}^{z_t=+L/2} \psi_n(z_t)\varphi_m(z_t) \mathrm{d}z_t$$
$$\int_{\phi_t=0}^{2\pi} \left(1 + i\left(\xi_n + \xi'_m\right) a \cos\phi_t\right) \cos\phi_t \mathrm{d}\phi_t$$

$$\begin{aligned} &= -(4\pi i) \sum_{n=1}^{\infty} \sum_{m=1}^{\infty} (\xi_n a)\left(i\left(\xi_n + \xi'_m\right) a\pi\right) T_n\left(\mathbf{r_0}\right) V_m\left(\mathbf{r}\right) \int_{z_t=-L/2}^{z_t=+L/2} \psi_n(z_t)\varphi_m(z_t) \mathrm{d}z_t \\ &= (4\pi^2) \sum_{n=1}^{\infty} \sum_{m=1}^{\infty} (\xi_n a)\left(\left(\xi_n + \xi'_m\right) a\right) T_n(\mathbf{r_0}) V_m(\mathbf{r}) \int_{z_t=-L/2}^{z_t=+L/2} \psi_n(z_t)\varphi_m(z_t) \mathrm{d}z_t. \qquad \text{(Q.9)} \end{aligned}$$

Q.2 The second integral (I_2) in Equation 6.3

Using Equations O.5, B2 and B6 in Equation 6.3, we have

$$I_2 = P^{(2)}_{\rm scat} = \int_{z_t=-L/2}^{+L/2} \int_{\phi_t=0}^{2\pi} \int_{\phi'_t=0}^{2\pi} \sum_{n=0}^{\infty} (4\pi) G(\mathbf{r}|a, z_t, \phi_t) G(a, z_t, \phi'_t|\mathbf{r_0}) \cos(n\phi_t) \cos(n\phi'_t)$$
$$\frac{\left[-k\mathrm{H}^{(1)}_{n+1}(ka) + \frac{n}{a}\mathrm{H}^{(1)}_{n}(ka)\right]}{B_n \pi \mathrm{H}^{(1)}_0(ka)} a \, \mathrm{d}z_t \, \mathrm{d}\phi_t. \quad \text{(Q.10)}$$

$$= -\int_{z_t=-L/2}^{+L/2} \sum_{m=1}^{\infty} \sum_{l=1}^{\infty} (4\pi)(ka) \frac{\mathrm{H}^{(1)}_1(ka)}{2\pi \mathrm{H}^{(1)}_0(ka)} V_m(\mathbf{r}) \varphi_m(z_t) T_l(\mathbf{r_0}) \psi_l(z_t)$$
$$\int_{\phi_t=0}^{2\pi} \mathrm{e}^{i\xi'_m a\cos\phi_t} \mathrm{d}\phi_t \int_{\phi'_t=0}^{2\pi} \mathrm{e}^{i\xi_l a\cos\phi'_t} \mathrm{d}\phi'_t \mathrm{d}z_t$$
$$+ \int_{z_t=-L/2}^{+L/2} \sum_{n=1}^{\infty} \sum_{m=1}^{\infty} \sum_{l=1}^{\infty} (4\pi) V_m(\mathbf{r}) \varphi_m(z_t) T_l(\mathbf{r_0}) \psi_l(z_t) \Omega_n(k, a)$$
$$\int_{\phi_t=0}^{2\pi} \mathrm{e}^{i\xi'_m a\cos\phi_t} \cos(n\phi_t) \mathrm{d}\phi_t \int_{\phi'_t=0}^{2\pi} \mathrm{e}^{i\xi_l a\cos\phi'_t} \cos(n\phi'_t) \mathrm{d}\phi'_t a \mathrm{d}z_t \quad \text{(Q.11)}$$

where

$$\Omega_n(k, a) = \frac{\left[-k\mathrm{H}^{(1)}_{n+1}(ka) + \frac{n}{a}\mathrm{H}^{(1)}_{n}(ka)\right]}{\pi \mathrm{H}^{(1)}_0(ka)} \quad \text{(Q.12)}$$

For $\xi'_m a, \xi_l a \ll 1$, we have

$$I_2 = -\sum_{m=1}^{\infty} \sum_{l=1}^{\infty} T_l(\mathbf{r_0}) V_m(\mathbf{r}) (4\pi)^2 \frac{\bar{k}a}{2} \frac{\mathrm{H}^{(1)}_1(\bar{k}a)}{\mathrm{H}^{(1)}_0(\bar{k}a)} \int_{z_t=-L/2}^{+L/2} \varphi_m(z_t) \psi_l(z_t) \mathrm{d}z_t + \mathrm{O}((\bar{k}a)^3) \quad \text{(Q.13)}$$

In other words, only the zeroth mode ($n = 0$) or "breathing mode" is expected to be dominant for narrow targets. Note that even though $k = 2\pi f/c(z_t)$, its variation over depth is expected to be less than about 3% for shallow water environments, which corresponds to a sound speed variation of 50 m/s, and so $k(z_t) \approx \bar{k}$, the wavenumber corresponding to an average sound speed.

Neglecting higher order terms in $\bar{k}a$, the second term in Equation 6.3 becomes:

$$P^{(2)}_{scat}(\mathbf{r}|\mathbf{r_0}, f) \approx S(\bar{k}a) \int_{z_t=-L/2}^{z_t=+L/2} (4\pi)^2 G(\mathbf{r}|\rho_t = 0, z_t; f) G(\rho_t = 0, z_t|\mathbf{r_0}; f) \, \mathrm{d}z_t \quad \text{(Q.14)}$$

where $\bar{k} = 2\pi f/c(z_t = 0)$ and $S(\bar{k}a) = -(\bar{k}a)\mathrm{H}^{(1)}_1(\bar{k}a)/(2\mathrm{H}^{(1)}_0(\bar{k}a))$ is an effective scattering function for the BBN target.

Q.3 $P^{(2)}_{\mathbf{scat}}(\mathbf{r}|\mathbf{r_0}, f) \gg P^{(1)}_{\mathbf{scat}}(\mathbf{r}|\mathbf{r_0}, f)$

We compare the relative contributions of $P^{(1)}_{\text{scat}}(\mathbf{r}|\mathbf{r_0}, f)$ and $P^{(2)}_{\text{scat}}(\mathbf{r}|\mathbf{r_0}, f)$ to the total scattered field from the target by taking the ratio of Equations Q.9 and Q.13 and neglecting second order terms in $\bar{k}a$. This ratio is given by

$$\frac{P^{(2)}_{\text{scat}}(\mathbf{r}|\mathbf{r_0}, f)}{P^{(1)}_{\text{scat}}(\mathbf{r}|\mathbf{r_0}, f)} \geq \frac{S(\bar{k}a)(4\pi)^2}{2\left(\bar{k}a\right)^2(4\pi^2)}. \quad \text{(Q.15)}$$

Here, we have taken the upper bound of Equation Q.9, by noting that the maximum value of ξ_n and ξ'_m is $\bar{k}$. Therefore,

$$\frac{P^{(2)}_{\text{scat}}(\mathbf{r}|\mathbf{r_0}, f)}{P^{(1)}_{\text{scat}}(\mathbf{r}|\mathbf{r_0}, f)} \geq \frac{\mathrm{H}^{(1)}_1(\bar{k}a)}{(\bar{k}a)\mathrm{H}^{(1)}_0(\bar{k}a)}. \quad \text{(Q.16)}$$

For the targets used in all three experiments and at a frequency of 415 Hz, for example, the ratio in Equation Q.16 is approximately 82 or, in terms of intensity level, 40 dB. So, $P^{(2)}_{\text{scat}}(\mathbf{r}|\mathbf{r_0}, f)$ can be used to approximate the total received scattered return from the target:

$$P_{scat}(\mathbf{r}|\mathbf{r_0}, f) \approx S(\bar{k}a) \int_{z_t=-L/2}^{z_t=+L/2} (4\pi)^2 G(\mathbf{r}|\rho_t = 0, z_t; f) G(\rho_t = 0, z_t|\mathbf{r_0}; f) \, \mathrm{d}z_t \quad \text{(Q.17)}$$

where $\bar{k} = 2\pi f/c(z_t = 0)$ and $S(\bar{k}a) = -(\bar{k}a)\mathrm{H}^{(1)}_1(\bar{k}a)/(2\mathrm{H}^{(1)}_0(\bar{k}a))$ is an effective scattering function for the BBN target.

Appendix R

Effect of Target Tilt on Scattered Returns

In the theoretical formulation (Sec. 6.4.2), we have assumed that the air-filled cylindrical targets remain vertical in the water column. During field measurements, however, there is the possibility that the targets may tilt due to the action of underwater currents.

To quantify the effect of target tilt on target scattered field measurements, the VETWS model, strictly developed for vertically extended targets, is modified to include target tilt. The effect of target tilt on the received scattered level is expected to be maximum when the tilt is in the plane defined by the target/receiver, and the vertical through the target center because, the target beams like a vertical array (Equation 6.16). The modified VETWS model is used to compute the scattered levels as a function of in-plane tilt by averaging Monte-Carlo simulations, following the procedure described in Sec. 6.5.2. The approach is also repeated for different source frequencies.

For illustration, the New Jersey environment is used in our modified-VETWS model simulations, with a monostatic source-receiver configuration. Figure R-2 shows the expected SMF for 415 Hz and 950 Hz as a function of target tilt angle after averaging over N = 50 Monte-Carlo simulations. We find that the average SMF is most sensitive to tilt at the higher frequency of 950 Hz, and least sensitive at 415

Hz. The next step is to quantify the target tilt that we expect in the New Jersey continental shelf.

In the absence of other external biological or man-made disturbances, target-tilt depends on the prevailing underwater currents at the target depth. The tilt, as a function of current speed, shown in Figure R-1, is calculated by balancing the buoyant force of the air-filled target with the current-induced drag force on the target.

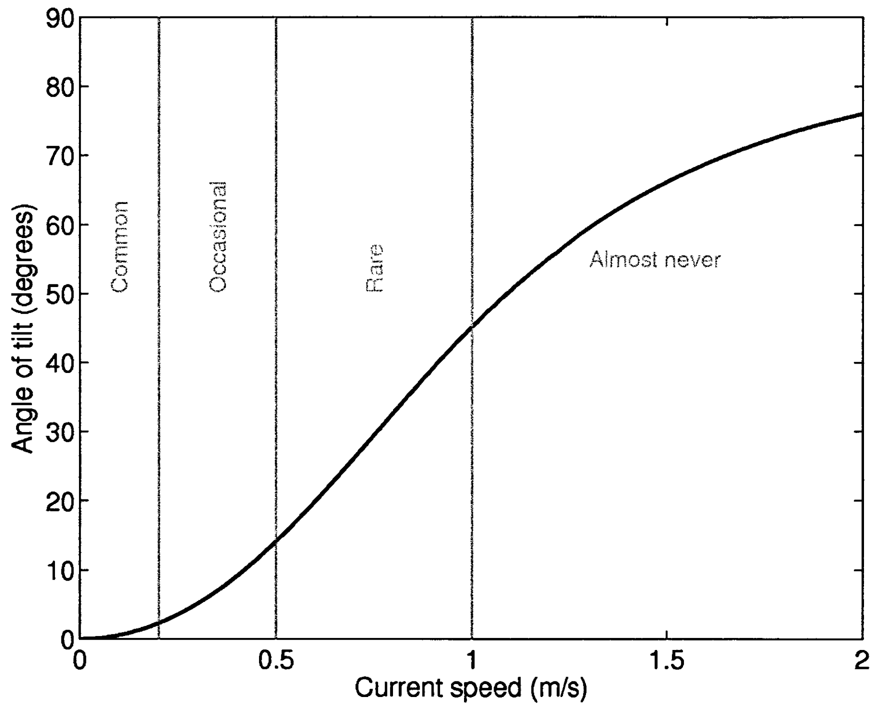

Figure R-1: Expected target tilt as a function of current speed. The target is assumed to tilt in the direction of the current. For usual expected current speeds of 0.1 m/s in all three experiments, tilts of up to 2° are expected. For occasional 0.5-m/s current speeds, tilts of ~12° are expected.

In the New Jersey strataform, the strongest currents are found just off the continental shelf, along the shelf break, at water depths $\geq$ 100 m[5, 53]. During the OAWRS 2001 and OAWRS 2003 experiments, the targets were deployed in much shallower waters on the shelf (water depth $\approx$ 70 m), where current speeds are expected to be low (about 0.1 m/s)[97]. However, occasional episodic incursions of the along-shelf-break currents into shallower waters due to internal waves[97] or Ekman transport[186] have been observed. During such episodes, which can last from about

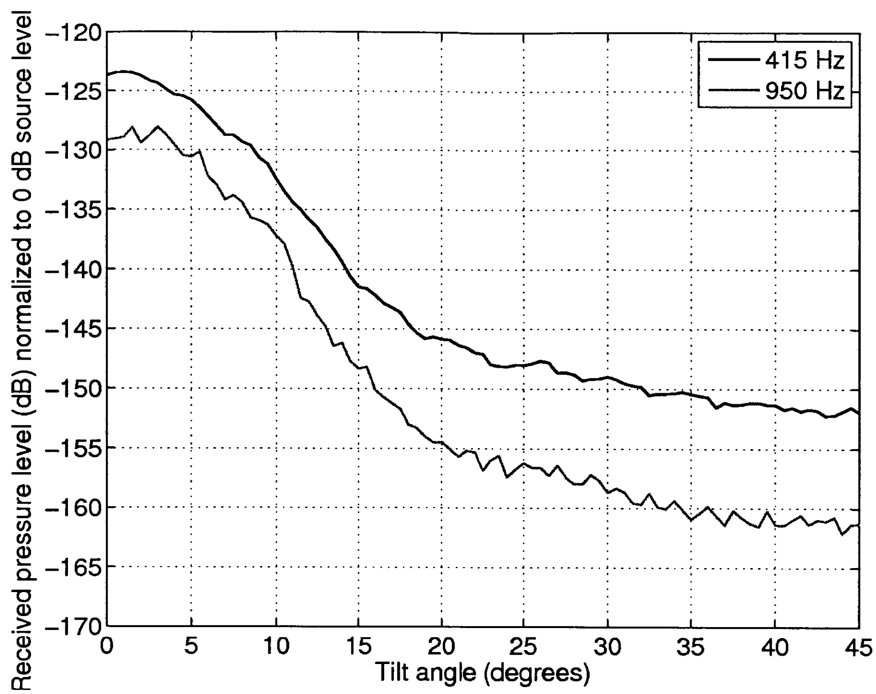

Figure R-2: Effect of target tilt on received pressure levels. Simulations of target-scattered levels, computed using a modified VETWS model described in Section 5.6, as a function of target-tilt angle for two different frequencies used during OAWRS 2003. A monostatic source-receiver configuration as described in Section 5.6 is used. The target is assumed to tilt in the plane formed by the vertical through the target center and the source location. The figure shows that small in-plane tilts of less than 5° do not cause significant change in received levels. For the usual tilts of $\sim 2°$ expected in all three OAWRS experiments (Figure R-1), there is no significant change expected in target-scattered levels.

several hours to a few days[186, 97, 103], the current speeds may go up to 0.5 m/s at target depth[97].

The usual 0.1-m/s current speeds lead to target tilts of ≈ 2 degrees (Fig. R-1), which suggests very small changes in target-scattered levels (Fig. R-2). The occasional 0.5-m/s current speeds however, can result in target tilts of 12 degrees (Fig. R-1), which suggests a reduction in target-scattered levels of 10 dB (Fig. R-2). Such current bursts would then result in a dramatic reduction (10s of dB) in target scattered levels over a period of several hours, a phenomenon that was not observed during both the OAWRS 2001 and OAWRS 2003 experiments.

In the Gulf of Maine though, there exists a steady current along the 100-150 m isobath[5, 53] shown in Fig. 6-2, the deep location of the targets (140-180 m) ensures that current speeds of less than 0.1 m/s prevail at the target depth[5, 53]. For such small current speeds, the target tilts and subsequently its effect on target scattered levels are negligible.

Bibliography

[1] M. Ablain, J. Dorandeu, P. Y. Le Traon, and A.Sladen. High resolution altimetry reveals new characteristics of the december 2004 indian ocean tsunami. *Geophysical Research Letters*, 33:L21602, 6 pp, 2006.

[2] J. D. Achenbach. *Wave Propagation in Elastic Solids.* North-Holland, Amsterdam, 1973.

[3] D. J. Agnew. Critical aspects of the Falkland islands pelagic ecosystem: distribution, spawning and migration of pelagic animals in relation to oil exploration. *Aquatic Conservation: Marine and Freshwater Ecosystems*, 12(1):39–50, 2002.

[4] K. Aki and P. G. Richards. *Quantitative Seismology.* University Science books, CA, USA, 2002.

[5] J. S. Allen, R. C. Beardsley, J. O. Blanton, W. C. Boicort, B. Butman, L. K. Coachman, T. H. Kinder A. Huyer, T. C. Royer, J. D. Schumacher, R. L. Smith, W. Sturges, and C. D. Winant. Physical oceanography of continental shelves. *Rev. Geophys. Space. Phys.*, 21:1149–1181, 1983.

[6] M. K. Alonso, E. A. Crespo, S. N. Pedraza, N. A. Garcia, and M. A. Coscarella. Food habits of the South American sea lion, *Otaria flavescens*, off Patagonia, Argentina. *Fish. Bull. (Wash DC)*, 98:250–263, 2000.

[7] W. Alt and G. Hoffman, editors. *Biological motion.* Springer-Verlag, 1989.

[8] A. Amini. A scalar function formulation for optical flow. *Proc. European Conf. Computer Vision*, pages 125–131, 1994.

[9] P. Anandan. A computational framework and an algorithm for the measurement of visual motion. *J. Comput. Vis.*, 2:283–310, 1989.

[10] I. B. Andreeva. Scattering of sound by air bladders of fish in deep sound-scattering ocean layers. *Akust Zh*, 10:20–24 (English translation in Soviet Phys–Acoust 10:1720), 1964.

[11] I. B. Andreeva. Acoustical characteristics of sonic scattering layers in ocean. In *Proc. 5th Int. Congr. Acoustics, paper E68*, Liége, 1965.

[12] I. B. Andreeva and Y. G. Chindonova. On the nature of soundscattering layers. *Okeanologiya*, 1:112–124, 1964.

[13] Mark Andrews, Tianrun Chen, and Purnima Ratilal. Empirical dependence of acoustic transmission scintillation statistics on bandwidth, frequency, and range in new jersey continental shelf. *The Journal of the Acoustical Society of America*, 125(1):111–124, 2009.

[14] Mark Andrews, Zheng Gong, and Purnima Ratilal. High resolution population density imaging of random scatterers with the matched filtered scattered field variance. *J. Acoust. Soc. Am.*, 126(3):1057–1068, 2009.

[15] P. Athukorala and B. P. Resosudarmo. The Indian Ocean Tsunami: Economic Impact, Disaster Management, and Lessons. *Asian Economic Papers*, 4(1):1–39, 2005.

[16] M. Ballerini, N. Cabibbo, R. Candelier, A. Cavagna, E. Cisbani, I. Giardina, A. Orlandi, G. Parisi, A. Procaccini, M. Viale, and V. Zdravkovic. Empirical investigation of starling flocks: a benchmark study in collective animal behaviour. *Animal behaviour*, 76:201–215, 2008.

[17] R. Balls. Herring fishing with the echometer. *J. Cons. Int. Explor. Mer.*, 15:193–206, 1948.

[18] R. Balls. Environmental changes in herring behavior: a theory of light avoidance, as suggested by echo-sounding observations in the north sea. *J. Cons. Int. Explor. Mer.*, 17:274–198, 1951.

[19] J. Barron, D. Fleet, and S. Beauchemin. Performance of optical flow techniques. *Intl. J. Computer Vision*, 12(1):43–77, 1994.

[20] G. K. Batchelor. *An Introduction to Fluid Dynamics.* Cambridge University Press, Cambridge, 1967.

[21] R. Battiti, E. Amaldi, and C. Koch. Optical Flow across Multiple Scales: An Adaptive Coarse-to-Fine Strategy. *Int. Journal of Computer Vision*, 6(2):133–145, June 1991.

[22] D. Béréziat, I. Herlin, and L. Younes. A generalized optical flow constraint and its physical interpretation. *Proc. Conf. Computer Vision Pattern Recognition*, 2:487–492, 2000.

[23] P. G. Bergmann. Intensity fluctuations. In *The physics of sound in the sea, Part 1: Transmission.* National Defense Research Committee, Washington D.C., 1948.

[24] E. N. Bernard, F. I. González, C. Meinig, and H. B. Milburn. Early detection and real-time reporting of deep-ocean tsunamis. In *ITS 2001 Proceedings, NTHMP Review Session*, volume R-6, pages 97–108, 2001.

[25] R. T. Beyer. *Nonlinear Acoustics.* Acoustical Society of America, New York, 1997.

[26] J. L. Blanco, P. Barra, J. Castillo, and L. P. Atkinson. Response of anchovy (engraulis ringens) off northern chile to the 19971999 el niola nia sequence. *Investig Mar Valparaiso*, 30:107–108, 2002.

[27] J. H. S. Blaxter. The herring swimbladder as a gas reservoir for the acoustico-lateralis system. *J. Mar. Biol. Assoc. UK.*, 59:1–10, 1979.

[28] J. H. S. Blaxter and R. S. Batty. The herring swimbladder: loss and gain of gas. *J Mar Biol Assoc UK*, 64:441–459, 1984.

[29] J. H. S. Blaxter and P. Tytler. Physiology and function of the swimbladder. *Adv. Comp. Physiol. Biochem.*, 7:311–367, 1978.

[30] J.H.S. Blaxter and J.R. Hunter. The biology of the clupeoid fishes. volume 20 of *Advances in Marine Biology*, pages 1 – 223. Academic Press, 1982.

[31] M. Bouchon, E. Daz, S. Cahuin, and M. Ochoa. Effects of el niño 1997-98 on the schooling behaviour of the peruvian anchovy (engraulis ringens). *Investig Mar Valparaiso*, 30:182–183, 2002.

[32] V. M. Brawn. Physical properties and hydrostatic function of the swimbladder of herring (clupea harengus l.). *J. Fish. Res. Board Can.*, 19:635–656, 1962.

[33] L. M. Brekhovskikh and Y. P. Lysanov. *Fundamentals of ocean acoustics*. Wave phenomena. Springer-Verlag, Heidelberg, 1991.

[34] H. I. Browman and K. I. Stergiou. Marine protected areas as a central element of ecosystem-based management: defining their location, size and number. *Mar. Ecol. Prog. Ser.*, 274:271–272, 2004.

[35] H. Bucker. Sound propagation in a channel with lossy boundaries. *J. Acoust. Soc. Am.*, 48:1187–1194, 1970.

[36] Michael J. Buckingham and Alexandra Tolstoy. An analytical solution for benchmark problem 1: The "ideal" wedge. *J. Acoust. Soc. Am.*, 87(4):1511–1513, 1990.

[37] J. Buhl, D. J. T. Sumpter, I. D. Couzin J. Hale, E. Despland, E. Miller, and S. J. Simpson. From disorder to order in marching locusts. *Science*, 312:1402–1406, 2006.

[38] A. Cascorbi and H. Chabot. Seafood report. tunas, vol ii: Atlantic bluefin tuna, northeast region. final report. Seafood report 2, Monterey Bay Aquarium, Monterey, CA, July 19 2004.

[39] M. C. Cassia. Age and growth of the southern blue whiting micromesistius australis in the sw atlantic. *Scientia Marina*, 64:269–274, 2000.

[40] T. Chen, P. Ratilal, and N. C. Makris. Mean and variance of the forward field propagated through three-dimensional random internal waves in a continental-shelf waveguide. *J. Acoust. Soc. Am.*, 118:3560–3574, 2005.

[41] T. Chen, P. Ratilal, and N. C. Makris. Temporal coherence after multiple forward scattering through random three dimensional inhomogeneities in an ocean waveguide. *J. Acoust. Soc. Am.*, 124:2812–2822, 2008.

[42] Y. Cherel, S. Waugh, and S. Hanchet. Albatross predation of juvenile southern blue whiting on campbell plateau. *N Z J. Mar. Freshw. Res.*, 33:437–441, 1999.

[43] C. S. Clay and H. Medwin. *Acoustical oceanography: principles and applications.* John Wiley & Sons, 1977.

[44] M. D. Collins. Benchmark calculations for higher-order parabolic equations. *J. Acoust. Soc. Am.*, 87:1535–1538, 1990.

[45] M. D. Collins. A split padé solution for the parabolic equation method. *J. Acoust. Soc. Am.*, 93:1736–1742, 1993.

[46] Stephane G Conti and David A Demer. Wide-bandwidth acoustical characterization of anchovy and sardine from reverberation measurements in an echoic tank. *ICES J. Mar. Sci.*, 60(3):617–624, 2003.

[47] T. Corpetti, D. Heitz, G. Arroyo, E. Mémin, and A. Santa-Cruz. Fluid experimental flow estimation based on an optical-flow scheme. *Experiments in Fluids*, 4:80–97, 2006.

[48] I. D. Couzin, J. Krause, N. R. Franks, and S. A. Levin. Effective leadership and decision making in animal groups on the move. *Nature*, 433:513–516, 2005.

[49] I. D. Couzin, J. Krause, R. James, G. D. Ruxton, and N. R. Franks. Collective memory and spatial sorting in animal groups. *J. Theor. Biol.*, 218:1–11, 2002.

[50] I.D. Couzin and J. Krause. Self-organization and collective behavior in vertebrates. *Advances in the Study of Behavior*, 32:1–75, 2003.

[51] M. J. Crocker. *Handbook of Acoustics.* John Wiley & Sons, New York, 1998.

[52] D. P. Croft, J. Krause, I. D. Couzin, and T. J. Pitcher. When fish shoals meet: outcomes for evolution and fisheries. *Fish and Fisheries*, 4(2):138–146, 2003.

[53] G. T. Csanady. On the theories that underlie our understanding of continental shelf circulation. *J. Oceanography*, 53:207–229, 1997.

[54] P. Cury, L. Shannon, and Y. J. Shin. The functioning of marine ecosystems, Accessed 26 Feb 2009 at ftp://ftp.fao.org/fi/document/reykjavik/pdf/07Cury.pdf. In *Reykjavik Conf. on Responsible Fisheries in the Marine Ecosystem*, Reykjavik, Iceland, 1-4 Oct 2001.

[55] A. Czirók, A. Barabási, and T. Vicsek. Collective motion of self-propelled particles: kinetic phase transition in one dimension. *Phys. Rev. Lett.*, 82:209–212, 1999.

[56] P. Dahl and O. Mathisen. Measurement of fish target strength and associated directivity at high frequencies. *J. Acoust. Soc. Am.*, 73:1205–1211, 1983.

[57] G. Danuser and C. M. Waterman-Storer. Quantitative fluorescent speckle microscopy: where it came from and where it is going. *J. Microscopy.*, 211:191–207, 2003.

[58] Argo Database. International argo project. http://www.argo.ucsd.edu, Accessed 20 May, 2009.

[59] P.L.M. de Maupertuis. Accord de différentes lois de la nature qui avaient jusquíci paru incompatibles. *Mém. As. Sc. Paris*, page 417, 1744.

[60] W. J. Devenport, M. C. Rife, S. I. Liapis, and G.J. Follin. The structure and development of a wing-tip vortex. *Journal of Fluid Mechanics*, 312:67–106, 1996.

[61] V. Devlaminck and Dubus J.-P. Estimation of compressible or incompressible deformable motions for density images. *Proc. International Conf. Image Processing*, 1:125–128, 1996.

[62] D. A. Dwyer, K. M. Bailey, and P. A. Livingston. Feeding habits and daily ration of walleye pollock (theragra chalcogramma) in the eastern bering sea, with special reference to cannibalism. *Can. J. Fish. Aquat. Sci.*, 44:1972–1984, 1987.

[63] I. Dyer. Statistics of sound propagation in the ocean. *J. Acoust. Soc. Am.*, 48:337–345, 1970.

[64] F. Dyson, W. Munk, and B. Zetler. Interpretation of multipath scintillations to eleuthera to bermuda in terms of internal waves and tides. *J. Acoust. Soc. Am.*, 59:1121–1133, 1976.

[65] L.G. Ekatarina, M.I. Maxim, I. A. Fazly, and J.R. McIntosh. Force production by disassembling microtubules. *Nature*, 438:384–388, 2005.

[66] D. Ellis. A shallow-water normal-mode reverberation model. *J. Acoust. Soc. Am.*, 97:2804–2814, 1995.

[67] W. Enkelmann. Investigation of Multigrid Algorithms for the Estimation of Optical Flow Fields in Image Sequences. *CVGIP(43)*, 2:150–177, 1998.

[68] M. Ewing and J. L. Worzel. Long range sound transmission. *Geol. Soc. Am. Mem.*, 27, 1948.

[69] W. M. Ewing, W. S. Jardetsky, and F. Press. *Elastic Waves in Layered Media.* McGraw-Hill, New York, 1957.

[70] D. M. Farmer, M. V. Trevorrow, and B. Pedersen. Intermediate range fish detection with a 12 kHz sidescan sonar. *J. Acoust. Soc. Am.*, 106:24812490, 1999.

[71] J. Fitzpatrick. A method for calculating fluid flow in time dependent images based on the continuity equation. *Proc. IEEE Conf. Comput. Vision, Pattern Recog. (CVPR-85), San Francisco, CA*, pages 78–81, 1985.

[72] D. J. Fleet and A. D. Jepson. Computation of component image velocity from local phase information. *Intl. J. Computer Vision*, 5:77–104, 1990.

[73] FAO (Food and Agriculture Organisation). Review of the state of world aquaculture. Technical Report FAO Fisheries Circular No. 886, Rev. 1, FAO, Rome, 1997.

[74] FAO (Food and Agriculture Organisation). Species fact sheets. merluccius hubbsi (marini, 1933), accessed feb 26, 2009 at www.fao.org/fishery/species/3027. Technical report, FAO, FAO Fisheries & Aquaculture, Rome, 2009.

[75] A. Fredricks, J. A. Colosi, J. F. Lynch, G. Gawarkiewicz, C. S. Chiu, and P. Abbot. Analysis of multipath scintillations from long range acoustic transmissions on the New England continental slope and shelf. *J. Acoust. Soc. Am.*, 117:1038–1057, 2005.

[76] S. Freeman. *Biological Science*, chapter Cell Division, page 155. Prentice Hall, Upper Saddle River, NJ, 2002.

[77] P. Freon and O. A. Misund. *Dynamics of pelagic fish distribution and behavior: effects on fisheries and stock assessment.* Fishing news books. Blackwell Publishing, Oxford, 1999.

[78] G. V. Frisk. *Ocean and seabed acoustics: a theory of wave propagation.* Prentice Hall, Upper Saddle River, NJ, 1994.

[79] R. Froese and D. Pauly. www.fishbase.org/summary/speciessummary.php?id=252&cfid=56355689&cftoken=78718322, Accessed 26 Feb, 2009.

[80] A. Galinde, N. Donabed, M. Andrews, S. Lee, N. C. Makris, and P. Ratilal. Range-dependent waveguide scattering model calibrated for bottom reverberation in a continental shelf environment. *J. Acoust. Soc. Am.*, 123:1270–1281, 2008.

[81] S. M. Garcia and K. L. Cochrane. Fisheries topics. governance. the ecosystem approach to fisheries management. Technical report, FAO, FAO Fisheries & Aquaculture, Rome, Accessed 27 May 2009 at www.fao.org/fishery/topic/13261/en.

[82] S. Gauhtier and J. K. Horne. Acoustic characteristics of forage fish species in the Gulf of Alaska and Bering Sea based on Kirchoff approximation models. *Can. J. Fish. Aquat. Sci.*, 61:1839–1850, 2004.

[83] F. Gerlotto, M. Soria, and P. Freon. From two dimensions to three: the use of multibeam sonar for a new approach in fisheries acoustics. *Can. J. Fish. Aquat. Sci.*, 56(1):6–12, 1999.

[84] K. E. Gilbert and X. Di. A fast green's function method for one-way sound propagation in the atmosphere. *J. Acoust. Soc. Am.*, 94(4):2343–2352, 1993.

[85] H. Gjosaeter. The population biology and exploitation of capelin (Mallotus villosus) in the Barents Sea. *Sarsia*, 83:453–496, 1998.

[86] O. R. Godø. *The future of fisheries science in North America*, chapter Technology answers to the requirements set by the ecosystem approach, pages 373–403. Fish and Fisheries series, Vol 31. Springer Science and Business Media B.V., Heidelberg, 2009.

[87] O. R. Godø, V. Hjellvik, S. A. Iversen, A. Slotte, E. Tenningen, and T. Torkelsen. Behaviour of mackerel schools during summer feeding migration in the Norwegian Sea, as observed from fishing vessel sonars. *ICES J. Mar. Sci.*, 61(7):1093–1099, 2004.

[88] J. A. Goff, B. J. Kraft, L. A. Mayer, S. G. Schock, C. K. Sommerfield, H. C. Olson, S. P. S. Gulick, and S. Nordfjord. Seabed characterization on the New Jersey middle and outer shelf: correlatability and spatial variability of seafloor sediment properties. *Marine Geology*, 209:147–172, 2004.

[89] Z. Gong, M. Andrews, S. Jagannathan, R. Patel, J. M. Jech, N. C. Makris, and P. Ratilal. Low-frequency target strength and abundance of shoaling Atlantic herring (Clupea harengus) in the Gulf of Maine during the Ocean Acoustic Waveguide Remote Sensing 2006 Experiment. *J. Acoust. Soc. Am.*, 127:104–123, 2010.

[90] J. W. Goodman. *Statistical Optics.* Wiley, New York, 1985.

[91] N. Gorska and E. Ona. Modeling the effect of swimbladder compression on the acoustic backscattering from herring at normal or near-normal dorsal incidences. *ICEA J. Mar. Sci.*, 60:1381–1391, 2003.

[92] J. Graves. Photographic method for measuring spacing and density within anchovy, Engraulis mordox, school groups. *Fish. Bull. (Wash. DC)*, 75:679–685, 1977.

[93] K. M. Gray. Intercellular communication and group behavior in bacteria. *Trends in Microbiology*, 5:184–188, 1997.

[94] G. Grégoire and H. Chaté. Onset of collective and cohesive motion. *Phys. Rev. Lett.*, 92(2):025702, Jan 2004.

[95] T. Guerrero, K. Sanders, E. Castillo, Y. Zhang, L. Bidaut, T. Pan, and R. Komaki. Dynamic ventialtion imaging from four-dimensional computed tomography. *Physics in Medicine and Biology*, 51(4):777–791, 2006.

[96] M. Gutierrez, G. Swartzman, A. Bertrand, and S. Bertrand. Anchovy (Engraulis ringens) and sardine (Sardinops sagax) spatial dynamics and aggregation patterns in the Humboldt Current ecosystem, Peru, from 19832003. *Fish. Oceanogr.*, 16:155–168, 2007.

[97] Z. R. Hallock and R. L. Field. Internal-wave energy fluxes on the New Jersey shelf. *J. Phys. Oceanography*, 35:3–12, 2005.

[98] W. J. Hamilton. *Animal Orientation and Navigation*, pages 57–71. Oregon State Univ. Press, Corvallis, 1967.

[99] A. J. Harding, M. A. H. Hedlin, and J. A. Orcutt. Migration of backscatter data from the Mid-Atlantic Ridge. *J. Acoust. Soc. Am.*, 103:1787–1803, 1998.

[100] D. J. Heeger. Optical flow using spatiotemporal filters. *Intern. J. Comput. Vis.*, 1:279–302, 1988.

[101] J. B. Hersey, R. Backus, and J. Hellwig. Sound-scattering spectra of deep scattering layers in the Western North Atlantic Ocean. *Deep Sea Res.*, 8:196–210, 1962.

[102] J. B. Hersey and R. H. Backus. *The sea, Vol 1*, chapter Sound scattering by marine organisms, page Chapter 13. Interscience Publications, New York, 1962.

[103] A. E. Hill. Leakage of barotropic slope currents onto the continental shelf. *J. Phys. Oceanography*, 25:1617–1621, 1995.

[104] P. C. Hines, D. V. Crowe, and D. D. Ellis. Extracting in-plane bistatic scattering information from a monostatic experiment. *J. Acoust. Soc. Am.*, 104:758–768, 1998.

[105] D. J. Hoare, G. D. Ruxton, J.-G. J. Godin, and J. Krause. The social organization of free-ranging fish shoals. *Oikos*, 89(3):546–554, 2000.

[106] D. Holliday and H. Larsen. Thickness and depth distribution of some epipelagic fish schools off southern California. *Fish. Bull. (Wash DC)*, 77:489–494, 1979.

[107] A. B. Hollowed, C. D. Wilson, P. J. Stabeno, and S. A. Salo. Effect of ocean conditions on the cross-shelf distribution of walleye pollock (Theragra chalcogramma) and capelin (Mallotus villosus). *Fish. Oceanogr.*, 16:142–154, 2007.

[108] B. Horn and B. Schunk. Determining Optical Flow. *Artificial Intelligence*, 17:185–203, 1981.

[109] C. C. Hsu, H. C. Liu, C. L. Wu, S. T. Huang, and H. K. Liao. New information on age composition and length-weight relationship of bluefin tuna, Thunnus thynnus, in the southwestern North Pacific. *Fish. Sci.*, 66:485–493, 2000.

[110] M. E. Huntley and M. Zhou. Influence of animals on turbulence in the sea. *Mar. Ecol. Prog. Ser.*, 273:65–79, 2004.

[111] I. Huse and E. Ona. Tilt angle distribution and swimming speed of overwintering Norwegian spring spawning herring. *ICES J. Mar. Sci.*, 53:863–873, 1996.

[112] A. Huth and C. Wissel. *Biological motion*, chapter The movement of fish schools: a simulation model. Springer-Verlag, 1989.

[113] F. Ingenito. Scattering from an object in a stratified medium. *J. Acoust. Soc. Am.*, 82:2051–2059, 1987.

[114] S. Inoue and E. D. Salmon. Force Generation by Microtubule Assembly/Disassembly in Mitosis and Related Movements. *Mol. Biol. Cell*, 6(12):1619–1640, 1995.

[115] S. Inoue and H. Sato. Cell motility by labile association of molecules: the nature of mitotic spindle fibers and their role in chromosome movement. *J. Gen. Physiol.*, 50:259–292, 1967.

[116] J. D. Isaacs and R. A. Schwartzlose. Migrant sound scatterers: interaction with the sea floor. *Science*, 150:1810–1813, 1965.

[117] T. Itoh, S. Tsuji, and A. Nitta. Migration patterns of young Pacific bluefin tuna (Thunnus orientalis) determined with archival tags. *Fish. Bull. (Wash. DC)*, 101:514–534, 2003.

[118] G. D. Jackson, N. G. Buxton, and M. J. A. George. Diet of the southern opah Lampris immaculatus on the Patagonian shelf; the significance of the squid Morotenthis ingens and anthropogenic plastic. *Mar. Ecol. Prog. Ser.*, 206:261–271, 2000.

[119] J. B. C. Jackson, M. X. Kirby, W. H. Berger, K. A. Bjorndal, L. W. Botsford, B. J. Bourque, R. H. Bradbury, R. Cooke, J. Erlandson, J. A. Estes, T. P. Hughes, S. Kidwell, C. B. Lange, H. S. Lenihan, J. M. Pandolfi, C. H. Peterson, R. S. Steneck, M. J. Tegner, and R. R. Warner. Historical overfishing and the recent collapse of coastal ecosystems. *Science*, 293:629–637, 2001.

[120] S. Jagannathan, I. Bertsatos, D. Symonds, H. T. Nia, A. Jain, M. Andrews, Z. Gong, R. Nero, L. Ngor, M. Jech, O. R. Godø, S. Lee, P. Ratilal, and N. Makris. Ocean Acoustic Waveguide Remote Sensing (OAWRS) of Marine Ecosystems. *Mar. Ecol. Prog. Ser.*, 365:137, 2009.

[121] S. Jagannathan, B. K. P. Horn, P. Ratilal, and N. C. Makris. Force estimation and prediction from time-varying density images. *IEEE Trans. Pattern Anal. Mach. Intell.*, page in press, 2010.

[122] J. M. Jech and W. L. Michaels. A multifrequency method to classify and evaluate fisheries acoustics data. *Can. J. Fish. Aquat. Sci.*, 63(10):2225–2235, 2006.

[123] F. B. Jensen and C. M. Ferla. Numerical solutions of rangedependent benchmark problems in ocean acoustics. *J. Acoust. Soc. Am.*, 87:1499–1510, 1990.

[124] F. B. Jensen, W. A. Kuperman, M. B. Porter, and H. Schmidt. *Computational ocean acoustics*. Springer-Verlag, New York, 2000.

[125] F. R. H. Jones and N. B. Marshall. The structure and functions of the teleostean swimbladder. *Biol. Rev. Camb. Philos. Soc.*, 28:16–82, 1953.

[126] R. Jorgensen. The effects of swimbladder size, condition and gonads on the acoustic target strength of mature capelin. *ICES J. Mar. Sci.*, 60:1056–1062, 2003.

[127] R. Jorgensen. *The effects of behaviour on the acoustic target strength of capelin (Mallotus villosus) and implications for acoustic abundance estimation.* Dr. Sci. dissertation, Norwegian College of Fishery Science, University of Tromso, 2004.

[128] S. A. Gauthreaux Jr. and C. G. Belser. Radar ornithology and biological conservation. *Auk*, 120:266–277, 2003.

[129] S. A. Gauthreaux Jr. and C. G. Belser. Radar ornithology and conservation of migratory birds. Technical report, USDA Forest Service General Technical Report 191: 871875, 2005.

[130] D. Kang, K. Sadayasu, T. Mukai, K. Iida, D. Hwang, K. Sawada, and K. Miyashita. Target strength estimation of black porgy *Acanthopagrus schlegeli* using acoustic measurements and a scattering model. *Fish. Sci.*, 70:819–828, 2004.

[131] M. Kardar. *Statistical Physics of Particles.* Cambridge University Press, 2007.

[132] K.E. Kasza, A.C. Rowat, J. Liu, T.E. Angelini, C.P. Brangwynne, G.H. Koenderink, and D.E. Weitz. The cell as a material. *Current Opinion in Cell Biology*, 19:101–107, 2007.

[133] S. M. Kay. *Fundamentals of statistical signal processing.* McGraw-Hill, New York, 1993.

[134] E. T. Küsel and P. Ratilal. Effects of incident field refraction on scattered field from vertically extended cylindrical targets in range-dependent ocean waveguides. *J. Acoust. Soc. Am.*, 125:1930–1936, 2009.

[135] L. D. Landau and E. M. Lifshitz. *Mechanics.* Pergammon Press, 1976.

[136] Thorne Lay, Hiroo Kanamori, Charles J. Ammon, Meredith Nettles, Steven N. Ward, Richard C. Aster, Susan L. Beck, Susan L. Bilek, Michael R. Brudzinski, Rhett Butler, Heather R. DeShon, Goran Ekstrom, Kenji Satake, and Stuart Sipkin. The Great Sumatra-Andaman Earthquake of 26 December 2004. *Science*, 308(5725):1127–1133, 2005.

[137] N. Levanon. *Radar Principles.* Wiley, New York, 1988.

[138] J. S. Link and J. Burnett. The relationship between stomach contents and maturity state for major northwest Atlantic fishes: new paradigms? *Journal of Fish BIology*, 59(4):783–794, 2001.

[139] H. Lodish, A. Berk, P. Matsudaira, C. A. Kaiser, M. Krieger, M.P. Scott, S.L. Zipursky, and J. Darnell. *Molecular Cell Biology.* Freeman and Company, New York, 2004.

[140] R. H. Love. Dorsal-aspect target strength of an individual fish. *J. Acoust. Soc. Am.*, 49:816–823, 1971.

[141] R. H. Love. Resonant acoustic scattering by swimbladder-bearing fish. *J. Acoust. Soc. Am.*, 64:571–580, 1978.

[142] R. H. Love. A comparison of volume scattering strength data with model calculations based on quasisynoptically collected fishery data. *J. Acoust. Soc. Am.*, 94:2255–2268, 1993.

[143] B. Lucas and T. Kanade. An iterative image registration technique with an application to stereo vision. *Proc. DARPA Image understanding workshop*, pages 121–130, 1981.

[144] M. E. Lutcavage, R. W. Brill, G. B. Skomal, B. C. Chase, J. L. Goldstein, and J. Tutein. Tracking adult north atlantic bluefin tuna (Thunnus thynnus) in

the northwestern Atlantic using ultrasonic telemetry. *Mar. Biol.*, 137:347–358, 2000.

[145] J. F. Lynch, A. E. Newhall, B. Sperry, G. Gawarkiewicz, A. Fredricks, P. Tyack, C. S. Chiu, and P. Abbot. Spatial and temporal variation in acoustic propagation characteristics at the New England shelfbreak front. *IEEE J. Oceanic Eng.*, 28:129–150, 2003.

[146] G. J. Macchi and M. Pajaro. Batch fecundity and spawning frequency of southern blue whiting (Micromesistius australis) in the southwest Atlantic ocean. *N Z J. Mar. Freshw. Res.*, 39:993–1000, 2005.

[147] G. J. Macchi, M. Pajaro, and C. Dato. Spatial variation of the Argentine hake (Merluccius hubbsi (Marini, 1933)) spawning shoals in the patagonian area during a reproductive Season. *Rev. Biol. Mar. Oceanogr.*, 42:345–356, 2007.

[148] S. Mackinson. Variation in structure and distribution of pre-spawning pacific herring shoals in two regions of british columbia. *Journal of Fish Biology*, 55(5):972–989, 1999.

[149] D. N. Maclennan, P. G. Fernandes, and J. Dalen. A consistent approach to definitions and symbols in fisheries acoustics. *ICES J. Mar. Sci.*, 59(2):365–369, 2002.

[150] D. N. MacLennan and E. J. Simmonds. *Fisheries Acoustics.* Chapman & Hall, London, 1992.

[151] N. C. Makris. A foundation for logarithmic measures of fluctuating intensity in pattern recognition. *Opt. Lett.*, 20:2012–2014, 1995.

[152] N. C. Makris. The effect of saturated transmission scintillation on ocean acoustic intensity measurements. *J. Acoust. Soc. Am.*, 100:769–783, 1996.

[153] N. C. Makris. Geoclutter acoustics experiment 2003 cruise report. Technical report, Massachusetts Institute of Technology, Cambridge, MA, 2003.

[154] N. C. Makris, L. Z. Avelino, and R. Menis. Deterministic reverberation from ocean ridges. *J. Acoust. Soc. Am.*, 97:3547–3574, 1995.

[155] N. C. Makris and J. M. Berkson. Long-range backscatter from the Mid-Atlantic Ridge. *J. Acoust. Soc. Am.*, 95:1865–1881, 1994.

[156] N. C. Makris and P. Ratilal. A unified model for reverberation and submerged object scattering in a stratified ocean waveguide. *J. Acoust. Soc. Am.*, 109:909–941, 2001.

[157] N. C. Makris, P. Ratilal, S. Jagannathan, Z. Gong, M. Andrews, I. Bertsatos, O. R. Godø, R. W. Nero, and J. M. Jech. Critical population density triggers rapid shoal formation in vast oceanic fish shoals. *Science*, 332:1734–1737, 2009.

[158] N. C. Makris, P. Ratilal, D. T. Symonds, S. Jagannathan, S. Lee, and R. W. Nero. Fish population and behavior revealed by instantaneous continental shelf-scale imaging. *Science*, 311:660–663, 2006.

[159] C. I. Malme. Development of a high target strength passive acoustic reflector for low-frequency sonar applications. *IEEE J. Ocean. Eng.*, 19:438–448, 1994.

[160] J. R. Marshall and R. P. Chapman. Reverberation from a deep scattering layer measured with explosive sound sources. *J. Acoust. Soc. Am.*, 36:164–167, 1964.

[161] N. B. Marshall. Bathypelagic fishes as sound scatterers in the ocean. *J. Mar. Res.*, 10:1–17, 1951.

[162] S. McClatchie, J. Alsop, and R. F. Coombs. A re-evaluation of relationships between fish size, acoustic frequency, and target strength. *ICES J. Mar. Sci.*, 53:780–791, 1996.

[163] S. McClatchie, G. Macauley, S. Hanchet, and R. F. Coombs. Target strength of southern blue whiting (Micromesistius australis) using swimbladder modelling, split beam and deconvolution. *ICES J. Mar. Sci.*, 55:482–493, 1998.

[164] H. Medwin. *Sounds in the Sea.* Cambridge University Press, Cambridge, 2005.

[165] H. Medwin and C. Clay. *Fundamentals of acoustical oceanography.* Academic Press, Boston, 1998.

[166] D. Metaxas and D. Terzopoulos. Shape and nonrigid motion and structure. *IEEE Trans. Pattern Anal. Mach. Intell.*, 15(6):580, 1993.

[167] H. B. Milburn, A. I. Nakamura, and F. I. Gonzalez. Real-time tsunami reporting from the deep ocean. In *Proceedings of the Oceans 96 MTS/IEEE Conference*, pages 390–394, Sep. 23-26 1996.

[168] M. Milinski. *Predation Risk and Feeding Behaviour*, chapter The Behaviour of Teleost Fishes, pages 285–305. Chapman and Hall, London, 1993.

[169] O. A. Misund. Underwater acoustics in marine fisheries and fisheries research. *Fish. Biol.*, 7:1–34, 1997.

[170] O. A. Misund, A. Aglen, and E. Froenaes. Mapping the shape, size, and density of fish schools by echo integration and a high-resolution sonar. *ICES J. Mar. Sci.*, 52(1):11–20, 1995.

[171] P. M. Morse and K. U. Ingard. *Theoretical Acoustics.* McGraw-Hill, New York, 1968.

[172] W. H. Munk, P. Worcester, and C. Wunsch. *Ocean acoustic tomography.* Cambridge University Press, Cambridge, 1995.

[173] R. A. Myers and B. Worms. Rapid worldwide depletion of predatory fish communities. *Nature*, 423:280–283, 2003.

[174] H.-H. Nagel. On the estimation of optical flow: relations between different approaches and some new results. *Artificial Intelligence*, 33:299–324, 1987.

[175] Y. Nakajima, H. Inomatad, H. Nogawab, Y. Satoa, S. Tamuraa, K. Okazakic, and Seiji Torii. Physics-based flow estimation of fluids. *Pattern Recognition*, 36(5):1203–1212, 2003.

[176] R. W. Nero, C. H.Thompson, and J. M. Jech. In situ acoustic estimates of the swimbladder volume of Atlantic herring (Clupea harengus). *ICES J. Mar. Sci.*, 61:323–337, 2004.

[177] R. W. Nero, C. H.Thompson, and R. Love. Low-frequency acoustic measurements of Pacific hake, Merluccius productus, off the west coast of the United States. *Fish. Bull. (Wash. DC)*, 96:329–343, 1998.

[178] R. W. Nero and M. E. Huster. Low-frequency acoustic imaging of Pacific salmon on the high seas. *Can. J. Fish. Aquat. Sci.*, 53:2513–2523, 1996.

[179] N. K. Newlands, M. E. Lutcavage, and T. J. Pitcher. Atlantic bluefin tuna in the Gulf of Maine, I: estimation of seasonal abundance accounting for movement, school and schoolaggregation behaviour. *Environ. Biol. Fishes.*, 77:177–195, 2006.

[180] J. N. Newman. *Marine Hydrodynamics.* MIT Press, Cambridge, 1977.

[181] M. Niquen and E. Diaz. Advances in research on the spatial distribution of anchovy and sardine off the peruvian coast. Document, 2001.

[182] M. Niquen and P. Freon. A new record set by the Peruvian fishery: 2.5 million tonnes of anchovy landed in November 2005. *Globec Int Newsletter*, 12:56, 2006.

[183] L. Nottestad, M. Aksland, A. Beltestad, A. Ferno, A. Johannessen, and O. A. Misund. Schooling dynamics of Norwegian spring spawning herring (Clupea harengus L) in a coastal spawning area. *SARSIA*, 80(4):277–284, 1996.

[184] O.A.Misund, A. Fernö, T. Pitcher, and B. Totland. Tracking herring schools with a high resolution sonar. Variations in horizontal area and relative echo intensity. *ICES J. Mar. Sci.*, 55:58, 1998.

[185] R. L. O'Driscoll, P. J. Grimes, S. M. Hanchet, and A. Dunford. Acoustic estimates of southern blue whiting from the campbell island rise, august-september 2004. Document, N Z Fish Assess Rep 2005/41, 2005.

[186] L.-Y. Oey and L. P. Atkinson. Shoreward intrusion of upper gulf stream water onto the U.S southeastern continental shelf. *J. Phys. Oceanography*, 17:2318–2333, 1987.

[187] C. B. Officer. *Introduction to the theory of sound transmission.* McGraw-Hill, New York, 1958.

[188] A. Okubo. Dynamical aspects of animal grouping. *Adv. Biophys.*, 22:1–94, 1986.

[189] E. Ona. Physiological factors causing natural variations in acoustic target strength of fish. *J. Mar. Biol. Assoc. UK*, 70:107–127, 1990.

[190] E. Ona. An expanded target-strength relationship for herring. *ICES J. Mar. Sci.*, 60:493–499, 2003.

[191] R. Ortega, G. Devés, and A. Carmona. Bio-metals imaging and speciation in cells using proton and synchrotron radiation X-ray microspectroscopy. *J. R. Soc. Interface*, 6:S649–S658, 2009.

[192] W. J. Overholtz. The gulf of maine-georges bank atlantic herring (clupea harengus): spatial pattern analysis of the collapse and recovery of a large marine fish complex. *Fisheries Research*, 57(3):237 – 254, 2002.

[193] W. J. Overholtz, J. M. Jech, L. Michaels, L. D. Jacobson, and P. J. Sullivan. Empirical Comparisons of Survey Designs in Acoustic Surveys of Gulf of Maine-Georges Bank Atlantic Herring. *J. Northw. Atl. Fish. Sci.*, 36:127–144, 2006.

[194] W. J. Overholtz and J. S. Link. Consumption impacts by marine mammals, fish, and seabirds on the Gulf of MaineGeorges Bank Atlantic herring (Clupea harengus) complex during the years 19772002. *ICES J. Mar. Sci.*, 64(1):83–96, 2007.

[195] B. L. Partridge, J. Johansen, and J. Kalish. School structure of giant bluefin tuna in Cape Cod Bay. *Environ. Biol. Fish.*, 9:253–262, 1983.

[196] C. L. Pekeris. The propagation of a pressure pulse in the atmosphere. *Physical Review*, 73:145–154, 1948.

[197] H. Peltonen and H. Balk. The acoustic target strength of herring *Clupea harengus*l. in the northern baltic sea. *ICES J. Mar. Sci.*, 60:493–499, 2005.

[198] A. Pentland and B. Horowitz. Recovery of nonrigid motion and structure. *IEEE Trans. Pattern Anal. Mach. Intell.*, 13(7):730, 1991.

[199] A. Le Pichon, P. Herry, P. Mialle, J. Vergoz, N. Brachet, M. Garcés, D. Drob, and L. Ceranna. Infrasound associated with 2004-2005 large sumatra earthquakes and tsunami. *Geophysical Research Letters*, 32:L19802, 5 pp., 2005.

[200] A. D. Pierce. Guided infrasonic modes in a temperature- and wind-stratified atmosphere. *Journal of the Acoustic Society of America*, 41:597–611, 1967.

[201] E. K. Pikitch, C. Santora, E. A. Babcock, A. Bakun, R. Bonfil, D. O. Conover, P. Dayton, P. Doukakis, D. Fluharty, B. Heneman, E. D. Houde, J. Link, P. A. Livingston, M. Mangel, M. K. McAllister, J. Pope, and K. J. Sainsbury. Ecosystem-based fishery management. *Science*, 305:346–347, 2004.

[202] T. J. Pitcher. *Encyclopedia of Ocean Sciences*, pages 978–987. Academic Press, London, 2001.

[203] T. J. Pitcher and J. Parrish. *The behavior of teleost fishes.* Chapman and Hall, London, 1993.

[204] T. J. Pitcher and B. L. Partridge. Fish school density and volume. *Mar. Biol.*, 54:383–394, 1979.

[205] M. B. Porter. The kraken normal mode program, user's manual. Technical report, SACLANT Undersea Research Centre, La Spezia, Italy, 1991.

[206] M. B. Porter and E. L. Reiss. A numerical method for bottom interacting ocean acoustic normal modes. *J. Acoust. Soc. Am.*, 77:1760–1767, 1985.

[207] T. Potapova and G. Gorbsky. Classic mitosis in a vertebrate cell. SCB Image & Video Library. VID-31. Available at: http://cellimages.ascb.org/u?/p4041coll12,233, Accessed August 2007.

[208] J. R. Preston. Reverberation at the Mid-Atlantic ridge during the 1993 AR-SRP experiment seen by R/V Alliance from 200-1400 Hz and some modeling inferences. *J. Acoust. Soc. Am.*, 107:327–259, 2000.

[209] J. L. Prince. Motion estimation from tagged MR image sequences. *IEEE Trans. Med. Imag.*, 11(2):238, 1992.

[210] D. V. Radakov. *Schooling in the ecology of fish*, chapter Characteristics and biological importance of schools, pages 77–99. Wiley, New York, 1973.

[211] P. Ratilal, Y. Lai, and N. C. Makris. Validity of the sonar equation and Babinets principle for scattering in a stratified medium. *J. Acoust. Soc. Am.*, 112:1797–1816, 2002.

[212] P. Ratilal, Y. Lai, D. T. Symonds, L. A. Ruhlman, J. R. Preston, E. K. Scheer, M. T. Garr, C. W. Holland, J. A. Goff, and N. C. Makris. Long range acoustic imaging of the continental shelf environment: the acoustic clutter reconnaissance experiment 2001. *J. Acoust. Soc. Am.*, 117:1977–1998, 2005.

[213] P. Ratilal and N. C. Makris. Mean and covariance of the forward field propagated through a stratified ocean waveguide with three-dimensional random inhomogeneities. *J. Acoust. Soc. Am.*, 118:3532–3559, 2005.

[214] C. Ray, C. R. Robins, J. Douglass, and R. T. Peterson. *Peterson Field Guide: Atlantic Coast Fishes.* Houghton Mifflin, New York, 1999.

[215] J. W. S. Rayleigh. *The Theory of Sound: Vol 2*, pages 1–48. Dover, New York, 1976.

[216] Lord Rayleigh. *The Theory of Sound*, page 296. Dover, New York, 1896.

[217] S. G. Reebs. Can a minority of informed leaders determine the foraging movements of a fish shoal? *Anim. Behav.*, 59:403–409, 2000.

[218] F. Reif. *Fundamentals of Statistical and Thermal Physics.* McGraw-Hill, New York, 1965.

[219] C. W. Reynolds. Flocks, herds and schools: a distributed behavioral model. *Comp. Graph.*, 21:25–33, 1987.

[220] K. Rhode, T. Lambrou, D. J. Hawkes, G. Hamilton, and A. M. Seifalian. Validation of an optical flow algorithm to measure blood flow waveforms in arteries using dynamic digital x-ray images. volume 3979, pages 1414–1425. SPIE, 2000.

[221] J. S. M. Rusby, M. L. Somers, J. Revie, B. S. McCartney, and A. R. Stubbs. An experimental survey of a herring fishery by long-range sonar. *Mar. Biol.*, 22:271–292, 1973.

[222] J. M. Ruth, W. C. Barrow, R. S. Sojda, D. K. Dawson, R. H. Diehl, A. Manville, M. T. Green, D. J. Krueper, and S. Johnston. Advancing migratory bird conservation and management by using radar: an interagency collaboration. Open-File Report 2005-1173, US Geological Survey, 2005.

[223] P. G. Saffman, M. J. Ablowitz, E. Hinch, J. R. Ockendon, and P. J. Olver. *Vortex dynamics*, page 253. Cambridge University Press, Cambridge, 1992.

[224] R. S. Scorer. The dispersion of a pressure pulse in the atmosphere. *Proceedings of the Royal Society of London*, A201:137–157, 1950.

[225] L. I. Serberov. In H. Gjosaeter, editor, *Proc. Soviet-Norwegian Symp. on the Barents Sea Capelin*, pages 135–147. Institute of Marine Research, Bergen, 1985.

[226] National Marine Fisheries Service. NEFSC Resource Survey Report (2003) Spring bottom trawl survey. Technical Report Accessed on 26 Feb, 2009 at www.nefsc.noaa.gov/esb/index.html, NEFSC, 2003.

[227] E. Shaw. *Development and evolution of behavior*, chapter Schooling in fishes: critique and review, pages 452–480. Freeman, San Francisco, 1970.

[228] E. J. Simmonds and D. N. MacLennan. *Fisheries acoustics.* Chapman and Hall, London, second edition, 2005.

[229] A. Singh. An estimation-theoretic framework for image-flow computation. pages 168–177, dec. 1990.

[230] G. Skaret, L. Nottestad, A. Ferno, A. Johannessen, and B. E. Axelsen. Spawning of herring: day or night, today or tomorrow? *Aquatic Living Resources*, 16(3):299 – 306, 2003.

[231] K. B. Smith and E. B. Cushman. A comparison of quasi-continuous wave and broadband travel time techniques in the prediction of long-range reverberation. *J. Acoust. Soc. Am.*, 102:1063–1071, 1997.

[232] P. Smith. The horizontal dimensions and abundance of fish schools in the upper mixed layer as measured by sonar. In G. Farquhar, editor, *Int. Symp. on Sound Scattering in the Ocean*, pages 563–591. Department of the Navy, Washington DC, 1970.

[233] S. M. Song and R. M. Leahy. Computation of 3-d velocity fields from 3-d cine ct images of a human heart. *Medical Imaging, IEEE Transactions on*, 10(3):295–306, Sep. 1991.

[234] R. A. Stephen. Solutions to range-dependent benchmark problems by the finite-difference method. *J. Acoust. Soc. Am.*, 87:1527–1534, 1990.

[235] K. I. Stergiou and H. I. Browman. Bridging the gap between aquatic and terrestrial ecologyIntroduction. *Mar. Ecol. Prog. Ser.*, 304:271–272, 2005.

[236] K. D. E. Stokesbury, J. Kirsch, E. D. Brown, G. L. Thomas, and B. L. Notcross. Spatial distributions of Clupea pallasi and Theragra chalcogramma. *Fish. Bull. (Wash. DC)*, 98:400–409, 2000.

[237] M. Strasberg. The pulsation frequency of nonspherical gas bubbles in liquids. *J. Acoust. Soc. Am.*, 25:536–537, 1953.

[238] D. J. T. Sumpter. The principles of collective animal behaviour. *Philosophical Transactions of the Royal Society B: Biological Sciences*, 361(1465):5–22, 2006.

[239] O. Sund. Echo sounding in fishery research. *Nature*, 135:953, 1935.

[240] G. Sundnes and O. Sand. Studies of a physostome swimbladder by resonance frequency analyses. *J. Cons. Int. Explor. Mer.*, 36:176–182, 1975.

[241] D. Suter. Motion estimation and vector splines. pages 939–942, jun. 1994.

[242] T. J. S. Sykes. A correction for sediment load upon the ocean floor: Uniform versus varying sediment density estimations-implications for isostatic correction. *Marine Geology*, 133:35–49, 1996.

[243] D. Tang, F. S. Henyey, Z. Wang, K. L. Williams, D. Rouseff, P. H. Dahl, J. Quijano, and J. W. Choi. Mid-frequency acoustic propagation in shallow water on the New Jersey shelf II: intensity fluctuation. *J. Acoust. Soc. Am.*, 24:EL91EL96, 2008.

[244] D. Terzopoulos and K. Waters. Analysis of facial images using physical and anatomical models. pages 727–732, dec. 1990.

[245] D. Thompson, C. D. Buck, B. J. McConnell, and J. Garrett. Foraging behavior and diet of lactating female southern sea lions in the Falkland Islands. *J. Zool. (Lond.)*, 246:135–146, 1998.

[246] D. J. Thomson. Wide-angle parabolic equation solutions to two range-dependent benchmark problems. *J. Acoust. Soc. Am.*, 87:1514–1520, 1990.

[247] D. J. Thomson, G. H. Brooke, and J. A. DeSanto. Numerical implementation of a modal solution to a range-dependent benchmark problem. *J. Acoust. Soc. Am.*, 87:1521–1526, 1990.

[248] R. E. Thorne and G. L. Thomas. Acoustic observations of gasbubble release by Pacific herring (Clupea harengus pallasi). *Can. J. Fish. Aquat. Sci.*, 47:1920–1928, 1990.

[249] V. Ticina and I. Kacic. Some field observations on usefulness of searchlight sonar during bluefin tuna (Thunnus thynnus L.) fishing activities in the Adriatic Sea. *Inst Oceanog Ribar Split Biljeske*, 85, 2001.

[250] A. N. Tikhonov. On the stability of inverse problems. *Doklady Akademii Nauk SSSR*, 39:195–198, 1943.

[251] I. Tolstoy and C. S. Clay. *Ocean acoustics.* McGraw-Hill, New York, 1966.

[252] J. Toner and Y. Tu. Long-range order in a two-dimensional dynamical xy model: How birds fly together. *Phys. Rev. Lett.*, 75(23):4326–4329, Dec 1995.

[253] J. Toner and Y. Tu. Flocks, herds, and schools: a quantitative theory of flocking. *Phys. Rev. E. Stat. Phys. Plasmas Fluids Relat. Interdiscip. Topics*, 58:4828–4858, 1998.

[254] R. Toresen. Predation on the eggs of Norwegian spring-spawning herring (Clupea harengus L.) on a spawning ground on the west coast of Norway. *ICES J. Mar. Sci.*, 48(1):15–21, 1991.

[255] A. Tran. Anchovy industry data, North Carolina State University. www4.ncsu.edu/ dbeggles/education/synergy/anchovy/ashanch.html, Accessed 26 Feb, 2009.

[256] G. L. Turin. An introduction to matched filters. *IRE Trans. Inf. Theory*, IF6:311–329, 1960.

[257] S. Uras, F. Girosi, A. Verri, and V. Torre. A computational approach to motion perception. *Biological Cybernetics*, 60:79–87, 1988.

[258] R. J. Urick. *Principles of underwater sound.* McGraw-Hill, New York, third edition, 1983.

[259] R. Vabo and G. Skaret. Emerging school structures and collective dynamics in spawning herring: A simulation study. *Ecological Modelling*, 214(2-4):125 – 140, 2008.

[260] H. C. van de Hulst. *Light scattering by small particles.* Dover, New York, 1981.

[261] T. Vicsek, A. Czirók, E. Ben-Jacob, I. Cohen, and O. Shochet. Novel type of phase transition in a system of self-driven particles. *Phys. Rev. Lett.*, 75:1226–1229, 1995.

[262] S. V. Viscido, J. K. Parrish, and D. Grunbaum. The effect of population size and number of influential neighbors on the emergent properties of fish schools. *Ecological Modelling*, 183(2-3):347 – 363, 2005.

[263] A. Vlasenko and C. Schnörr. Variational approaches to image fluid flow estimation with physical priors. In Wolfgang Nitsche and Christoph Dobriloff, editors, *Imaging Measurement Methods for Flow Analysis*, volume 106 of *Notes on Numerical Fluid Mechanics and Multidisciplinary Design*, pages 247–256. Springer Berlin / Heidelberg, 2009.

[264] S. S. Voit. Tsunamis. *Annual Reviews of Fluid Mechanics*, 19:217–236, 1987.

[265] A. M. Waxman, J. Wu, and F. Bergholm. Convected activation profiles and receptive fields for real time measurement of short range visual motion. pages 723–771, 1988.

[266] USGS website. http://www.iris.iris.edu/sumatra/, Accessed Jan, 2011.

[267] D. Weston. *Underwater acoustics*, volume 2, chapter Sound propagation in the presence of bladder fish, pages 55–88. Plenum Press, New York, 1967.

[268] D. Weston and J. Revie. Fish echoes on a long-range sonar display. *J. Sound. Vibrat.*, 17:105–112, 1971.

[269] E. K. Westwood. Ray model solutions to the benchmark wedge problems. *J. Acoust. Soc. Am.*, 87:1539–1545, 1990.

[270] R. P. Wildes, M. J. Amabile, A.-M. Lanzillotto, and T.-S. Leu. Recovering estimates of fluid flow from image sequence data. *Computer Vision and Image Understanding*, 80(2):246 – 266, 2000.

[271] C. D. Wilson, A. B. Hollowed, M. Shima, P. Walline, and S. Stienessen. Interaction between commercial fishing and walleye pollock. *Alaska. Fish. Res. Bull.*, 10(1):61–77, 2003.

[272] J. D. Wilson. *Quantifying Hurricane Wind Speed with Undersea Sound.* PhD dissertation, Massachusetts Institute of Technology, Cambridge, MA, 2006.

[273] E. Yanez, C. Silva, K. Nieto M. A. Barbieri, and G. Martinez. Using satellite technology improve Chilean purseine fishing fleet. *Gayana (Concepc)*, 68(2):578–585, 2004.

[274] J. Zhu and J. S. Popovics. Leaky rayleigh and scholte waves at the fluid-solid interface subjected to transient point loading. *J. Acoust. Soc. Am.*, 116:2101 – 2110, 2004.

[275] V. N. Zinkevich. *ICNAF Bull.*, 4:101, 1967.